Modelling of friction contacts under dynamic loads with experimental comparison

Fabia Tubita

N° d'ordre NNT: 2023ECDL0021

THÈSE DE DOCTORAT DE L'UNIVERSITÉ DE LYON

Opérée au sein de l'**École Centrale de Lyon**

Unité de recherche: **LTDS**

École Doctorale N° 162

Mécanique - Énergétique - Génie civil - Acoustique

Spécialité: Génie Mécanique

Thèse présentée par:

Fabia TUBITA

Modelling of friction contacts under dynamic loads with experimental comparison

Soutenue publiquement le 12 juin 2023, devant le jury composé de:

Président du jury	E. JACQUELIN	Professeur, Université Claude Bernard Lyon 1, IUT Lyon 1
Rapporteure	E. SADOULET-REBOUL	Maître de conférence HDR, Université de Franche-Comté, FEMTO-ST
Rapporteur	S. ZUCCA	Professeur, Politecnico di Torino, DIMEAS
Co-encadrant	L. BLANC	Maître de conférence, École Centrale de Lyon, LTDS
Directeur de thèse	F. THOUVEREZ	Professeur, École Centrale de Lyon, LTDS

Acknowledgement

Au terme de ce projet de thèse, il est inévitable de regarder en arrière et de noter toutes les leçons, les défis et les enseignements qui m'ont accompagnée jusqu'au bout. Ce fût une expérience intense, souvent difficile et en même temps un voyage passionnant d'apprentissage et de développement, non seulement sur le plan strictement académique, mais aussi sur le plan humain et personnel. Pour cela, je ne peux qu'exprimer ma gratitude aux personnes qui, par leur soutien scientifique ou humain, mais aussi par un simple mot d'encouragement ou un sourire, ont contribué à la réalisation de ce travail de recherche.

Je tiens tout d'abord à remercier Emeline Sadoulet-Reboul et Stefano Zucca d'avoir accepté de rapporter ce travail de thèse ainsi que pour leurs remarques intéressantes et pour les échanges durant la soutenance. J'adresse également mes remerciements à Éric Jacquelin qui a présidé ce jury pour l'attention et l'intérêt portés à mes travaux.

J'adresse à présent mes sincères remerciements à mon directeur de thèse Fabrice Thouverez pour la confiance accordée en m'accueillant dans son équipe et pour m'avoir accompagnée avec bienveillance durant ces années de recherche. Je tiens ensuite à exprimer ma profonde gratitude envers Laurent Blanc pour sa disponibilité à toute épreuve, son optimisme contagieux, sa patience et pour tous les précieux conseils qu'il m'a prodigués ainsi que pour sa relecture rigoureuse de mes rapports et de ce manuscrit. Ce fût une grande chance de bénéficier de son encadrement.

Aussi, je souhaite adresser de chaleureux remerciements à l'ensemble du personnel du LTDS, doctorants et permanents, en particulier aux locataires des bâtiments G8(bis-ter-phare) et E6 que j'ai eu la chance de côtoyer tout au long de cette thèse. Toutes les discussions scientifiques, l'entraide sur Matlab, mais aussi les moments de détente ont été un soutien constant pour l'avancement de ce travail. À ce sujet, je tiens à adresser quelques remerciements particuliers: à Nicolas G. pour son aide pratique, notamment durant la première partie de la thèse, pour sa patience et pour le temps qui m'a accordé afin de répondre à mes nombreuses questions et doutes. Toutes les discussions que nous avons pu avoir (au tableau) et ses précieux conseils m'ont permis d'avoir des bons outils pour la suite de la thèse; à Samuel pour son énorme disponibilité et bienveillance et pour ses précieuses suggestions concernant l'implémentation en Matlab des méthodes numériques. Sans oublier bien sûr mes co-bureaux Corentin et Marine ainsi que Lionel et Stéphane pour tous les bons moments passés ensemble pendant les repas du midi, entre bonne humeur et mots fléchés. Je souhaite également remercier Isabelle pour tout le travail administratif réalisé et pour toutes les démarches concernant les déplacements à l'étranger prévus dans le cadre de la thèse.

Desidero inoltre ringraziare Giulia, collega durante questo percorso di tesi nonché concittadina, per tutti i tragicomici momenti trascorsi insieme, tra pause caffè, giri di campo dell'EC e passeggiate nella *forêt*, condividendo pensieri oscillanti tra euforia e demoralizzazione, espressioni e frasi idiomatiche non traducibili ma capaci di esprimere a pieno i nostri stati d'animo, oltre che cadute rovinose, sempre però con la capacità di rialzarci.

I also acknowledge the European Commission (EACEA) for providing and funding this research opportunity through Marie-Skłodowska Curie Action - Horizon 2020 ITN - Project EXPERTISE (models, EXperiments and high-PERformance computing for

Turbine mechanical Integrity and Structural dynamics in Europe). Being part of this project was a challenging experience that has enriched me personally and professionally.

At the EXPERTISE consortium, I have found a great and stimulating environment with inspiring professors and friendly colleagues. My gratitude goes to the early-stage researchers with whom I had the opportunity to exchange valuable conversations, giving me valid hints for improving my framework, and also to spend fun and memorable moments during the research activities and the summer school training periods at the Imperial College London (UK) and the Samara State Aerospace University (Russia). For a certain period, the pandemic situation limited our meetings, but not our exchanges and updates.

I would also like to express my gratitude to Iyabo Lawal from Texas University for the precious discussions about the test rig's experimental results, for having tried to answer (despite the different time zones) all my critical remarks and curiosities always encouraging me with a positive attitude and for the fun times spent in London.

Infine vorrei profondamente ringraziare la mia cara famiglia. I miei genitori, fonte di sostegno incondizionato, sempre presenti e vicini nonostante la distanza, per avermi trasmesso il valore della perseveranza e per aver sempre incoraggiato le mie scelte, anche se spesso il mio lavoro quotidiano risultasse per loro un mistero; le mie sorelle, Valeria e Gabriella, per loro capacità unica di comprendermi e accompagnarmi verso ogni gradino della vita, sia esso in salita o in discesa, e per ricordarmi sempre cosa è davvero importante. Ringrazio infinitamente Giuseppe per la pazienza, il supporto e l'incitamento a portare a termine questo lavoro, per aver condiviso con me anche questo traguardo, ma soprattutto per la metà di vita finora trascorsa insieme. A loro questo lavoro è dedicato, così come tutti i piccoli e grandi obiettivi fin qui raggiunti e quelli che ancora verranno. Ad maiora.

This project has received funding from the European Union's Horizon 2020 research and innovation program under the Marie Skłodowska-Curie grant agreement N° 72186.

Abstract

A typical aero engine is a complex mechanical structure made of many assemblies whose components are connected by mechanical joints. These joints introduce interfaces that are subjected to various static and dynamic loads during the engine's operational life. These conditions can lead to high structural vibrations and cycle fatigue failures, resulting in energy losses and reduced performance. The damages could be increased especially when the operating frequencies of the system are close to the resonant frequencies of the structure. Some common friction joints in turbomachines, such as interfaces between disk and blade, shroud contacts and friction under-platform dampers, are designed to undergo relative micro-sliding motion at the interfaces and provide friction damping at the contact interfaces to reduce the amplitude vibration levels by dissipating energy. However, dry friction is also one of the most critical sources of nonlinearities and uncertainty for predicting the global dynamic behaviour of assembled structures. The vibrations induced by repeated dynamic loads can cause fretting wear.

Friction and wear problems are multi-scale and multi-physical by nature. Fretting wear occurs at the micro-scale level of the asperities, over a long period, deteriorating the contact surface geometry by producing wear debris through material removal and dissipating energy. The worn geometry can affect the dynamic response of the whole system over time and limit the operating lifetime. With this aim, improving numerical simulation methods and developing predicting tools is essential to prevent when operational vibration levels become critical for anticipating potential failures in the first design phases and planning appropriate maintenance.

In this context, this PhD work aims at improving the understanding of the physics of frictional contacts by evaluating the effect of fretting wear on dynamics. This is achieved by validation through experimental evidence of an efficient prediction tool developed to simulate the nonlinear dynamic behaviour arising from friction contact. The proposed numerical method allows calculating simultaneously vibrational behaviour and wear evolution in fretting wear problems. The coupling between dynamics and wear is implemented through a multi-scale approach by considering two-time scales: a fast scale for dynamics and a slow scale for tribological phenomena. The numerical study of fretting wear under dynamic loading is based on a fretting test campaign performed at Imperial College London. In particular, the experimental test rig reproduces the dynamic behaviour observed in friction dampers. Hence, it can give an additional detailed description of contact interfaces and allow more accurate modelling of these elements.

The results obtained are consistent with those given from experimental evidence making it possible to demonstrate the method's applicability and evaluate the dynamic/wear coupling, with some limitations related to the assumptions used. In addition, numerical simulations enable the evaluation of local scenarios for quantities not directly measured by experiments, such as the distribution of wear over the interface and the evolution of the wear volume during the time, pointing out that the constant dialogue between experiments and updated simulations can enable one to go beyond the measurements or calculations alone.

Keywords: nonlinear dynamic, friction contact, fretting wear, multi-scale problem

Résumé

Un moteur d'avion est une structure mécanique complexe composée de nombreux assemblages dont les composants sont reliés par des jonctions mécaniques. Ces jonctions introduisent des interfaces qui sont soumises à diverses charges statiques et dynamiques au cours de la vie opérationnelle du moteur. Ces conditions peuvent entraîner des vibrations structurelles de niveau élevé et des défaillances causées par des chargements cycliques, entraînant des pertes d'énergie et des performances réduites. Les dommages pourraient être accentués surtout lorsque les fréquences de fonctionnement du système sont proches des fréquences de résonance de la structure. Certaines jonctions utilisées dans les turbomachines, tels que les surfaces entre l'aube et le disque et les d'amortisseurs par frottement sec situés sous les plate-formes, sont conçus pour subir un mouvement de microglissement relatif aux interfaces et fournir un amortissement de friction aux interfaces afin de réduire les niveaux vibratoires en dissipant l'énergie. Cependant, le frottement sec est également l'une des sources les plus critiques de non-linéarités et d'incertitude pour prédire le comportement dynamique global des structures assemblées et les vibrations induites par des charges dynamiques répétées peuvent provoquer une usure par fretting.

Les problèmes de frottement et d'usure sont multi-échelles et multiphysiques par nature. L'usure par frottement se produit au niveau microscopique des aspérités, sur une longue période, détériorant la géométrie de la surface de contact en produisant des débris d'usure par enlèvement de matière et par dissipation d'énergie. La géométrie usée peut affecter la réponse dynamique du système global et limiter sa durée de vie. Dans ce but, l'amélioration des méthodes de simulation numérique et le développement d'outils de prédiction sont essentiels pour prévenir le moment où les niveaux de vibration opérationnels deviennent critiques pour anticiper les dommages potentiels déjà dans les premières phases de conception.

Dans ce contexte, cette thèse vise à améliorer la compréhension de la physique des contacts frottants en évaluant l'effet de l'usure par fretting sur la dynamique vibratoire. Ceci est réalisé à travers la validation par des essais expérimentaux d'un outil de prédiction numérique efficace développé pour simuler le comportement dynamique non linéaire. La méthode numérique proposée permet de calculer simultanément le comportement en vibration et l'évolution de l'usure. Le couplage entre dynamique et usure est mis en œuvre à travers une approche multi-échelle en considérant deux échelles de temps : une échelle rapide pour la dynamique et une échelle lente pour les phénomènes tribologiques. En particulier, l'étude numérique de l'usure par fretting vibratoire est basée sur une campagne d'essais de fretting réalisée à l'Imperial College London. Le banc d'essai expérimental reproduit le comportement dynamique observé dans les amortisseurs à friction. Par conséquent, il peut donner une description détaillée supplémentaire des interfaces de contact et permettre une modélisation plus précise de ces éléments.

Les résultats obtenus de prévision numérique sont cohérents avec ceux donnés par les essais permettant de démontrer l'applicabilité de la méthode et d'évaluer le couplage dynamique/usure, avec quelques limitations liées aux hypothèses utilisées. De plus, des simulations numériques supplémentaires ont permis d'évaluer des scénarios locaux pour des grandeurs non directement mesurées par les essais, comme l'observation locale au niveau de la zone de contact c'est-à-dire la répartition de l'usure sur l'interface et

l'évolution du volume usé au cours du temps. Les résultats obtenus pourront aussi servir aux expérimentateurs pour proposer des protocoles expérimentaux pour l'étude du fretting sous chargement dynamique. Pour finir, la validation numérique d'un essai expérimental a permis de souligner l'importance d'un dialogue constant entre essais expérimentaux et simulations numériques pour aller au-delà des mesures et des calculs.

Mots-clés: dynamique non-linéaire, frottement, usure par fretting, problème multi-échelle

Contents

Introduction

Industrial context

Engineering systems consist of many assembled parts made up of several contacting elements. In particular, modern gas turbines are critical components whose design and manufacturing processes are optimised to improve performance, efficiency and safety/work-ability respecting the increasingly stringent environmental criteria. Due to the relatively high loads to which they are subjected, the structural and mechanical integrity of the rotating components strongly affects the successful operations of these machines [1]. However, a major problem with assembled components is that these

are highly stressed and subjected to severe conditions in terms of pressure and temperature, as well as to various static and dynamic loads, during the whole engine's operational life. These conditions can lead to high structural vibrations and cycle fatigue failures, resulting in energy losses and reduced performance. Vibrations can be induced by various sources, classified as structural and aeroelastic [1]. The maximum vibration amplitude at resonances must be controlled and maintained below a certain threshold to keep a reasonable service life and avoid premature failure.

A primary objective of the design process is to ensure structural and mechanical integrity. Hence, vibrations are a central problem in the design of aircraft engines. Predicting the lifetime of engine components as early as possible in the first design phases is a crucial step for manufacturers. Therefore, having tools to prevent when operational vibration levels become critical is crucial for anticipating potential failures and planning appropriate maintenance.

Different strategies have been devised to prevent the excitation of resonant frequencies and aeroelastic instabilities in the operative range. It is possible to act on the mechanical configurations by adjusting the system's dynamic characteristics, for example, by varying the number of blades or the natural frequencies, with appropriate design solutions. If resonances are not avoided despite these adjustments, it is necessary to ensure that the vibration response remains within acceptable limits. For this purpose, the damping of the system can be exploited. Damping in rotating turbine blades is mainly composed of aerodynamic and mechanical damping. The latter includes viscous and material hysteresis damping and damping due to mechanical joints. The best option at the moment is to provide external sources of damping, for example, in the form of dry friction devices. In such systems, friction is provided by adding special passive devices, so-called friction dampers, located at specifically selected points of the structures that need to be damped [2, 3]. Once adequately modelled, the parameters describing these friction interfaces can be optimised to achieve friction benefits. Hence, the joint damping by friction is the most considered and implemented [4]. Despite the significant reduction in maximum vibration

levels over the operating range, one of the main disadvantages of friction damping is that friction also introduces micro and/or macro slip at the contacts that can accompany fretting wear and energy dissipation. Fretting wear over a large number of cycles leads to High Cycle Fatigue (HCF), a dominant failure mode of turbomachinery components during operation. The energy dissipation accumulated leads to material loss, modifying the contact conditions. Moreover, a worn geometry induces a change in the vibration level [5], altering the dynamic response.

Some common friction joints in turbomachines include the surfaces between root-blade and slot-disk, shroud contacts and bolted flange joints, friction under-platform dampers, gears, bearing, and dovetail joints. The design of these devices provides friction damping undergoing relative micro-sliding motion at the contact interfaces, useful to reduce amplitude vibration levels [6–8].

Scientific context

Damping systems are based on friction energy dissipation and have a positive effect representing an effective means to reduce significant resonant stresses. However, dry friction in contact interfaces is one of the most critical sources of nonlinearities and uncertainty for predicting the global dynamic behaviour of built-up structures. Energy dissipation leads to fretting wear and material loss. Fretting wear is an alternating motion of small amplitude occurring between two surfaces in contact. It can be found in almost all mechanical connections subject to variable vibrations and represents one of the most critical surface premature failures of engine components, that may lead to severe engine damage. This phenomenon can modify the interfaces at a micro-scale level, influencing the dynamic response of the global system. For this reason, it is crucial to study the long-term effects of wear, its evolution, and its impact on dynamic response. Thus, the manufacturers need to understand and predict the wear effects on dynamics to estimate the performance and improve the design standards.

Faced with the complexity of such interactions at the interface, tribology, a science dedicated to the study of lubrication, friction and wear [9], provides a fundamentally scientific approach to understanding these phenomena at the contacting surfaces. Friction is a dissipative phenomenon; part of the energy dissipated by friction is worn out through various processes (physics-chemical processes, material transformations, formation of third bodies debris) that lead to wear. The investigation and modelling of fretting wear represent an acknowledged field of research. Many studies have been conducted for quasi-static problems, as examined in [10], but very few attempts have been made to include fretting wear in dynamic analysis and evaluate its influence on the dynamic response of a frictional contact system [11–17]. Improving numerical simulation methods and developing predicting tools are essential to achieve an optimised design in the first phases and verify the resistance and integrity of the different parts to the various loads.

More experimental studies are needed to validate numerical prediction and improve the understanding of these phenomena, numerically replicating the physics of the problem. The challenge is to investigate the impact of wear on the dynamics of structures having access to elements of scenarios under the scope of experimental tests and perform a more detailed local analysis. The design of industrial systems is too complex and difficult to understand through full-scale testing. Their cost is prohibitive for design phases,

with tests reserved for validation. The design of simplified experimental setups can help reproduce industrial components' configurations at a laboratory scale. Therefore, it is necessary to control all the physical phenomena from the design phase onward.

Research objectives

The main objective of this work is to improve the understanding of the physics of frictional contacts by evaluating the effect of fretting wear on the dynamics. This is achieved by developing and validating advanced models for dynamic simulations with experimental evidence. The numerical study of the fretting wear under dynamic loading is based on a fretting test campaign. In particular, the vibratory friction rig designed in the Dynamic group of the Imperial College London [18] and the series of fretting wear experiments published in [19] are considered here. The test rig reproduces the dynamic behaviour observed in friction dampers. Thus, it can give an additional detailed description of the contact interfaces, allowing more accurate modelling of these elements. FIGURE 1 illustrates an example of an industrial structure and its interfaces subjected to fretting wear and the corresponding test experiment at a laboratory scale.

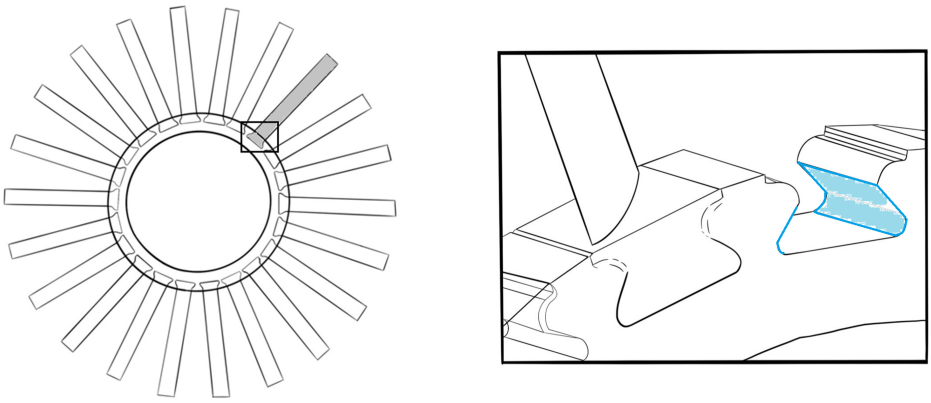

(a) Turbine blade with a zoom on a dovetail joint.

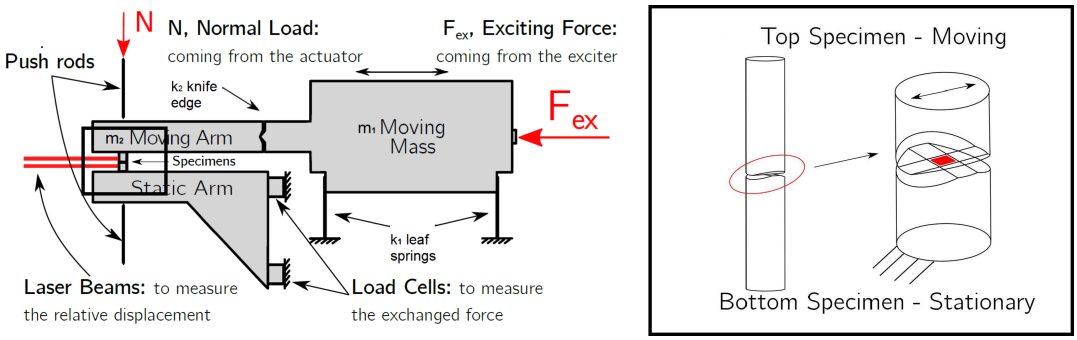

(b) Fretting test rig [19] with a zoom on the contact joint.

FIGURE 1: Example of an industrial structure and their interfaces subjected to fretting wear (a) and the corresponding at a laboratory scale (b).

More specifically, the following objectives are defined:

1. Validate through experimental evidence an efficient prediction tool to simulate the nonlinear dynamic behaviour arising from friction contact, implementing the

coupling between wear phenomena and dynamics.

2. Evaluate local scenarios numerically for quantities not directly measured by experiments, such as a local observation at the contact zone, the distribution of the wear over the interface and the evolution of the wear volume during the time. Additional numerical investigations point out where the constant dialogue between experiments and updated simulations can enable one to go beyond the measurements.

EXPERTISE project: an overview. This thesis has been funded by the European Commission's Framework Program Horizon 2020 through the Marie Sklodowska-Curie Innovative Training Networks (ITN) EXPERTISE [20] (EXperiments and high-PERformance computing for Turbine mechanical Integrity and Structural dynamics in Europe) grant agreement. The project, based on the collaboration between various academic and industrial partners from across Europe, has the ultimate goal of developing advanced tools for the dynamic analysis of large-scale models of turbomachinery components to pave the way for the virtual simulation of the whole engine. For this purpose, the EXPERTISE project is divided into four work packages as indicated in FIGURE 2. These relate to 1. Modelling of friction contact - 2. Joint identification - 3. Structural dynamics - 4. High-Performance Computing (HPC). The current research is part of work package 1 concerning advanced friction contact modelling. Improving the understanding of the physics of frictional contact interfaces is the first step required to develop highly efficient friction models, which, coupled with more efficient and accurate nonlinear dynamic analysis tools, enable much faster and more reliable computations. To further reduce computational costs and extend the analysis capabilities to much larger engineering structures, the final goal is to integrate the developed analysis framework with high-performance computing techniques, allowing more accurate dynamic analysis of a large-scale turbomachinery model.

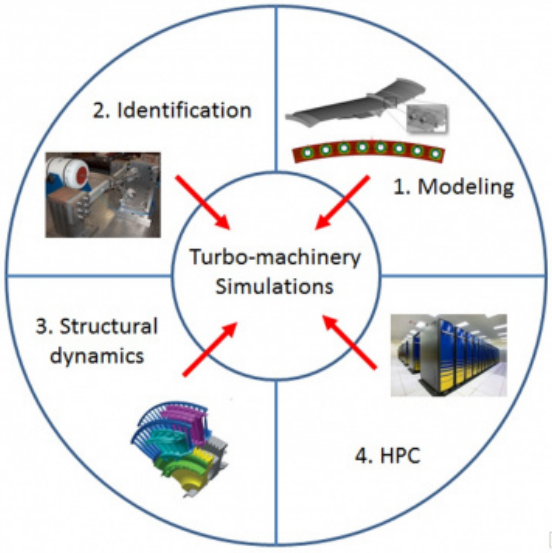

FIGURE 2: Work packages distribution in the EXPERTISE project.

Outlines

This manuscript is organized into five chapters.

Chapter I is dedicated to bibliographic research introducing the basic principles that will be considered in the manuscript. First, a review of the advances in dynamic analysis considering nonlinearities arising from friction contact, and then different wear models and fretting wear approaches are presented, with the most significant findings in fretting wear (definition, sliding modes, wear mechanisms and fretting maps). Finally, a review of the analytical formulations and numerical methods to solve contact problems is given, emphasising the influence of wear on the nonlinear dynamic analysis and highlighting the importance of experimental tests.

Chapter II is concerned with solving the dynamic problem with contact nonlinearities. Different resolution methods are presented, focusing on the frequency method of harmonic balance. For the nonlinear contact problem, not having expression in a frequency domain, a method for calculating the contact forces in the time domain based on the dynamic Lagrangians is considered. Due to the high computational times caused by a nonlinear dynamic resolution, the models' size is reduced using a substructuring method.

Chapter III introduces the numerical strategy to account for wear in a nonlinear dynamic problem. The system evolution is studied by splitting time into two scales: a fast scale for dynamics and a slow scale for wear phenomena. The chosen approach simultaneously calculates the wear evolution and the vibration response. An academic numerical example is used to validate the method and introduce various aspects and quantities concerning the evolution of contact interface (hysteresis loops, wear volume and forced dynamic response).

Chapter IV focuses on the description and the pre-test calibration of the Imperial College vibratory test rig. First, by performing a finite element modelling of the experiments, followed by an efficient reduction of the problem's size and then by conducting a sensitivity analysis to justify the choice of the numerical and physical parameters. Finally, the nonlinear dynamic analysis of the unworn system is performed and evaluated to validate the model.

Chapter V provides a numerical investigation of the series of fretting wear tests performed by the vibratory test rig previously introduced. The numerical results are compared with the experimental ones, making it possible to demonstrate the method's applicability and evaluate the dynamic/wear coupling. In addition, numerical simulations enable the evaluation of the change of specific parameters not directly provided by experimental evidence, such as the wear depth distribution over the interface, and the wear volume over time.

Finally, the conclusion summarises the main contributions and findings achieved. Areas for further development are identified with a perspective on how the current work, supported by experimental results, fits into the general framework of the nonlinear dynamic analysis with friction contact.

Chapter I

State-of-the-art of contact modelling

This chapter provides a brief literature review concerning the dynamic analysis of generic structures with friction contact nonlinearities. Starting from an introductory description of classical contact models, the first part goes on to present different wear models and fretting wear approaches with the most significant findings in fretting wear. The second part moves on to describe the modelling of friction and wear in contact mechanics and discuss the effect of wear on the nonlinear dynamic analysis, highlighting the importance of experimental tests.

Outline of the chapter

1.1 Research topics addressed in this manuscript

Tribology. Modelling a tribological interface is a very complex task due to the multi-physical and multi-scale nature of the various phenomena involved. Understanding and evaluating this type of problem requires the consideration of multiple aspects: loading conditions, different mechanical behaviours of the materials of the contacting surfaces, debris production and loss of material, as well as thermodynamic and physico-chemical processes, which lead to surface modifications and, consequently, to a degradation of the performance of the structures. In the FIGURE I.1, proposed by Vakis [21], the different nature of all variables implied in these kinds of problems is illustrated, providing an overview of the many aspects to be addressed in tribological issues. However, the context of turbomachinery components involves only some of the effects indicated, but these result in significant contributions to introducing difficulty in modelling their impact on the dynamic response of the whole engine.

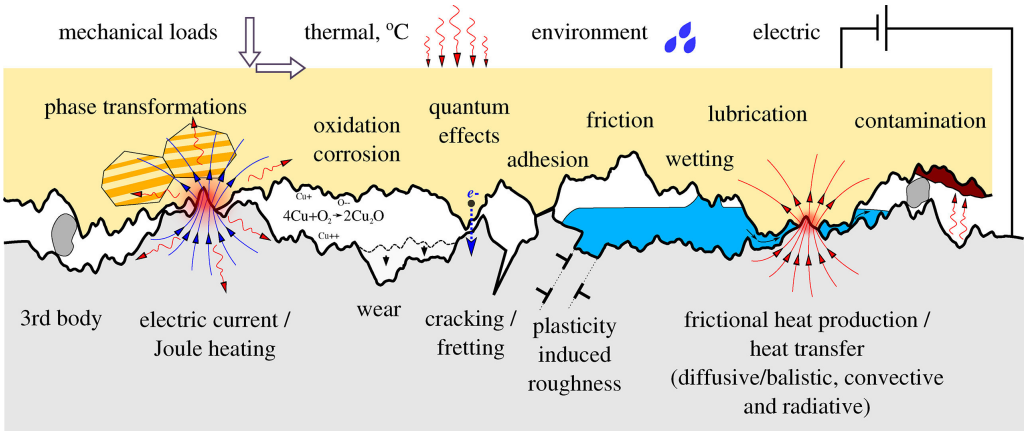

FIGURE I.1: A schematic representation of the multi-physical nature of tribological interfaces: two bodies into contact under different loading conditions [21].

Generally, wear is defined as the progressive loss of material from the surface of a body, occurring as a result of a relative movement over another one [22]. Different classes of wear can be distinguished, including adhesive, abrasive, surface fatigue, corrosive and erosive wear, cavitation and fretting wear. Of all these different types of wear, fretting wear is the dominant one observed experimentally during the series of fretting tests performed at the Imperial College London and published in [19]. Fretting wear is a kind of damage in contact surfaces caused by oscillatory relative displacements of small amplitude between them. This phenomenon is difficult to quantify: it produces modifications of the surfaces caused by material removal and debris flow in and out of the contact interface.

Dynamics. The interaction between vibrations and tribological mechanisms has only rarely been investigated. The dynamic response of a system can normally be considered a macro-scale problem of short duration. Instead, the fretting wear, caused by the dynamic response, occurs at the micro-scale level of the asperities over a long period, deteriorating the contact surface geometry by producing wear debris through material removal and

dissipating energy. Therefore, the worn geometry can affect the dynamic response of the whole system over time and limit the operating lifetime for a large number of industrial applications characterized by vibrating interfaces. Almost all engine vibrating interfaces are susceptible to failure due to fretting if not well designed. In the case of under-platform dampers, for example, the alternating displacements at friction interfaces can cause a strongly nonlinear dynamic response and lead to fretting wear at the contact.

Experimental tests help researchers better understand the phenomenon and find the best way to predict it with more certainty and confidence. Wear effects should be considered early in the design process of the components because:

1. wear phenomena occur in service. Thus, it would be appropriate to predict the behaviour of the structures to take solutions in advance by reducing wear rates to an acceptable level within the economic and design constraints imposed;

2. an understanding of the factors that control wear phenomena can help manufacturers propose palliative methods for minimising the problem.

The challenges aim to ensure the safety and integrity of components, optimizing maintenance and technological innovation. The difficulty arises because of the multi-scale and multi-physics nature of the interactions occurring on contact. Hence, the importance of developing prediction tools able to couple tribological and dynamic problems. The durability and reliability of mechanical structures are significant in industry, especially in the aerospace field, where environmental and technological challenges are constantly increasing.

Contact is a nonlinear and non-regular phenomenon, being the contact's laws discontinuous. Several contact and friction laws have been developed in the literature, some of them discontinuous to get closer to the real physics of a frictional contact, others regularized to enhance their integration in the numerical solvers and improve the convergence of the solution algorithm. The next section aims to explain the classical contact and friction laws used in the rest of this manuscript.

1.2 Classical contact modelling

Contact laws establish the relationships between local contact loadings (pressure or force) and local kinematics (gap or velocity). In general, they should be as simple as possible, involving only a small number of empirical parameters derived from measurements or experience, without losing the main tribological characteristics of the interacting surfaces. Thus, contact laws identify the contact's status: the separation, stick or slip between two solids. From these statuses, the contact forces can be evaluated.

1.2.1 Contact law in the normal direction (Signorini conditions)

When two bodies are in contact, the unilateral interactions at the interface are fundamentally modelled by a unilateral contact's law that states the relationship between the normal forces and the relative motion in the normal direction. The so-called Signorini conditions [23] are illustrated in FIGURE I.2. From a mathematical standpoint, these constraints may be defined as a set of complementary conditions as follows:

$$\begin{cases} \delta_N \geq 0 \\ f_N \geq 0 \\ \delta_N f_N = 0 \end{cases} \tag{I.1}$$

where f_N are the normal contact forces (chosen to be positive by convention) and δ_N is a gap representing the non-negative normal distance between surfaces in contact. These contact conditions or boundary conditions are:

- the first inequality in (I.1) represents the geometric condition of no-penetration:

$$\delta_N \geq 0 \Leftrightarrow \begin{cases} \delta_N > 0 & \text{no contact,} \\ \delta_N = 0 & \text{contact,} \end{cases} \tag{I.2}$$

- the second inequality in (I.1) represents a static condition of non-sticking:

$$f_N \geq 0 \Leftrightarrow \begin{cases} f_N > 0 & \text{contact,} \\ f_N = 0 & \text{no contact,} \end{cases} \tag{I.3}$$

- the third condition in (I.1) is a mechanical complementarity condition, indicating that there may be contact or separation at one point:

$$\delta_N f_N = 0 \Leftrightarrow \begin{cases} f_N = 0 & \text{separation,} \\ \delta_N = 0 & \text{contact.} \end{cases} \tag{I.4}$$

In a more compact form, the Signorini conditions can be expressed as:

$$0 \leq \delta_N \perp f_N \geq 0. \tag{I.5}$$

This law is strongly irregular. Its implementation in the different numerical methods for resolving a nonlinear problem is very complex, but it has the advantage of being exact. To avoid the numerical problems caused by non-regular laws, a contact stiffness k_N (i.e. a penalty factor) at the contact interface [24] is used to linearly regularize the unilateral contact's law This regularized law, represented in FIGURE I.2b can be expressed as:

$$f_N = \begin{cases} k_N \delta_N & \text{if} \quad \delta_N \leq 0, \\ 0 & \text{if} \quad \delta_N > 0. \end{cases} \tag{I.6}$$

Other regularized laws have been introduced, including an exponential law [25], as shown in FIGURE I.2c, more regular than the linear one.

1.2.2 Contact law in the tangential direction (Coulomb friction)

The interface behaviour has been modelled [26] through free energy and a specific pseudo-potential, including thermal effect and wear phenomena. Strömberg [27, 28] formalised the laws at the interface, taking into account thermodynamic principles and all possible

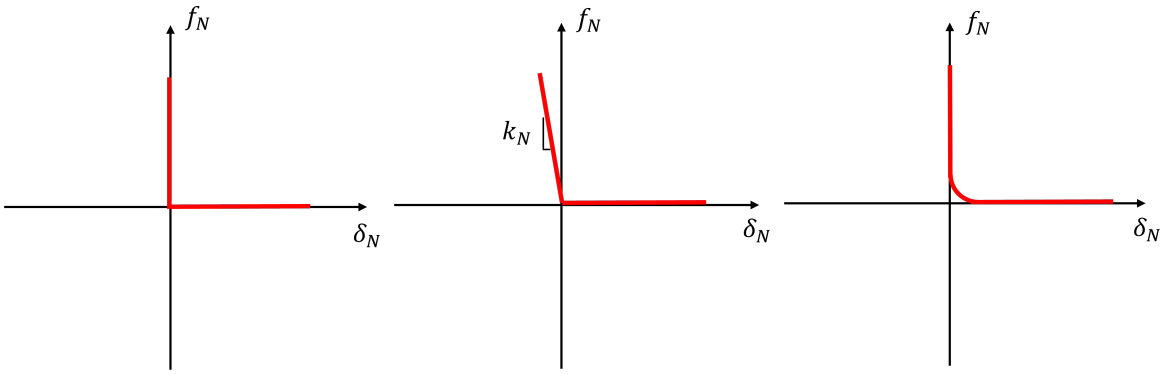

(a) Unilateral (b) Linear (c) Exponential

FIGURE I.2: Contact laws representation.

wear mechanisms. Theoretical developments will not be repeated here, but readers may refer to them in [27, 28]. Here, the different adhesion and sliding regimes between dry surfaces are commonly distinguished in the tangential contact plane. Friction can be defined as the resistance (friction force) encountered by one body in a relative tangential movement (sliding) over another. Friction is a dissipative phenomenon and is the leading cause of damping in mechanical joints.

In the same way, as for the contact laws, several models have been developed to capture the behaviour at the contacting interface and integrate it into the structural response. Most of them are empirically based and need to be calibrated with experimental results to be considered valid for a specific contact. The most basic dry-friction model available in the literature is the Coulomb friction law or, more accurately, the Amontons-Coulomb friction law. It was initially based on two postulates by Amontons [29] to which, later, Coulomb [30] added a third one: (1) friction force is directly proportional to the applied load (Amontons 1st law, 1699); (2) friction force is independent of the apparent contact area (Amontons 2nd law, 1699); (3) kinetic friction is independent of the sliding velocity (Coulomb friction law, 1790). In 1833, Morin found that the static friction, i.e. the friction at zero sliding speed, is larger than the Coulomb one [31]. With regard to static friction, Coulomb friction is also called dynamic friction.

According to the Coulomb friction model, it is impossible to have a relative motion if the tangential force f_T is less than the Coulomb limit force $f_{lim} = \mu|f_N|$. The Coulomb law for dry friction can be formulated as follow:

$$\begin{cases} \dot{\delta}_T = 0 & \text{if} \quad ||f_T|| \leq f_{lim}, \\ f_T = -\mu|f_N|\frac{\dot{\delta}_T}{||\dot{\delta}_T||} & \text{if} \quad ||\dot{\delta}_T|| > 0, \end{cases} \tag{I.7}$$

where μ is the friction coefficient, δ_T and $\dot{\delta}_T$ are the vectors of the relative tangential displacement and velocity, respectively. Coulomb's friction law does not include asperities interactions. FIGURE I.3a shows the Coulomb friction law without any softening.

As well as the contact laws, alternative formulations for the friction laws are generally developed to simplify the numerical solutions [25, 32]. It is possible to regularize Coulomb's law by adding tangential stiffness k_T, which is representative of the elasto-plastic behaviour of the asperities of the interface. This stiffness enables a nonzero tangential relative displacement when the tangential force at the interface is lower than

the Coulomb limit. The Coulomb law is then modified, taking this form:

$$f_T = \begin{cases} k_T(\delta_T - z) & \text{if} \quad ||f_T|| \leq f_{lim}, \\ -\mu|f_N|\frac{\dot{\delta}_T}{||\dot{\delta}_T||} & \text{if} \quad ||\dot{\delta}_T|| > 0, \end{cases} \tag{I.8}$$

in which z is the relative displacement of the contact point. Its value is calculated by respecting that $f_T \leq f_{lim}$. This formulation thus allows elastic displacement when the tangential stress at the interface is less than the Coulomb limit as illustrated in FIGURE I.3b. It is also possible to regularize Coulomb's friction law by following an arc-tangent evolution, FIGURE I.3c.

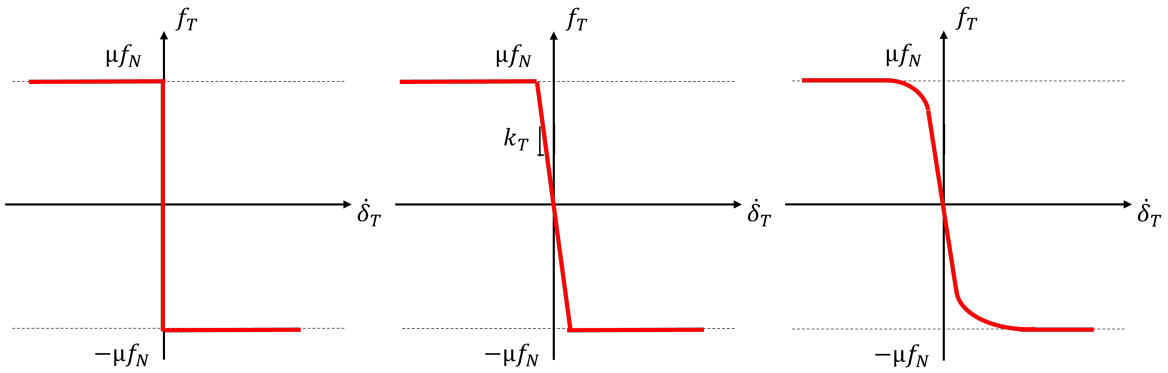

(a) Coulomb (b) Linear regularization (c) Arc-tangent regularization

FIGURE I.3: Friction laws representation.

In 1886, Reynolds introduced the concept of viscous friction in relation to lubricants [33]. In the viscous model, the friction force is a linear function of the sliding velocity. This model is often combined with the Coulomb friction model. In 1901, Stribeck observed that the friction force decreases with increased sliding velocity from the static friction ($\mu_s f_N$) to the Coulomb friction (μf_N) [34], as represented in FIGURE I.4.

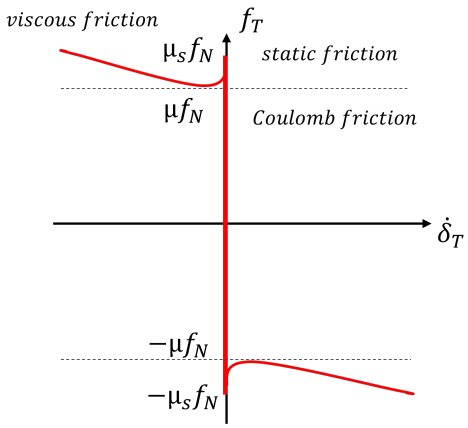

FIGURE I.4: Stribeck friction model.

Several frictional models have been developed and used to capture interface behaviour and integrate it with structural response models [35]. Among them, the Bouc-Wen differential model [36, 37] allows to represent the microscopic behaviours of the micro-slip

type through macroscopic models. This model provides a gradient in the frictional force, not present in the Coulomb one. It is also possible to mention the Dahl [38] and LuGre [39] models, also expressed in a differential form but simpler than the Bouc-Wen model. These models do not take into account wear or plasticity.

1.3 Fretting wear

Friction has the positive effect of dampening vibrations, but it also introduces micro and/or macro slip that may be accompanied by fretting wear. This section introduces the phenomenon of fretting wear from its definition to the classical configurations and parameters defined for testing, with the classification of the different fretting regimes.

1.3.1 Fretting phenomena

Definitions. Fretting can be defined as a micro-displacement oscillatory motion occurring between two loaded surfaces in contact. The sliding between the two contacting surfaces can lead to various surface damage phenomena, such as wear (fretting wear), crack propagation (fretting-fatigue) and corrosion (fretting-corrosion), depending on the amplitude of slip, frequency of vibration, and loading. The magnitude of the movement is typical of the order of micrometres.

Fretting wear indicates a surface degradation process that leads to material removal at the contact interface, for which the small displacements result from external vibrations. If the displacements resulting from the deformation of one of the two surfaces in contact are subjected to cyclic loading, the phenomenon is called fretting fatigue, which causes crack propagation. A sequential oxide formation causes fretting corrosion by chemical reactions and its destruction by wear. Thus, the slipped interface undergoes corrosion. Fretting wear, which will be the subject of this study, is encountered in many industrial contexts where vibrations occur, including the surfaces between root-blade and slot-disk, shroud contacts and bolted flange joints, friction dampers under the platform, gears, bearing, and dovetail joints. Thus, the manufacturers need to understand and predict the wear effects on dynamics to estimate the performance and improve the design standards.

The different contact configurations studied in fretting. The fretting phenomenon is primarily a contact problem. The interface geometry of the two opposing bodies plays an essential role in the redistribution of stresses, influencing their damage. Real mechanical interfaces in industrial components are normally complicated. Hence, it is more suitable for experimental fretting wear studies to refer to simplified geometries able to model degradation mechanisms. The three most common configurations, illustrated in FIGURE I.5, are:

(a) **Sphere/plane**. The contact between a sphere and a flat surface reproduces a punctual contact, as described by Hertz [40] for the first study of fretting phenomena, normal contact indentation. The evaluation of the elastic load distribution in the contact plan was introduced by Hamilton [41, 42] and later deepened by Sackfield and Hills [43]. This contact set, not requiring a particular alignment device, is often used in experiments. However, this configuration needs 3D modelling, resulting in costly computational time.

(b) **Cylinder/plane**. The contact between a cylinder and a flat surface reproduces a linear 2D contact. Analytical solutions in the presence of tangential loads were proposed by Cattaneo [44], and Midlin [45], and the characterization of the stress distributions by McEwen [46]. A 2D contact problem is easier to model. This contact configuration allows to carry out of experimental tests, requiring specific devices to align the cylinder's axis with the plane. Indeed this configuration is often used to analyze cracking phenomena [47–49].

These first two contact settings are similar to most industrial configurations, such as the contact in the blade-disk interface or between rolling elements and the race of a bearing.

(c) **Plane/plane**. This configuration consists of two flat surfaces in contact. This type of contact is the most complicated to set up because of the difficulty of assessing the imposed load correctly. Moreover, the pressure distribution is characterized by an indeterminate discontinuity in the pressure and shear stress fields at the edges of the contact area. Analytical solutions were proposed by Ciavarella et al. [50].

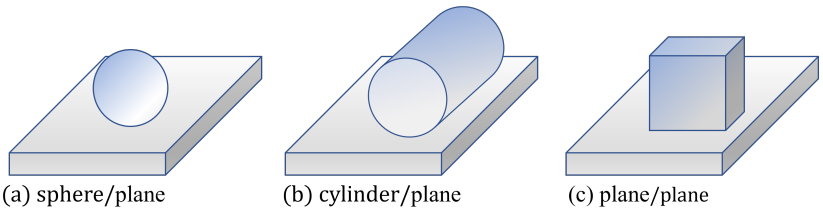

FIGURE I.5: Contact geometry configurations used in fretting wear tests.

Fretting modes. In the framework of a sphere-on-flat contact configuration and defining the parameters of contact as f_N the imposed normal load, f_R the radial force and δ the tangential displacement, three fretting modes have been defined by Mohrbacher et al. [51] and by Blampain et al. [52]:

- Mode I: linear tangential displacements
- Mode II: radial displacements
- Mode III: circumferential displacements

These three fretting modes are shown in FIGURE I.6, where the arrows represent the sliding zones while the white areas are the adherent zones. The work in this manuscript refers only to linear fretting (Mode I), which is undoubtedly the most studied mode due to many industrial applications for which it can be taken as a reference.

Fretting loops. A typical fretting (or hysteresis) loop is illustrated in FIGURE I.7. It represents the relationship between the friction force f_T and the amplitude of relative displacements δ_T occurring between contacting surfaces during a fretting cycle. The shape of a hysteresis loop for the frictional force is due to the oscillatory nature of the excitation.

From the study of the fretting loop, it is possible to define the following parameters:

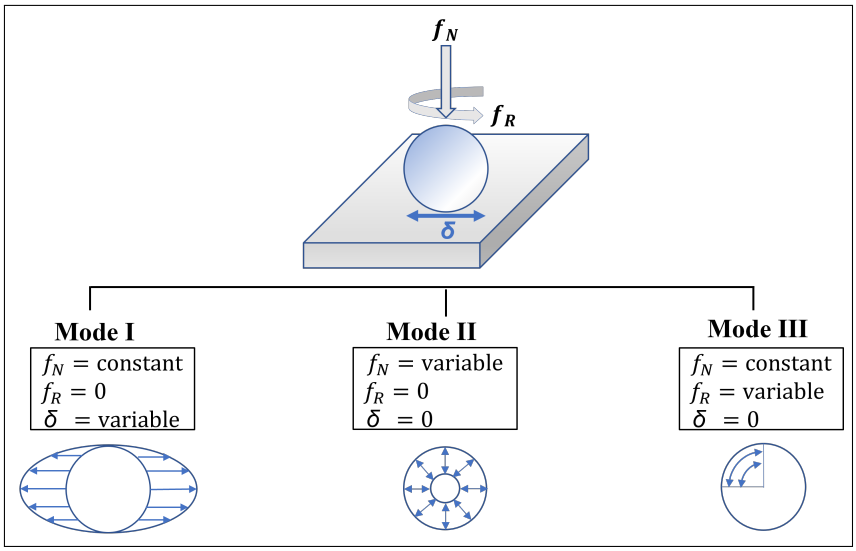

FIGURE I.6: Fretting modes (adapted from Blamplain et al. [52]).

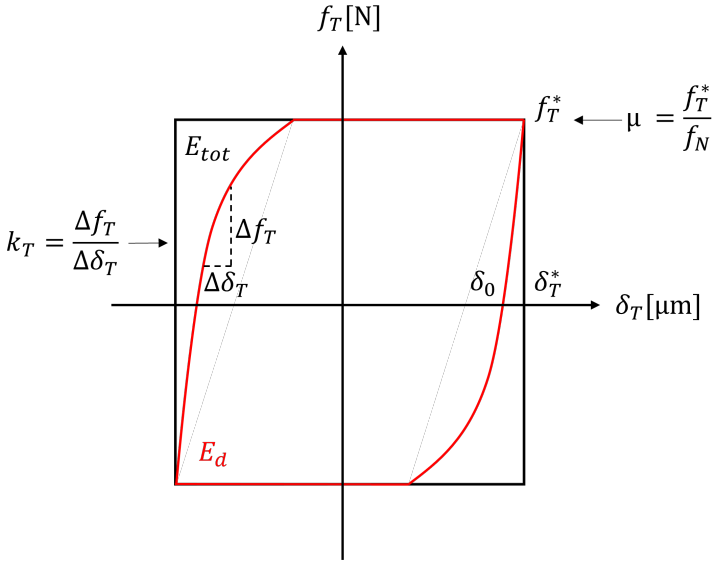

FIGURE I.7: Schema of a typical fretting loop and its parameters.

- f_T^* is the maximum tangential force amplitude. It allows calculating the friction coefficient μ via the normal applied force f_N as:

$$\mu = \frac{f_T^*}{f_N}. \tag{I.9}$$

- δ_T^* is the maximum displacement amplitude reached in a cycle. This is the parameter directly controlled in the fretting wear tests. This amplitude is measured as close as possible to the contact.

- δ_0 is the sliding amplitude also defined as the cycle aperture, representing the residual relative displacement when $f_T = 0$.

- k_T is the tangential contact stiffness. It is evaluated as the slope of the fretting

loop following the sliding direction and estimated as:

$$k_T = \frac{\Delta f_T}{\Delta \delta}. \tag{I.10}$$

- E_d is the dissipated energy due to friction [53, 54] during a fretting loop and is represented by the area enclosing the fretting cycle. It is estimated as:

$$E_d = \int_{-\delta^*}^{\delta^*} f_T(\delta)\, d\delta \approx 4\ f_T^*\ \delta_0. \tag{I.11}$$

  The energy dissipation occurs through various mechanisms such as the creation of wear debris, increase of temperature, cracking, plastic deformation, and physico-chemical transformation. For a rectangular fretting cycle, the energy dissipated is equal to: $E_d = 4\ f_T^*\ \delta_T^*$.

FIGURE I.8 illustrates the hysteresis loops for the Coulomb friction model, for a regularized Coulomb friction model and for the Bouc-Wen model, previously mentioned in section I.1.2.2.

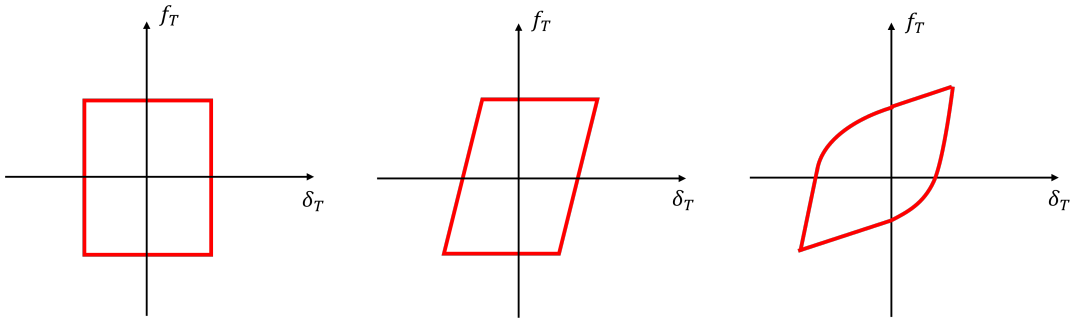

(a) Coulomb (b) Regularized Coulomb (c) Bouc-Wen

FIGURE I.8: Hysteresis loop for different friction models.

Parameters defining a test. During a test, the evolution of the parameters derived from the fretting loop can provide indications about the nature of the contacting surface and give information about potential damages.

The characterisation of the fretting in experimental tests is mainly carried out for the Mode I illustrated in FIGURE I.6. Indeed, as it is close to most industrial configurations, it allows simple testing, especially for fretting wear. A classic test consists of imposing a normal force f_N on a sphere or cylinder in contact with a plane. A tangential displacement is then imposed on one of the solids, being the other fixed. The measured tangential force is noted as f_T.

A distinction must be made between fretting and alternating sliding conditions associated with larger amplitudes. In order to formalise this transition, the fretting test is characterised by the sliding ratio e [54] between the sliding amplitude δ_0 and the contact size in the sliding direction a_s, such as:

$$e = \frac{\delta_0}{a_s}. \tag{I.12}$$

If the sliding ratio is smaller than 1 ($e < 1$), whatever the contact geometry, the central zone of the interface is always in contact, and other zones periodically change between contact and no contact. This situation is called fretting. If the sliding ratio is larger than 1 ($e > 1$), the whole contact surface is out of contact during a part of a sliding cycle. This corresponds to an alternating sliding condition.

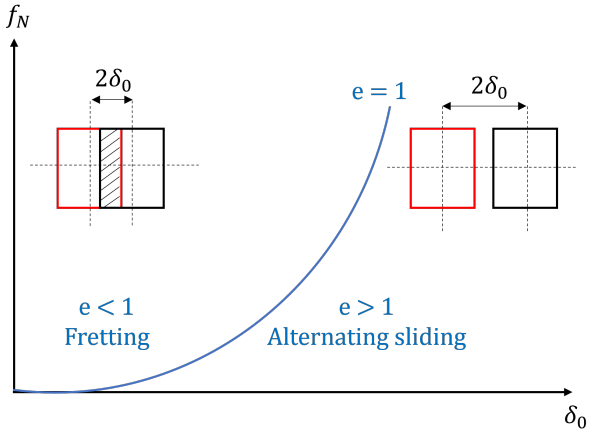

FIGURE I.9: Identification of the transition states between fretting and alternating sliding.

1.3.2 Fretting regimes classification

According to the magnitude of the displacement δ_T for a given normal force f_N, the fretting phenomenon leads to three different regimes, which impose a particular degradation of the materials in contact. Each regime corresponds to different sliding conditions, characterised by a different fretting loop shape. In FIGURE I.10 the three different fretting regimes and the related fretting loop shapes are illustrated according to the following classification:

(a) **Stick regime**. The full contact is adherent (low damage). This condition is encountered in several types of situations, such as minimal relative displacement of the contacting bodies, high normal force, high friction coefficients or low stiffness of the device. In this case, there is no hysteresis, and the fretting loop has a closed linear shape.

(b) **Partial slip regime**. As soon as the friction force locally reaches the Coulomb threshold μf_N, there is a local slip of the surfaces around a stuck zone. This means that the centre of the contact area remains adherent, but slip occurs at the edges. The fretting loop assumes an elliptical shape with a slight opening of the cycle and the linear parts curving slightly at the ends of the contact.

(c) **Gross slip regime**. For larger displacement amplitudes, there is no more stick behaviour at the interface, but the whole contacting surface is in sliding. According to Coulomb's law, the tangential force reaches its limit value $f_T^* = \mu f_N$ and is no longer proportional to the displacement (fretting wear). The tangential force is constant during the period of sliding. The fretting loop assumes a trapezoidal

shape. Typically, it has an approximately flat top and bottom where the friction force has reached its limiting value, as predicted by Coulomb's law.

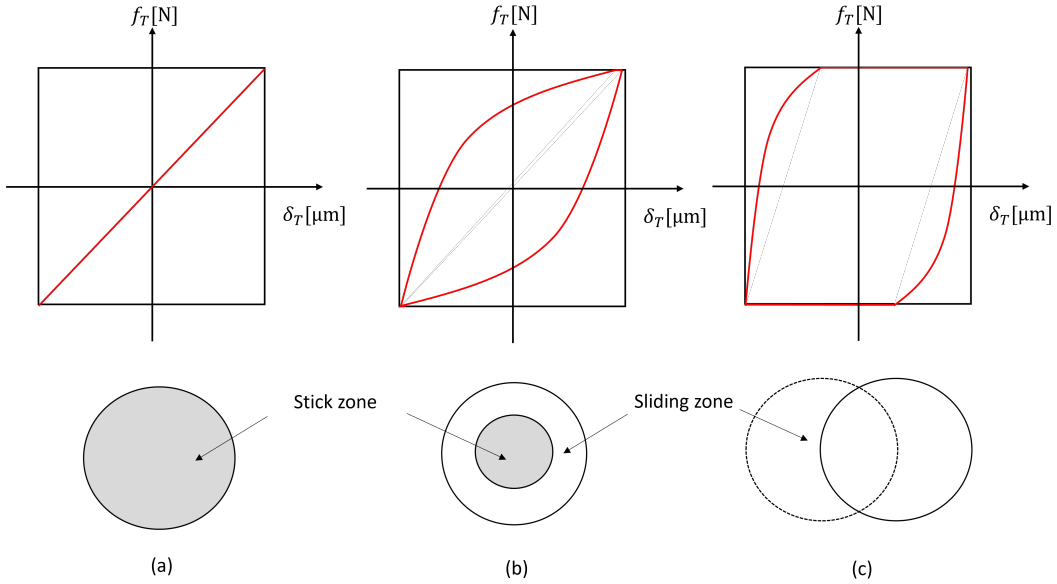

FIGURE I.10: Representation of the fretting loops and corresponding sliding conditions: (a) stick, (b) partial slip, (c) gross slip.

Fretting maps. After having performed fretting experiments for a contact configuration sphere/plane, Vingsbo and Söderberg [55] established the concept of fretting maps to plot the different wear regimes and transitions between them observed in practice. A fretting map consists of a 2D graph where the normalised applied pressure is plotted against the normalised relative displacement amplitude, as illustrated in FIGURE I.11, where three regimes are mapped.Later, Vincent et al.[53] introduced an experimental mapping of the material response, showing the significant dependence of the evolution of fretting damage on the type of fretting regime. This map is shown in FIGURE I.12.

1.4 Tools for wear prediction at local scale

Fretting wear is a complex phenomenon involving a critical number of mechanisms. It requires considering debris formation, surface modifications, and thermodynamic and physical-chemical phenomena. Quantifying wear is difficult because of the lack of universal and well-formulated wear models. To define wear kinetics, in 1995, Meng and Ludema reviewed some 5466 articles and listed more than 300 different formulations for wear [10], providing an exhaustive summary of a large number of wear models and equations existing in literature, achieving that each model or equation refers to particular experimental conditions, generally not transferable to industrial problems.

1.4.1 Approaches for wear kinetics evaluation

Archard's wear law. In 1953, Archard [56] proposed a wear formulation which quantifies the adhesive wear of sliding contact. A typical measure of wear is the volume

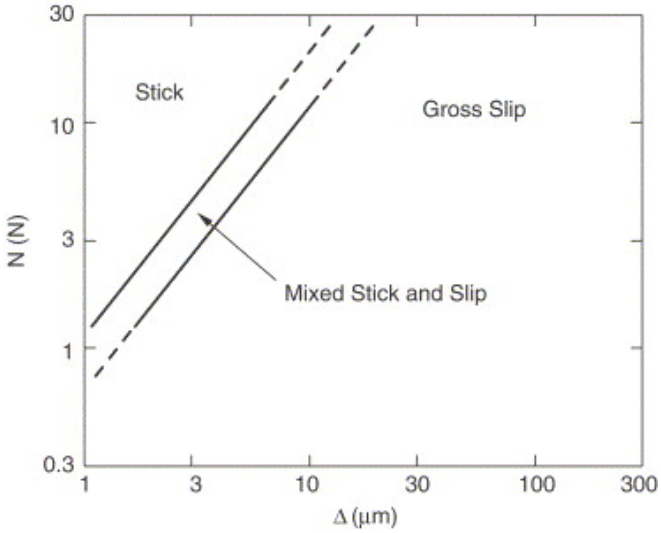

FIGURE I.11: Fretting map in terms of normal load N vs. displacement amplitude Δ [55].

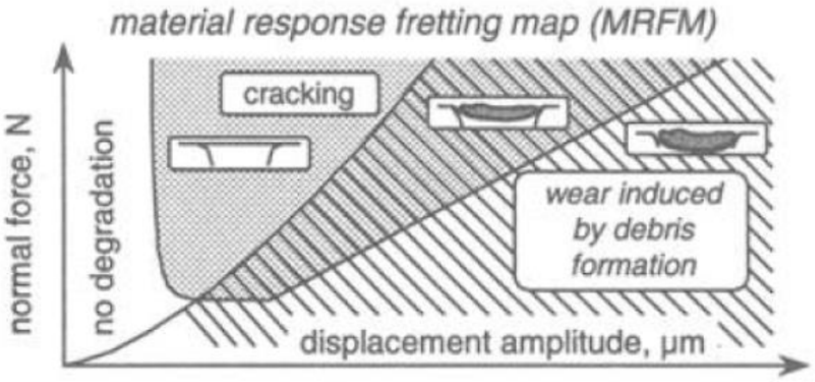

FIGURE I.12: Material response fretting map [53].

of material removed per unit of sliding distance. In particular, Archard's wear equation states that the volume of lost material, as a result of a tribological interaction, denoted as V_w, is directly proportional to the product of the applied normal load N and the total relative sliding distance L. Therefore, since less wear is observed when the hardness H of the softer material in contact increases, the worn volume V_w can also be considered inversely proportional to the hardness H of the material to be worn. The Archard's wear equation is then expressed as

$$V_w = \frac{k_w}{H} NL, \tag{I.13}$$

or, in terms of the worn volume per unit sliding distance, as:

$$\frac{V_w}{L} = \frac{k_w}{H} N, \tag{I.14}$$

where k_w is the dimensionless Archard's wear coefficient which represents the probability that an asperity interaction results in the production of wear particles. This coefficient,

determined experimentally, depends on material properties and operating conditions.

Noting that if the sliding distance L is the result of sliding at a constant velocity v_r, it is given by $L = v_r t$, where t is the sliding time, for an infinitesimal time increment dt, Eq. (I.13) can be expressed in a differential form:

$$\frac{dV_w}{dL} = \frac{k_w}{H} N^{(t)}, \tag{I.15}$$

where dV_w, dL and $N^{(t)}$ are the wear volume increment, the sliding distance increment and the normal interface contact force, at the time instant t, respectively.

Assuming that the wear depth increment on the microelement area ΔA is dw, the instantaneous wear volume increment dV_w can be expressed as:

$$dV_w = \Delta A \cdot dw. \tag{I.16}$$

To simulate the evolution of wear along the contact surface and substituting Eq. (I.16) in Eq. (I.15), this latter can be reformulated in terms of wear rate, i.e. the increment of local wear depth dw for increment of local slip dL as:

$$\frac{dw}{dL} = K_w P_N, \tag{I.17}$$

where $P_N = N^{(t)}/\Delta A$ is the contact pressure at the contact microelement ΔA and K_w is the dimensional Archard's wear coefficient [57] or specific wear rate, usually expressed in $[\mathrm{mm^3 m^{-1} N^{-1}}]$. This coefficient replaces the k_w/H previously defined. The wear rate K_w changes drastically in the range of $10^{-15} - 10^{-1}$ $[\mathrm{mm^3 m^{-1} N^{-1}}]$, depending on operating conditions and type of material in contact ([56, 58–60]). Since the relative sliding distance dL is the integral of the relative velocity v_r versus time t, Eq. (I.17) can be rewritten as:

$$dw = K_w P_N v_r \; dt. \tag{I.18}$$

One should observe that this law does not consider the friction coefficient μ. Indeed, it is noted that Archard's law is well adapted to provide wear predictions of tribosystems showing a stable friction behaviour.

Energy-based models. Mohrbacher [51] was the first to introduce the concept of cumulative dissipated energy in the study of fretting wear. Later, specific wear laws, formulated in terms of energy from the sliding on the whole interface, were developed by a team from the LTDS [54, 61]. In order to evaluate the total worn volume, Fouvry et al. [54] proposed a wear law based on the friction dissipated energy during a fretting test of N_c cycles. The dissipated energy E_d, defined in SECTION I.1.3.1, is equal to the sum of the work of the tangential forces f_T during each fretting cycle:

$$E_d = \sum_{c=1}^{N_c} E_d(c) = \sum_{c=1}^{N_c} f_T \delta_T. \tag{I.19}$$

Following the relationship (I.19), the total worn volume V_w, due to friction, is assumed to be proportional to the accumulated energy E_d, dissipated by friction, after N_c cycles:

$$V = \alpha_u \sum_{c=1}^{N_c} E_d(c), \tag{I.20}$$

where α_u is a wear coefficient, the so-called energy wear rate, experimentally determined and associated with the material. It is defined as the slope of the wear volume versus the cumulative energy dissipated. Indeed, a linear relationship has been found several times in experiments ([61, 62]) between the worn volume and dissipated energy as illustrated in FIGURE I.13.

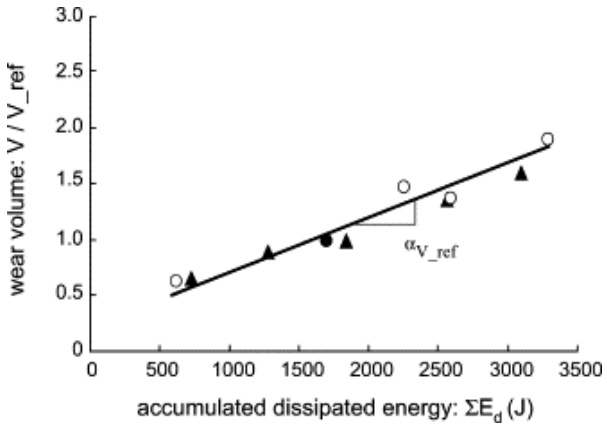

FIGURE I.13: Evolution of the wear volume as a function of the cumulative dissipated energy [63].

The energy-based approaches are widely used in the literature because they provide an accurate estimation of the wear in sliding contact.

It is interesting to observe that the energy wear approach is equivalent to Archard's wear approach for a constant coefficient of friction μ:

$$K_w = \mu\ \alpha_u. \tag{I.21}$$

However, these two descriptions do not explicitly consider the debris layer entrapped in the interface.

Thermodynamic approach. There are also attempts to model wear from a thermodynamic standpoint. Dragon-Louiset et al. [64] considered wear as a dissipative phenomenon linked to the process of particle detachment. They proposed a thermodynamic model for wear analysis of two bodies with a fluid-contact interface, and then a wear criterion is formulated based on the energy release. The thermodynamic approach mesoscopically models the third body. The difficulties are linked to the passage from the microscopic aspects of the wear (third body scale) to the mesoscopic model.

1.4.2 Approaches for wear mechanisms description

Third body concept. In the 1970s, Godet [65] was the first to introduce the concept of "third body" to understand and unify the friction and wear behaviour of sliding

materials. This concept is based on the particles detachment mechanism [66] that arises when two bodies, the so-called "first bodies", are in sliding or fretting contact, generating at the interface an intermediate heterogeneous layer composed of wear debris or particles, the so-called "third body", results of the tribo-mechanical reactions between the first two contacting bodies. The mechanical properties of the third body are separated from those of the two first bodies. FIGURE I.14 provides a simplified scheme of this concept. The third body performs three main functions:

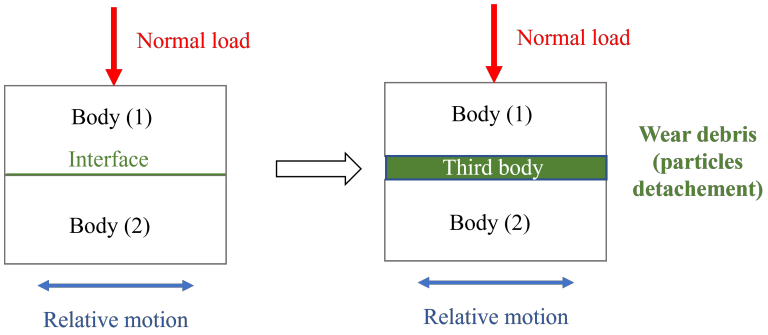

FIGURE I.14: Progression from conventional two bodies wear to three-body wear concept.

1. it separates the first bodies and transmits the load (normal force);
2. it accommodates the relative velocities (tangential forces) at the contact interface;
3. it separates the surfaces in contact, avoiding direct interactions and allowing heat dissipation from the contact.

According to Godet's approach, it is more realistic to associate degradation with the amount of debris ejected from the contact, calculated from the debris flow, rather than the complete wear volume.

The third body concept was then extended by Berthier [67] who proposed the additional conceptual tool of "tribological circuit", illustrated in FIGURE I.15. This concept physically explains the third body phenomenon. The different contributions to the tribological circuit are defined as follows: Q_s is the source flow, corresponding to the particles' detachment mechanism between the first bodies (such as adhesion, abrasion or cracking); it is composed of two contributes: the internal source flow $Q_{s,i}$, representing the flow of particles from the surfaces of the first bodies and $Q_{s,e}$, the external source flow, due to the introduction of an artificial lubricant; Q_r is the re-circulation flow or flow of third body re-introduced into the contact; Q_w is the wear flow, related to the particles ejected from the interface. This phenomenological model can be written in the form of the mass balance equation inside the contact interface.

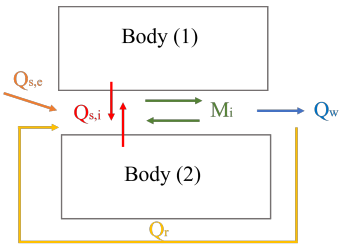

FIGURE I.15: Tribological circuit (simplified form, from [67]).

$$\frac{dM_i}{dt} = Q_s - Q_w. \tag{I.22}$$

In more recent studies, Denape [68] has shown the validity of such phenomenological methods for practical applications. However, these approaches are not predictive models, but they can help to identify the multi-physics and multi-scale interactions occurring in a tribological interface.

Another possibility is modelling the third body as a granular material due to its highly heterogeneous nature. Granular materials are defined as a large collection of discrete, macroscopic particles. In this case, the physical particle detachment, a consequence of the degradation of the materials, can be described as the movement of these particles within the contact and their ejection. The length scale is of great importance in this

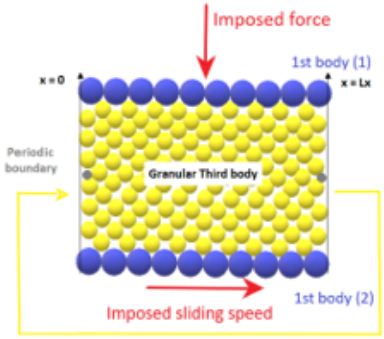

FIGURE I.16: Discrete element modelling of interface [69].

type of problem. In particular, two length scales can be distinguished: a microscopic scale, related to the interactions of the particles, and a macroscopic scale, corresponding to the global behaviour of the bodies in contact. In this regard, a different approach can be found in the literature for solving a three-body frictional system with a granular third body, which corresponds to contact homogenization [70], where a macroscopic contact law based on micro-scale information such as the topography and constitutive properties of the surfaces in contact, is formulated.

To mitigate the scale problem between the first two bodies and the third body, it is also interesting to refer to an asymptotic approach. Studies have been conducted by Bayada [71] and developed by Linck [72]. This approach focused on evaluating the asymptotic behaviour of the third body, considered a thin layer, between an elastic body and a rigid one with a zero-displacement condition, as shown in FIGURE I.17. The introduction of a specific contact law allows taking into account the thin layer's behaviour to evaluate its thickness's influence.

Despite these approaches being very complicated to formalise and do not facilitate the introduction of all variables able to compare the material behaviour, they can help to identify the multi-scale interactions occurring in a tribological process. The third body approach provides a more physical description of wear processes. Furthermore, it is not as clear how to incorporate the effect of wear debris into a mathematical model. In cases where wear debris is more easily removed from the contact area, and the metal-to-metal

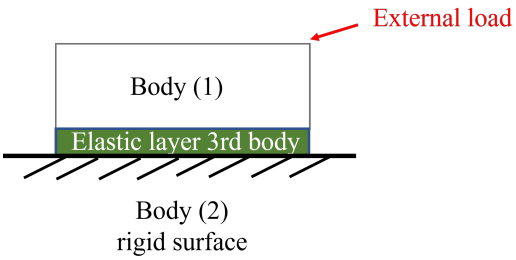

FIGURE I.17: Thin layer: asymptotic approach.

contact is kept, the influence of debris can be reasonably neglected.

1.5 Modelling of friction and wear in contact mechanics

Special friction conditions exist in fretting contacts. Two frictional sliding regimes have been introduced in section I.1.3.2: a total sliding regime, for which the two bodies are in a gross sliding contact during the cyclic movement, and a partial sliding regime for which only a part of the contact surface slides while others remain in a stuck condition during the entire fretting cycle. Only when the whole contact area is in a sliding condition a coefficient of friction can be obtained by measuring the tangential force and the normal load during a fretting test. Many efforts were made to find a realistic model of friction modelling.

1.5.1 Solution approaches for contact problems

Different contact resolution methods have been developed. It is possible to separate them into two main categories: analytical and numerical.

Analytical solutions. The first solution to the problem of contact between two elastic bodies was developed by Hertz [40] on elliptical and non-conforming contacts without friction within the framework of the assumptions of semi-infinite elastic massifs. Hertz's theory results as quite restrictive because of its assumptions. This non-conformity indicates that the non-deformed surfaces of the two bodies are not superimposable other than at a point (punctual contact) or a line (linear contact), as seen in FIGURE I.5. Following this study, many analytical formulations for non-Hertzian contact problems have been developed. A detailed description of them can be found in Johnson's reference book [73].

The contact with friction was later considered, using Coulomb's law. First analytical solutions of the stress field for sliding contacts were provided by McEwen [46] for cylindrical contact, and Hamilton [41] for spherical contact. These solutions are extended to elliptical contacts by Sackfields and Hills [74]. Cattaneo [44], and Mindlin [45] expanded these problems to the case of partial slip by considering a sphere under normal and tangential loads. Later, in a 2D formulation, Ciavarella et al. [50] proposed an analytical solution for a more realistic flat punch with rounded edges. Nowell and Hills [75] proposed closed-form analytical solutions for shear traction distribution at different positions in a fretting cycle. Goryacheva et al. [76] presented an analytical solution evaluating the wear profile in fretting under partial slip conditions.

In more recent analytical formulations, Andresen et al. [77] proposed closed-form solutions for general asymmetrical half-plane contact problems with normal and shear loads and moments. Then, they also considered [78] half-plane frictional contact problems subjected to alternating normal and shear loads in the steady-state and, in the following study [79], the steady state cyclic behaviour of a half-plane contact with partial slip subject to a combination of normal and shear load, moment and differential bulk tension. Latest, Chauda and Segalman [80] proposed a 2D contact analysis using trigonometric polynomials. Analytical formulations give a theoretical basis. However, they are limited to simple contact geometries, which are difficult to apply to more complex industrial structures.

Numerical methods. In continuum mechanics, the Finite Element Method (FEM) [81] is the most popular method in the static and dynamic analysis of structures. It consists of discretizing the system and proving good accuracy and robustness. All aspects related to the finite element method in the field of contact mechanics have been given in [82]. The FEM is the most commonly adopted numerical tool to deal with wear, based on the local implementation of Archard's wear law or the energy wear approach. Johansson [83] used FEM to simulate the evolution of the contact pressure in fretting. McColl et al. [84] used a FEM for simulating the fretting wear considering an incremental wear approach based on Archard's law equation. Paulin et al. [85] used FEM considering an energy wear approach to model the progressive evolution of the wear.

An alternative is the Boundary Element Method (BEM) [86]. In the BEM, only the boundary variables of the domain are considered so that this method can be less expensive in terms of computational time. Several works exist on the application of BEM to sliding wear problems [87]. Sfantos et al. [88, 89] proposed a wear simulation using an incremental sliding BEM. More recent applications for fretting wear prediction can be found in [90, 91]. However, BEM is based on solving partial differential equations that require a formulation in the form of integral equations [92], which is not always possible. When it is difficult to obtain analytical solutions, it is possible to discretize the interface and solve the global problem numerically by summing the analytical solutions of the elementary problem for each discretized element. This latter is the semi-analytical method (SAM), derived from the BEM.

A discrete element method (DEM) is the most appropriate to model discontinuous and heterogeneous media, such as the third body in a worn contact. Another numerical approach, taking into account the thin layer of a third body at the contact interface, can be found in the literature. This approach has been developed by Iordanoff [69] and extended by Fillot [93] to simulate a third granular body layer. An interesting extension to this method is the FDEM [94, 95], a multi-scale method coupling the FEM, used to model the first contact bodies, with the DEM, used to model the third body particles as spherical rigid elements.

1.5.2 Wear and nonlinear dynamic analysis

Most research has been conducted on fretting wear modelling for quasi-static load conditions [12, 84, 96–98]. Further detailed discussion about these methods can be found in [10].

Due to its complexity, few studies have attempted to model the coupling between dynamics and fretting wear. Thus, modelling fretting wear and its effects on the dynamics response is becoming a significant challenge in the field of joint structures. The main goal of modelling contact problems in fretting wear is to obtain the most accurate results by reducing the calculation time and evaluating the mechanical behaviour at the interface and the effect of wear on the global system after a certain number of cycles. Archard's law, or energy formulations for wear, is almost systematically used to determine wear rates.

The first studies about the effect of fretting wear on nonlinear impact oscillators were performed by Knudsen [99, 100]. However, in these works, a Newmark's time integration technique was used for dynamic analysis, while the wear damage was quantified with the impact work rate. The analysis was limited to small systems, with a few DOFs, having this methodology high computational costs. Jareland and Csaba [11] investigated friction damper wear for a tuned bladed disk, using a wear energy approach to estimate the worn volume at the damper interface. The works done by Salles et al. [13, 14, 101] are one of the first studies to use a numerical analysis of coupling dynamics and wear. The dynamic response is evaluated using approximated methods, such as the Harmonic Balance Method (HBM) [102]. Within the HBM framework, the Dynamic Lagrangian Frequency-Time (DLFT) method, developed by Nacivet [103], is considered, and a multi-scale approach is introduced to analyze the effect of wear and its influence on the dynamic behaviour of under-platform dampers and at the blade root joints simultaneously. Also, Petrov [15] studied the impact of wear on realistic turbine-bladed discs equipped with friction dampers, showing the progressive damper loss caused by wear generated at the contact. The HBM has also been coupled with a semi-analytical contact solver to study the contact interface behaviour. In this regard, Gallego et al. [104] proposed a computational method based on a three-scale analysis to solve a fretting wear problem based on a semi-analytical formulation, applied to a test case of turbine blades equipped with an under-platform damper. Semi-analytical methods have been used to evaluate fretting wear in dovetail joints at the turbine blade-disk interface [17]. In the context of the dynamic study of under-platform dampers, Armand et al. [16, 105] implemented a multi-scale approach using a semi-analytical method coupling the BEM, used for fretting wear predictions, and the HBM technique, used for the prediction of the effect of wear on the dynamic response. In a subsequent study, they also included the roughness in the contact area [106].

1.6 Need for experimental studies

Nevertheless, the numerical investigations mentioned in the previous section represent preliminary attempts to model the effects of fretting wear on the forced dynamic response of jointed structures and are, so far, only numerical predictions. There is still a lack of experimental results [19], which limits the understanding of how joints deteriorate at work and reduces the possibility of optimising the design and maintenance of joint structures. Due to the high costs of a full-scale experimental observation, the design of simplified experimental setups is essential for reproducing the configurations of the industrial components at a laboratory scale. Moreover, experimental results are useful for validating numerical predictions.

Several experimental academic test rigs have been designed and found in the literature to reproduce the dynamic behaviour of low-pressure rotating turbine blades, whose behaviour is nonlinear due to frictional contact. Some test rigs were designed in the 1970s to study the damping of the frictional contact on a simplified blade [107–109]. These test rigs made it possible to compare the experimental results with the analytical results and study the influence of the amplitude of the frictional force on the structure's response according to the state of the contact at the interface (sliding or stuck conditions). Experimental validations also exist to investigate the dynamic response of systems with friction contact, mainly focused on friction damping in bladed disks assemblies [110–113], However, all these approaches did not account for the presence of a third body layer entrapped in the interface.

Concerning the wear phenomenon, various studies have provided methods to describe fretting wear using different numerical approaches relying on experimental evidence. Arnaud et al. [114] proposed a new FEM strategy with a friction energy wear model to predict gross slip fretting wear profiles, taking account of the presence of a third body layer evolving over time. Li et al. [115] investigated the effect of fretting wear on the behaviour of bolted joint interfaces and discussed the impact of fretting wear on the tangential contact stiffness. In more recent work, Li et al. [116] analysed the evolution of contact parameters of bolted joint interfaces under tangential random vibrations but without studying the changes in wear volume and wear rate. These correlated models can be used effectively to develop predictive tools and integrate parametric sensitivity studies with adequate confidence.

Additionally, most studies coupling fretting wear and vibrations investigate wear due to the structure's vibrations rather than wear's effects on the structural dynamics [117–119]. Nevertheless, certain experimental studies have investigated the effect of frequency on fretting wear [95, 120, 121]. Recent research that experimentally studies the impact of fretting wear on the evolution of the system dynamic with friction contact was performed by Fantetti et al. [19]. In this study, fretting tests were performed to capture the evolution of hysteresis loops and the correspondent contact parameters of a flat-on-flat contact pair.

Anticipating and incorporating the contact condition changes due to wear in the dynamics prediction tools is necessary. Experimental evidence can help researchers to better understand the phenomenon, validate the numerical methods and find the best way to predict these phenomena more confidently. The importance of experimental observations has mainly the following purposes:

- validating the numerical methods;
- developing efficient dynamic prediction tools;
- studying the evolution of the wear "at work".

To this aim, it is increasingly necessary to progress in both numerical prediction and experimental observation combining the wear and dynamics.

1.7 Retained strategy for the present work

This chapter has introduced different existing methods for contact problems and wear modelling. The coupling between fretting wear and dynamics was discussed, highlighting experimental evidence's importance in validating and improving numerical simulations.

As part of the EXPERTISE collaboration, in this manuscript, the series of fretting experiments, published in [19] and provided by the Imperial College test rig built at Imperial College of London [122], are considered to verify and validate the results and the conclusions of the numerical investigations. The test rig dynamics [19] reproduces the dynamic behaviour observed in friction dampers and may give a detailed frictional description of contacting interfaces, to allow more accurate modelling of assembled structures.

State-of-the-art in contact modelling has confirmed the choice of using the finite element method to model the experiments. In particular, a fined mesh of the contact interface is performed to obtain a complete understanding of the interface behaviour. Vibration and wear phenomena present very different scales in both time and space. The challenge, therefore, lies in finding methods that allow the nonlinear problem to be solved with a good compromise between the approximations made to the dynamic aspects and those related to the wear problems. The multi-scale aspect in space is treated by assuming the wear is localized only at the contact interface nodes. Thus, wear is considered as a gap between corresponding nodes. This strategy avoids expensive remeshing of the interface. The multi-scale aspect in time is treated by considering dedicated methods for each time scale. This approach allows the use of frequency methods to solve the dynamic problem.

A review of methods for solving nonlinear dynamic problems follows in chapter II. Due to the complexity of a nonlinear system, the dynamic response is evaluated using approximated methods, such as the Harmonic Balance Method [102], assuming the periodic system's response under periodic excitation. Within the framework of the HBM, the numerical treatment of fretting wear, under vibratory loading proposed by Salles [101] is performed. The method is based on the Dynamic Lagrangian Frequency-Time (DLFT) method [123] and models contact using the unilateral contact law (I.1) and the Coulomb friction law (I.7) without any softening. A local form of Archard's law [56] is used and embedded in the nonlinear dynamic solver to include wear, being simple enough to be integrated into numerical simulations. The idea of this method consists of separating time into two scales, a slow scale for tribological phenomena (wear) and a fast scale for dynamics (vibrations). The first example treated by the DLFT with wear method can be found in [124], where a model stemming from the literature is proposed.

This manuscript applies the DLFT with wear method increasing wear depth over time, developed by Salles in [101]. In addition to these studies, in this work, numerical results are validated and verified with experimental evidence. Furthermore, by adding some new numerical simulations, this analysis proposes local interface evaluation scenarios for quantities not directly measured by experiments.

Chapter II

Numerical method of resolution for a nonlinear dynamic problem

This chapter aims to explain the choice of the methods adopted in this manuscript for solving the dynamic problem. First, some methods for solving and finding periodic solutions are introduced, highlighting their interest and limitations, with a particular emphasis on the frequency approach, complemented by various tools such as continuation techniques. Then, a sub-structuring method to reduce the size of the system to be solved is presented. Finally, the method for resolving the nonlinear dynamic problem with friction contacts is detailed before applying it in the next chapter, including the wear phenomenon.

Outline of the chapter

2.1 Reference problem: governing equations

In this section, the contact problem with friction is formulated in the context of continuum mechanics. Two types of nonlinearities are considered: one is related to the unilateral contact and concerns the direction normal to the contact surface; the other is related to the friction and occurs in tangential directions. The materials are considered linear, and the assumption of small displacements and strains is made. For the contact interface, the unilateral contact law is used for the normal direction, and Coulomb's law is chosen to model friction.

2.1.1 Continuous formulation

Let $s = [1, 2]$ be two continuous bodies in contact with friction, occupying two distinct domains Ω^s defined in $\mathbb{R}^3$, as illustrated in FIGURE II.1. For each body, the continuously differentiable boundary, denoted as $\partial\Omega^s$, is divided into three disjoint parts such that:

$$\partial\Omega^s = \Gamma_u^s \cup \Gamma_f^s \cup \Gamma_c^s.$$

More precisely, Γ_u^s denotes the parts where displacements $\mathbf{U}^s$ are prescribed, Γ_f^s the parts where traction forces $\mathbf{f_T}^s$ are applied, and Γ_c^s represents the frictional contact interface, so that $\Gamma_c = \Gamma_c^1 = \Gamma_c^2$, on which the contact conditions are imposed. $\mathbf{n}^s$ designates the outward normal unit vector to $\partial\Omega^s$. $\mathbf{n_c^s}$ designates the outward normal unit vector to Γ_c so that $\mathbf{n_c^1} = -\mathbf{n_c^2}$. The elastodynamics problem consists of finding a displacement field

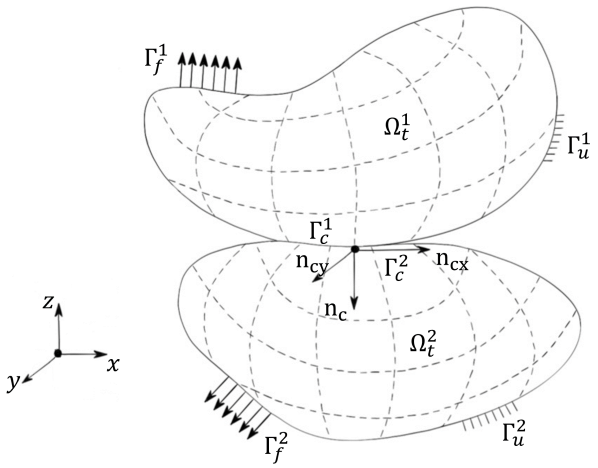

FIGURE II.1: Problem of two elastic bodies in contact.

$\mathbf{u}^s(x, y, z, t)$ satisfying the equilibrium equations. The law of conservation of momentum allows establishing the equation of motion (II.1) in both solids. Using the classical laws of continuum mechanics in the framework described above, the strong formulation of a contact problem in dynamics in the presence of inertial forces can be expressed as follows.

- Dynamic equilibrium equations in Ω^s:

$$\text{div}\boldsymbol{\sigma}^s + \mathbf{f_T}^s = \rho^s \ddot{\mathbf{u}}^s \quad \text{in} \quad \Omega^s, \tag{II.1}$$

with ρ^s the density of the bodies and the symbol div representative of the divergence operator of a tensor $\boldsymbol{\sigma}$ is the Cauchy stress tensor, related to displacements through a constitutive equation.

- Boundary conditions on displacements:

$$\mathbf{u^s} = \mathbf{U^s} \qquad \text{on} \quad \Gamma_u. \tag{II.2}$$

- Boundary conditions on surface forces:

$$\boldsymbol{\sigma^s}\mathbf{n} = \mathbf{f_T^s} \qquad \text{on} \quad \Gamma_f. \tag{II.3}$$

- Initial conditions for displacements and velocities in Ω^s:

$$\begin{cases} \mathbf{u^s}(0) = \mathbf{u_0^s} \\ \dot{\mathbf{u}}^{\mathbf{s}}(0) = \dot{\mathbf{u}}_{\mathbf{0}}^{\mathbf{s}} \end{cases} \tag{II.4}$$

- Material behaviour law: in the hypothesis of small deformations and considering an isotropic linear elastic material for the bodies in contact, the Green-Lagrange strain tensor $\boldsymbol{\varepsilon}$ is expressed as:

$$\boldsymbol{\varepsilon}(\mathbf{u}^s) = \frac{1}{2}\left[\nabla \mathbf{u}^s + (\nabla \mathbf{u}^s)^{\mathrm{T}}\right]. \tag{II.5}$$

Thus, the law describing the material's behaviour is the classical Hooke's linear relation between the Cauchy stress tensor $\boldsymbol{\sigma}$ and the strain tensor $\boldsymbol{\varepsilon}$, through Hooke's tensor $\mathbf{E}^s$:

$$\boldsymbol{\sigma}^s(\mathbf{u}^s) = \mathbf{E}^s\boldsymbol{\varepsilon}(\mathbf{u}^s). \tag{II.6}$$

- In the presence of a discontinuity surface Γ_c it is necessary to add the discontinuity relation given by:

$$\boldsymbol{\sigma^1}\mathbf{n_c^1} = -\boldsymbol{\sigma^2}\mathbf{n_c^2} = -\mathbf{p} \quad \text{on} \quad \Gamma_c, \tag{II.7}$$

where $\mathbf{p}$ represents the constraints of contact. On the frictional interface Γ_c the displacement field is expressed in terms of relative displacements $\mathbf{u_r} = \mathbf{u^1} - \mathbf{u^2}$ between the two bodies. Contact forces $\mathbf{p}$ and displacements $\mathbf{u_r}$ are decomposed into normal (index N) and tangential (index T) components:

$$p_N = \mathbf{p}\cdot\mathbf{n_c}, \quad \mathbf{p_T} = (\mathbf{I} - \mathbf{n_c}\otimes\mathbf{n_c})\mathbf{p}, \tag{II.8}$$

$$u_N = \mathbf{u}\cdot\mathbf{n_c}, \quad \mathbf{u_T} = (\mathbf{I} - \mathbf{n_c}\otimes\mathbf{n_c})\mathbf{u}. \tag{II.9}$$

- The contact constraints given by the unilateral contact law (I.1) and the Coulomb friction law (I.7), defined in section I.1.2, are included in the discontinuity relation (II.7) and must be verified.

However, the strong formulation of an elastodynamic problem can only be solved in certain classical cases. Thus, it is necessary to refer to a weak formulation.

2.1.2 Variational or weak formulation

The weak or variational formulation can be used as a basis for a future discretization of the elastodynamic problem presented in section II.2.1.1. It is obtained by applying the principle of virtual work.

By integrating over the domain Ω the scalar product of the balance Eq. (II.1) with a compatible virtual displacement $v \in \mathcal{V}$, with $\mathcal{V}$ a suitable function space that satisfies the displacement boundary conditions.

$$\int_\Omega \rho \ddot{u}_i v_i \, \mathrm{d}\Omega^s + \int_\Omega E_{ijkl} \frac{\partial u_k}{\partial x_l} \frac{\partial v_i}{\partial x_j} \, \mathrm{d}\Omega + \int_{\Gamma_c} p_i v_i \, \mathrm{d}\Gamma_c + \int_{\Gamma_f} f_i v_i \, \mathrm{d}\Gamma_f = 0 \quad \forall \mathbf{v} \in \mathcal{V}. \tag{II.10}$$

Thus, the principle of virtual work can be written as follows:

$$\forall \mathbf{v} \in \mathcal{V} \quad (\rho \ddot{\mathbf{u}}, \mathbf{v}) + a(\mathbf{u}, \dot{\mathbf{v}}) = L(\dot{\mathbf{v}}) + \langle \mathbf{f_c}, \dot{\mathbf{v}} \rangle \,, \tag{II.11}$$

where the different terms represent:

- the virtual work of inertial forces:

$$(\rho \ddot{\mathbf{u}}, \mathbf{v}) = \sum_{s=1}^{2} \int_\Omega \rho^s \ddot{\mathbf{u}}^s \cdot \dot{\mathbf{v}}^s \mathrm{d}\Omega^s, \tag{II.12}$$

- the virtual work of the internal forces:

$$a(\mathbf{u}, \dot{\mathbf{v}}) = \int_\Omega E_{ijkl} \frac{\partial u_k}{\partial x_l} \frac{\partial v_i}{\partial x_j} \, \mathrm{d}\Omega, \tag{II.13}$$

- the virtual work of the external forces:

$$L(\dot{\mathbf{v}}) = \int_{\Gamma_f} f_i v_i \, \mathrm{d}\Gamma_f, \tag{II.14}$$

- the virtual work of the contact forces, which need to be divided into normal and tangential components:

$$\langle \mathbf{f_c}, \dot{\mathbf{v}} \rangle = \int_{\Gamma_c} p_i v_i \, \mathrm{d}\Gamma_c. \tag{II.15}$$

Regarding these formulations, a more detailed description of a generalized standard model for contact, including friction and wear, will be presented in chapter III.

2.1.3 Finite element discretization

Within the framework of the study of vibrations of mechanical structures subjected to nonlinear forces, the objective is to determine the displacement field $\mathbf{u}(x, y, z, t)$ of a structure at any point (x, y, z) and for any time t. The knowledge of the field of displacement will make it possible thereafter to reach the stress field.

This type of system generally involves a discretization for solving differential equations (Finite Element discretization, Rayleigh-Ritz's method, Galerkin's method [125]), which leads to a search for the displacement field in the form $\mathbf{U}(x, y, z, t) = \mathbf{N}(x, y, z)\mathbf{u}(t)$, where $\mathbf{N}$ is the matrix of the shape functions used for the discretization, and $\mathbf{u}$ is the

vector of the degrees of freedom. The partial differential equations are projected onto the space generated by the shape functions to obtain a discretized version of the equations of motion that only involves time derivatives. Capital letters indicate the FEM counterpart of the variables designated by small letters before: they represent vectors of nodal quantities.

For an elastic structure with n degrees of freedom, after finite element discretization, the equations take the following second-order differential form in time:

$$\mathbf{M}\ddot{\mathbf{U}}(t) + \mathbf{C}\dot{\mathbf{U}}(t) + \mathbf{K}\mathbf{U}(t) + \mathbf{F_{nl}}(\mathbf{U}(t), \dot{\mathbf{U}}(t)) = \mathbf{F_{ex}}(t), \tag{II.16}$$

where $\mathbf{U}$ is a vector of displacements $(n \times 1)$, which are the unknowns of the problem, $\dot{\mathbf{U}}$ and $\ddot{\mathbf{U}}$ are its first (velocity) and second (acceleration) time derivatives, respectively. $\mathbf{M}$, $\mathbf{C}$ and $\mathbf{K}$ are the structural matrices $(n \times n)$, i.e. mass, damping and stiffness matrices, respectively.

The inclusion of nonlinear phenomena, such as contact or friction, results in the addition of the term $\mathbf{F_{nl}}$ in the spatially discretized equations of motion. This term is representative of non-proportional and dissipative effects on nodal displacements and velocities. The $\mathbf{F_{nl}}$ vector $(n \times 1)$ refers to the nonlinear forces generated between coupled nodes. Wear is not yet considered in the nonlinear term for the moment. It will be introduced in chapter III. $\mathbf{F_{ex}}$ is the vector $(n \times 1)$ of the applied external forces acting on the system and assumed to be periodic with a period $T = 2\pi/\omega$.

Excitation forces. In the present manuscript, the external excitation forces $\mathbf{F_{ex}}$ are expressed as harmonic excitation forces of period T. This type of force corresponds to typical forces applied in experimental tests. The corresponding term in Eq. II.16 takes the following generic form:

$$\mathbf{F_{ex}}(t) = \mathbf{f_A}\cos(\omega t), \tag{II.17}$$

where $\omega = 2\pi/T$ is the pulsation of the excitation and $\mathbf{f_A}$ is the spatial distribution of the forcing amplitudes.

Structural damping. The matrices of mass and stiffness (resp. $\mathbf{M}$ and $\mathbf{K}$) are built by assembling the mass and stiffness matrices of the substructures, and they are most often available from finite element software. The structural damping matrix $\mathbf{C}$ is introduced using the classical Rayleigh damping model [126], as a linear combination of the mass $\mathbf{M}$ and stiffness $\mathbf{K}$ matrices.

$$\mathbf{C} = \alpha\mathbf{M} + \beta\mathbf{K}, \tag{II.18}$$

where α and β are two arbitrary positive coefficients determining the influence of the mass and the stiffness on the system, respectively. For a given mode i, the modal damping ξ_i can be expressed in terms of the damping factors α and β as [126]:

$$2\xi_i(\omega_i) = \left(\frac{\alpha}{\omega_i} + \beta\omega_i\right), \tag{II.19}$$

where ω_i is the natural frequency at this mode i. By selecting two vibration modes i and j as a reference and after having obtained their damping ratios ξ_i and ξ_j through measurements or reliable test data evaluation, using their frequencies ω_i and ω_j, the coefficients α and β can be determined. The Eq. (II.19) implies that generally speaking, the mass proportional Rayleigh damping, α, damps the lower frequencies and the stiffness proportional Rayleigh damping, β damps the higher frequencies. The efficiency of the Rayleigh damping and its simplicity of implementation leads to adopting this method to evaluate the damping matrix $\mathbf{C}$ in the following of this study.

Nonlinearities. As introduced in the previous chapter, assembled mechanical systems are often complex structures in the field of dynamics. The elements and the connections between the different parts are generally sources of nonlinearities. These nonlinearities appearing in the nonlinear term $\mathbf{f_{nl}}$ can be of various origins, such as:

- **Material nonlinearities.** Material nonlinearity involves the nonlinear behaviours of material based on deformation history, current deformation, pressure, and temperature. The widely used materials encountered in turbomachinery and aerospace fields, such as titanium or nickel alloys, can be a source of nonlinearities if plasticity is considered in the models. More recently, the introduction of composite materials, mainly for fan blades, has presented a considerable technological advance, but requires working with non-isotropic material, more difficult to characterise, and whose constitutive laws may be nonlinear [127].
- **Geometrical nonlinearities.** In structural dynamics, numerical simulations are based mainly on a linearisation of the model using the hypothesis of small displacements. Geometric nonlinearities concern structures whose stiffness depends on displacements to which they are subjected. In aero engines, these include blade stiffening due to centrifugal forces. In the case of fan blades, which are the largest, these forces can lead to large displacements that must be taken into account to predict the actual behaviour of the structure. From an algebraic point of view, the nonlinear force $\mathbf{F_{nl}}$ is, in this case, expressed in the form of quadratic or cubic polynomial terms, generating an entirely new phenomenology compared to the linear case [128].
- **Nonlinearities resulting from contact.** The models associated with contact nonlinearities, of type unilateral and frictional contact, have been introduced in section I.1.2. Some dedicated numerical techniques have been developed to consider these constraints. In this regard, a detailed description can be found in [48].
  - Regularisation techniques or penalisation methods aim at approximating the contact force/displacement (gap distance) relationship, which typically takes the form of a linear or exponential function as previously described in FIGURE I.2. Thanks to this approximation, the numerical implementation is easier. Nevertheless, it causes the presence of residual penetrations and/or "non-physical" contact forces.
  - On the other hand, non-regulated techniques aim at completely satisfying the non-penetration conditions of Eq. (I.5) using an implicit calculation of the contact forcing term. In this case, the numerical implementation is computationally more expensive and the contact forces are calculated to ensure that no residual penetrations occur.

2.2 Solution estimation methods

Solving the nonlinear equation of motion (II.16) can be complex and very expensive in terms of computational time. However, within the framework of vibrational dynamics, one is often brought to find the steady state of the dynamical system. Different resolution methods can be considered to obtain an approximate solution to the system of differential equations (II.16). This section presents two categories of methods: time domain and frequency domain methods of the Galerkin type.

2.2.1 Time resolution methods

Direct time integration. A way of solving the problem in the time domain is to integrate the equation of motion directly from a given initial condition. This approach uses few hypotheses. Therefore it is often used as a reference to validate the other methods.

Several numerical integration schemes are available to resolve first-order differential equations systems. Time integration methods are mainly formalized for systems of first-order differential equations in time. It is then convenient to convert the second-order differential Eq. (II.16) into a system of first-order differential equations (state-space formulation) of size $2n$, as follows:

$$\dot{\mathbf{y}}(t) = f(t, \mathbf{y}(t)), \tag{II.20}$$

with

$$\mathbf{y}(t) = \begin{pmatrix} \mathbf{u}(t) \\ \dot{\mathbf{u}}(t) \end{pmatrix}, \tag{II.21}$$

$$f(t, \mathbf{y}(t)) = \begin{pmatrix} \dot{\mathbf{u}}(t) \\ -\mathbf{M}^{-1}[\mathbf{C}\dot{\mathbf{u}}(t) + \mathbf{K}\mathbf{u}(t) + \mathbf{f_{nl}}(\dot{\mathbf{u}}(t), \mathbf{u}(t)) - \mathbf{f_{ex}}(t)] \end{pmatrix}. \tag{II.22}$$

Eq. (II.21) is the state-space vector, and Eqs. (II.22) represents the consequently first-order system equations. The most classical approach for solving a time-dependent system of differential equations is to use a direct time integration [129], whereby the solution is successively approximated over time using a step-by-step procedure. Firstly, it is necessary to discretize the time range $[0, T]$ over which the analysis is performed. This interval is discretized in $n_t + 1$ time instants t_k, such that:

$$0 = t_0 < t_1 < t_k < \ldots < t_{n_t} = T \quad \text{with} \quad k = 0, 1, \ldots, n_t - 1. \tag{II.23}$$

The time step between two successive time instants is $\Delta t_k = [t_k, t_{k+1}]$. The purpose is then to determine the solution at each instant t_k as a function of one or more instants, previous to or after the considered one.

In the framework of a direct time integration, the most basic of the single-step algorithm is the Euler integration scheme for which, denoted as $\mathbf{y}(t_k) = \mathbf{y}_k$, the following expression gives the formulation:

$$\mathbf{y}_{k+1} = \mathbf{y}_k + \Delta t_k (1 - \theta)\dot{\mathbf{y}}_k + \Delta t_k \theta \dot{\mathbf{y}}_{k+1}. \tag{II.24}$$

The choice of the parameter θ affects the scheme's quality, and properties [129].

- The choice $\theta = 0$ in the expression (II.24) gives an explicit Euler scheme. In explicit schemes, solutions at the time instant t_{k+1} are expressed in terms of the previously known solution at the time instant t_k enabling a quick estimation of the solution since it only requires a simple computation. On the other hand, this scheme is conditionally stable, depending on the length of the time step between two instants to ensure the stability of the scheme.
- The choice $\theta = 1$ expression (II.24) gives an implicit Euler scheme. In implicit schemes, the solution is reached from the equation of the motion itself at time instant t_{k+1}. For the latter scheme, the stability is assured, allowing even larger time steps, but the determination of the solution requires the resolution of a system of algebraic equations at each time step, which can considerably increase the computational cost.
- The choice $\theta = 1/2$ gives an approximation of the integral by the trapezoidal method and allows better accuracy. This scheme is called the Cranck-Nicolson scheme.

These schemes are single-step schemes. This means that the search for a solution at time t_k only involves the quantities of the previous step at most. These schemes are of order 1, which means that the error committed is of the order of $t_{k+1} - t_k$. These schemes are generally exposed to problems of precision and stability. Thus, it is preferred to refer to multi-step schemes, more complex but more stable. The most commonly used error reduction is the Runge-Kutta scheme in the fourth order (RK4) [130]. This scheme ensures good accuracy, despite a longer computation time, due to the four evaluations of the function f per instant.

When the nonlinear forces contained in the vector $\mathbf{F_{nl}}$ are reasonably regular or the laws defining them are regularised, there are also methods capable of dealing directly with the second-order problems. This has the advantage of eliminating the need to switch to a state system avoiding doubling the number of unknowns of the problem. Among these methods, one can be mentioned in particular, the family of Newmark algorithms [131], which allows an approximation of the time derivatives using the finite difference method, avoiding the doubling of the number of variables induced by the state representation.

However, for any integration scheme, it is necessary to study the stability and consistency of the solution to ensure convergence. Time integration methods have the advantage of applying to any system, particularly to studying nonlinear models. In addition, they are generally easy to implement as they are included in the great majority of calculation software. On the other hand, the research of the periodic solution based on a direct time integration can be prohibitive in terms of computational time, especially for calculating the transient phase until a steady state is established, particularly in the case of systems with a large number of DOFs. This point makes them unsuitable for the study of industrial systems characterized by a large number of DOFs. Due to these limitations, frequency methods are an interesting alternative for the search for periodic solutions to nonlinear systems. They are based on transposing the differential problem into the frequency domain, which generates smaller systems than temporal methods. However, time methods can be used as a reference to validate the frequency methods.

Time integration will be used in the following as a reference for some numerical solutions.

Shooting method. Shooting methods are time-based methods used to search for periodic solutions. The principle of this method is to reformulate the boundary condition problem into a problem with initial conditions. The objective of shooting methods is to avoid the calculation of the transient response of the system by iteratively correcting the initial conditions of the problem. Each step involves a time integration over a period $[0, T]$ allowing the evaluation of the solution in a state formulation using one of the previous schemes. The time integration is performed by correcting the initial conditions of the problem [132]. The correction process is applied to the initial conditions until these correspond to a periodic solution. Generally, this method is more efficient in terms of computational time than direct time integration. However, shooting methods result in being efficient in the case of systems with a small number of variables. For large systems, the computation time can quickly become high due to the iterative nature of the method.

2.2.2 Formulation and resolution in frequency domain

Methods in the frequency domain transform the nonlinear problem expressed in the time domain into a nonlinear algebraic problem formulated in the frequency domain. Most of these methods belong to the family of Ritz-Galerkin methods. The principle of this method is to approximate the solution of Eq. (II.16) into a series of time-dependent functions:

$$\mathbf{U}(t) = \sum_{k=1}^{N} \mathcal{H}_k \mathbf{x}_k(t), \tag{II.25}$$

where $\mathbf{x}_k$ are approximated functions fixed *a priori* and $\mathcal{H}_k$ are unknown coefficients to determine. By differentiating Eq. (II.25) and replacing the expression in the general Eq. (II.16), the following expression as a residual $\mathbf{r}(\mathcal{H}, \mathbf{x})$ can be obtained:

$$\mathbf{r}(\mathcal{H}, \mathbf{x}) = \sum_{k=1}^{N} [\mathbf{M}\mathcal{H}_k \ddot{\mathbf{x}}_k + \mathbf{C}\mathcal{H}_k \dot{\mathbf{x}}_k + \mathbf{K}\mathcal{H}_k \mathbf{x}_k] + \mathbf{F_{nl}}(\mathcal{H}, \mathbf{x}) - \mathbf{F_{ex}}(t). \tag{II.26}$$

For an harmonic response of period T the coefficients $\mathcal{H}_k$ are determined by orthogonalizing the residual $\mathbf{r}$ with respect to a basis of test functions $[\boldsymbol{\eta}_k(t)]_{k=1,\dots,N}$ by finding those that satisfy the following projection equations:

$$\int_0^T \mathbf{r}(\mathcal{H}, \mathbf{x}(t)) \boldsymbol{\eta}_k(t) \mathrm{d}t, \qquad \forall k \in [\![1, N]\!]. \tag{II.27}$$

If the test functions are equal to the functions used for the approximation that is $\mathbf{x}_k = \boldsymbol{\eta}_k$ (with $k = 1..N$), one talks of Galerkin's projection. Different basis functions can be used depending on the type of case to be treated. In the search for periodic solutions, trigonometric functions are often used as approximation functions. For non-regular impact contact problems, for example, it has been considered to use wavelet bases as approximation functions [133].

Harmonic Balance Method. When only the steady-state is of interest, frequency-domain resolution methods are an alternative to the time-domain numerical integration. In the Fourier space, it is possible to have direct access to periodic solutions, which

generally allow a significant reduction in computational costs compared to the time-domain numerical integration. The frequency method presented here is the Harmonic Balance Method (HBM) [102], which is the widely used method for researching periodic solutions in the frequency domain. The HBM is a direct application of the Galerkin procedure [134]. It consists of projecting the dynamic residual on a trigonometric basis to remove the time dependency from the system. This strategy allows finding periodic solutions to the dynamic behaviour of a system subjected to a single-frequency harmonic excitation of frequency ω. This method has been improved thanks to many variants, among which the Incremental Harmonic Balance Method (IHBM) [135], the Multi-frequency dimensional Harmonic Balance Method (MHBM) [136], and the Adaptive Harmonic Balance Method (AHBM) [137],

The influence of wear on dynamic behaviour will not be considered for now.

Theoretical principle. The principle is to approximate the T-periodic solution of the system (II.16) as a truncated Fourier series (II.28). This assumption ensures the solution's periodicity, imposed here *a priori*.

$$\mathbf{U}(t) \simeq \mathbf{a}_0 + \sum_{k=1}^{N_h} (\mathbf{a}_k \cos(k\omega t) + \mathbf{b}_k \sin(k\omega t)), \tag{II.28}$$

with N_h the number of retained harmonics in the HBM resolution. $\mathbf{a}_0$ represents the constant coefficients of the Fourier series, the terms $(\mathbf{a}_k)_{k\in[0,N_h]}$ and $(\mathbf{b}_k)_{k\in[0,N_h]}$ are the coefficients of the Fourier decomposition. Each Fourier coefficient is a vector of size n. This solution is, therefore, an approximation since it is truncated at a particular order N_h. The more significant the number of harmonics N_h retained, the closer the approximate solution will be to the exact solution.

Substituting the Eq. (II.28) and its derivatives into the general Eq. (II.16) of motion gives a solution error or residual $\mathbf{r}(t)$, resulting from the error generated by the approximation of $\mathbf{u}(t)$. The residual $\mathbf{r}(t)$ is then expressed in the following form:

$$\begin{aligned}\mathbf{r}(t) = &\sum_{k=1}^{N_h} [(\mathbf{K} - (k\omega)^2\mathbf{M})\mathbf{a}_k + (k\omega\mathbf{C})\mathbf{b}_k] \cos(k\omega t) + \\ &+ \sum_{k=1}^{N_h} [(\mathbf{K} - (k\omega)^2\mathbf{M})\mathbf{b}_k - (k\omega\mathbf{C})\mathbf{a}_k] \sin(k\omega t) + \\ &+ \mathbf{K}\mathbf{a}_0 + \mathbf{F_{nl}} - \mathbf{F_{ex}}.\end{aligned} \tag{II.29}$$

The principle of the HBM is based on the removal of the time dependence of the residual by expressing the relation (II.29) in the frequency domain. By applying the Galerkin procedure, the residual $\mathbf{r}(t)$ is projected on trigonometric basis (i.e. the Fourier basis) $\mathcal{B}(t)$:

$$\mathcal{B}(t) = [1 \;\; \cos(k\omega t) \;\; \sin(k\omega t) \;\; \dots]^T, \quad \forall k \in [1, N_h], \tag{II.30}$$

by means of the inner product $\langle \cdot \mid \cdot \rangle$, defined on the set of continuous functions C over the interval $[0, T]$ of $\mathbb{R}$:

$$\forall (f,g) \in \mathrm{C}([0,T]), \quad \langle f(t) \mid g(t) \rangle = \frac{2}{T} \int_0^T f(t)g(t)dt. \tag{II.31}$$

Denoted as $c_0 = 1$, $c_k = \cos(k\omega t)$ and $s_k = \sin(k\omega t)$ and considering the orthogonality of the basis functions with respect to the chosen scalar product, the Eq. (II.29) can be simplified, yielding a system of nonlinear algebraic equations:

$$\begin{cases} \langle \mathbf{r} \mid c_0 \rangle = (2\mathbf{K})\mathbf{a}_0 + \langle \mathbf{F_{nl}} \mid c_0 \rangle - \langle \mathbf{F_{ex}} \mid c_0 \rangle \\ \langle \mathbf{r} \mid c_k \rangle = (\mathbf{K} - (k\omega)^2\mathbf{M})\mathbf{a}_k + (k\omega\mathbf{C})\mathbf{b}_k + \langle \mathbf{F_{nl}} \mid c_k \rangle - \langle \mathbf{F_{ex}} \mid c_k \rangle \\ \langle \mathbf{r} \mid s_k \rangle = (\mathbf{K} - (k\omega)^2\mathbf{M})\mathbf{b}_k - (k\omega\mathbf{C})\mathbf{a}_k + \langle \mathbf{F_{nl}} \mid s_k \rangle - \langle \mathbf{F_{ex}} \mid s_k \rangle . \end{cases} \tag{II.32}$$

In a more compact form, the system of equations (II.29) becomes:

$$\mathbf{r}(\tilde{\mathbf{u}}) = \mathbf{Z}\tilde{\mathbf{u}} + \tilde{\mathbf{f}}_{\mathbf{nl}}(\tilde{\mathbf{u}}) - \tilde{\mathbf{f}}_{\mathbf{ex}}, \tag{II.33}$$

where $\sim$ denotes a multi-harmonic frequency-domain vector. According to this notation, $\tilde{\mathbf{u}}$, $\tilde{\mathbf{f}}_{\mathbf{nl}}$ and $\tilde{\mathbf{f}}_{\mathbf{ex}}$ are then the multi-harmonic vectors of displacements, nonlinear forces and external forces, respectively. $\mathbf{Z}$ is a block-diagonal matrix, the so-called dynamic stiffness matrix, defined as:

$$\mathbf{Z} = \begin{bmatrix} 2\mathbf{K} & & & & & \\ & \mathbf{Z}_1 & & & & \\ & & \ddots & & & \\ & & & \mathbf{Z}_k & & \\ & & & & \ddots & \\ & & & & & \mathbf{Z}_{N_h} \end{bmatrix}, \tag{II.34}$$

whose each k_{th} block defines the dynamic stiffness matrix for the k_{th} harmonic:

$$\mathbf{Z}_k = \begin{bmatrix} \mathbf{K} - (k\omega)^2\mathbf{M} & k\omega\mathbf{C} \\ -k\omega\mathbf{C} & \mathbf{K} - (k\omega)^2\mathbf{M} \end{bmatrix} \quad k = 1, \ldots, N_h. \tag{II.35}$$

The HBM allows to transform the system of differential equations (II.16) into a system of $(2N_h + 1)n_{\text{dofs}}$ algebraic equations, with n_{dofs} the number of DOFs of the structure.

In the Eq. (II.33), external forces are generally periodic excitations which can be easily decomposed into a sum of cosine and sine functions and the associated harmonic coefficients $\tilde{\mathbf{f}}_{\mathbf{ex}}$ arise naturally from this decomposition. The determination of the Fourier coefficients of the nonlinear forces $\tilde{\mathbf{f}}_{\mathbf{nl}}(\tilde{\mathbf{u}})$ can be done either analytically or numerically. In the case of simple nonlinearity, where analytical expressions can be derived, the nonlinearity can be processed directly in the frequency domain, as for the external forces. In the case of more complex nonlinearity, such as the nonlinearities of contact or friction, numerical methods are needed to evaluate the harmonic coefficients of the nonlinear forces in the time domain. This aspect will be detailed in the next paragraph.

Evaluation of the nonlinear terms. The transposition of the initial differential problem (II.16) into the frequency domain (II.29) yields the harmonic vector $\tilde{\mathbf{f}}_{\mathbf{nl}}(\tilde{\mathbf{u}}, \omega)$

containing the coefficients of the Fourier series of the nonlinear forces $\mathbf{F_{nl}}(\dot{\mathbf{U}}(t), \mathbf{U}(t))$. The expression of these coefficients is not readily computable analytically, except for simple cases, since the relationship relating nonlinear forces $\tilde{\mathbf{f}}_{\mathbf{nl}}$ to frequency variables $\tilde{\mathbf{u}}$ and ω is in most cases not directly known, being given only the laws relating the nonlinear forces $\mathbf{F_{nl}}$ to the time variables $\mathbf{U}$ and $\dot{\mathbf{U}}$. There are several methods for assessing contact forces in the time domain. The simplest procedure is by regularising the *sign* function with another continuous function for evaluating the Coulomb force, enabling a direct computation of the nonlinear friction forces [138]. The penalty method is another widely used strategy [24, 139]. It softens the contact at the interface with additional stiffnesses in the normal (unilateral contact condition) and tangential (Coulomb friction law) direction.

In the case of nonlinearities explicitly expressed in the time domain, two methods are particularly well suited to overcome this difficulty: the trigonometric collocation method and the Alternating Frequency-Time (AFT) procedure, introduced by Cameron and Griffin [140]. The trigonometric collocation method, described in detail in [141], assumes the accuracy of the solution to be found at a fixed number of time instants. However, it relies on a least squares inversion, which forces the use of a pseudo-inverse matrix that can be expensive in terms of numerical cost. In the following, the alternating Frequency-Time approach will be preferred. The Alternating Frequency-Time (AFT) method consists of transposing the frequency vector of unknowns $\tilde{\mathbf{u}}$ into the time domain to determine the nonlinear forces as a function of time, and then re-evaluate these forces in the frequency domain using a Fourier transform. This approach takes advantage of the fact that the relationship between the vector of unknowns in the time domain $\mathbf{F}(t)$ and the nonlinear forces $\mathbf{F_{nl}}(\dot{\mathbf{U}}(t), \mathbf{U}(t))$ is generally known. The use of Fourier transforms takes place to the extent that nonlinear forces inherit the periodicity of the researched solution and can therefore be expressed into a form similar to (II.28) as follows:

$$\mathbf{F_{nl}}(\dot{\mathbf{U}}(t), \mathbf{U}(t)) \simeq \mathbf{c}_0 + \sum_{k=1}^{N_h} (\mathbf{c}_k \cos(k\omega t) + \mathbf{d}_k \sin(k\omega t)), \tag{II.36}$$

where $\mathbf{c}_0$ are the constant Fourier coefficients, $\mathbf{c}_k$ and $\mathbf{s}_k$ the coefficients of the Fourier decomposition.

Starting from the vector $\tilde{\mathbf{u}}$ the transformation from the frequency to the time domain is accomplished through an Inverse Discrete Fourier Transform (IDFT) matrix denoted as $\bar{\mathcal{F}}$.

$$\mathbf{U}(t) \quad = \bar{\mathcal{F}}\tilde{\mathbf{u}}, \tag{II.37}$$

where the IDFT matrix $\bar{\mathcal{F}}$ is built as:

$$\bar{\mathcal{F}} = \begin{bmatrix} 1 & \cos(\omega t_1) & \sin(\omega t_1) & \dots & \cos(N_h \omega t_1) & \sin(N_h \omega t_1) \\ \vdots & \vdots & \vdots & & \vdots & \vdots \\ 1 & \cos(\omega t_k) & \sin(\omega t_k) & \dots & \cos(N_h \omega t_k) & \sin(N_h \omega t_k) \\ \vdots & \vdots & \vdots & & \vdots & \vdots \\ 1 & \cos(\omega T) & \sin(\omega T) & \dots & \cos(N_h \omega T) & \sin(N_h \omega T) \end{bmatrix} \otimes \mathbf{I}_{n_{\text{dofs}}}, \tag{II.38}$$

in which $\otimes$ is the Kronecker product and $\mathbf{I}_{n_{\text{dofs}}}$ is the identity matrix of size n_{dofs} x n_{dofs}.

This step allows the signal $\mathbf{u}(t)$ to be sampled into n_t time instants of the period T, denoted t_k and generally equidistant. They are defined as:

$$t_k = \frac{k}{n_t} T \quad \text{with} \quad k = 0, \ldots, n_t. \tag{II.39}$$

More specifically, the discretization of the period T is based on the compromise between the computational time, the convergence of the iterative solver, and the capability to capture nonlinear effects. To capture all the information from a continuous-time signal of finite bandwidth, it is appropriate that the discretization of the signal satisfies the criteria of the Nyquist-Shannon theorem [142], which states that the frequency sampling of a signal must be greater than twice the maximum frequency contained in this signal.

Similarly, it is possible to determine the sampled vectors in the time domain of velocity $\dot{\mathbf{u}}(t)$ and acceleration $\ddot{\mathbf{u}}(t)$ using a differential operator ∇, expressed as:

$$\nabla = \begin{bmatrix} 0 & & & & & \\ & \nabla_1 & & & & \\ & & \ddots & & & \\ & & & \nabla_k & & \\ & & & & \ddots & \\ & & & & & \nabla_{N_h} \end{bmatrix}, \tag{II.40}$$

whose each k_{th} block defines the derivative operator for the k_{th} harmonic:

$$\nabla_k = \begin{bmatrix} 0 & k\omega \\ -k\omega & 0 \end{bmatrix} \otimes \mathbf{I}_{n_{\text{dofs}}}, \quad \forall k \in [\![1, N_h]\!]. \tag{II.41}$$

Thus, the sampled vectors for velocity and acceleration are derived using the following relationships:

$$\dot{\mathbf{U}}(t) = \bar{\mathcal{F}} \nabla \tilde{\mathbf{u}}, \tag{II.42}$$

$$\ddot{\mathbf{U}}(t) = \bar{\mathcal{F}} \nabla^2 \tilde{\mathbf{u}}. \tag{II.43}$$

Once the nonlinear forces $\mathbf{F_{nl}}(\mathbf{U}(t))$ are calculated in the time domain, their expression in the frequency domain is computed using a Direct Fourier Transform (DFT) matrix, denoted as $\mathcal{F}$, whose expression is:

$$\mathcal{F} = \frac{2}{n_t} \begin{bmatrix} 1/2 & \ldots & 1/2 & \ldots & 1/2 \\ \cos(\omega t_1) & \ldots & \cos(\omega t_k) & \ldots & \cos(\omega T) \\ \sin(\omega t_1) & \ldots & \sin(\omega t_k) & \ldots & \sin(\omega T) \\ \vdots & & \vdots & & \vdots \\ \cos(N_h \omega t_1) & \ldots & \cos(N_h \omega t_k) & \ldots & \cos(N_h \omega T) \\ \sin(N_h \omega t_1) & \ldots & \sin(N_h \omega t_k) & \ldots & \sin(N_h \omega T) \end{bmatrix} \otimes \mathbf{I}_{n_{\text{dofs}}}. \tag{II.44}$$

The general AFT procedure is summarized as follows:

$$\tilde{\mathbf{u}} \xrightarrow{\text{IDFT}} \mathbf{U}(t) \longrightarrow \mathbf{F_{nl}}(\mathbf{U}(t)) \xrightarrow{\text{DFT}} \tilde{\mathbf{f}}_{\mathbf{nl}}(\tilde{\mathbf{u}}) \tag{II.45}$$

and graphically illustrated in FIGURE II.2. Moreover, it is important to note that the

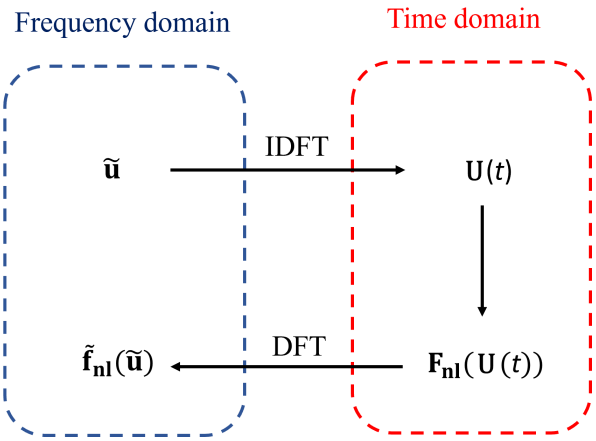

FIGURE II.2: Scheme of the Alternating Frequency-Time (AFT) procedure.

Fourier matrices are not dependent on ω, considering that $\omega t_k = 2k\pi/n_t$. Thus, it is not necessary to recalculate them at each iteration, representing a significant numerical advantage.

Numerical resolution by an iterative method. The solution of the algebraic system (II.33), obtained by harmonic balance, is usually done using iterative solving methods. Several optimization algorithms are described in [143]. The Newton-Raphson method is one of the most commonly used for solving nonlinear algebraic systems. Other approaches present in the literature also allow for solving this type of problem. For example, one can mention the methods based on Krylov spaces [144], techniques based on trust-region algorithms [145] and approaches using pseudo-time [5].

Within the framework of the HBM, the iterative Newton-Raphson type algorithm, initially introduced by Lau [146], is commonly used. Assuming the rewriting of the system (II.33) in the form:

$$\mathbf{r}(\tilde{\mathbf{u}}) = \mathbf{Z}\tilde{\mathbf{u}} + \tilde{\mathbf{f}}_{\mathbf{nl}}(\tilde{\mathbf{u}}) - \tilde{\mathbf{f}}_{\mathbf{ex}} = 0, \tag{II.46}$$

the principle of the method is to determine the solution iteratively, denoted $\tilde{\mathbf{u}}_{\mathbf{s}}$, of the Eq. (II.46), starting from an initial value $\tilde{\mathbf{u}}^{(0)}$. A correction $\Delta\tilde{\mathbf{u}}^{(i)}$ is evaluated at each iteration (i) and added to $\tilde{\mathbf{u}}^{(i)}$ to get closer to the solution. The iterative procedure of Newton, written at each step (i), is:

$$\tilde{\mathbf{u}}^{(i+1)} = \tilde{\mathbf{u}}^{(i)} + \Delta\tilde{\mathbf{u}}^{(i)}, \tag{II.47}$$

where $\tilde{\mathbf{u}}^{(i+1)}$ is the solution at the iteration $(i+1)$ and $\tilde{\mathbf{u}}^{(i)}$ is the known solution at the iteration (i). In Newton-Raphson's algorithm, the calculation of the corrective increment $\Delta\tilde{\mathbf{u}}^{(i)}$ is based on the first-order Taylor expansion of the Eq. (II.46):

$$\mathbf{r}(\tilde{\mathbf{u}}^{(i)} + \Delta\tilde{\mathbf{u}}^{(i)}) = \mathbf{r}(\tilde{\mathbf{u}}^{(i)}) + \frac{\partial \mathbf{r}(\tilde{\mathbf{u}}^{(i)})}{\partial \tilde{\mathbf{u}}}\Delta\tilde{\mathbf{u}}^{(i)} + o(\Delta\tilde{\mathbf{u}}^{(i)}) \approx 0, \tag{II.48}$$

from which the expression of the correction $\Delta\tilde{\mathbf{u}}^{(i)}$ is obtained as:

$$\Delta\tilde{\mathbf{u}}^{(i)} = -\left[\frac{\partial \mathbf{r}(\tilde{\mathbf{u}}^{(i)})}{\partial \tilde{\mathbf{u}}}\right]^{-1} \mathbf{r}(\tilde{\mathbf{u}}^{(i)}). \tag{II.49}$$

The presence of the Jacobian matrix in the Eq. (II.49) gives to the Newton-Raphson algorithm the notation of gradient method. An approximation of this matrix can be obtained using finite differences. However, the numerical costs can be greatly reduced if an analytical expression of the Jacobian matrix is provided to the solver. Generally, obtaining an analytical expression for the Jacobian matrix in the Eq. (II.49) does not pose any particular problem, except for the terms related to the components of the nonlinear forces $\tilde{\mathbf{f}}_{\mathbf{nl}}(\tilde{\mathbf{u}})$, whose treatment requires some attention. The evaluation of the analytical Jacobian matrix is detailed in Appendix A.

The Newton-Raphson iterative process may be repeated as many times as necessary to get the desired accuracy, which verifies an arbitrary stopping criterion set by the user and generally based on the norm of the residue. For example

$$\left\|\boldsymbol{\Delta}\mathbf{r}(\tilde{\mathbf{u}}^{(i)})\right\| \leq \varepsilon, \tag{II.50}$$

with ε the tolerance of the stop tests of the iterative process.

The speed of convergence of the Newton-Raphson algorithm depends on the accuracy of the initial condition. Initialising the algorithm accurately is the whole point of the prediction methods, this aspect will be considered in the next section.

2.3 Continuation of the solution

Contrary to the dynamic study of a linear system, a nonlinear analysis may often exhibit multiple solution branches featuring bifurcation points, so that the convergence of the algorithms can be complicated. Thus, continuation methods are effective for dealing with this type of phenomenon. This approach enhances the following solution branches, according to the evolution of a so-called control parameter, optimizing the time-cost reduction, and allowing to overcome the problem of multiple solutions. In the context of an application to the algebraic system of the HBM, this parameter corresponds to the system excitation pulsation ω. The left-hand side of the system (II.29) is rewritten in the following form to show the dependence on the control parameter ω:

$$\mathbf{r}(\tilde{\mathbf{u}}, \omega) = \mathbf{Z}(\omega)\tilde{\mathbf{u}} + \tilde{\mathbf{f}}_{\mathbf{nl}}(\tilde{\mathbf{u}}, \omega) - \tilde{\mathbf{f}}_{\mathbf{ex}}. \tag{II.51}$$

The most widely used continuation or path-following techniques are based on a parametrization of the solution branches, using the curvilinear abscissa s of the solution path and a prediction-correction type algorithm. First, the prediction step approximates the solution at the next iteration. Then, this solution is iteratively corrected in the correction step until it converges towards the desired solution.

2.3.1 Continuation algorithms

The inclusion of the control parameter ω as an unknown of the system (II.51) makes the system under-determined: the problem is composed of $((2N_h + 1)n_{\text{dofs}} + 1)$ unknowns

correspondent to the $(2N_h+1)n_{\text{dofs}}$ Fourier coefficients of the displacements plus the control parameter ω. The following paragraphs describe the main prediction and correction methods used.

Prediction step. The nonlinear resolution depends on the prediction, which is chosen as the initialisation of the nonlinear solver. Assuming known the solution $(\tilde{\mathbf{u}}, \omega)_i$, the prediction step consists in finding an approximation of the next solution $(\tilde{\mathbf{u}}, \omega)_{i+1}$ from the previous one. For this purpose, various predictors can be used. The ones presented in the following are also shown in FIGURE II.3.

- **Secant predictor.** This type of method consists of estimating the prediction by building a polynomial interpolation on the two previously calculated points $(\tilde{\mathbf{u}}, \omega)_i$ and $(\tilde{\mathbf{u}}, \omega)_{i-1}$. The number of required points depends on the degree of the considered polynomial. In the case of first-order interpolation, the last two points are necessary. In this way, the predicted point, noted as $(\tilde{\mathbf{u}}, \omega)_{pred}$, belongs to the path passing through the points $(\tilde{\mathbf{u}}, \omega)_i$ and $(\tilde{\mathbf{u}}, \omega)_{i-1}$. The norm of the prediction, corresponding to the continuation step $\mathrm{d}s$, determines the direction of the predicted point on the path. The prediction is determined by the following equation:

$$(\tilde{\mathbf{u}}, \omega)_{pred} = (\tilde{\mathbf{u}}, \omega)_i + \mathrm{d}s \frac{(\tilde{\mathbf{u}}, \omega)_i - (\tilde{\mathbf{u}}, \omega)_{i-1}}{\|(\tilde{\mathbf{u}}, \omega)_i - (\tilde{\mathbf{u}}, \omega)_{i-1}\|}. \tag{II.52}$$

  The secant predictor is simple to implement as it does not require the evaluation of the Jacobian matrix. However, this method requires at least two previous points, and it can lead to predictions far from the solution in areas of high curvature, which implies more iterations to converge.
- **Tangent predictor.** It consists of estimating the Jacobian of the residual, as expressed in the Eq. (II.53), evaluated at the last calculated point, to determine the direction of the prediction. In this regard, only one calculation point is needed to obtain a tangent prediction direction.

$$\frac{\partial \mathbf{r}}{\partial \tilde{\mathbf{u}}}(\tilde{\mathbf{u}}_i, \omega_i)\Delta\tilde{\mathbf{u}} + \frac{\partial \mathbf{r}}{\partial \omega}(\tilde{\mathbf{u}}_i, \omega_i)\Delta\omega = 0. \tag{II.53}$$

  Thus, starting from the solution pair $(\tilde{\mathbf{u}}_i, \omega_i)$, it is necessary to obtain the two increments $\Delta\tilde{\mathbf{u}}$ and $\Delta\omega$ of the solution and the control parameter, respectively, to estimate the solution pair at the next point, so that:

$$\begin{aligned} \tilde{\mathbf{u}}_{pred} &= \tilde{\mathbf{u}}_i + \Delta\tilde{\mathbf{u}}, \\ \omega_{pred} &= \omega_i + \Delta\omega. \end{aligned} \tag{II.54}$$

  The increment between two successive points of the response curve is approximated by $\mathrm{d}s^2$, defined as:

$$\mathrm{d}s^2 = \|\Delta\tilde{\mathbf{u}}\|^2 + |\Delta\omega|^2, \tag{II.55}$$

  in which $\|\Delta\tilde{\mathbf{u}}\| = \|\tilde{\mathbf{u}}_{\mathbf{i+1}} - \tilde{\mathbf{u}}_{\mathbf{i}}\|$ and $|\Delta\omega| = |\omega_{i+1} - \omega_i|$. From the combination of the Eqs. (II.55) and (II.53), the two increments obtained are the follows:

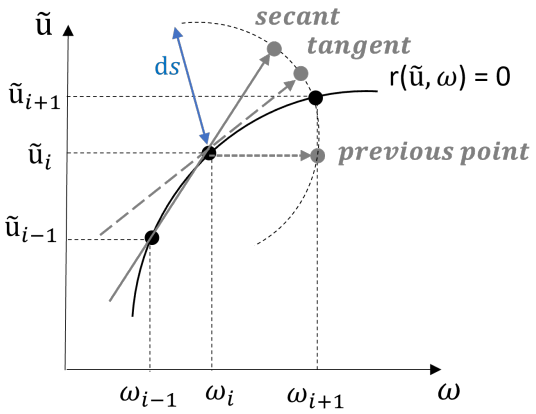

FIGURE II.3: Different prediction methods.

$$\begin{aligned} \Delta\tilde{\mathbf{u}} &= -\left[\frac{\partial \mathbf{r}}{\partial \tilde{\mathbf{u}}}\right]^{-1} \frac{\partial \mathbf{r}}{\partial \omega}\Delta\omega, \\ \Delta\omega &= \frac{\pm \mathrm{d}s}{\sqrt{1+\left\|\left[\frac{\partial \mathbf{r}}{\partial \tilde{\mathbf{u}}}\right]^{-1}\frac{\partial \mathbf{r}}{\partial \omega}\right\|^2}}. \end{aligned} \tag{II.56}$$

Although very efficient, this method produces high numerical costs, especially due to the inversion of the Jacobian matrix of the system with respect to the variables $\tilde{\mathbf{u}}$ for the calculation of the increments.

- **Prediction by the previous point.** It consists of using the previous value as a prediction point for the next one, $\tilde{\mathbf{u}}_{i+1} = \tilde{\mathbf{u}}_i$. This method is the simplest to implement and is used when it is not expected to handle nonlinear responses with bifurcation points.

Correction step. The previous paragraph has presented the main predictors used in the continuation algorithms. In most cases, the predicted point is not a solution of the Eq. (II.29), so the prediction step is completed by a correction one. The correction step iteratively corrects the predicted point to satisfy the system (II.51). This consists in constraining the system by adding an equation characterising the type of correction. The main methods are described in the following and illustrated in FIGURE II.4.

- **Sequential continuation.** This technique consists of fixing one of the unknowns, the control parameter ω and calculating the solution for this chosen predictive value. The value of the control parameter can be set in different ways, the simplest one is to divide the range of interest $\Omega = [\omega_1, \ldots, \omega_{n_\omega}]$ into n_ω calculation points, regularly spaced. Thereby, the system's dependence on ω can be ignored, and the equations to be solved are then:

$$\begin{cases} \omega_i \in \Omega \\ \mathbf{r}(\tilde{\mathbf{u}}) = \mathbf{Z} + \tilde{\mathbf{f}}_{\mathbf{nl}}(\tilde{\mathbf{u}}) - \tilde{\mathbf{f}}_{\mathbf{ex}} = 0 \end{cases} \tag{II.57}$$

The last converged solution is usually used to calculate the next one. The sequential

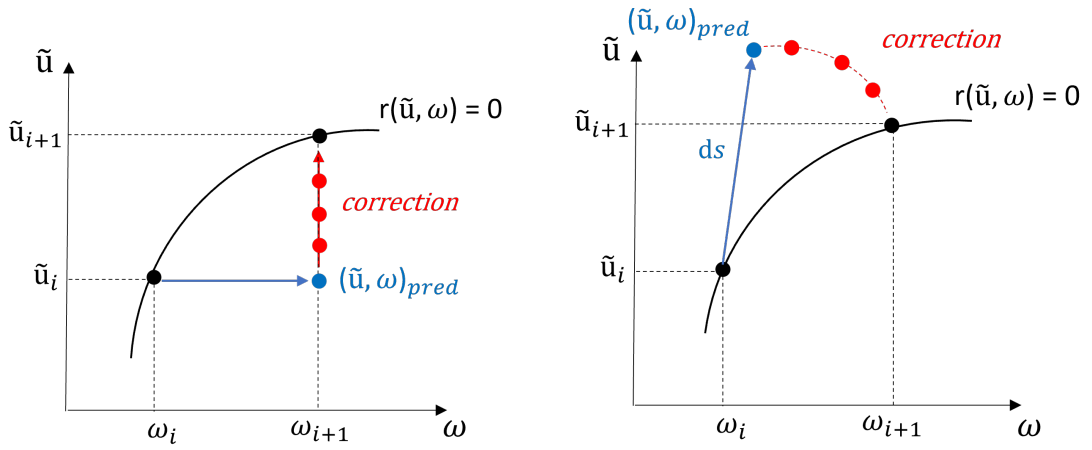

(a) Sequential continuation (b) Arc-length continuation

FIGURE II.4: Different types of continuation techniques.

continuation is illustrated in FIGURE II.4(a). This continuation technique is very simple and convenient to implement, but it is not practical when handling nonlinear responses with turning points, which can be encountered in the case of nonlinearities. However, reversal phenomena are mainly present for nonlinearities involving strong changes in modal characteristics [128], which are not observed in the type of study conducted in this manuscript for which this continuation will be retained.

- **Arc-length continuation.** In the presence of bifurcation points, an arc-length continuation is preferred. This continuation technique considers the control parameter ω as a variable. Consequently, an additional equation must be added to the nonlinear system. The equations to be solved are then:

$$\begin{cases} \mathbf{p}(\tilde{\mathbf{u}}, \omega) = \|\tilde{\mathbf{u}}_{i+1} - \tilde{\mathbf{u}}_i\|^2 + (\omega_{i+1} - \omega_i)^2 - \mathrm{d}s^2 = 0 \\ \mathbf{r}(\tilde{\mathbf{u}}, \omega) = \mathbf{Z}(\omega) + \tilde{\mathbf{f}}_{\mathbf{nl}}(\tilde{\mathbf{u}}, \omega) - \tilde{\mathbf{f}}_{\mathbf{ex}} = 0 \end{cases} \tag{II.58}$$

The objective is to find the solution on a hyper-sphere of radius ds and centred on the last converged solution $(\tilde{\mathbf{u}}_i, \omega_i)$. The arc-length continuation is illustrated in FIGURE II.4(b). Since the hyper-sphere has at least two intersection points with the desired solution path, it may happen that the convergent solution is not the desired one. To force the convergence to the desired point, it is possible to modify the previous equation by looking for the solution on the hyperplane orthogonal to the tangent plane of the curve. In this case, the technique is called pseudo-arc-length continuation [147].

Continuation through Asymptotic Numerical Method. An alternative continuation technique can be found in literature, the so-called Asymptotic Numerical Method (ANM) [148, 149]. This method is based on the development of the solution into a high-order Taylor series expansion of a path parameter α, truncated at the order N_p and given by:

$$\mathbf{u}_{\mathrm{ANM}}(\alpha) = \sum_{p=0}^{N_p} \alpha^p \mathbf{u}^p. \tag{II.59}$$

To compute the series coefficients $\mathbf{u}^p$, the vector of the equation in the form of a residual needs to be reformulated in a polynomial and quadratic form:

$$\mathbf{r}_{\mathrm{ANM}} = \mathbf{L_0} + \mathbf{L_1}(\mathbf{u}) + \mathbf{Q}(\mathbf{u}, \mathbf{u}) = 0, \tag{II.60}$$

where $\mathbf{L_0}$, $\mathbf{L_1}$ and $\mathbf{Q}$ are a constant vector, a linear function with respect to $\mathbf{u}$ and a quadratic function with respect to $\mathbf{u}$, respectively. One new contribution to the field is described in a recent work co-authored by the present author in Woiwode et al. [150]. This paper presents the comparison between two algorithms for Harmonic Balance solutions and path continuation for different mechanical systems. These two algorithms are the AFT scheme with a predictor-corrector procedure, performed using the open-source Matlab tool NLvib [102, 151] that implements the pseudo-arc-length technique for the continuation of a single-parameter family, and the ANM, performed using the Matlab tool MANLAB [152], also freely available online. The main findings of this study are summarized as follows. The ANM can only be implemented when the derivatives for the Taylor series expansion exist. It can only be applied to differential equation systems containing analytical terms or sufficiently smooth nonlinearities. A regularization would be necessary to approximate the non-smooth terms with analytic ones. Moreover, it is necessary to consider a high number of harmonics for convergence [150]. In these cases, the ANM can outstand very high performance. Further, even if many nonlinear systems can be represented in a quadratic form by introducing new variables, the size of the resulting system can quickly become significant, especially for systems with many DOFs and consequently prohibitive in terms of computational cost. On the contrary, the AFT with a predictor/corrector continuation technique is well-adapted to treat non-smooth nonlinearities resulting from contact constraints, such as impacts or friction. Moreover, a very low truncation order can already achieve reasonable accuracy.

In this manuscript, the modelling of an experimental vibratory test rig involving two structures with a common contact interface where dry friction occurs will be performed. The introduction of the wear in the numerical simulations makes the problem even more computationally complex. The AFT scheme with a sequential continuation will be preferred since the experimental results considered do not show reversal phenomena. In addition, when large finite element models with a fine mesh at the contact interface are required, as in this case, a reduction of the problem's size is needed to perform dynamic analysis in reasonable computational times. The following section briefs on performing a Craig-Bampton Component Mode Synthesis (CB-CMS) reduced order modelling technique for a generic system with friction contact. The system is condensed to a small set of DOFs, retaining the dynamic properties of the structure.

2.4 Reduced-order modelling technique

The finite element method is commonly applied to simulate the dynamic behaviour of industrial mechanical systems featuring complex geometries. However, industrial

finite element models often handle millions of DOFs [153]. Consequently, the sparse matrices describing these systems can become very large, especially if a fine mesh is required, making the dynamic response calculation very time-consuming. This problem is even more evident with contact or friction nonlinearities for which the evaluation of the iterative solution and the corresponding updates are computationally costly, both for resolution by time integration and frequency-based methods, such as the HBM. Considering that the main challenge in solving such complex systems is to compromise between low computational costs and high accuracy, substructuring methods, also known as Component Mode Synthesis (CMS), have been developed. These substructuring methods in dynamic calculation can be divided into two main families: methods with fixed interfaces developed by Hurty [154] and of which the Craig-Bampton approach [155] is among the most popular, and the free interface methods initiated by Hou [156] and generalised by MacNeal [157].

The first step in applying a substructuring method is to divide the complete structure into smaller substructures. The next step is the partitioning of the full set of DOFs of each substructure into two subsets:

- the set of boundary or interface DOFs (index b);
- the set of internal DOFs (index i).

The boundary DOFs correspond to those physically retained after the reduction, denoted as master DOFs; the internal DOFs are all the remaining ones, approximated by chosen mode shapes, denoted as slave DOFs. This distinction is significant when handling contact problems since the contact forces are directly applied to the interface DOFs of the reduced model. As a result of the DOFs partitioning, it is possible to reorganize the displacement vectors and the structural matrices of the isolated substructures. The equations of motion can be written in the following form (damping is not mentioned for simplification):

$$\left(\begin{bmatrix} \mathbf{K}_{\mathrm{ii}} & \mathbf{K}_{\mathrm{ib}} \\ \mathbf{K}_{\mathrm{bi}} & \mathbf{K}_{\mathrm{bb}} \end{bmatrix} - \omega^2 \begin{bmatrix} \mathbf{M}_{\mathrm{ii}} & \mathbf{M}_{\mathrm{ib}} \\ \mathbf{M}_{\mathrm{bi}} & \mathbf{M}_{\mathrm{bb}} \end{bmatrix} \right) \begin{pmatrix} \mathbf{u}_{\mathrm{i}} \\ \mathbf{u}_{\mathrm{b}} \end{pmatrix} = \begin{pmatrix} \mathbf{f}_{\mathrm{i}} \\ \mathbf{f}_{\mathrm{b}} \end{pmatrix}. \tag{II.61}$$

2.4.1 Dynamic condensation with fixed interfaces

The Craig-Bampton method [155] is a well-known component mode synthesis technique. The first step of a CB reduction is the repartition of the DOFs in internal ($\mathbf{u}_{\mathrm{i}}$) and boundary ($\mathbf{u}_{\mathrm{b}}$), as detailed in (II.61). The second step consists in building the reduced basis on which to project the equation of motion. The reduced basis of the Craig-Bampton method requires the definition of two types of modes, each one associated with a type of unknown, i.e. internal ($\mathbf{u}_{\mathrm{i}}$) and boundary ($\mathbf{u}_{\mathrm{b}}$), for each substructure. They are defined as follows.

- The first one includes the constrained modes, which represent the static modes. Static modes are the displacements of the substructure's internal DOFs ($\mathbf{u}_{\mathrm{i}}$), obtained by successfully imposing unitary displacements on each boundary DOFs ($\mathbf{u}_{\mathrm{b}}$) when all the other boundary DOFs remain fixed. Thus, considering the static problem associated with the Eq. (II.61) with $\omega = 0$ and $\mathbf{f}_{\mathrm{i}} = 0$, it is then possible to evaluate the static modes of the substructure, using the first line of this equation as:

$$\mathbf{\Psi_{CB}} = -\mathbf{K}_{\mathrm{ii}}^{-1}\mathbf{K}_{\mathrm{ib}}. \tag{II.62}$$

The matrix $\mathbf{\Psi_{CB}}$ contains the static modes on each column.

- The second ones are the fixed-boundary eigenmodes computed by solving the internal eigenvalue problem (II.63), by imposing that the displacements of the boundary DOFs are null ($\mathbf{u}_{\mathrm{b}} = 0$).

$$(\mathbf{K}_{\mathrm{ii}} - \omega^2\mathbf{M}_{\mathrm{ii}})\mathbf{\Phi_{CB}} = 0. \tag{II.63}$$

The matrix $\mathbf{\Phi_{CB}}$ contains the fixed-interface modes shape, arranged by columns. The reduction of the system is carried out via the transformation matrix $\mathbf{T_{CB}}$, defined by:

$$\mathbf{T_{CB}} = \begin{bmatrix} \mathbf{\Phi_{CB}} & \mathbf{\Psi_{CB}} \\ \mathbf{0} & \mathbf{I} \end{bmatrix}, \tag{II.64}$$

where $\mathbf{I}$ is the identity matrix. Using the transformation matrix as defined above gives an exact result. The reduction is then performed by retaining only the first N_m modes of the substructure, i.e. the first N_m columns of the CB matrix. The terms of the equations of motion are reduced by projecting them into the reduced basis of Craig-Bampton using the transformation matrix $\mathbf{T_{CB}}$, leading to:

$$\mathbf{M_{CB}} = \mathbf{T_{CB}^T}\mathbf{M}\mathbf{T_{CB}}, \tag{II.65}$$

$$\mathbf{K_{CB}} = \mathbf{T_{CB}^T}\mathbf{K}\mathbf{T_{CB}}, \tag{II.66}$$

$$\mathbf{f_{CB}} = \mathbf{T_{CB}^T}\mathbf{f}. \tag{II.67}$$

Once the matrices are reduced, solving the problem in terms of reduced variables is possible. The vector of reduced coordinates is indicated as $\mathbf{v} = [\mathbf{q}_{N_m}; \mathbf{u}_{\mathrm{b}}]^T$, where $\mathbf{q}_{N_m}$ are the generalized coordinates corresponding to the N_m fixed interface modes considered in $\mathbf{\Phi_{CB}}$ and $\mathbf{u}_{\mathrm{b}}$ are the displacements preserved from the original equations of motion as boundary physical DOFs. The initial system can be reduced using the Craig-Bampton transformation matrix $\mathbf{T_{CB}}$, defined by:

$$\begin{pmatrix} \mathbf{u}_{\mathrm{i}} \\ \mathbf{u}_{\mathrm{b}} \end{pmatrix} = \mathbf{T_{CB}} \begin{pmatrix} \mathbf{q}_{N_m} \\ \mathbf{u}_{\mathrm{b}} \end{pmatrix} = \mathbf{T_{CB}}\mathbf{v}. \tag{II.68}$$

The Craig-Bampton method offers a good approximation, provided that a sufficient number of modes are used. The modes are usually chosen using a frequency criterion [129]. It is particularly suitable for studying systems with localized nonlinearities because the size of the reduced system essentially depends on the size of the boundary DOFs between the considered substructures [25]. The interfaces are related according to the chosen laws of contact or friction, and the conservation of physical DOFs at the interfaces makes it possible to apply the forces directly to them. Because of its simplicity of implementation in the case of localized nonlinearities, such as the friction treated in this manuscript, and its efficiency, the Craig-Bampton method with fixed interfaces will be retained in the following.

2.4.2 Convergence of the reduced model

Several indicators can be considered to evaluate the performance of a reduced order technique and estimate the quality of the reduced solution with respect to the solution of the global problem. The number of component modes assembled in the transformation matrix should be as large as necessary to capture the vibrational behaviour in the dynamic regime of interest with sufficient accuracy and as small as possible to perform a significant model order reduction.

Criterion based on the natural frequencies. The easiest and fastest criterion to assess the reduced model quality consists of calculating the natural frequencies of the reduced model f_{red} and comparing them to the natural frequencies of the full model f_{full}. The error is then expressed as a frequency deviation as follows:

$$\Delta f = \frac{f_{red} - f_{full}}{f_{red}}(\%). \tag{II.69}$$

Criterion based on the mode shapes. It is also possible to compare the modal vectors of the reduced model with the modal vectors of the full model through the Modal Assurance Criterion (MAC) [158]. From a mathematical standpoint, consider two vectors $\{\phi_{red}\}$ and $\{\phi_{full}\}$, representing the mode shapes of the reduced model and the full model, respectively, the MAC matrix is expressed as the normalized scalar product of the two defined sets of vectors:

$$\mathrm{MAC}(\{\phi_{red}\}, \{\phi_{full}\}) = \frac{\left|(\{\phi_{red}\}^T \{\phi_{full}\})\right|^2}{(\{\phi_{red}\}^T \{\phi_{red}\})(\{\phi_{full}\}^T \{\phi_{full}\})}. \tag{II.70}$$

The MAC value ranges between 0 and 1. A value close to 1 represents a fully consistent mode shape. A low value of the MAC indicates that the modes are not consistent.

2.5 Contact problem resolution by the DLFT

In this study, the Dynamic Lagrangians Frequency-Time procedure proposed by Nacivet et al. [103, 123] is performed. This method uses augmented Lagrangians to calculate without softening the non-smooth frictional contact laws, as will be detailed in section II.2.5.3. This avoids approximation enabling the simulation of real physical behaviours. Compared to the conventional contact penalty approach, the advantage of the DLFT method is that, at convergence, results do not depend on any penalty coefficient; thus, the term "pseudo-penalty" is used to indicate the control coefficient of the approach. Moreover, the contact handling is done directly on the mesh of the contacting interface without remeshing. Following its development, the DLFT method has been successfully employed to study friction-damping blade attachments of rotating bladed disks [159], evaluate the contribution of friction ring dampers on the forced response of blisks [160], as well as to estimate the influence of wear related to friction at the blade root [161].

2.5.1 Contact hypothesis

The problem is limited to small displacements and small deformations. The DLFT method is based on the following contact hypotheses:

- a compatible mesh at the contact interface is needed (FIGURE II.5);
- each contact element is constrained by the unilateral contact condition defined by Eq. (I.1), illustrated in FIGURE II.6(b), and by the Coulomb friction defined by Eq. (I.7), represented in FIGURE II.6(c).
- the contact zone is defined by a node-to-node frictional contact element, as illustrated in FIGURE II.6(a) and a relative displacement is defined between the corresponding nodes;

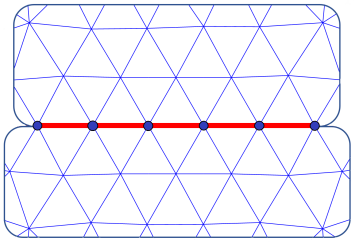

FIGURE II.5: Compatible mesh at the interface.

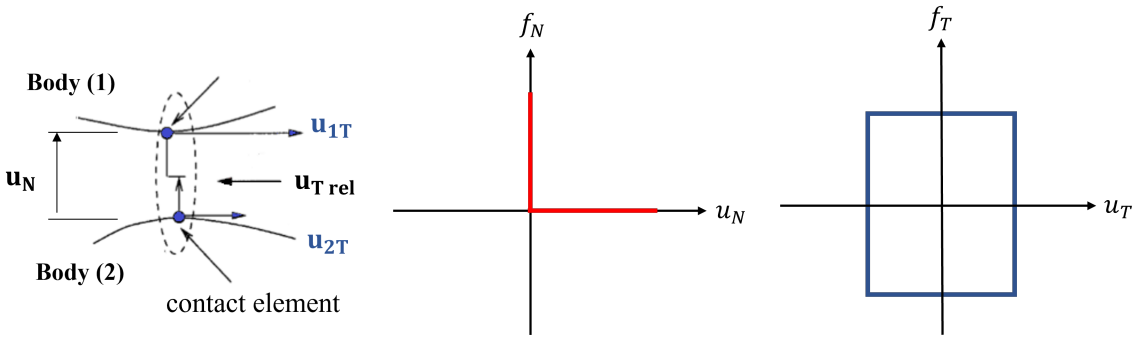

FIGURE II.6: DLFT - Contact hypothesis: (a) zoom on the contact element, (b) unilateral contact condition, (c) Coulomb friction law.

By noting s the number of the solids under consideration such that $s = [1, 2]$ in contact, the equations of motion in time (II.16), written for each solid s are:

$$\mathbf{M}^s\ddot{\mathbf{u}}^s(t) + \mathbf{C}^s\dot{\mathbf{u}}^s(t) + \mathbf{K}^s\mathbf{u}^s(t) + \mathbf{f}_\mathbf{c}^s(\mathbf{u}^s(t), \dot{\mathbf{u}}^s(t)) = \mathbf{f}_\mathbf{ex}^s(t), \tag{II.71}$$

where the matrices $\mathbf{M}^s$, $\mathbf{C}^s$, and $\mathbf{K}^s$ are, respectively, the mass, damping, and stiffness matrices. $\mathbf{f}_\mathbf{c}^s$ represent the nonlinear contact forces due to friction and $\mathbf{f}_\mathbf{ex}^s$ are the external forces. $\mathbf{u}^s(t)$ is the displacement vector, the unknown of the problem. Assuming steady state periodic response, the system of equations (II.71) is transformed to the frequency domain, as detailed in section II.2.2.2. Thus, after reduction to the nonlinear DOFs, as presented in section II.2.4, for both solids s it can be written in the frequency domain as

$$\mathbf{Z}_r^s\tilde{\mathbf{u}}_\mathbf{r}^s + \tilde{\boldsymbol{\lambda}}^s = \tilde{\mathbf{f}}_\mathbf{r}^s, \tag{II.72}$$

with $\mathbf{Z}_r^s$ the dynamic stiffness matrix, and $\tilde{\boldsymbol{\lambda}}^s$, $\tilde{\mathbf{f}}_\mathbf{r}^s$ and $\tilde{\mathbf{u}}_\mathbf{r}^s$ the multi-harmonic vectors of the contact forces, external forces and displacements, respectively, of the solid s.

2.5.2 Condensation of the model in frequency domain

In the case of localised nonlinearities, such as contact problems at interfaces, the size of the problem expressed by Eq. (II.72) can be reduced using a condensation in the frequency domain, as introduced by Nacivet in [123]. This condensation is made for both solids $s = [1, 2]$ in contact. In the next paragraphs, the s-index referring to the solids is omitted for simplicity of reading.

Condensation on the nonlinear degrees of freedom. The DOFs of the system can be distinguished into linear (index l) and nonlinear (index nl). The first exact reduction in the frequency domain consists of condensation on the nonlinear DOFs, coinciding with the DOFs on which the contact forces act. The reduced system (II.72) can be partitioned as:

$$\begin{bmatrix} \mathbf{Z}_{nl,nl} & \mathbf{Z}_{nl,l} \\ \mathbf{Z}_{l,nl} & \mathbf{Z}_{l,l} \end{bmatrix} \begin{bmatrix} \tilde{\mathbf{u}}_{nl} \\ \tilde{\mathbf{u}}_{l} \end{bmatrix} + \begin{bmatrix} \tilde{\mathbf{f}}_{\mathbf{c}_{nl}} \\ 0 \end{bmatrix} = \begin{bmatrix} 0 \\ \tilde{\mathbf{f}}_{\mathbf{ex}_l} \end{bmatrix}, \tag{II.73}$$

where, clearly, for each solid in contact, the nonlinear forces are zero for the linear DOFs, $\tilde{\mathbf{f}}_{\mathbf{c}_l} = 0$. $\tilde{\mathbf{f}}_{\mathbf{ex}_l}$ is the vector of the external forces (periodic excitation at frequency ω). Thus, Eq. (II.73) can be reduced to the nonlinear DOFs only as:

$$\mathbf{Z}_{\mathbf{red}}\tilde{\mathbf{u}}_{nl} + \tilde{\mathbf{f}}_{\mathbf{c}_{nl}} = \tilde{\mathbf{f}}_{\mathbf{red}}, \tag{II.74}$$

where $\mathbf{Z}_{\mathbf{red}}$ and $\tilde{\mathbf{f}}_{\mathbf{red}}$ are, respectively, the reduced dynamic stiffness matrix and the reduced external force vector:

$$\mathbf{Z}_{\mathbf{red}} = \mathbf{Z}_{nl,nl} - \mathbf{Z}_{nl,l}(\mathbf{Z}_{l,l})^{-1}\mathbf{Z}_{l,nl}, \tag{II.75a}$$

$$\tilde{\mathbf{f}}_{\mathbf{red}} = \tilde{\mathbf{f}}_{\mathbf{ex}_{nl}} - \mathbf{Z}_{nl,l}(\mathbf{Z}_{l,l})^{-1}\tilde{\mathbf{f}}_{\mathbf{ex}_l}. \tag{II.75b}$$

The unknowns of the system (II.74) are now equal to $(2N_h + 1)n_{nl}$, where N_h is the number of harmonics and n_{nl} is the number of nonlinear DOFs.

Once the displacements of the nonlinear DOFs are known, $\tilde{\mathbf{u}}_l$ can be simply obtained by isolating the second line of the Eq. (II.73), corresponding to the linear part, as:

$$\tilde{\mathbf{u}}_l = (\mathbf{Z}_{l,l})^{-1}(\tilde{\mathbf{f}}_{\mathbf{ex}_l} - \mathbf{Z}_{l,nl}\tilde{\mathbf{u}}_{nl}). \tag{II.76}$$

Condensation on relative displacement. Because the computational time increases rapidly with the number of nonlinear unknowns, a further reduction is proposed to divide the size of the nonlinear system by two. This condensation consists of pairing the contact nodes at the interface and solving the system only in relative displacement. The mesh is therefore assumed to be coincident at the contact interface between the two solids.

Considering the Eq. (II.74), obtained for the two solids $s = [1, 2]$, the contact problem can be express as:

$$\mathbf{Z}_{\mathbf{red}}^{(1)}\tilde{\mathbf{u}}_{nl}^{(1)} + \tilde{\mathbf{f}}_{\mathbf{c}_{nl}}^{(1)} = \tilde{\mathbf{f}}_{\mathbf{red}}^{(1)}, \tag{II.77}$$

$$\mathbf{Z}_{\mathbf{red}}^{(2)}\tilde{\mathbf{u}}_{nl}^{(2)} + \tilde{\mathbf{f}}_{\mathbf{c}_{nl}}^{(2)} = \tilde{\mathbf{f}}_{\mathbf{red}}^{(2)}. \tag{II.78}$$

The multi-harmonic vector of the Lagrange multipliers $\tilde{\boldsymbol{\lambda}}$ is defined as:

$$\tilde{\boldsymbol{\lambda}} = \tilde{\mathbf{f}}_{\mathbf{c}_{nl}}^{(1)} = -\tilde{\mathbf{f}}_{\mathbf{c}_{nl}}^{(2)}. \tag{II.79}$$

The Lagrange multipliers can be expressed as the tangential contact forces due to friction and the normal contact forces that ensure no interpenetration. The relative displacement vector is given by:

$$\tilde{\mathbf{u}}_{\mathbf{r}} = \tilde{\mathbf{u}}_{nl}^{(1)} - \tilde{\mathbf{u}}_{nl}^{(2)} = (\mathbf{Z}_{\mathbf{red}}^{(1)})^{-1}(\tilde{\mathbf{f}}_{\mathbf{red}}^{(1)} - \tilde{\boldsymbol{\lambda}}) - (\mathbf{Z}_{\mathbf{red}}^{(2)})^{-1}(\tilde{\mathbf{f}}_{\mathbf{red}}^{(2)} + \tilde{\boldsymbol{\lambda}}). \tag{II.80}$$

Thus, the Eq. (II.80) can be reformulated in terms of relative variables. The final system condensed on the nonlinear relative DOFs is as follows:

$$\mathbf{Z}_{\mathbf{r}}\tilde{\mathbf{u}}_{\mathbf{r}} + \tilde{\boldsymbol{\lambda}} = \tilde{\mathbf{f}}_{\mathbf{r}}, \tag{II.81}$$

where $\mathbf{Z}_{\mathbf{r}}$ is the dynamic stiffness matrix reduced to relative displacements and $\tilde{\mathbf{f}}_{\mathbf{r}}$ is the vector of the external forces reduced to relative displacements:

$$\mathbf{Z}_{\mathbf{r}} = \left[(\mathbf{Z}_{\mathbf{red}}^{(1)})^{-1} + (\mathbf{Z}_{\mathbf{red}}^{(2)})^{-1}\right]^{-1}, \tag{II.82}$$

$$\tilde{\mathbf{f}}_{\mathbf{r}} = \mathbf{Z}_{\mathbf{r}}\left[(\mathbf{Z}_{\mathbf{red}}^{(1)})^{-1}\tilde{\mathbf{f}}_{\mathbf{red}}^{(1)} - (\mathbf{Z}_{\mathbf{red}}^{(2)})^{-1}\tilde{\mathbf{f}}_{\mathbf{red}}^{(2)}\right]. \tag{II.83}$$

The final size of the harmonic system is equal to $(2N_h + 1)(n_{nl}/2)$.

Solving the system (II.81) by the nonlinear resolution algorithm yields the relative displacements $\tilde{\mathbf{u}}_{\mathbf{r}}$ and the contact forces $\tilde{\boldsymbol{\lambda}}$. Thus, using the relation (II.79) in Eqs. (II.77) and (II.78), it is possible to obtain the displacements on each of the contacting surfaces $\tilde{\mathbf{u}}_{nl}^{(1)}$ and $\tilde{\mathbf{u}}_{nl}^{(2)}$.

These two reduction steps do not lead to any approximation of the dynamics of the system. Nevertheless, the numerical quality of $\mathbf{Z}_{\mathbf{r}}$ and $\tilde{\mathbf{f}}_{\mathbf{r}}$ may be affected as their expressions given by Eq. II.82 and Eq. II.83 involve the inversion of matrices, introducing numerical errors.

2.5.3 Evaluation of the contact forces by AFT

Solving the previous algebraic system (II.81) requires a prior computation of the contact forces $\tilde{\boldsymbol{\lambda}}$. Unfortunately, it is difficult to develop a strategy in which the nonlinear forces are handled in the frequency domain because of their dependence on the state of each contact node (stick, slip, or separation) which is, *a priori*, unknown. Thus, an alternating Frequency-Time (AFT) procedure is used to estimate the contact forces in the time domain, using a discrete Fourier transform, before going back to the frequency domain to evaluate the Eq. (II.81). This procedure, called Dynamic Lagrangian Frequency-Time (DLFT), uses a prediction-correction process to determine the contact state and

the associated forces. It enables the verification of Coulomb's friction law, as well as the ensuring of the non-interpenetration condition between the contacting bodies, as presented in section I.1.2. Because of the prediction-correction process performed by the DLFT, it allows to ensure the exact verification of the non-regular contact laws without adding an approximation due to the use of regularised contact laws.

Formulation of the dynamic Lagrangians. This method is based upon the augmented Lagrangians approach but adapted to a frequency-domain framework. In the DLFT method developed by Nacivet [103], the nonlinear contact forces are implemented with a time-domain procedure by introducing a dynamic Lagrangian formulation based on penalising the difference between the relative displacements at the interface, calculated by the nonlinear solver in the frequency domain, and the relative displacements calculated in the time domain from the nonlinear contact forces by verifying the Coulomb friction and non-penetration conditions. Indeed, these nonlinearities cannot be dealt with a simple AFT procedure since they cannot be written as analytical expressions in the time domain.

Remembering the reduced equation of the system Eq. (II.81) in the frequency domain, expressed in terms of relative displacements and defined in section II.2.5.2:

$$\mathbf{Z_r}\tilde{\mathbf{u}}_\mathbf{r} + \tilde{\boldsymbol{\lambda}} = \tilde{\mathbf{f}}_\mathbf{r},$$

its solution consists in minimizing the following residual function:

$$\mathbf{r}(\tilde{\mathbf{u}}_\mathbf{r}) = \mathbf{Z_r}\tilde{\mathbf{u}}_\mathbf{r} + \tilde{\boldsymbol{\lambda}} - \tilde{\mathbf{f}}_\mathbf{r}. \tag{II.84}$$

In the framework of the DLFT method, the unknown contact forces $\tilde{\boldsymbol{\lambda}}$ are expressed as dynamic Lagrangians, formulated as penalisation of the equations of motion in the frequency domain, using a pseudo-penalty coefficient ε, used to enforce the correspondence between the time and frequency descriptions of displacements, as follows:

$$\tilde{\boldsymbol{\lambda}} = \tilde{\mathbf{f}}_\mathbf{r} - \mathbf{Z_r}\tilde{\mathbf{u}}_\mathbf{r} + \varepsilon(\tilde{\mathbf{u}}_\mathbf{r} - \tilde{\mathbf{x}}_\mathbf{r}). \tag{II.85}$$

A new unknown vector of relative displacements $\tilde{\mathbf{x}}_\mathbf{r}$ is introduced. To calculate $\tilde{\boldsymbol{\lambda}}$, it is necessary to calculate $\tilde{\mathbf{x}}_\mathbf{r}$. This vector is evaluated in the time domain, as will be detailed in section II.2.5.4, to ensure compliance with contact and friction conditions. When the convergence is reached, $\tilde{\mathbf{x}}_\mathbf{r}$ verifies:

$$\tilde{\mathbf{u}}_\mathbf{r} = \tilde{\mathbf{x}}_\mathbf{r}. \tag{II.86}$$

The value of $\tilde{\mathbf{u}}_\mathbf{r}$ provides a prediction of the contact state, while the verification of the contact laws is imposed by $\tilde{\mathbf{x}}_\mathbf{r}$, which represents the term of correction.

More precisely, the contact forces in Eq. (II.85) are computed in the normal and tangential directions, as follows:

$$\tilde{\boldsymbol{\lambda}}^\mathbf{N} = \tilde{\mathbf{f}}_\mathbf{r}^\mathbf{N} - (\mathbf{Z_r}\tilde{\mathbf{u}}_\mathbf{r})^\mathbf{N} + \varepsilon_N(\tilde{\mathbf{u}}_\mathbf{r}^\mathbf{N} - \tilde{\mathbf{x}}_\mathbf{r}^\mathbf{N}), \tag{II.87a}$$

$$\tilde{\boldsymbol{\lambda}}^\mathbf{T} = \tilde{\mathbf{f}}_\mathbf{r}^\mathbf{T} - (\mathbf{Z_r}\tilde{\mathbf{u}}_\mathbf{r})^\mathbf{T} + \varepsilon_T(\tilde{\mathbf{u}}_\mathbf{r}^\mathbf{T} - \tilde{\mathbf{x}}_\mathbf{r}^\mathbf{T}). \tag{II.87b}$$

According to the formulations of Nacivet [123], it is also possible to formulate the

problem in terms of pseudo-penalisation on the relative velocities.

Choice of the pseudo-penalty coefficient. The pseudo-penalty coefficient ε can be chosen arbitrarily since, at convergence, the results do not depend on it. However, its value influences the speed of convergence and the quality of the result [159]. To ensure good convergence of the nonlinear algorithm, it is necessary to select a suitable value for ε. In this regard, the value of the pseudo-penalty coefficient ε should be chosen to balance in the Eq. (II.85), the contributions of the equation of motion $(\tilde{\mathbf{f}}_\mathbf{r} - \mathbf{Z}_\mathbf{r}\tilde{\mathbf{u}}_\mathbf{r})$ and the contributions of the contact constraints $\varepsilon(\tilde{\mathbf{u}}_\mathbf{r} - \tilde{\mathbf{x}}_\mathbf{r})$. Charleux [110] proposed to take ε of the same order of magnitude of the spectral radius ϱ[1] of the stiffness matrix $\mathbf{Z}_\mathbf{r}$ corresponding to the predominant harmonic, i.e. the harmonic of the excitation, so denoted as $\mathbf{Z}_{\mathbf{r(ex)}}$:

$$\varepsilon \approx \varrho(\mathbf{Z}_{\mathbf{r(ex)}}). \tag{II.88}$$

2.5.4 Prediction/correction procedure

The contact forces $\tilde{\boldsymbol{\lambda}}$, both in normal and tangential directions (the exponents N and T are omitted for simplicity of notation), can be split as follows:

$$\tilde{\boldsymbol{\lambda}} = \tilde{\boldsymbol{\lambda}}_\mathbf{u} - \tilde{\boldsymbol{\lambda}}_\mathbf{x}, \tag{II.89}$$

with

$$\tilde{\boldsymbol{\lambda}}_\mathbf{u} = \tilde{\mathbf{f}}_\mathbf{r} - \mathbf{Z}_\mathbf{r}\tilde{\mathbf{u}}_\mathbf{r} + \varepsilon\tilde{\mathbf{u}}_\mathbf{r}, \tag{II.90a}$$

$$\tilde{\boldsymbol{\lambda}}_\mathbf{x} = \varepsilon\tilde{\mathbf{x}}_\mathbf{r}. \tag{II.90b}$$

In the Eq. (II.89), the term $\tilde{\boldsymbol{\lambda}}_\mathbf{u}$, dependent on $\tilde{\mathbf{u}}_\mathbf{r}$, represents the term of prediction used to determine the stick or slip behaviour of the system since every term is known. The term $\tilde{\boldsymbol{\lambda}}_\mathbf{x}$, dependent on $\tilde{\mathbf{x}}_\mathbf{r}$, is the correction term. The correction is applied by imposing its value to ensure the validation of Coulomb's friction law and unilateral contact law.

The pair of unknowns $(\tilde{\boldsymbol{\lambda}}, \tilde{\mathbf{x}}_\mathbf{r})$ in the Eq. (II.85) is computed through an AFT procedure. For this purpose, the period T is divided into n_t time steps. An iDFT is used to transform the multi-harmonic vectors $\tilde{\boldsymbol{\lambda}}$, $\tilde{\boldsymbol{\lambda}}_{\boldsymbol{u}}$ and $\tilde{\boldsymbol{\lambda}}_{\boldsymbol{x}}$ in the time domain, where they assume the form of the vectors $\left\{\boldsymbol{\lambda}^{\boldsymbol{k}}\right\}_{k=1,\ldots,n_t}$, $\left\{\boldsymbol{\lambda}^{\boldsymbol{k}}_\mathbf{u}\right\}_{k=1,\ldots,n_t}$ and $\left\{\boldsymbol{\lambda}^{\boldsymbol{k}}_\mathbf{x}\right\}_{k=1,\ldots,n_t}$, respectively. These vectors represent the values of the contact forces for each time instant, denoted with the exponent k, over the period T. The dimension of the vector of the contact forces in the time domain is $(n \text{ x } n_t)$.

(a) Initialisation at the first time instant. The contact forces are calculated with a prediction-correction process using an iterative method. However, it is necessary to initialise the value of the contact forces at the first time instant $k = 0$. The initialisation can be chosen arbitrarily. To correct the initialisation error contact forces are calculated

[1] Let $(\lambda_1, ..., \lambda_n)$ be the eigenvalues of a matrix $\mathbf{A} \in C_{nxn}$ the spectral radius ρ of $\mathbf{A}$ is defined as: $\rho(\mathbf{A}) = max\{|\lambda_1|, ..., |\lambda_n|\}$

at each instant over one period T, and then one can use the last value $\boldsymbol{\lambda}_{\mathrm{x}}^{T}$, to recompute over another complete period $2T$.

(b) Contact state prediction. In the time domain, it is easier to check the transition criteria between the three possible contact states: separation, stick, and slip. The prediction step consists in evaluating a first predictive value of the contact forces $\boldsymbol{\lambda}_{\mathrm{pred}}^{k}$. This evaluation is done by assuming a stick contact state at each contact node as the initial condition. In this condition, the relative displacement in the normal direction is null $\mathrm{x}_{\mathrm{r}}^{\mathrm{N}} = 0$, and the vector of relative displacements in the tangential directions $\mathrm{x}_{\mathrm{r}}^{\mathrm{T}}$ is constant between two-time steps t_k and t_{k-1}. This means that the node does not move. Consequently, the prediction is done by:

$$\begin{cases} \lambda_{\mathrm{pre}}^{k,\mathrm{N}} = \lambda_{\mathrm{u}}^{k,\mathrm{N}} \\ \boldsymbol{\lambda}_{\mathrm{pre}}^{k,\mathrm{T}} = \boldsymbol{\lambda}_{\mathrm{u}}^{k,\mathrm{T}} - \boldsymbol{\lambda}_{\mathrm{x}}^{k-1,\mathrm{T}} \end{cases} \tag{II.91}$$

(c) Correction of the contact forces. The contact forces at each instant k, are then determined by correcting the prediction $\boldsymbol{\lambda}_{\mathrm{pre}}^{k}$, by evaluating $\boldsymbol{\lambda}_{\mathrm{x}}^{k}$ to verify the unilateral and the Coulomb friction laws.

$$\boldsymbol{\lambda}^{k} = \boldsymbol{\lambda}_{\mathrm{u}}^{k} - \boldsymbol{\lambda}_{\mathrm{x}}^{k}. \tag{II.92}$$

The correction term $\boldsymbol{\lambda}_{\mathrm{x}}^{k}$ is determined by the function of the predicted contact state: separation, stick or slip.

- **Separation:** $\lambda_{\mathrm{pre}}^{k,\mathrm{N}} \geq \mathrm{N}_{0\mathrm{t}}$, where $\mathrm{N}_{0\mathrm{t}}$ is the static pre-load.
  If the predicted normal force is positive, it corresponds to a tensile force. This means a separation between the contact nodes, i.e. the contact is lost, and the contact forces should be zero:

$$\begin{cases} \lambda_{\mathrm{x}}^{k,\mathrm{N}} = \lambda_{\mathrm{u}}^{k,\mathrm{N}} \\ \lambda_{\mathrm{x}}^{k,\mathrm{T}} = \lambda_{\mathrm{u}}^{k,\mathrm{T}} \end{cases} \tag{II.93}$$

- **Stick:** $\lambda_{\mathrm{pre}}^{k,\mathrm{N}} < \mathrm{N}_{0\mathrm{t}}$ and $||\boldsymbol{\lambda}_{\mathrm{pre}}^{k,\mathrm{T}}|| < \mu \left|\lambda_{\mathrm{pre}}^{k,\mathrm{N}} - N_{0t}\right|$.
  If the predicted normal force is negative, it corresponds to a compressive force. This means a contact assured between contact nodes. According to Coulomb's law, the second condition implies that the contact is in a stuck condition. In this case, the prediction is correct since the relative displacements in the normal direction $\mathrm{x}_{\mathrm{r}}^{\mathrm{N}}$ are null, and the relative displacements in the tangential direction $\mathrm{x}_{\mathrm{r}}^{\mathrm{T}}$ are constant, between two consecutive time steps. Thus, according to the Eq. (II.90b):

$$\begin{cases} \lambda_{\mathrm{x}}^{k,\mathrm{N}} = 0 \\ \boldsymbol{\lambda}_{\mathrm{x}}^{k,\mathrm{T}} = \boldsymbol{\lambda}_{\mathrm{x}}^{k-1,\mathrm{T}} \end{cases} \tag{II.94}$$

- **Slip:** $\lambda_{\mathrm{pre}}^{k,\mathrm{N}} < \mathrm{N}_{0\mathrm{t}}$ and $||\boldsymbol{\lambda}_{\mathrm{pre}}^{k,\mathrm{T}}|| \geq \mu \left|\lambda_{\mathrm{pre}}^{k,\mathrm{N}} - N_{0t}\right|$.
  Also, in this case, contact is ensured between correspondent nodes. The second condition means that the solid is sliding according to the Coulomb friction law. The normal relative displacement is null $\mathrm{x}_{\mathrm{r}}^{\mathrm{k,N}} = 0$, so that the correction of the normal force is:

$$\begin{cases} \lambda_{\mathrm{x}}^{k,\mathrm{N}} = 0 \\ \boldsymbol{\lambda}_{\mathrm{x}}^{k,\mathrm{T}} = \boldsymbol{\lambda}_{\mathrm{x}}^{k-1,\mathrm{T}} + \left(1 - \mu \left|\lambda_{\mathrm{pre}}^{k,\mathrm{N}} - N_{0t}\right| \dfrac{\boldsymbol{\lambda}_{\mathrm{pre}}^{k,\mathrm{N}}}{\left\|\boldsymbol{\lambda}_{\mathrm{pre}}^{k,\mathrm{T}}\right\|}\right) \boldsymbol{\lambda}_{\mathrm{pre}}^{k,\mathrm{T}} \end{cases} \tag{II.95}$$

About the correction of the tangential contact forces $\boldsymbol{\lambda}_{\mathrm{x}}^{k,\mathrm{T}}$, its evaluation is based on the Coulomb friction law that imposes the value $||\boldsymbol{\lambda}_{\mathrm{pre}}^{k,\mathrm{T}}|| = \mu \left|\lambda_{\mathrm{pre}}^{k,\mathrm{N}} - N_{0t}\right|$ and its direction, which is the same of the relative tangential velocities, defined as:

$$\dot{\mathbf{u}}_{\mathbf{r}}^{k,\mathrm{T}} = \frac{\mathbf{u}_{\mathbf{r}}^{k,\mathrm{T}} - \mathbf{u}_{\mathbf{r}}^{k-1,\mathrm{T}}}{t^k - t^{k-1}}. \tag{II.96}$$

Thus, Coulomb's law enables to write of the vector of the tangential contact forces as a function of the tangential relative velocities and in the same directions:

$$\boldsymbol{\lambda}^{k,\mathrm{T}} = \mu \left|\lambda_{\mathrm{pre}}^{k,\mathrm{N}} - N_{0t}\right| \frac{\dot{\mathbf{u}}_{\mathbf{r}}^{k,\mathrm{T}}}{\left\|\dot{\mathbf{u}}_{\mathbf{r}}^{k,\mathrm{T}}\right\|}. \tag{II.97}$$

Using the Eq. (II.91) and the Eq. (II.92), it is possible to express:

$$\boldsymbol{\lambda}_{\mathrm{pre}}^{k,\mathrm{T}} - \boldsymbol{\lambda}^{k,\mathrm{T}} = \boldsymbol{\lambda}_{\mathrm{u}}^{k,\mathrm{T}} - \boldsymbol{\lambda}_{\mathrm{u}}^{k-1,\mathrm{T}}. \tag{II.98}$$

Then, combining the Eqs. (II.96), (II.97), (II.98) and (II.90b) it results:

$$\boldsymbol{\lambda}_{\mathrm{pre}}^{k,\mathrm{T}} = \left(\mu \frac{\left|\lambda_{\mathrm{pre}}^{k,\mathrm{N}} - N_{0t}\right|}{\left\|\dot{\mathbf{u}}_{\mathbf{r}}^{k,\mathrm{T}}\right\|} + \varepsilon(t^k - t^{k-1})\right) \dot{\mathbf{u}}_{\mathbf{r}}^{k,\mathrm{T}}. \tag{II.99}$$

The last equation shows the co-linearity relation between the vectors $\boldsymbol{\lambda}_{\mathrm{pre}}^{k,\mathrm{T}}$ and $\dot{\mathbf{u}}_{\mathrm{r}}^{k,\mathrm{T}}$, so it can be written that:

$$\frac{\dot{\mathbf{u}}_{\mathbf{r}}^{k,\mathrm{T}}}{\left\|\dot{\mathbf{u}}_{\mathbf{r}}^{k,\mathrm{T}}\right\|} = \frac{\boldsymbol{\lambda}_{\mathrm{pre}}^{k,\mathrm{T}}}{\left\|\boldsymbol{\lambda}_{\mathrm{pre}}^{k,\mathrm{T}}\right\|}, \tag{II.100}$$

so that the Eq. (II.97) becomes:

$$\boldsymbol{\lambda}^{k,\mathrm{T}} = \mu \left|\lambda_{\mathrm{pre}}^{k,\mathrm{N}} - N_{0t}\right| \frac{\boldsymbol{\lambda}_{\mathrm{pre}}^{k,\mathrm{T}}}{\left\|\boldsymbol{\lambda}_{\mathrm{pre}}^{k,\mathrm{T}}\right\|}. \tag{II.101}$$

Finally, by substituting the Eq. (II.101) into the Eq. (II.98) the second condition of the system (II.95) is obtained.

As the last step, the updated Lagrangians, expressed in time domain $\left\{\boldsymbol{\lambda}^{\boldsymbol{k}}\right\}_{k=1,\ldots,n_t}$, are transformed back in the frequency domain $\tilde{\boldsymbol{\lambda}}$, using a DFT. In addition, to reduce the computational time of the Newton-Raphson algorithm, in this work, the Jacobian matrix of the contact forces has been computed analytically. The calculation of this matrix is proposed in the Appendix A.

2.6 Concluding remarks

After having discretized the variational equations of the problem, this chapter has described different methods for solving and studying the periodic solutions of the nonlinear equations. First with attention to time integration schemes and then with reliable methods for finding periodic solutions in the frequency domain, with a focus on the Harmonic Balancing Method. These methods are complemented by various tools, such as continuation techniques, enabling to study of the evolution of systems dynamics as a function of a chosen control parameter. The Craig-Bampton reduction method has been presented to reduce the system's size to be solved. Finally, the last section focuses on solution methods for contact problems. The Dynamic Lagrangian Frequency-Time (DLFT) method is chosen for solving the dynamic problem with friction contacts. The following advantages support this choice: the DLFT method uses augmented Lagrangians, which directly allow the non-smooth frictional contact law without any softening, avoiding approximation and simulating real physical behaviour. In addition, compared to the conventional contact penalty methods, the convergence results do not depend on any penalty coefficient (hence the term pseudo-penalty coefficients used to enforce the contact constraints).

The wear phenomenon will be introduced and coupled with dynamics in chapter III. The evaluation of wear will be embedded in the DLFT algorithm, splitting time into two scales: a fast one associated with vibratory phenomena and a slow one related to wear.

Chapter III

Wear introduction strategy in a nonlinear dynamics problem

This chapter aims to present the method chosen for the numerical treatment of contact problems with wear under dynamic loading. The first part introduces a strategy for coupling fretting wear and dynamics. It is based on the Dynamic Lagrangian Frequency-Time method (DLFT) developed by Nacivet et al. [123] and on a multiscale approach to reduce computational costs: the DLFT with wear method, developed and validated by Salles [13, 124]. It consists of studying the system evolution, splitting the time into two scales: a fast scale for dynamics and a slow scale for wear phenomena. An academic numerical model will be considered and evaluated to (i) serve as a phenomenological example to understand basic phenomena at work when coupling wear and dynamics and (ii) introduce various concepts concerning the evolution of contact interface, worn volume, hysteresis loops and forced response dynamics. This chapter's conclusions will be useful for studying an experimental test case in the following.

Outline of the chapter

3.1 Reference problem with wear: governing equations

Moreau [26, 162] has shown that it is possible to include discontinuous phenomena such as friction in the class of generalized standard materials by selecting a convex but not necessarily differentiable dissipation potential, called pseudo-potential. In this regard, a generalized standard model has been developed by Strömberg [27] for studying interface phenomena in the situation of fretting wear. It is derived from the principle of virtual power and the fundamental thermodynamics laws. The local constitutive equations are built by defining two specific surface potentials: a free energy potential Ψ, which corresponds to the Signorini unilateral contact condition, and a dissipation pseudo-potential Φ, which corresponds to the Coulomb's friction and Archard's wear laws. This approach allows the construction of laws representing the mechanics of the interface by respecting the thermodynamics laws. The derivation of all equations and conditions for developing the constitutive model at the interface and the definition of the free energy and dissipation potentials are detailed in the works of Strömberg [27, 28] and Klarbring [163], whose studies originate from the works of Lemaitre and Chaboche [164].

Following the works of Salles [13, 161] and Strömberg [27], two state variables $\mathbf{u_T}$ and w are introduced to represent friction and wear. These variables define the tangential displacement and the wear depth at the interface. Wear mechanisms occur at the microscopic scale. At a macroscopic scale, wear is characterised by debris detachment and a modified contact profile. In the proposed model, wear is therefore identified as a variable w, interpreted as a gap in the normal direction between the contacting surfaces.

3.1.1 Variational or weak formulation

The reference contact problem of two elastic bodies with a frictional contact interface, previously defined in section II.2.1.1 and illustrated in FIGURE II.1, is considered. The variational formulation associated with the dynamical fretting wear problem is defined by three integral equations (III.1a), (III.1b),(III.1c), and one constitutive law (III.3). These equations originate respectively from the principle of virtual work, the weak formulation of Signorini's unilateral contact conditions, Coulomb's complementary law and Archard's wear local law.

For each time instant $t \in [0, T]$, the displacement field $\mathbf{u}(\mathbf{x})$ for each point $\mathbf{x}$ of both solids Ω^s (with u_N and $\mathbf{u_T}$ its normal and tangential components) and the contact pressure field $\mathbf{p}$ (with $p_N = \mathcal{W}$ and $\mathbf{p_T}$ its normal and tangential components), are searched. $\mathcal{W}$ has the same physical meaning as p_N. It indicates the dual of w, i.e. the driving force for wear. Defined $\mathbf{v}$, $\mathbf{p}'$ and $\mathcal{W}'$ the test fields related to $\mathbf{u}$, $\mathbf{p}$ and $\mathcal{W}$, respectively, the variational equations are then expressed as:

$$\int_{\Omega^s} \rho \ddot{u}_i v_i \,\mathrm{d}V + \int_{\Omega^s} E_{ijkl} \frac{\partial u_k}{\partial x_l} \frac{\partial v_i}{\partial x_j} \,\mathrm{d}V + \int_{\Gamma_c} p_i v_i \,\mathrm{d}A - \int_{\Gamma_f^s} f_i v_i \,\mathrm{d}A = 0 \quad \forall \mathbf{v} \in \mathcal{V}, \tag{III.1a}$$

$$\int_{\Gamma_c} (u_N - w - g)(p'_N - p_N) \,\mathrm{d}A \leq 0 \quad \forall p'_N \in \mathcal{K}_N, \tag{III.1b}$$

$$\int_{\Gamma_c} (\dot{u}_{T_\alpha}(p'_{T_\alpha} - p_{T_\alpha}) + \dot{w}(\mathcal{W}' - \mathcal{W})) \,\mathrm{d}A \leq 0 \quad \forall (p'_T, W') \in \mathcal{F}(p_N). \tag{III.1c}$$

The dual spaces are defined as follows:

$$\begin{aligned}\mathcal{V} &= \{\mathbf{v}|\mathbf{v}(\mathbf{x}) = 0, \quad \mathbf{x} \in \Gamma_u\}\,,\\ \mathcal{K}_N &= \{p_N|p_N(\mathbf{x}) \geq 0, \quad \mathbf{x} \in \Gamma_c\}\,,\\ \mathcal{F}(p_N) &= \{(\mathbf{p_T}, \mathcal{W})|(\mathbf{p_T}(\mathbf{x}, \mathcal{W}(\mathbf{x})) \in F(P_N), \quad \mathbf{x} \in \Gamma_c\}\,.\end{aligned}$$

$F(p_N)$ is the closed convex set which describes the friction and the wear limit criterion. It is expressed as:

$$F(p_N) = \{||\boldsymbol{p_T}|| - \mu p_N + K_w p_N \mathcal{W} - K_w p_N^2 \leq 0\},$$

with μ and K_w the Coulomb's friction coefficient and Archard's wear constant, respectively. In Eq. (III.1c), the components of each vector are represented in an orthonormal basis $\mathbf{n}_\alpha$ (with $\alpha = 1, 2$), perpendicular to $\mathbf{n_c}$. The constitutive law expressing Archard's local formulation is the following:

$$\dot{w} = K_w p_N ||\dot{\mathbf{u}}_\mathbf{T}||, \tag{III.3}$$

in accordance with Eq. (I.18) defined in section I.1.4.1.

3.1.2 Finite element discretization

A finite elements discretization of Eq. (III.1a) is performed to numerically solve the problem defined above. This strategy, introduced in section II.2.1.3, is coupled with a component mode synthesis, reducing the size of the problem. In the considered case, all the DOFs where friction and wear occur must be retained as physical coordinates. In addition to the Eqs. (II.16) obtained for the problem without wear (studied in chapter II), the wear contribution $\mathbf{W}^s(t)$ is here introduced in the nonlinear terms $\mathbf{F}^s_\mathbf{c}$. The governing equations of both structures ($s = 1, 2$) with a common contact interface are then the following:

$$\mathbf{M}^s\ddot{\mathbf{U}}^s(t) + \mathbf{C}^s\dot{\mathbf{U}}^s(t) + \mathbf{K}^s\mathbf{U}^s(t) + \mathbf{F}^s_\mathbf{c}(\mathbf{U}^s(t), \dot{\mathbf{U}}^s(t), \mathbf{W}^s(t)) = \mathbf{F}^s_\mathbf{ex}(t). \tag{III.4}$$

Wear is calculated at each interface node (index m) through the following equation:

$$\dot{\mathbf{W}}^m = \frac{K_w}{I^m}|P_N^m|||\dot{\mathbf{U}}^m_\mathbf{T}||, \tag{III.5}$$

where P_N^m is the nodal normal force and $\dot{\mathbf{U}}^m_\mathbf{T}$ is the tangential velocity of each node m. I^m is a weighting factor for node m. It depends on the quadrature rule used to calculate the integrals on each elementary contact area.

In the FEM formalism, the constraints introduced by Eqs. (III.1b) and (III.1c) and correspondent to Signorini's unilateral contact condition and Coulomb's friction law, respectively, become:

$$(\mathbf{U_N} - \mathbf{W} - \mathbf{G})(\mathbf{P'_N} - \mathbf{P_N}) \leq 0 \quad \forall \mathbf{P'_N} \in \mathcal{K}^h_N, \tag{III.6a}$$

$$\dot{\mathbf{U}}_\mathbf{T}(\mathbf{P'_T} - \mathbf{P_T}) \leq 0 \quad \forall \mathbf{P'_T} \in \mathcal{F}^h(\mathbf{P_N}), \tag{III.6b}$$

where $\mathcal{K}_N^h$ and $\mathcal{F}^h(\mathbf{P_N})$ are the finite element approximations of $\mathcal{K}_N$ and $\mathcal{F}(p_N)$, respectively.

Time homogenization of the wear problem under dynamic loading. Wear phenomena under dynamic loads are multi-scale in time. The idea is to separate time into slow and fast time to overcome this added difficulty. The slow time is related to tribological phenomena, while the fast time is the scale of the dynamic problem.

Following the formalism used in [165], where the problem of fatigue life prediction is modelled as a multi-scale phenomenon in the time domain using a mathematical homogenization theory with two-time coordinates, Salles [161] proposed a time homogenisation of the wear problem under dynamic loading. Noted as ϕ, a generic response field (displacement, strain or stress) can be defined as:

$$\phi(\mathbf{x}, t) = \phi(\mathbf{x}, \tau, \eta), \tag{III.7}$$

where τ is the fast time scale, such that $\tau = \omega t$ and η is the slow time scale related to the time t, such that $\eta = \xi t$ where ξ is a very small parameter ($\xi \ll \omega$). By calculating the first and second derivatives of ϕ with respect to the time, one can obtain:

$$\dot{\phi}(\mathbf{x}, t) = \omega \frac{\partial \phi}{\partial \tau} + \xi \frac{\partial \phi}{\partial \eta}, \tag{III.8a}$$

$$\ddot{\phi}(\mathbf{x}, t) = \omega^2 \frac{\partial^2 \phi}{\partial \tau^2} + 2\omega\xi \frac{\partial^2 \phi}{\partial \eta \partial \tau} + \xi^2 \frac{\partial \phi}{\partial \eta^2}. \tag{III.8b}$$

This strategy can be applied to the dynamic wear problem III.4 (the s-index is omitted for ease of reading). Thus, the following system for displacements can be obtained:

$$\mathbf{M}(\omega^2 \frac{\partial^2 \mathbf{U}}{\partial \tau^2} + 2\omega\xi \frac{\partial^2 \mathbf{U}}{\partial \eta \partial \tau} + \xi^2 \frac{\partial \mathbf{U}}{\partial \eta^2}) + \mathbf{C}(\omega \frac{\partial \mathbf{U}}{\partial \tau} + \xi \frac{\partial \mathbf{U}}{\partial \eta}) + \mathbf{K}\mathbf{U} + \mathbf{F_c}(\mathbf{x}, \tau, \eta) = \mathbf{F_{ex}}(\mathbf{x}, \tau),$$

and then noted that the wear process is much slower than the vibratory phenomenon, it is possible to neglect the terms associated with ξ compared to the ones in ω:

$$\omega^2 \mathbf{M} \frac{\partial^2 \mathbf{U}}{\partial \tau^2} + \omega \mathbf{C} \frac{\partial \mathbf{U}}{\partial \tau} + \mathbf{K}\mathbf{U} + \mathbf{F_c}(\mathbf{x}, \tau, \eta) = \mathbf{F_{ex}}(\mathbf{x}, \tau), \tag{III.9}$$

in which the term $\mathbf{F_c}(\mathbf{x}, \tau, \eta)$ allows to couple wear and dynamics.

3.2 DLFT method with wear

The solution of Eq. (III.4) is studied in the frequency analysis framework. The solution method follows the same steps as the nonlinear dynamic problem without wear defined in section II.2.2.2.

3.2.1 Hypotheses to introduce wear

The hypotheses on the contact zone have been presented in section II.2.5.1. In addition to the assumptions made and illustrated in FIGURE II.6, wear is introduced. Wear is identified as a gap distance between corresponding nodes, which increases over time and,

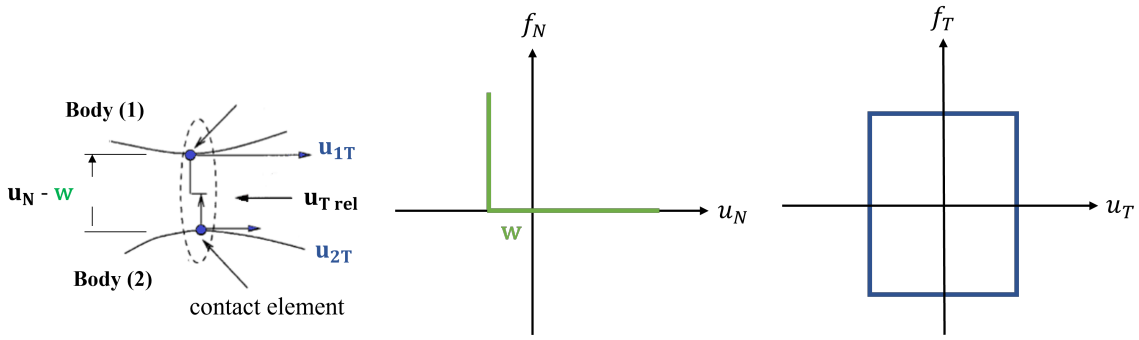

(a) Zoom on contact element (b) Unilateral contact law (c) Coulomb friction law

FIGURE III.1: DLFT - Contact hypothesis with wear.

as such, comes to correct the expressions of the relative displacements in the normal directions, as shown in FIGURE III.1.

Archard's wear formulation is integrated over the interface. This approach makes it possible not to mesh the interface with too fine elements, which would increase time due to remeshing and calculation. This study does not directly consider the roughness of the surfaces and all the microscopic effects like asperities and deformations. These phenomena are taken into account globally through the macroscopic wear coefficient K_w introduced in section I.1.4.1 in Archard's wear law. As previously mentioned, this coefficient is obtained from experiments and its value depends on material properties and operating conditions. The temperature effects are neglected, and the friction coefficient is assumed unaffected by the wear evolution.

Wear is a very slow phenomenon, and wear depths are very small compared to the characteristic dimensions of the structures in contact. Thus, the modifications of the mass and stiffness matrices due to wear are neglected.

Harmonic Balance Method with two-time scales. This method belongs to the family of multi-scale approaches described by Meirovitch [125] for a single harmonic balance. The Harmonic Balance Method is used to solve the system (III.9), considering two-time scales to couple the dynamics and wear phenomena. Thus, the approximate periodic solution (II.28), expressed in the form of a truncated Fourier series, becomes:

$$\mathbf{u}(\tau,\eta) = \tilde{\mathbf{u}}_{\mathbf{0}}(\eta) + \sum_{k=1}^{N_h} \left(\tilde{\mathbf{u}}_{\mathbf{k,c}}(\eta)cos(k\tau) + \tilde{\mathbf{u}}_{\mathbf{k,s}}(\eta)sin(k\tau)\right), \tag{III.10}$$

where τ represents the "fast" time scale related to vibrations and η the "slow" time scale related to wearing. η can therefore be regarded as a significant multiple of the period $T = 2\pi/\omega$ of the fretting wear cycles.

It is therefore supposed that wear does not change the appearance of the periodic response during a short lapse of time during which it is possible to evaluate displacements and forces with the Fourier series of τ. For a longer duration, Fourier coefficients evolve as functions of η, being η associated with a much longer time scale than the time period $T = 2\pi/\omega$ of the fretting wear cycles. Subsequently, Eq. (III.10) can be expressed as a multi-harmonic vector:

$$\tilde{\mathbf{u}}(\eta) = [\tilde{\mathbf{u}}_0, \tilde{\mathbf{u}}_{\mathbf{1,c}}, \ldots, \tilde{\mathbf{u}}_{\mathbf{N_h,c}}, \tilde{\mathbf{u}}_{\mathbf{1,s}}, \ldots, \tilde{\mathbf{u}}_{\mathbf{N_h,s}}], \tag{III.11}$$

where the index **c** and **s** indicate the cosine and sine functions.

Calculation of the contact forces. Contact forces are treated by the DLFT method as presented in section II.2.5.3. Thus, the introduction of Eq. (III.10) into Eq. (III.4) and the application of a Galerkin procedure, give the following set of nonlinear algebraic equations:

$$f(\tilde{\mathbf{u}}(\eta)) = \mathbf{Z_r}\tilde{\mathbf{u}}_\mathbf{r}(\eta) + \tilde{\boldsymbol{\lambda}}(\eta) - \tilde{\mathbf{f}}_\mathbf{r} = 0, \tag{III.12}$$

where $\tilde{\mathbf{u}}_\mathbf{r}$ and $\tilde{\mathbf{f}}_\mathbf{r}$ are respectively the multi-harmonic vectors of relative displacements and reduced external forces. $\boldsymbol{\lambda}(\eta)$ is the vector of the Lagrange multipliers, which represents the unknown contact force vector in the frequency domain, as defined in section II.2.5.3.

The system (III.12) has been condensed on the nonlinear DOFs and then on the relative displacements. It is solved by a nonlinear Newton-type solver in the same way as presented in the previous chapter, and the Jacobian matrix used to compute Eq. (III.12) is evaluated analytically as indicated in Appendix A, obtaining a significant reduction in the computational time.

The contact forces are then computed in normal and tangential directions, as detailed in section II.2.5.3. More precisely, to introduce the presence of wear, the normal contact forces previously expressed by Eq. (II.87a), are modified as follows:

$$\tilde{\boldsymbol{\lambda}}^\mathbf{N} \quad = \tilde{\mathbf{f}}_\mathbf{r}^\mathbf{N} - (\mathbf{Z_r}\tilde{\mathbf{u}}_\mathbf{r})^\mathbf{N} + \varepsilon_N(\tilde{\mathbf{u}}_\mathbf{r}^\mathbf{N} - \mathbf{G} - \tilde{\mathbf{x}}_\mathbf{r}^\mathbf{N}), \tag{III.13}$$

where the wear depth is implemented as an interface gap $\mathbf{G} = \tilde{\mathbf{W}}^\mathbf{N}$ in normal direction.

3.2.2 Wear depth calculation

After having updated $\tilde{\mathbf{u}}_\mathbf{r}$, as the nonlinear solver has converged (internal loop of the algorithm shown in Figure III.3), the wear depth is calculated locally at each interface node. The nodal (index m) wear is calculated by integrating the wear rate defined by Eq. (III.5). As mentioned in section III.3.2.1, the wear depth W does not depend on τ because it does not evolve too much in a single period. For this reason, the wear depth depends only on η (slow time scale):

$$W^m = W^m(\tau, \eta) = W^m(\eta). \tag{III.14}$$

Thus, by integrating for a single fretting cycle, the evolution of wear after one period for each contact node is:

$$\delta W^m(\eta) = \int_\eta^{\eta+T} K_w |P_N^m(\tau, \eta)| \, \|\dot{\mathbf{u}}_\mathbf{T}^m(\tau, \eta)\| \, \mathrm{d}\tau, \tag{III.15}$$

in which $\eta = nT$, with T is the time period of the harmonic excitation and η the time scale related to wear. K_w is the Archard's wear coefficient, defined by Eq. (I.17). P_N^m

and $\dot{\mathbf{u}}_{\mathbf{T}}^{m}$ are, respectively, the normal local load and the relative tangential velocity at each node m, calculated through Eq. (III.12).

The local Archard's formulation adequately represents the wear problem while remaining relatively simple to integrate within the numerical simulations.

Calculation by wear increment. The DLFT with wear method developed by Salles in [13] is implemented. This approach is chosen to represent an improvement compared to previous ones performed in [124], where an arbitrary number of cycles was chosen before updating wear depth. This strategy consists of implementing a cycles jump strategy to decrease the computational costs and the number of slow-time steps, by increasing the wear depth instead of the time. This cycles jump strategy has also been used for the computation of fretting wear coupling a semi-analytical (SA) contact solver with the FE method in [17, 166].

A maximum authorized total wear depth, denoted as W_{max}^{tot}, is set heuristically for the considered duration up to the period T. This value is divided into c intermediate slow wear steps ΔW^{*}. Also, c is chosen heuristically to provide a good compromise between good accuracy and a reasonable calculation time. The interface gap can be updated using Eq. (III.15). η is chosen equal to N_c, the number of fretting cycles. The relation between the jumped cycles ΔN_c and W_{max}^{tot} is:

$$\Delta N_c(\eta) = \frac{W_{max}^{tot}}{c \max\limits_{m}(\delta W^{m}(\eta))}. \tag{III.16}$$

The wear nodal depth W^m, $\Delta N_c(\eta)$ cycles later, is obtained by integrating the following explicit scheme:

$$W^{m}(N_c + 1) = W^{m}(N_c) + \Delta N_c \delta W^{m}(\eta). \tag{III.17}$$

The integration following the explicit scheme is shown in FIGURE III.2:

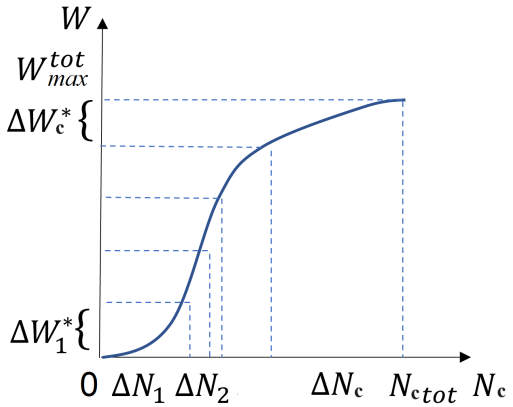

FIGURE III.2: Explicit scheme for wear depth calculation.

Once the maximum number of cycles $N_{c_{tot}}$ has been reached, the calculation stops. Physically, this means that the wear rate becomes too small, and it no longer wears out, or it wears out at a constant wear rate if it exists. The algorithm of the DLFT with wear is illustrated in FIGURE III.3.

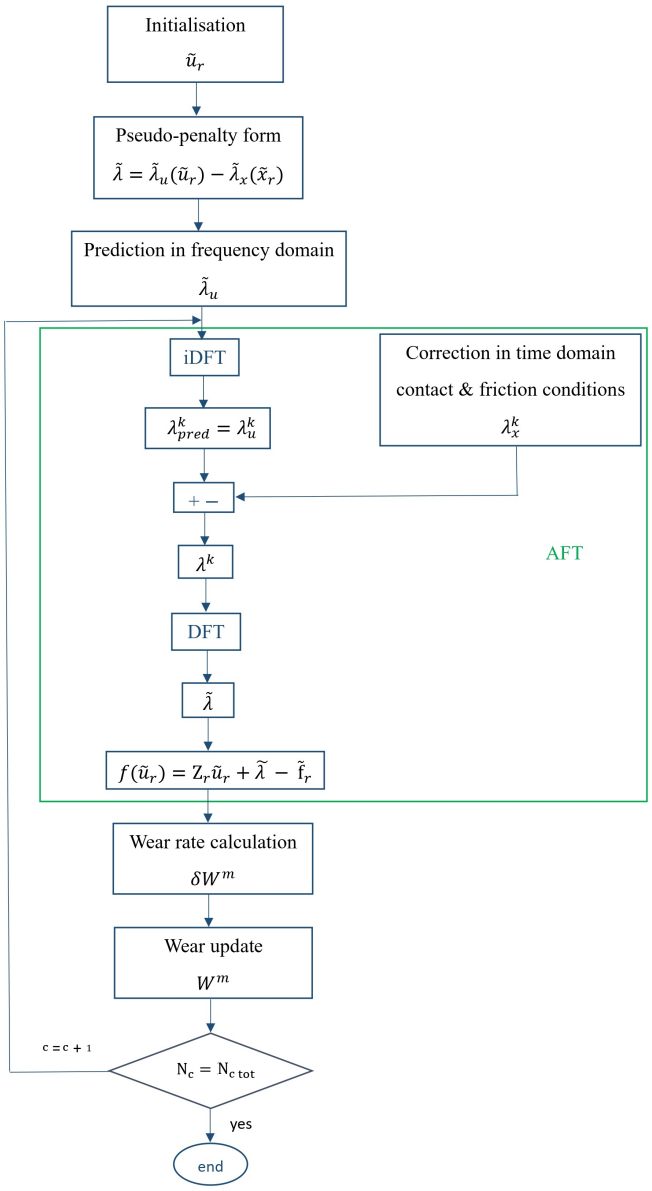

FIGURE III.3: DLFT with wear algorithm.

The next section uses an academic numerical example to apply the methodology, assessing difficulties or correcting implementation problems. This model serves as a phenomenological example and guide to understanding basic phenomena at work when coupling wear and dynamics. Moreover, it introduces various concepts concerning the evolution of contacting interfaces, worn volume, hysteresis loops and forced response dynamics, which are helpful for studying an experimental test case in the following chapters. Concerning the methodology, it gives information about the robustness of the calculation and looks at what scenarios it is possible to reconstruct to feed the test-calculation dialogue, which will be considered in chapter IV and chapter V.

3.3 Academic numerical example

3.3.1 Description of the model

The first examples treated by the DLFT with wear method were reported in [13, 101]. The academic example proposed in [101] is reconsidered here, but adding a more detailed parametric analysis and evaluating some variables to build, for example, the numerical hysteresis cycles, introduced in section I.1.3.1. The model comprises two masses in contact with friction, as illustrated in FIGURE III.4. The equations of the motion of the

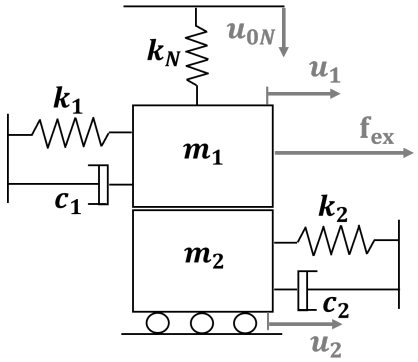

FIGURE III.4: 2-DOFs contact friction model.

system are only in the tangential directions and expressed as follows:

$$\begin{aligned} m_1\ddot{\mathbf{u}}_1 + c_1\dot{\mathbf{u}}_1 + k_1\mathbf{u}_1 + \mathbf{f_c} &= \mathbf{f_{ex}}, \\ m_2\ddot{\mathbf{u}}_2 + c_2\dot{\mathbf{u}}_2 + k_2\mathbf{u}_2 - \mathbf{f_c} &= 0, \end{aligned} \tag{III.18}$$

where $\mathbf{f_c}$ are the tangential friction forces which must respect the unilateral contact and Coulomb conditions. The external excitation force is imposed in cosine, such as $\mathbf{f_{ex}} = F_{ex}\cos(\omega t)$. The 2-DOFs model is reduced in a relative displacement system, becoming a 1-DOF system. In the normal direction, a displacement $\mathbf{u_{0N}}$, which constrains a spring k_N, is imposed. Thus, the normal force $\mathbf{f_N}$, due to the preload of k_N per $\mathbf{u_{0N}}$, is:

$$\mathbf{f_N} = k_N\mathbf{u_{0N}}. \tag{III.19}$$

Thus, the wear occurs in the normal direction at the interface. The wear depth conducts to the relaxation of the spring k_N, leading to the decrease of the normal contact force. The choice of relaxing the normal force when wear increases is because, in a real 3D problem, the entire contact surface is not in a stick-slip situation, so some surfaces remain without wear (total sticking zone). As a result, the normal force in the worn area decreases. The simulations with a phenomenological model aim at determining the influence of friction and wear on the dynamic behaviour.

3.3.2 Preliminary studies: parametric analysis

The system consists of two unit masses $m_1 = m_2 = 1$ kg, with $k_1 = \pi^2$ N.mm^{-1} and $k_2 = 7\pi^2$ N.mm^{-1} and a viscous damping ratio of $\xi_1 = \xi_2 = 0.1\%$. An initial normal load $\mathbf{f_N} = 10$ N, as defined by Eq. (III.19), is applied ($k_N = 1 \cdot 10^4$ N.mm^{-1} and $u_{0N} = 1 \cdot 10^{-3}$ mm). Preliminary simulations are performed without friction ($\mu = 0$)

and wear ($K_w = 0$). The input parameters of the 2-DOFs model are summarised in TABLE III.1.

m_1	k_1	ξ_1	m_2	k_2	ξ_2	k_N	u_{0N}
1	π^2	0.1	1	$7\pi^2$	0.1	$1 \cdot 10^4$	$1 \cdot 10^{-3}$
[kg]	[N.mm^{-1}]	[%]	[kg]	[N.mm^{-1}]	[%]	[N.mm^{-1}]	[mm]

TABLE III.1: 2-DOFs input parameters.

First, two linear states are evaluated, corresponding to two significant modes. Then the system's dynamic behaviour is studied by referring to them. These two modes, illustrated in FIGURE III.5, can be distinguished as follows:

- the first one corresponds to the mass m_1 free, indicating a total sliding state, at 0.5 Hz;
- the second one corresponds to the case when the two masses m_1 and m_2 are in a stick situation at 1 Hz, which is equivalent to studying a model of mass $m = m_1 + m_2$.

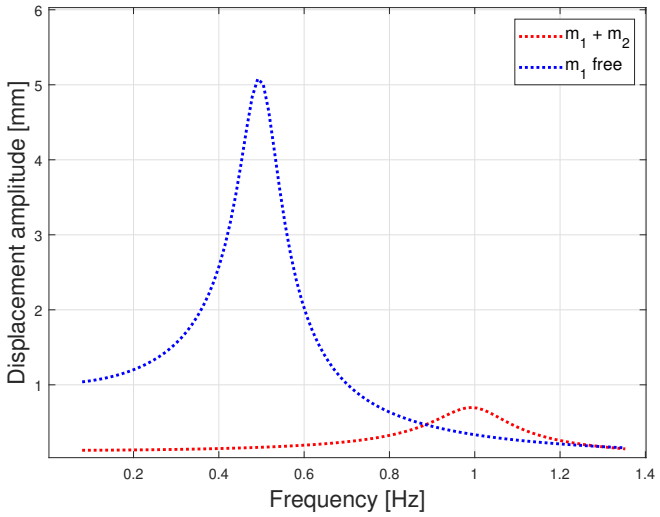

FIGURE III.5: Linear displacement response amplitudes.

Once the two linear cases have been calculated, these will represent the two asymptotic cases from which to start studying the system's dynamic behaviour as the numerical (number of harmonics, amplitude of the external excitation force) and physical (friction coefficient) parameters vary.

Influence of the excitation force. It is possible to study the model's behaviour between the two asymptotic states, previously described, by varying the amplitude F_{ex} of the external force. A friction coefficient $\mu = 1$ is imposed. FIGURE III.6 and FIGURE III.7 illustrate the influence of the amplitude of the external force on the frequency response, in terms of displacement of the mass m_1 and relative displacement, respectively. Starting from a low amplitude value, the two masses m_1 and m_2 are always in a predominant

sticking situation. In this case, it can be observed (see FIGURE III.7) that there is no relative displacement. As the amplitude of the excitation force increases the two masses start to slip. As a result, the response amplitude decreases the natural frequency moves toward the left, and the system becomes less stiff. For very high values of the excitation force, the response tends to overlap the FRF curve correspondent to the mass m_1 free.

For these simulations, $N_h = 7$ harmonics were considered. This choice will be justified in the next paragraph.

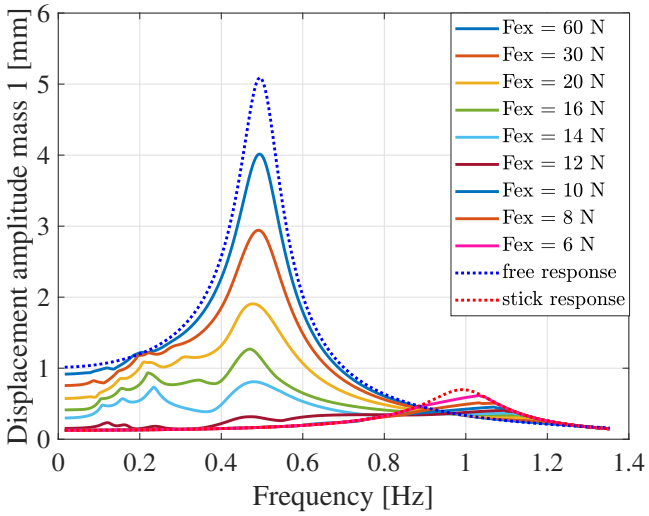

FIGURE III.6: Influence of the external excitation force on the FRFs of the mass m_1 for $N_h = 7$ and $\mu = 1$.

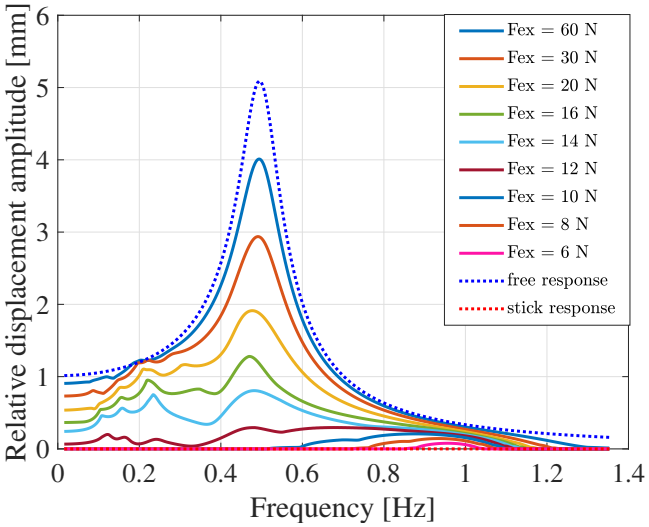

FIGURE III.7: Influence of the external excitation force on the FRFs of the relative displacement for $N_h = 7$ and $\mu = 1$.

Influence of the number of harmonics. One of the parameters to be fixed when setting up a harmonic balance resolution method is the number of harmonics N_h to

approximate the solution. The objective is to estimate the minimum number of harmonics to retain to ensure reasonable computation times and accuracy of the results, as introduced in section II.2.2.2.

The 2-DOFs system illustrated in FIGURE III.4 is reconsidered, with an excitation force of amplitude $F_{ex} = 10$ N imposed in cosine on the mass m_1. In this regard, it is advisable to consider an intermediate situation between the two asymptotic states because these two situations correspond to linear behaviours. An intermediate situation is rather constraining from the point of view of the number of harmonics to keep since it corresponds to most irregular responses due to sliding/stacking behaviour and it will require more harmonics to be represented accurately.

FIGURE III.8 shows the forced response of the mass m_1 for different numbers of harmonics N_h retained. The number of harmonics given in the figure's legend refers to the maximum order of the harmonics considered. The reference is here given by a direct time integration.

In the case of keeping only one harmonic, the result is considerably overestimated, being the nonlinear displacements represented only by a sinusoidal oscillation. The convergence of the solution becomes slower when more harmonics are considered to approach the reference solution given by the time integration. Thus, the choice of 7 harmonics, represents a good compromise in terms of convergence and time of calculation.

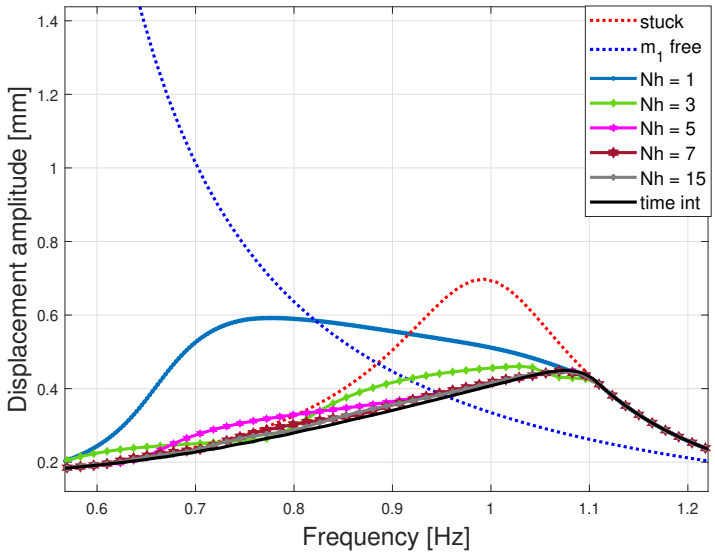

FIGURE III.8: Influence of the number of harmonics on the FRFs of the mass m_1 for $F_{ex} = 10$ N and $\mu = 1$.

Influence of the friction coefficient. FIGURE III.9 shows the influence of the friction coefficient μ on the nonlinear forced response for a given excitation amplitude $F_{ex} = 10$ N. It can be observed that when the friction coefficient is low, there is a predominant slip behaviour. Then, as the friction coefficient increases, the response amplitude decreases. If it increases too much, the system behaves as when there is no friction, tending to the limit behaviour of the two masses glued together.

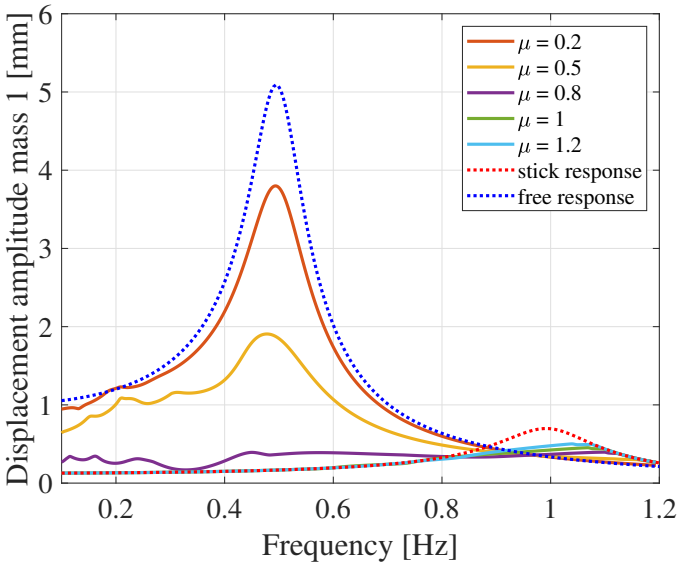

FIGURE III.9: Influence of the friction coefficient on the FRFs of the mass m_1 for $N_h = 7$ and $F_{ex} = 10$ N.

3.3.3 Influence of wear on dynamics

The 2-DOFs friction contact model illustrated in FIGURE III.4 is now considered to understand the coupling between dynamics and wear. The DLFT method with wear, detailed in section III.3.2, is applied. In addition to the equations of motion in the tangential directions previously expressed by Eqs. (III.18), it is necessary to consider the wear contribution by adding to the system the following equations in the normal direction:

$$\mathbf{f_N} = k_N \ (\mathbf{u_{0N}} - w), \tag{III.20a}$$

$$\Delta W(\eta) = K_w \int_{\eta}^{\eta+T} \mathbf{f_N} \, \|\dot{\mathbf{u}}_\mathbf{2} - \dot{\mathbf{u}}_\mathbf{1}\| \, \mathrm{d}\tau, \tag{III.20b}$$

where $\mathbf{f_N}$ is the normal force acting on the first mass m_1. Concerning the normal force, for Eq. (III.19), the variable w is introduced. It represents the gap in the normal direction increasing due to the wear. $\dot{\mathbf{u}}_\mathbf{2}$ and $\dot{\mathbf{u}}_\mathbf{1}$ are the tangential velocities of the mass m_1 and m_2, respectively.

Simulations, including wear, are carried out with a friction coefficient $\mu = 1$. Regarding Archard's wear coefficient K_w, it calculates the wear rate over a cycle. Its value is quite arbitrary in the resolution strategy since the wear levels are updated in wear steps. It is important to note that depending on the wear kinetics (wear depth as a function of the number of cycles) on K_w, its value needs to be re-calibrated by experiments. Thus, not having for this example a value obtained from experiments, it is taken arbitrarily equal to $K_w = 1 \cdot 10^{-11}$ Pa^{-1}, as suggested by Strömberg in [28]. It should be observed that this value chosen for the wear coefficient, i.e. the wear rate, is indicative of a very slow wear rate. Consequently, the wear evolution is rather slow, and a high number of cycles is required to evaluate the wear evolution. However, this value has proved useful in [101] for representing the results of the academic example.

Dynamic response and wear evolution. The dynamic response of the system in presence of wear and the evolution of the wear depth will be studied for three amplitudes of excitation force: $F_{ex} = [6\ \text{N}, 10\ \text{N}, 16\ \text{N}]$. This choice is related to three states of interest which modify the system's dynamic response and give information about the wear evolution corresponding to a fully sticking state, an intermediate condition and a fully sliding state, as detailed in studying the influence of the external excitation force on the model's dynamic response (see FIGURE III.6).

In the following, the evolution of wear is plotted at multiple frequencies over a given frequency range. Starting from a condition without wear, the dynamic response is computed at a first prescribed frequency up to maximum wear. Then the solver proceeds to the subsequent frequency with unworn surfaces, and so on.

For an imposed amplitude $F_{ex} = 6$ N, the evolution of wear as a function of the number of cycles and frequencies is shown in FIGURE III.10b. In this condition, the two masses m_1 and m_2 are mostly stuck. The wear does not occur over the whole frequency range but increases approaching the adherent mode at about 1 Hz. After a certain number of cycles, wear evolution stops since, with an imposed displacement constrained a spring, the more the masses wear out, the more the normal force tends towards zero because of the release of the spring. FIGURE III.10a illustrates the influence of wear on the dynamic response. During the first fretting cycles the wear evolution is very slow, then it accelerates reaching the stuck mode, beyond which the system returns to an adherent state.

For an imposed amplitude $F_{ex} = 10$ N, the evolution of wear as a function of the number of cycles and frequencies is shown in FIGURE III.11b. This represents an intermediate situation. During the first few fretting cycles, the wear process is more important for frequencies close to the resonance at 1.1 Hz, for which the two masses are stuck together. FIGURE III.11a illustrates the influence of wear on the dynamic response. The increase of wear produces a transfer of the maximum of the vibration amplitude from the stuck mode to the sliding mode at about 0.5 Hz. The vibration amplitude becomes very large at 0.5 Hz. This behaviour has also been observed in [13] for bladed disk interfaces.

For an imposed amplitude $F_{ex} = 16$ N, the evolution of wear as a function of the number of cycles and frequencies is shown in FIGURE III.12b. In this case, it can be observed that wear appears in a frequency range more important than the previous ones. In particular, there is a frequency where wear evolution is faster at about 0.5 Hz where the system's behaviour is in a sliding situation (see FIGURE III.12a).

Fretting loops evolution with wear. The evolution of the fretting loop with wear for the case ($F_{ex} = 10$ N) is shown in FIGURE III.13. It can be observed that a decrease of the friction force leads to an increase of the relative displacement. This behaviour is expected for the proposed example because simulations started with a displacement $\mathbf{u_{0N}}$ which constrains a spring k_N imposed in the normal direction.

This behaviour is confirmed by studying the evolution of the wear depth as a function of the number of cycles. In FIGURE III.14, this evolution is represented for different N_h. As the number of cycles increases, an asymptotic behaviour corresponding to the imposed displacement $\mathbf{u_{0N}}$ can be reached. The mass m_1 wears in the normal direction, that is, the direction of the imposed displacement $\mathbf{u_{0N}}$. The increase of the wear depth

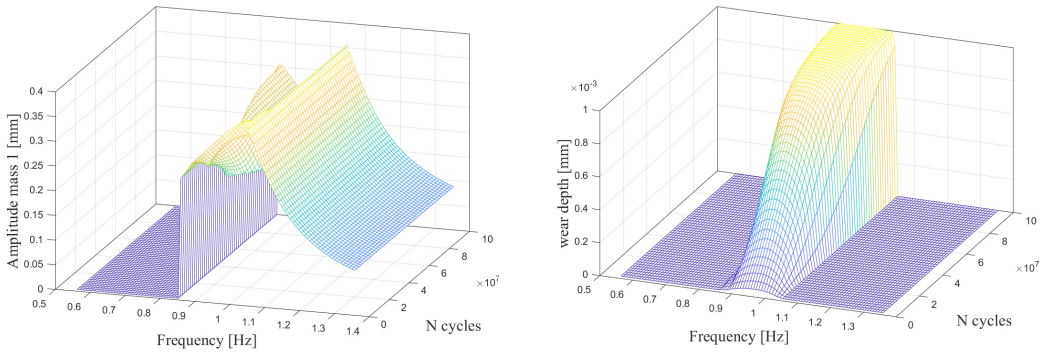

(a) (b)

FIGURE III.10: For an imposed amplitude $F_{ex} = 6$ N: (a) frequency response of the vibration amplitude of the mass 1, (b) wear depth evolution.

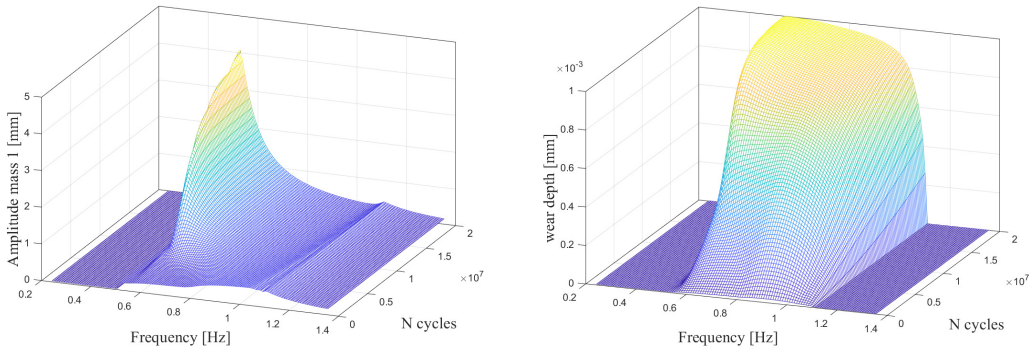

(a) (b)

FIGURE III.11: For an imposed amplitude $F_{ex} = 10$ N: (a) frequency response of the vibration amplitude of the mass 1, (b) wear depth evolution.

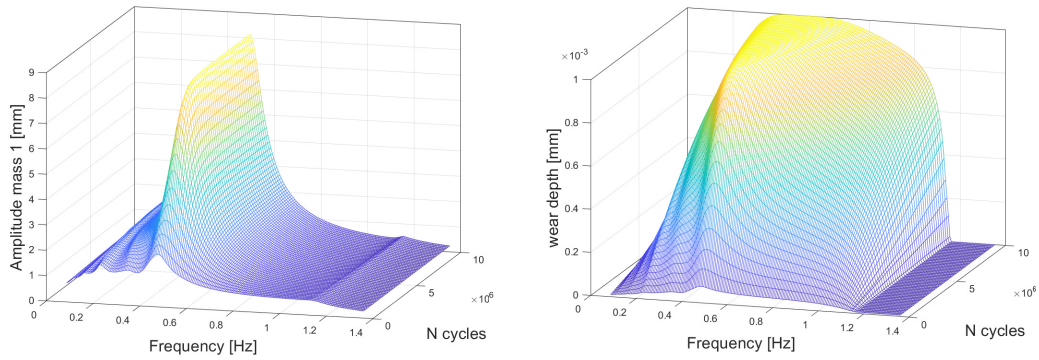

(a) (b)

FIGURE III.12: For an imposed amplitude $F_{ex} = 16$ N: (a) frequency response of the vibration amplitude of the mass 1, (b) wear depth evolution.

w leads to slackness of the spring and consequently to a decrease of the normal contact force $\mathbf{f_N}$, as expressed by Eq. (III.20a). In FIGURE III.14, it can also be observed that

the choice of $N_h = 7$ is good for the convergence of the results.

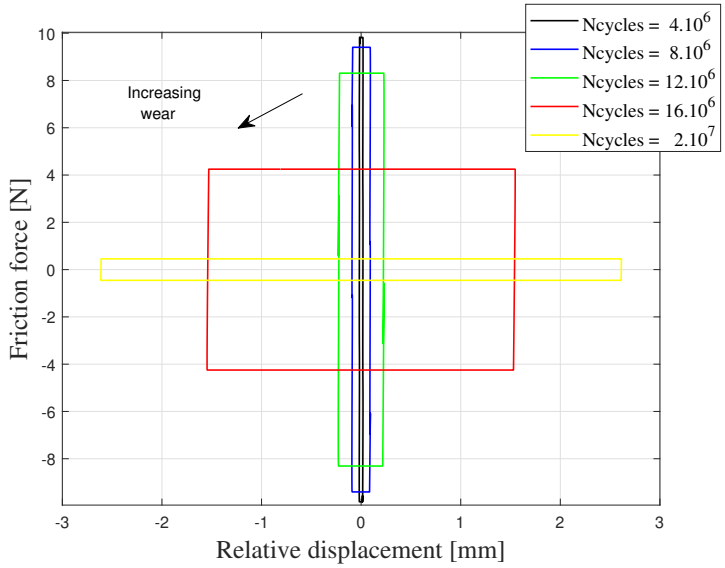

FIGURE III.13: Fretting loops for the case $F_{ex} = 10$ N with $N_h = 7$.

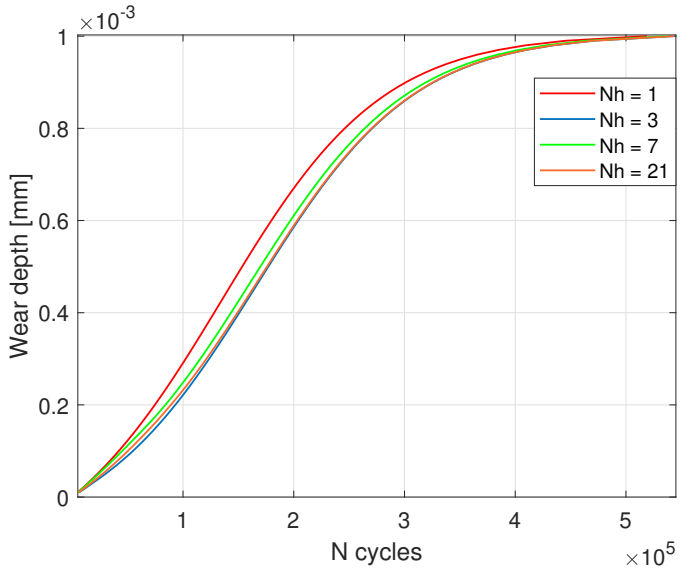

FIGURE III.14: For an imposed amplitude $F_{ex} = 16$ N at $f = 0.5$ Hz. Wear depth evolution for different values of N_h.

3.4 Concluding remarks

This chapter has described an approach for the numerical treatment of contact problems with wear under dynamic loading. The vibrational behaviour is analysed in the frequency domain using the harmonic balance method and AFT procedure. The wear evolution is integrated on a slow time scale through an explicit scheme coupled with a strategy in which a jumps cycles strategy is applied. More particularly, a DLFT with wear method is retained for simultaneously calculating the vibrational behaviour, and the

wear in situations of fretting wear is retained based on the assumption that dynamics and tribological phenomena can be separated into two-time scales.

Wear kinetics and their influence on dynamics have been studied using a simple numerical academic example. Results show that although the wear depths are minimal (a few microns), they significantly alter the vibratory behaviour of the system. The considered method to simulate the evolution of wear in frictional contacts confirms its adequacy for coupling dynamic and wear as demonstrated in [13]. The present study confirms previous findings and contributes additional results. The example has made it possible to numerically introduce critical parameters of the phenomenon, such as fretting cycles, contact states, and the influence of excitation levels. It also allows an understanding of where numerical simulations need special requirements, such as the values of wear constant and friction coefficient. Thus, the support of experimental input is essential, and calibration tests must be carried out to ensure that the life expectancy calculations are accurate to reality. In this regard, as part of the collaboration between the members of the EXPERTISE project, in chapter IV the experimental test rig built at the Imperial College London [18] will be modelled and its experimental data will be used to identify the parameters for the simulations of the nonlinear dynamics. Next, in chapter V, the DLFT with wear numerical approach will be applied for coupling wear and dynamics and evaluating the impact of fretting wear. Numerical simulations provide access to what measurement cannot be done locally and allow useful perturbation studies of some key parameters, which would be costly in the experiments.

Chapter IV

Pre-test calibration of a vibratory test rig

This chapter presents the vibratory test rig, designed at Imperial College London [167]. After a brief description of the design, instrumentation used, and setup of the vibratory test rig, a finite element modelling of the test rig and the fretting specimens is performed, using the design parameters of the test rig and the preliminary dynamic tests results, performed in [19]. Once modelled, an appropriate reduction method is applied to reduce adequately the problem's size. This chapter aims at identifying the parameters for the simulations of the nonlinear dynamics, performing sensitivity analysis of numerical and physical parameters and validating the numerical investigations for the unworn system.

Outline of the chapter

4.1 Experimental setup

Due to the high cost of full-scale industrial systems, the design of simplified experimental setups is essential for reproducing the configurations of industrial components at a laboratory scale. This section briefly describes the vibratory friction rig built in the Dynamic group of the Imperial College London [18]. This rig typically provides input contact parameters for aero engine applications by measuring friction hysteresis loops. More specifically, it allows the reproduction of the dynamic behaviour observed in friction dampers. Essential contacts, such as blade-root joints, under-platform dampers and bladed disk shroud contacts, are also carefully designed to ensure friction damping by allowing micro-slip at these contacts, which naturally leads to unwanted fretting wear. The rig gives then a more detailed description of the friction at the contact interfaces to allow more accurate modelling of these elements.

The experimental tests performed by Fantetti et al. [19] study the impact of fretting wear on the forced response of systems with dry friction contact. In this chapter, these series of fretting experiments are considered to validate the numerical simulations to be done in the next chapter.

4.1.1 Description of the Imperial College test rig

A simplified scheme of the test rig is illustrated in FIGURE IV.1. It consists of a moving block sliding on a static arm. The moving block is composed of a moving arm with a low mass, connected to a bigger moving mass by a knife edge, required to avoid any bending resulting from the normal load applied by a pneumatic actuator. This bigger moving mass is linked to the ground by two very flexible leaf springs, allowing purely horizontal displacements at the scale of fretting studies.

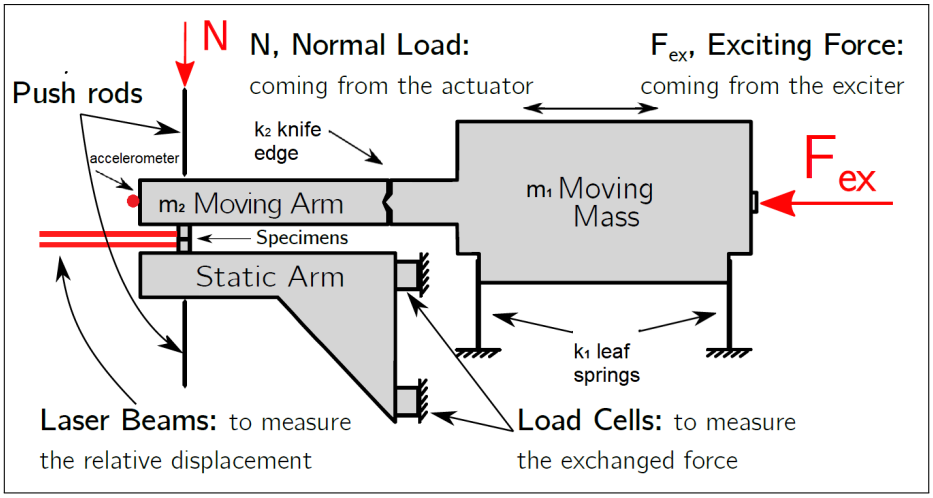

FIGURE IV.1: Simplified scheme of the test rig (adapted from [19]).

The photo of the test rig is shown in FIGURE IV.2 and the specimens' contact is zoomed in FIGURE IV.3. The contact couple is made of two cylindrical specimens rotated about their axis such that the two flat rectangular surfaces (visible in FIGURE IV.3a) become orthogonal, generating a flat-on-flat square contact configuration: the specimens form a 1 mm x 1 mm contact interface when assembled. The resulting nominal contact

area is then 1 mm^2. This arrangement is illustrated in FIGURE IV.3a. The top specimen is clamped to the moving arm, and the bottom specimen is fixed to the static arm.

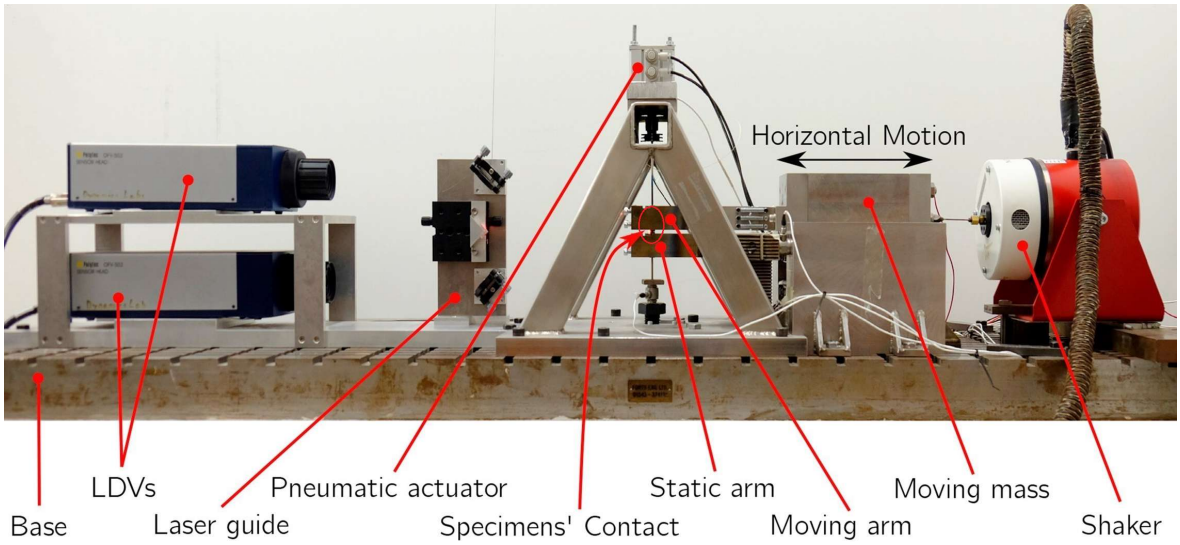

FIGURE IV.2: Photo of the Imperial College friction rig [19].

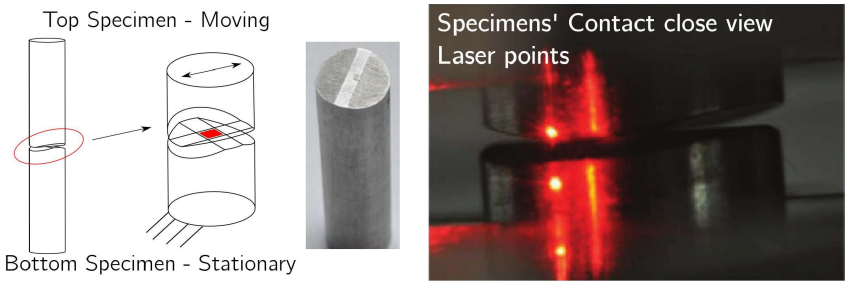

(a) (b)

FIGURE IV.3: Specimens contact [19]: (a) 90° orthogonal arrangement ensuring a squared nominal contact area, with a photo of an original specimen. (b) Close view of the two friction specimens, showing the laser measurement points.

The following criteria are adopted for the justification of the design of the test rig: (i) the capability to measure displacements and contact forces close to the contact area allows for capturing more accurate measurement data at the interface concerning the stick-slip behaviour to determine the hysteresis loops at each fretting cycle; (ii) the resonance peaks are well separated in the dominant sliding direction to isolate and study the effect of wear on the mode of interest; (iii) the tangential relative displacements are large enough to dissipate high energy per cycle and introduce wear effect.

The normal load is applied through a pneumatic actuator placed on the top of the moving block, ensuring continuous contact between the two specimens. The load is transmitted through rods pushing the specimens against each other; the rod located below the bottom specimen is used to complete the load path and avoid significant bending moments in the static arm (see FIGURE IV.1).

The excitation for the shaker is generated at the required frequency, and its amplitude is adjusted to control the relative displacement between the contact surfaces. The excitation frequency was fixed at 100 Hz, which represents the best working frequency for the test rig [122] i.e., relative movement amplitude allows to have the expected tribological conditions.

As specified above, the test rig provides measurements of the two parameters needed to obtain hysteresis loops: the relative displacement between the specimens and the friction force exchanged during this interaction. More precisely:

- the relative displacements between the two sliding specimens are measured through two Laser Doppler Vibrometers (LDVs) at points very close to the contact area, less than 1 mm above and below the interface, as illustrated in FIGURE IV.3b. These Laser Doppler Vibrometers measure the velocities, which are then integrated to obtain the displacements. This accurate measurement method does not affect the bulk elastic deformation of the specimens.
- The friction force is derived from dynamic load cell measurements attached to the static support, as illustrated in FIGURE IV.1.

For more details about the test rig's configuration, readers can refer to [18, 122].

4.1.2 Test rig and fretting specimens finite element modelling

An equivalent FE model of the whole test rig is generated using a 3D CAD model to perform the numerical analysis. The idea is to create a numerical model to reproduce the geometry and simulate equivalent tests, boundary conditions and external excitation dynamics. More specifically:

- The rig is modelled with a lumped-element model to approximate the rig's dynamic behaviour (i.e. the natural frequencies). Lumped parameter models have been widely used to investigate the dynamic system at the initial design stage because they can provide a basic understanding of the system with low computational costs.
- The specimens are modelled with a FE model to study the contact interface behaviour more accurately.

Test rig modelling. The rig dynamics is modelled through a simple 2-DOFs lumped mass model with two springs, as illustrated in FIGURE IV.4. Thus, the mass matrix $\mathbf{M_{rig}}$ and the stiffness matrix $\mathbf{K_{rig}}$ of the rig are expressed as:

$$\mathbf{M_{rig}} = \begin{bmatrix} m_1 & 0 \\ 0 & m_2 \end{bmatrix}, \quad \mathbf{K_{rig}} = \begin{bmatrix} k_1 + k_2 & -k_2 \\ -k_2 & k_2 \end{bmatrix}. \tag{IV.1}$$

A summary of the parameters characterising the 2-DOFs model of the test rig is given in TABLE IV.1. Solving the typical eigenvalue problem $([\mathbf{K_{rig}}] - \omega_i^2[\mathbf{M_{rig}]})\,\{\phi\}_i = 0$, it is possible to find both eigenvalues ω_i and eigenvectors $\{\phi\}_i$. ω_i is the angular frequency related to the natural frequency by $f_i = \omega_i/2\pi$ in Hz. $\{\phi\}_i$ is the mode shape corresponding to f_i. It refers to the deformation pattern at certain natural frequencies. The two natural frequencies are $f_1 = 39.7$ Hz and $f_2 = 2467.6$ Hz.

Specimens modelling. The specimens geometry is detailed in FIGURE IV.5. The main dimensions are listed in TABLE IV.2.

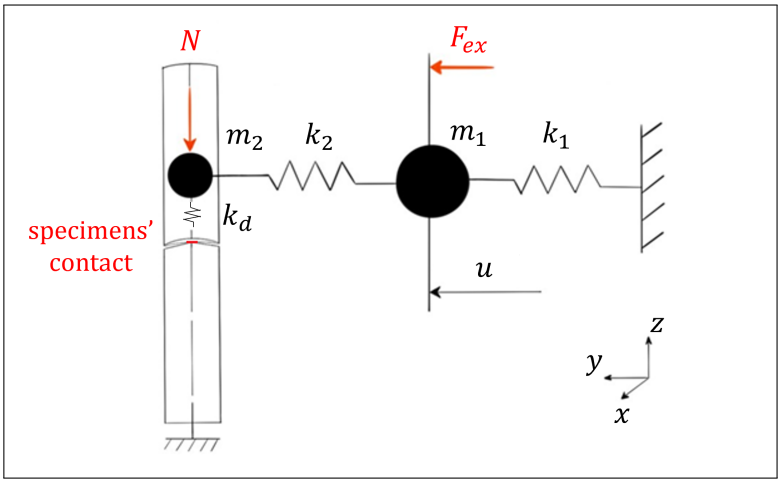

FIGURE IV.4: 2-DOFs Lumped model of the test rig.

	Parameter	Value	
Moving Mass	m_1	21.2	[kg]
Moving Arm	m_2	1.2	[kg]
Leaf spring stiffness	k_1	$1.4.10^6$	[N.m^{-1}]
Knife edge stiffness	k_2	273.10^6	[N.m^{-1}]

TABLE IV.1: 2-DOFs lumped model parameters.

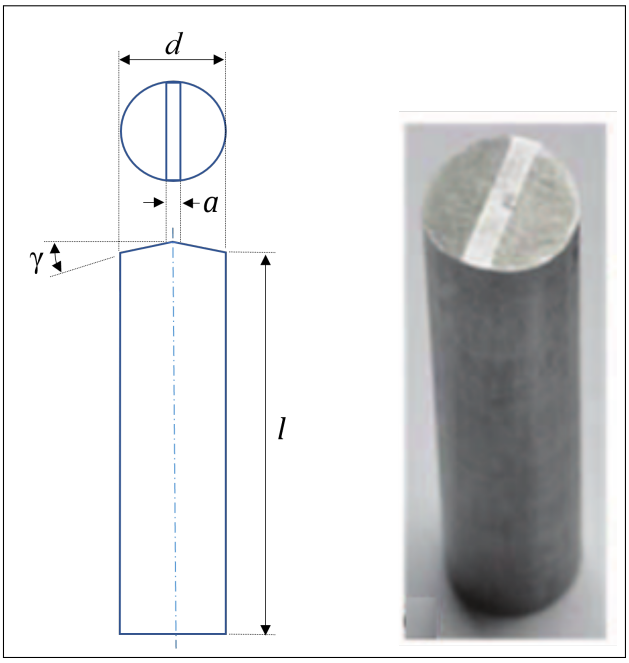

FIGURE IV.5: Photo of a real specimen with its geometrical dimensions.

Parameter	Value	
l	33	[mm]
a	1	[mm]
d	8	[mm]
γ	10°	

TABLE IV.2: Specimens geometry.

The specimens are made of standard stainless steel (SS304). The material's mechanical properties are detailed in TABLE IV.3.

	Parameter	Value	
Young's modulus	E	$190 \cdot 10^9$	[Pa]
Hardness	H	$1700 \cdot 10^6$	[Pa]
Density	ρ	7800	[kg.m^{-3}]
Poisson's ratio	ν	0.3	

TABLE IV.3: Mechanical properties - Specimens Material: Stainless Steel (SS304).

First, a CAD model for the specimens is realised, as illustrated in FIGURE IV.6.

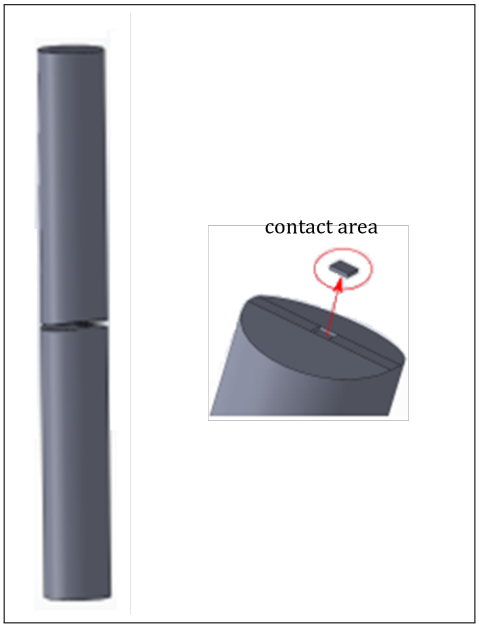

FIGURE IV.6: Specimen modelling: CAD model.

Then a detailed FE model is created to evaluate the system's dynamic behaviour at the interface. The commercial software employed for mesh generation is Ansys APDL. The specimens are modelled separately and meshed with 8-nodes quadratic brick elements. The contact area is modelled with a finer mesh of 10x10 elements with 121 contact nodes. The choice of the meshing done for the contact area for both specimens considers that the increment in the number of elements increases the computational

time for solving the nonlinear dynamic problem. Thus, to perform nonlinear dynamics calculations, this choice represents a good compromise between the accuracy of results and time calculations. At the interface, the mesh for each specimen is compatible at each contact node. The loss of compatibility due to movement will be considered to be negligible. FIGURE IV.7 shows the Finite Element Model of the specimens. The mesh of

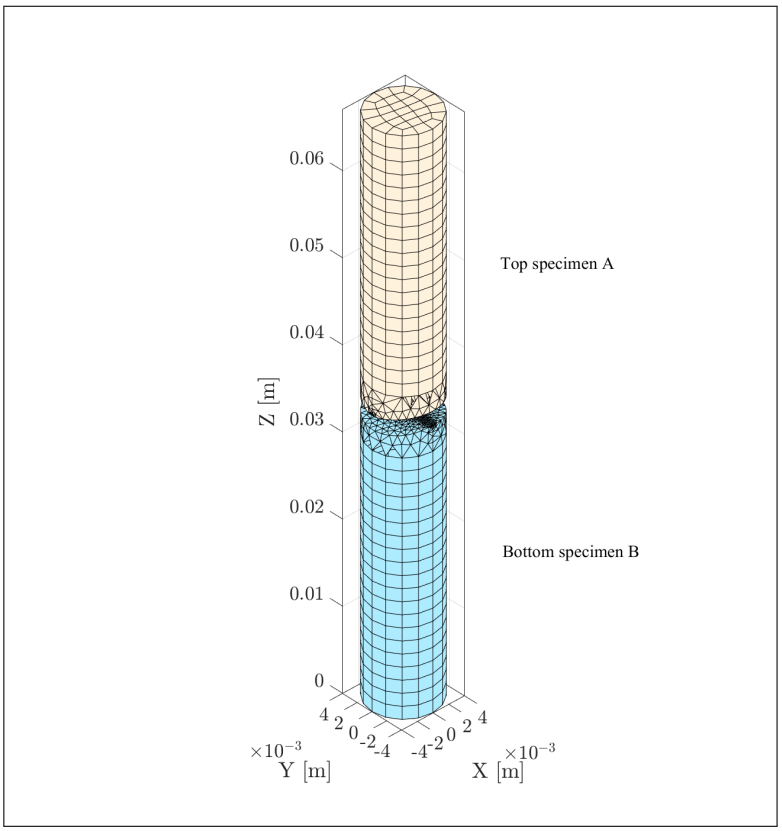

FIGURE IV.7: Specimens modelling: FE model.

the top and bottom specimens is detailed in FIGURE IV.8, where it is possible to note the orthogonality of the specimens, which forms a square contact area with a finer mesh. The specimen's inner mechanical behaviour is studied in the linear elastic field in the hypothesis of small deformations. In this numerical study, the roughness is neglected so that the contacting surfaces are assumed to be perfectly smooth.

The mass and stiffness matrices of the bottom and top specimens are previously calculated using the commercial FE solver Ansys APDL. At this stage, the number of DOFs equals 7278 DOFs for each specimen. The original mesh generated in Ansys and the mass and stiffness matrices of the specimens are then imported from Ansys to Matlab, where:

1. the boundary conditions are imposed to replicate the ones imposed experimentally;
2. the size of the model is appropriately reduced to gain numerical efficiency;
3. the frequency-time alternation based on dynamic Lagrangians is fully coded and implemented. The method aims at solving the contact problem under the nonlinear constraints defining the contact forces expressed in the time domain, as detailed in section II.2.5. The contact conditions are implemented between pairs of corresponding nodes over the interface. The results then being returned to the frequency

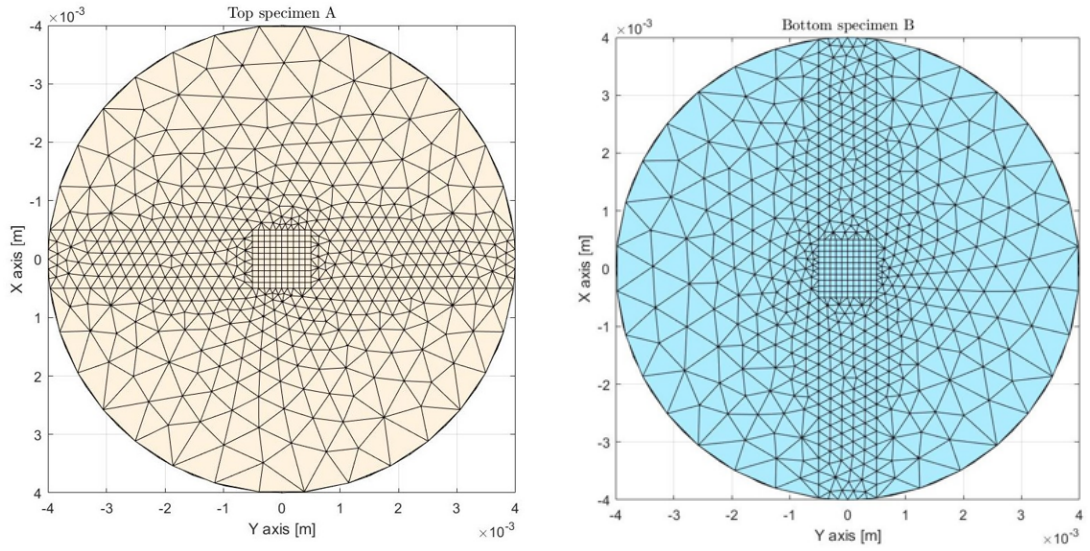

(a) (b)

FIGURE IV.8: Finite element modelling: (a) top specimen and (b) bottom specimen.

domain using discrete Fourier transforms to study the vibrational behaviour in the frequency domain.

Boundary and load conditions. The boundary conditions have been chosen to approach as the ones imposed experimentally. The system's configuration is clearly illustrated in FIGURE IV.4. The top specimen is rigidly linked to the moving arm m_2 and, together with the test rig's two masses m_2 and m_1, slides in the horizontal direction (y) over the bottom one, which is clamped to the static arm. However, the top specimen would not be constrained in the vertical direction (z) in this case. To avoid any numerical problem in Matlab simulations, due to the presence of a rigid body motion, a dummy spring k_d, with very low stiffness, is added in the vertical direction (z).

The normal load is constant and controlled during the whole test duration. Thus, the normal pressure is applied on the top face of the top specimen to simulate the experiment as closely as possible to reality. The external excitation force is applied on the mass m_1 allowing a motion in the horizontal direction (y) depending on the tribological conditions.

4.1.3 Reduction of the model's size

First, a reduction of the model is required to limit the high numerical costs induced by nonlinear phenomena in large FE models. To save computational time and capture the essential dynamic response, the FE model is reduced through the Craig-Bampton method with fixed interfaces [155]. The reduction has been realised with the help of the Craig-Bampton super-element, as detailed in section II.2.4. This method considerably reduces the number of DOFs in the model by keeping only the nodes of interest as well as the dynamic and static modes representing the behaviour of the full model. The first step for the reduction is the partitioning of the complete set of DOFs of the system into two subsets: the interface (denoted as master DOFs), corresponding to the ones physically retained after the reduction, and the internal (indicated as slave DOFs), corresponding

to the remaining ones, approximated by chosen mode shapes. In this way, it is possible to reorganise the structural matrices. Thanks to this distinction, it is easier to manage contact problems since the contact forces are applied directly to the physical DOFs of the reduced model (i.e. the contact DOFs).

The super-elements retain as physical nodes the contact nodes necessary for the nonlinear analysis (corresponding to 121 nodes x 3 DOFs = 363 DOFs for each specimen), an excitation node, on which the external excitation is applied later (corresponding to the mass m_1 of the rig) and an observation node, on which the amplitude results of the global behaviour of the test rig will be observed (located at 1 mm above the contact interface of the top specimen). The bottom and top specimens' super-elements are constructed independently to deal afterwards with the contact problem between pairs of corresponding nodes at the interface using the DLFT strategy (see section II.2.5.1). The remaining internal DOFs are reduced to N_m modal participation controlling the accuracy of the reduction basis. More specifically, $N_m = 16$ dynamic modes for the bottom specimen and $N_m = 19$ dynamic modes for the top specimen, ranging beyond the operating frequencies, have been retained on a reduced basis, for the analysis.

Precision of the reduced model. The convergence criteria presented in section II.2.4 are applied to assess the quality of the reduced models.

- **Criterion based on the eigenfrequencies**. The first natural frequencies of the reduced model are compared with the natural frequencies of the full-size model to validate the considered super-elements. The error is expressed as a frequency discrepancy $\Delta f(\%)$. For the bottom specimen, the frequency error for the first 16 modes is displayed in FIGURE IV.9a. It is less than 0.01%, which validates the sufficiency of the conservation of 16 dynamic modes in the reduction. For the top specimen, the choice of keeping the first 19 modes beyond the operating frequencies is validated since the relative discrepancy remains under the 1% as illustrated in FIGURE IV.9b.
- **Criterion based on eigenvectors**. The second most common criterion for evaluating the convergence of the reduced model is the Modal Assurance Criterion (MAC), allowing for comparison of the reduced model's mode shapes with the full one's modal vectors. The results obtained from the calculation of the MAC criterion are usually presented in a matrix form. It should be remembered that there is a very good correlation between the eigenvectors when the diagonal of this matrix is equal to or close to 1. For both specimens, a value of 1 on the diagonal indicates a very good correlation between the first mode shapes considered, as illustrated in FIGURE IV.10a and in FIGURE IV.10b

Reduction in the frequency domain. The system can be further reduced in the frequency domain, following the steps detailed in section II.2.5.2. A first condensation is performed on the nonlinear DOFs. In this case, the nonlinear DOFs are the contact DOFs. The linear DOFs are those retained as linear modes in Craig-Bampton reduction. It is always possible to determine the linear displacements of the rest of the structure from the displacements of the contact nodes through the Eq. (II.76).

Finally, a second condensation is applied to express the problem by means of the relative variables. This step is particularly well-suited when a node-to-node formulation

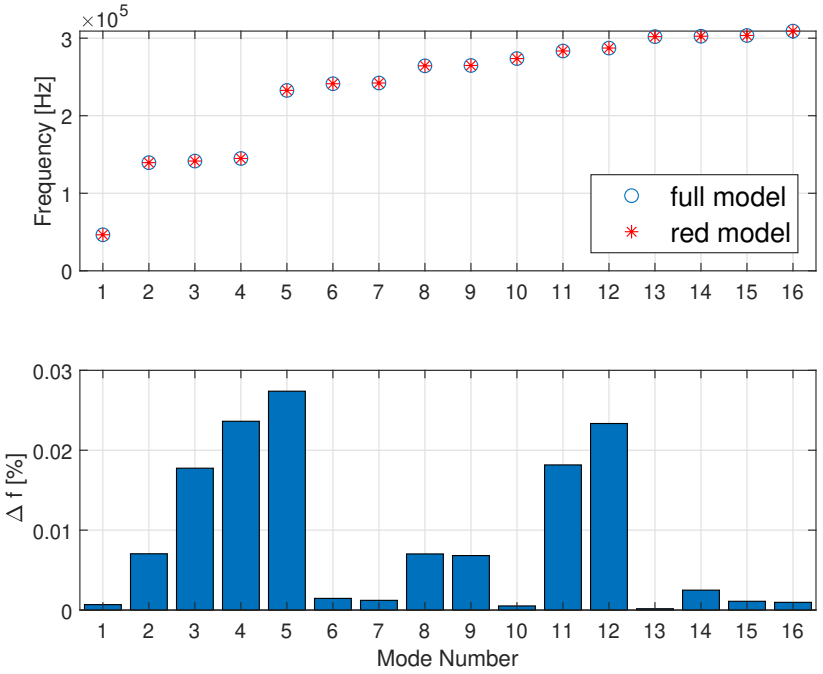

(a) Bottom specimen

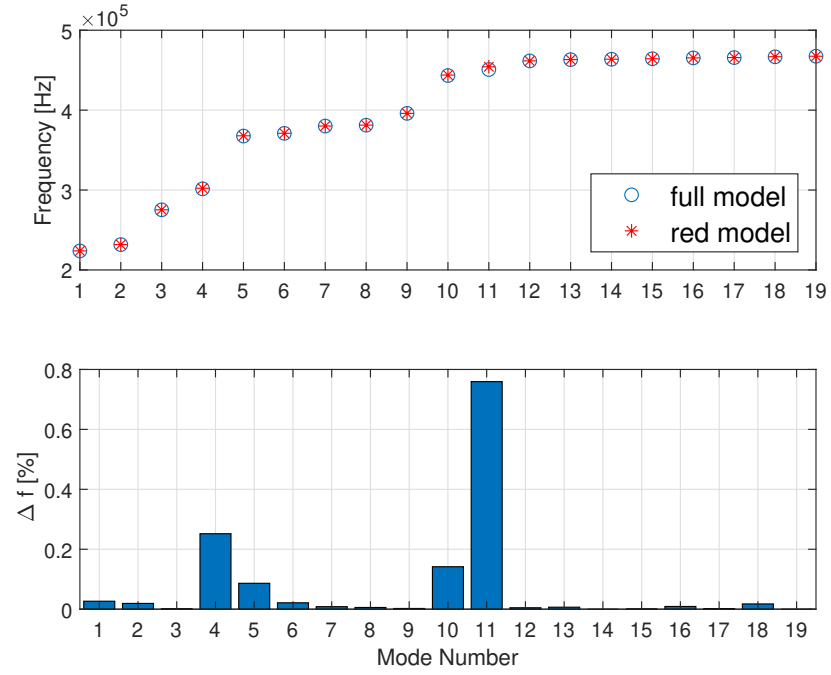

(b) Top specimen and rig

FIGURE IV.9: Precision of the reduced model: criterion based on eigenfrequencies.

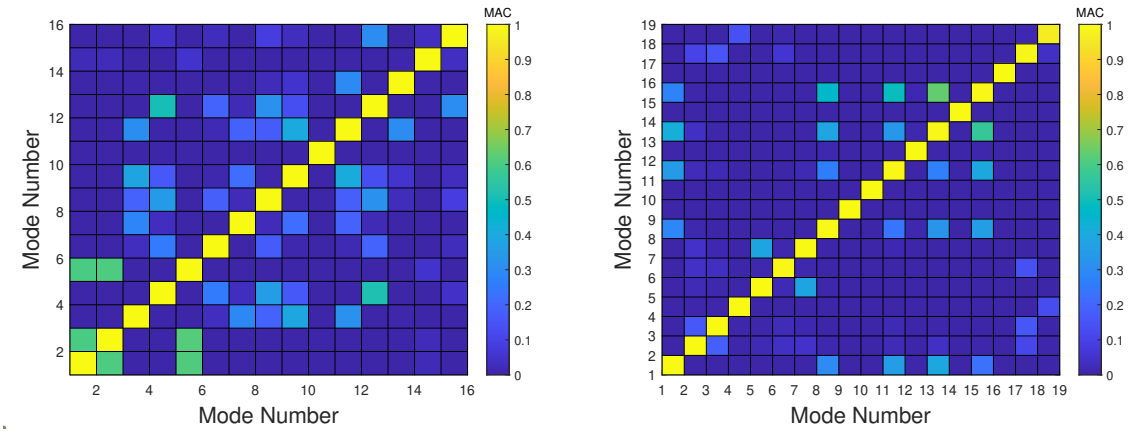

(a) Bottom specimen (b) Top specimen and rig

FIGURE IV.10: Precision of the reduced model: MAC criterion.

for the contact laws is used. Thus, the system is reduced by a further factor 2, becoming a system of 363 (contact or interface) DOFs.

4.2 Preliminary dynamic analysis and update of the test rig global behaviour

4.2.1 Input parameters updating for dynamic analysis

The input data referring to test 1, arbitrarily chosen as reference for numerical simulations, are summarised in TABLE IV.4. The properties of the material remain those of a stainless steel, listed in TABLE IV.3.

	Parameter	Value	
Normal load	N	60	[N]
Excitation frequency	f	100	[Hz]
Excitation amplitude	F_{ex}	53	[N]

TABLE IV.4: Summary test 1.

Non-frictional damping. In the reference experiments, damping is not due only to friction contact. There is also a dissipation of energy in materials and in instrumentation. All these other sources of damping are represented by an equivalent viscous damping ratio. For numerical simulations, an average value of $\zeta = 0.7\%$ is used, with reference to the experimental ones obtained pre-wear, given in [19]. It is in practice introduced in the reduced model in the form of a Rayleigh damping matrix $\mathbf{C}$, expressed by Eq. II.18. The Rayleigh model approximates the damping coefficient as a linear combination of mass and stiffness matrices, as introduced in section II.2.1.3.

Normal forces over the interface. The normal static load is required to initialize the dynamic analysis. The normal load applied over the top specimen is 60 N. This

value is kept constant during all the tests. The average contact pressure is then 60 MPa. The normal nodal forces over the full contacting surface are calculated by performing a static analysis on the specimens assembled by coupling a corresponding pair of nodes at the interface. The normal forces repartition obtained over the interface is shown in FIGURE IV.11a. This distribution is the typical one expected for a flat-to-flat contact configuration [50], as previously mentioned in section I.1.3.1, with higher values exhibited on the corners of the interface, given the singularity of the stress fields at these locations. This behaviour is shown in FIGURE IV.11b which represents the nodal forces along the sliding direction (x) for the middle nodes of the interface (indicated by a dotted line in FIGURE IV.11a).

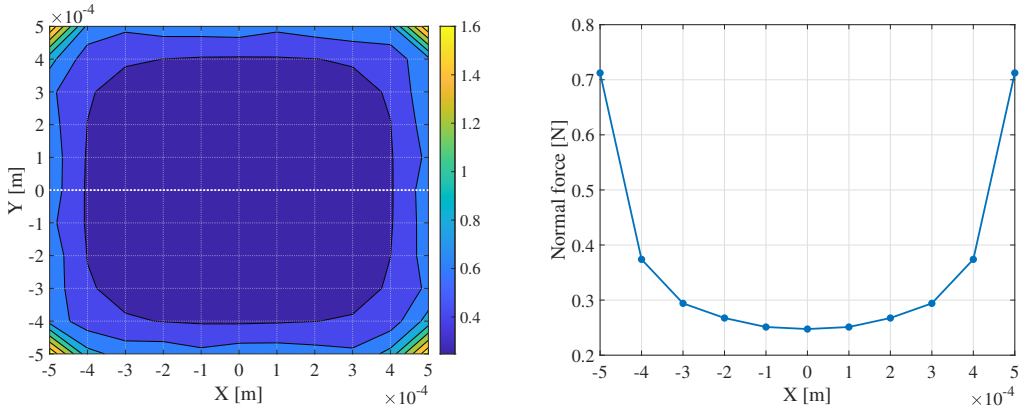

(a) (b)

FIGURE IV.11: Nodal forces over the interface: (a) 2D distribution: the white dotted line indicates the middle nodes in the sliding horizontal direction (x), (b) normal forces along the dotted line.

The normal forces over the contact interface are calculated locally on each node. The sum of all the nodal forces over the interface gives the normal load applied on the top specimen equal to 60 N, as expected.

4.2.2 Description of the test rig dynamics

The test rig dynamic behaviour has been preliminary modelled by means of a simple 2 DOFs lumped parameter model, which reproduces the two main modes of the friction rig. The specimens have been modelled with a FE approach (see section IV.4.1.2). Thus, it is essential to verify that the modal situation of the test rig is close to what the numerical analysis would predict.

Before and after every wear test, a hammer test was conducted [122] to get information about the rig's dynamic behaviour and identify the FRFs over a wide frequency range. Experimental results for a normal load $N = 7$ N are illustrated in FIGURE IV.12. The hammer hit was made at the excitation point placed at the shaker attachment and an accelerometer was set on the moving arm to measure the fretting rig response (see FIGURE IV.1). This analysis served to complete the knowledge of the test rig and specify the range of excitation frequencies for the forced response tests so that the accuracy of the contact force measurement system would not be influenced by resonance frequencies.

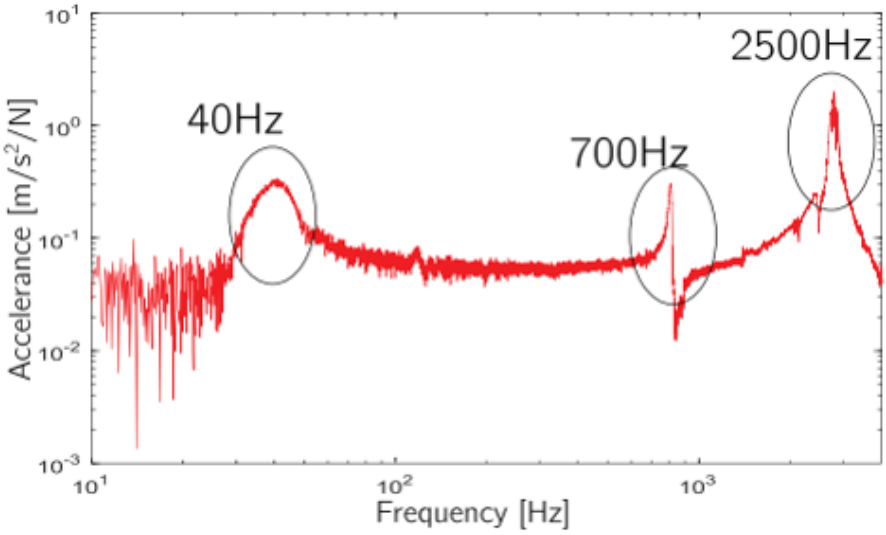

FIGURE IV.12: Hammer test experimental results: FRF in $m/s^2/N$ for a normal load $N = 7$ N (from [19]).

In this regard, a preliminary numerical analysis is performed to simulate the hammer test. The lumped element model of the rig with the two specimens always in contact pressed together with an applied normal load of $N = 7$ N. Numerical results are displayed in terms of accelerance (units of acceleration over external force) to be coherent with the experimental results produced by the hammer test, as shown in FIGURE IV.13. The numerical FRF is evaluated only in the longitudinal direction, i.e. the direction of application of the external excitation force. Numerically, two main natural frequencies can be distinguished in the sliding direction:

- the first one is the **in-phase mode** corresponding to the rig's first longitudinal mode, for which the moving mass m_1 and the moving arm m_2 move in the same direction, at about 39.7 Hz;
- the second one is the **out-of-phase mode** corresponding to the rig second longitudinal mode, for which the moving mass m_1 and moving arm m_2 move in opposite directions, at about 2456 Hz.

The mathematical model created for the test rig effectively reproduces the two main modes of the friction rig (in-phase and out-of-phase modes) and the natural frequency values of this model coincide with the experimentally measured ones. Experimental results also exhibit an out-of-plane mode at about 700 Hz, linked to a lateral rotation of the moving arm (see FIGURE IV.12), that does not affect the sliding of the specimens [19]. The 2-DOFs test rig model can not reproduce it because it corresponds to an additional dynamic range that remains outside the field of this study.

These results can be used as a linear reference to highlight nonlinearities due to friction contact and fretting wear's impact on the system dynamics' evolution. It is expected that the longitudinal modes will be affected by wear. The influence of the wear on the dynamics will be studied in chapter V.

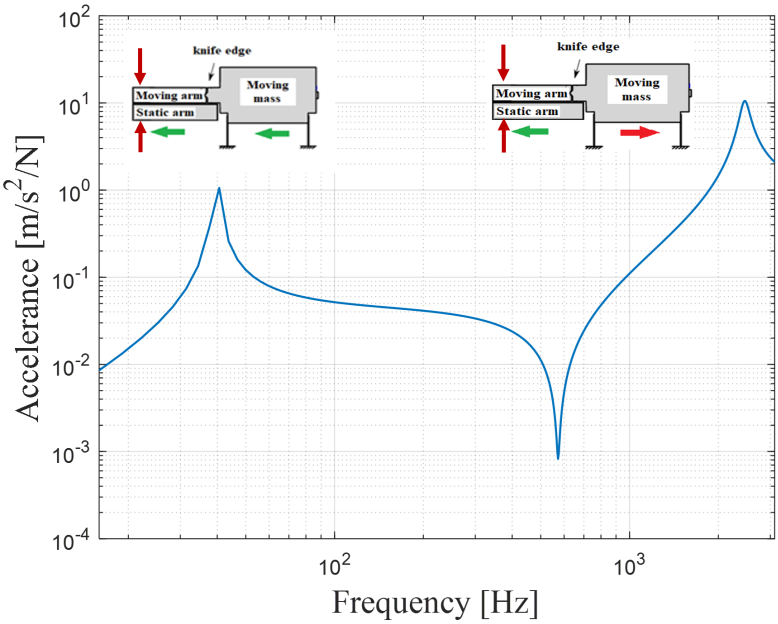

FIGURE IV.13: Numerical FRF in m/s^2/N for a normal load $N = 7$ N

4.3 Nonlinear dynamic analysis of the unworn system

4.3.1 Influence of the numerical analysis parameters

Before performing nonlinear numerical analyses, it is advisable to evaluate the best parameters to choose related to the Fourier transforms, namely the number of time instants N_t per period and the number of harmonics N_h to retain for the calculations, as performed in section III.3.3.2 for the academic numerical example. For this purpose, in this section, a study of the influence of these parameters is performed to fix them for the following calculations.

Number of time instants. FIGURE IV.14 shows the linear forced response and the nonlinear forced responses for different numbers of time instants N_t considered, over a period T. The simulations are performed for $N_h = 3$. This choice will be justified in the following paragraph. The limitation to $N_t = 32$ time instants per period does not capture all the dynamic behaviour generating a significant error during the Fourier transform to return to the frequency domain. The forced response for $N_t = 64$ time instants also presents errors. However, these are much smaller. The error between the results is negligible between $N_t = 128$ and $N_t = 256$. Thus, $N_t = 128$ time instants will be kept for the following calculations, taking the results obtained with $N_t = 256$ time instants as a reference.

Harmonic order. It is advisable to consider an intermediate situation between the fully sliding and fully stuck conditions to study the dynamic behaviour of the test rig because these two situations correspond to relatively linear behaviours. Instead, the solution will be much less regular in an intermediate situation with alternately sliding/stacking behaviour. It will require more harmonics to be represented accurately.

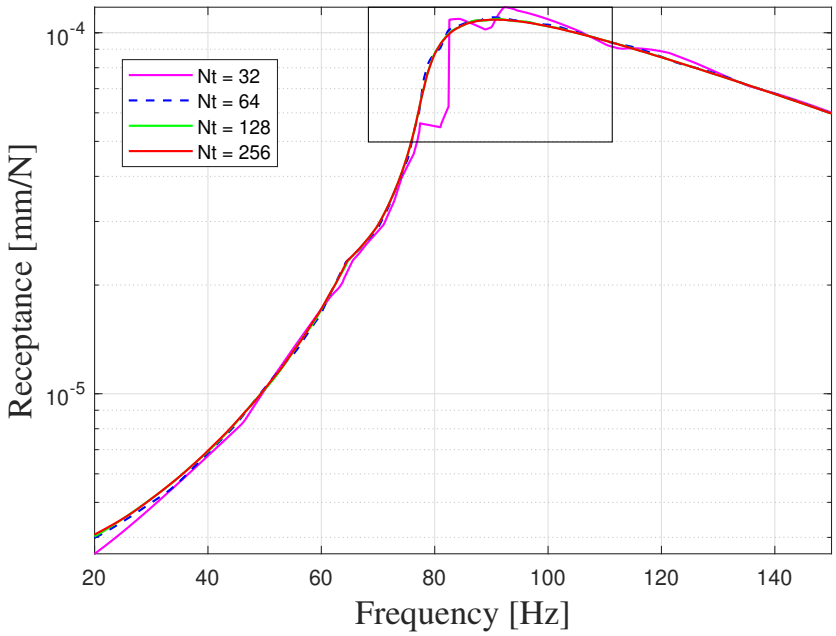

(a)

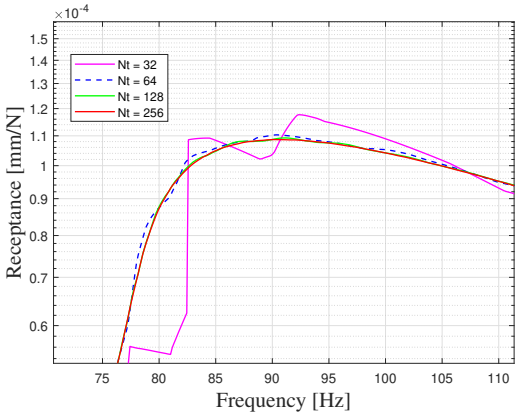

(b) Zoom

FIGURE IV.14: Influence of the number of time instants N_t on the forced response, for $N_h = 3$.

Considering the $F_{ex} = 50$ N, FIGURE IV.15 shows the forced responses for different numbers of harmonics N_h. In the case of keeping only one harmonic, the nonlinear displacements are represented only by a sinusoidal oscillation, so the results are underestimated. From $N_h = 3$ harmonics, the forced response of the system seems to converge well. There is still a slight underestimate compared to the results for $N_h = 5$ and $N_h = 7$. However, taking the results obtained with $N_h = 7$ harmonics as a reference, $N_h = 3$ harmonics will be considered for the numerical simulations because this value represents a good compromise in terms of convergence and calculation time.

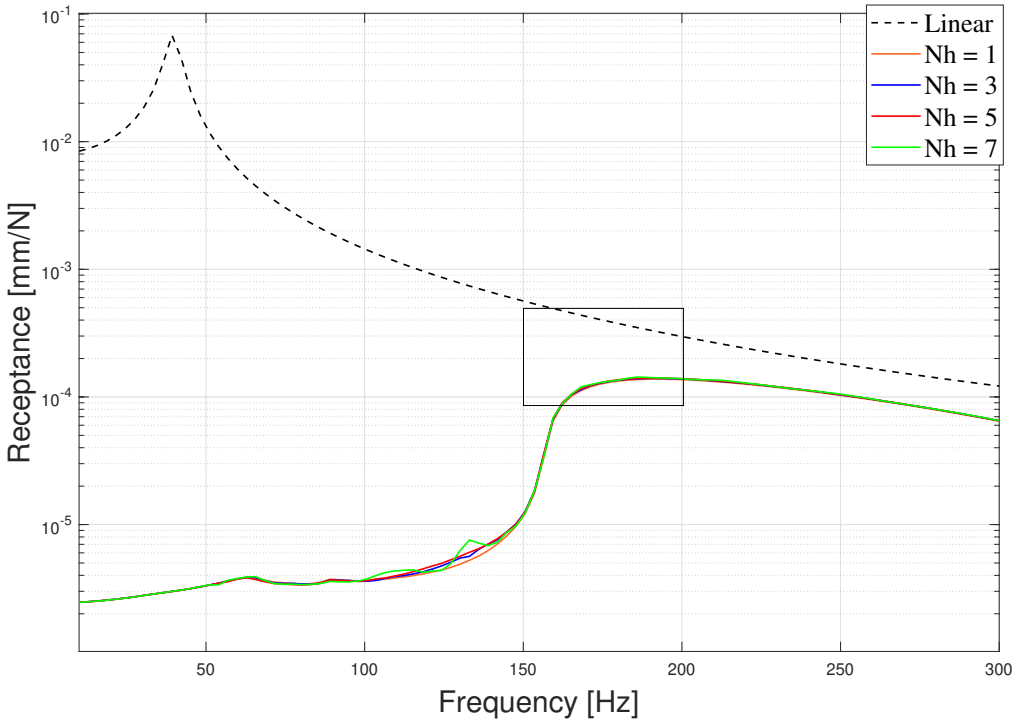

(a)

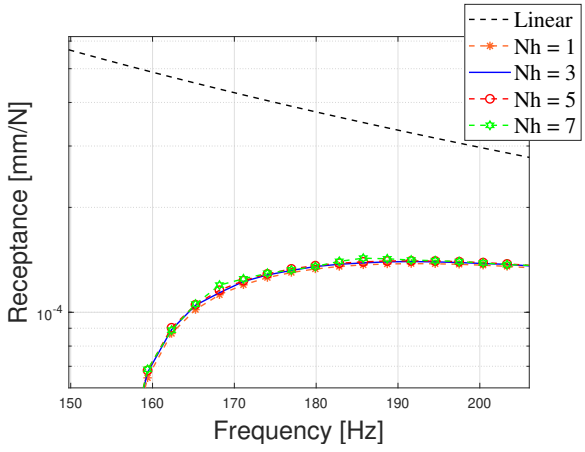

(b) Zoom

FIGURE IV.15: Influence of the number of harmonics N_h on the forced response, for $N_t = 128$.

4.3.2 Influence of excitation and contact parameters

Following the study of the numerical parameters for calculating the forced response in the previous section, $N_h = 3$ harmonics will be used in the DFT procedure, with $N_t = 128$ time instants.

The influence of the external excitation level and the friction coefficient on the frequency response is evaluated to determine the predominant influencing factors for the following nonlinear dynamic analysis with wear, which will be performed in chapter V.

Effect of the external excitation amplitude. The mode of interest is the first longitudinal one. Different contact conditions (stick, slip or a combination) can be distinguished by varying the amplitude of the external forces. FIGURE IV.16 shows the FRFs in terms of the ratio between the relative displacement and the external force, for the range of $F_{ex} = [1\ \text{N}, 10\ \text{N}, 30\ \text{N}, 50\ \text{N}, 70\ \text{N}, 90\ \text{N}]$.

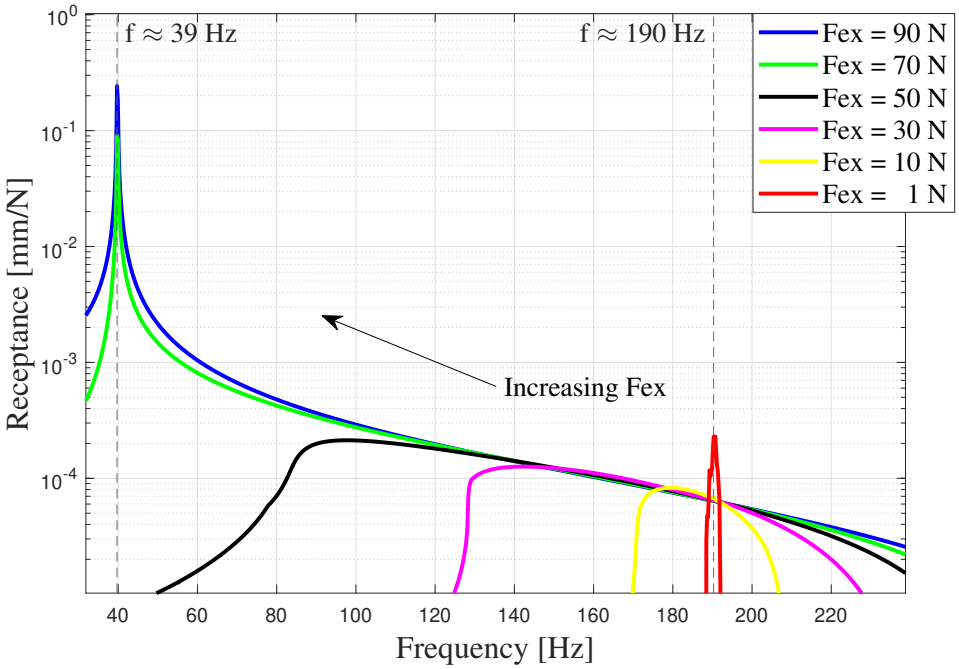

FIGURE IV.16: Influence of the external amplitude F_{ex} on the FRFs plotted as the ratio between the relative displacement amplitude and the externally applied force in N/mm.

It can be observed how the first mode varies between $f \approx 39$ Hz, corresponding to a fully sliding condition, and $f \approx 190$ Hz, corresponding to a fully stuck condition. The contact behaviour over the interface is evaluated at the resonance frequency for these 3 cases, related to external amplitudes $F_{ex} = [1\ \text{N}, 50\ \text{N}, 90\ \text{N}]$ and illustrated in FIGURE IV.17. FIGURE IV.17 describes the corresponding hysteresis loops.

The stick case in FIGURE IV.17a is characterized by very small relative displacement (in this case, tending to zero). There is no hysteresis, and the fretting loop has a closed linear vertical shape, following the DLFT contact conditions. The case in FIGURE IV.17b represents an intermediate case characterized by a stick-slip behaviour over the interface, for which the centre of the contact area remains adherent ($\mathbf{f_T} \leq \mu \mathbf{N}$) and slip occurs

at the edges (where $\mathbf{f_T} = \mu\mathbf{N}$). The fretting loop tends to assume a trapezoidal shape. In the case displayed in FIGURE IV.17c the curve tends almost to overlap the free case at 39 Hz. There is no more stuck behaviour at the interface for larger displacement amplitudes, but the whole interface is in sliding. According to Coulomb's law, the tangential force reaches its limit value $\mathbf{f_T} = \mu\mathbf{N}$ and remains constant during sliding. The fretting loop assumes a classical rectangular shape following the Coulomb and unilateral contact conditions.

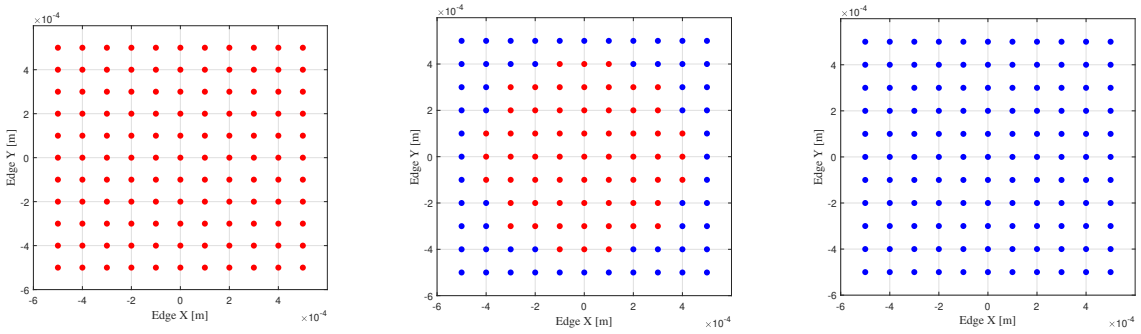

(a) $F_{ex} = 1$ N (b) $F_{ex} = 50$ N (c) $F_{ex} = 90$ N

FIGURE IV.17: Contact states at the interface for different external excitation forces, evaluated at the resonance frequencies: • stick • slip.

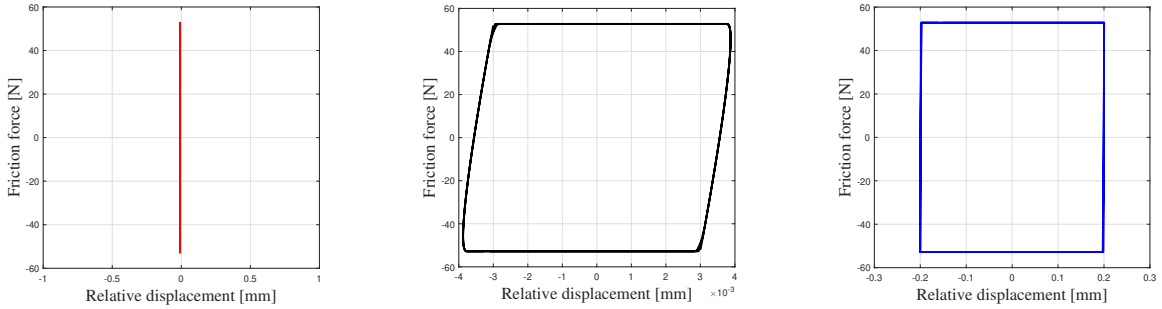

(a) $F_{ex} = 1$ N (b) $F_{ex} = 50$ N (c) $F_{ex} = 90$ N

FIGURE IV.18: Hysteresis loops at the interface for different external excitation forces, evaluated at the resonance frequencies.

Effect of the friction coefficient. FIGURE IV.19 displays the influence of the friction coefficient μ on the FRF for a case where contacts slip during one vibration period. It is observed that the expected value of the FRF amplitude is different for different values of μ, for a given value of the excitation force equal to $F_{ex} = 50$ N. When the coefficient of friction is low, sliding is facilitated. A higher coefficient of friction tends to minimise the slip behaviour.

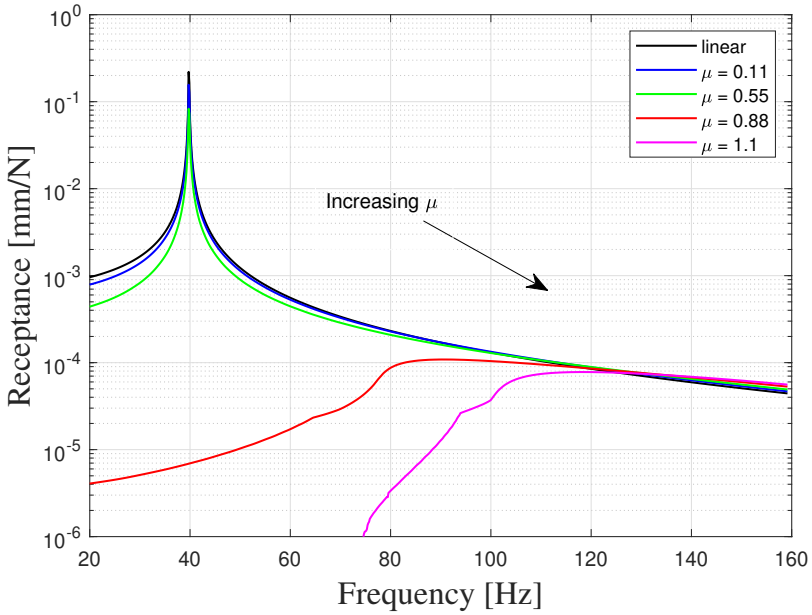

FIGURE IV.19: Influence of the friction coefficient μ on the FRFs plotted as the ratio between the relative displacement amplitude and the external applied force in mm/N.

4.4 Concluding remarks on the validation of the rig's model

A model of the experimental Imperial College test rig was built, and numerical results were obtained without considering wear phenomena. Firstly, the number of DOFs was reduced by the Craig-Bampton component modes synthesis method. In the first step, the dynamic study of the model was carried out using the harmonic balance method and the DLFT procedure for solving the nonlinear contact problems, demonstrating the effectiveness and applicability of this numerical method to updated simulations, as well as the consistency of the results obtained.

The evaluation of the results and the study of the influence of the various parameters involved have allowed to (i) calibrate the vibrating test rig and (ii) validate the expected behaviour of the model, highlighting the effectiveness of the methods considered for the dynamic analysis. The nonlinear behaviour observed experimentally at resonances was reproduced well. The 2-DOFs test rig model replicates the impact tests from a dynamic point of view (see FIGURE IV.12 and FIGURE IV.13) and an acceptable correlation was found with experimental resonant frequencies.

The dynamic response presented in this chapter will be now coupled with the wear using as input parameters the results of the experiments and applying the resolution strategy introduced in chapter III. This coupling strategy will enable to study of the behaviour at the interfaces and the impact of the wear on the dynamics.

Chapter V

Fretting wear parameters identification and numerical investigation

In this chapter, the prediction tool for the coupled calculation of both the wear kinetics and dynamics has been applied to study the impact of fretting wear on the Imperial College test rig dynamics, investigated within the framework of the EXPERTISE project. The influence of fretting wear on dynamics and the local behaviour at the interface, including wear phenomena, are studied. In addition to enabling cross-comparison and model updating and validation, these numerical investigations propose local scenarios for quantities not directly measured by experiments.

Outline of the chapter

5.1 Identification of input fretting wear parameters for simulations

5.1.1 Overview of fretting wear experiments

In the recent past, several test rigs have been designed to extract contact parameters, namely friction coefficient and contact stiffness, in controlled laboratory conditions, by measuring relative displacement and tangential force for oscillating contacts harmonically excited [168–170]. An experimental setup in [168] was set to determine the hysteresis between two surfaces as a result of a small-amplitude tangential relative motion. One dimensional friction rig in [169] was used to measure the relative displacement and friction force with a normal load applied on the contact to study the effect of the normal stress distribution on the micro-slip behaviour over the contact area.

Another experimental test rig was designed at Politecnico di Torino [170] to extract contact parameters and study the influence of a large number of wear cycles on friction coefficient, contact stiffness and energy dissipation, even at high temperatures Another group of experimental rigs were previously developed to experimentally investigate the effect of under-platform dampers on the blade dynamics and the periodic contact forces [171, 172]. A significant limitation of these studies is the assumption that the contact interface does not change over time and therefore the dynamic response remains unchanged. More recently, a novel test rig simulating contacts similar to the type present between the shrouds at the blade tip has studied the effect of fretting wear on the forced dynamic response with a friction contact and changing preload [173].

An experimental set-up specially designed at LTDS [98, 174] was developed in order to broaden the understanding of fretting mechanisms, focusing on the characterisation of the contact damage and surface degradation process induced by mall-amplitude oscillatory movements. A global energy wear law was experimentally defined in [174] for a given contact and locally implemented in a finite element modelling, giving an efficient prediction of the contact durability and geometrical changes of the two contacting surfaces. Nevertheless, fretting wear occurring at the interface leads to a change in the contact conditions and hysteresis modifying the surface geometry and impacting the dynamic response.

The test rig built by the Dynamics Group of Imperial College London [169] includes the two aspects previously mentioned, allowing to measure experimentally and extract the contact parameters, leading to the evaluation of hysteresis loops for typical materials used in aero engine applications, and to investigate the effect of the fretting wear on the dynamic response. The series of experimental fretting tests performed in [19] are here taken into account for performing numerical simulations to evaluate the influence of fretting wear on dynamics and propose local scenarios for quantities not directly measured by experiments. In the next section, these experiments are briefly described.

5.1.2 Description of Imperial College fretting wear experiments

To carry out the experiments, the system described in section IV.4.1.1 is excited by a harmonic force and undergoes a large number of friction wear cycles. The series of experimental fretting tests performed in [19] are briefly described.

A series of five fretting tests, ranging from 3 to 9 hours in duration, was conducted

using different couples of specimens. For each test, an unworn pair of stainless-steel (SS304) samples were tested for different test duration. Experiments were performed at room temperature and under a harmonic excitation of 100 Hz. This frequency is of interest because leads to high-quality hysteresis loops [122] in terms of the realism of tribological conditions and because is far from the resonance frequencies in order to reduce the interference of test rig dynamics. Also, this frequency is in the middle of the range of frequencies which characterize the first mode behaviour (between 39 Hz and 190 Hz). The fretting test rig operates under a constant normal load throughout the duration of the tests, without the possibility to study the effect of changing normal load conditions within the experimental tests. In difference to the academic example, illustrated in section III.3.3.3, here the normal pressure is kept constant at 60 N throughout the duration of the tests. Two tangential excitation forces were imposed: two tests were conducted at 53 N, on average 14 μm of full relative sliding (for about 5.5 h each) and three tests were conducted at 73 N, on average 22 μm of full relative sliding (for 0.6, 3.6 and 9 h respectively), in order to assess the repeatability of the experiments.

Test 1 was considered in [19] as a reference for the numerical simulations. The same one is retained in this work. Data referring to test 1 are summarised in TABLE V.1

	Parameter	Value	
Normal load	P	60	[N]
Excitation amplitude	F_{ex}	53	[N]
Steady Friction Coefficient	μ	0.88	
Average Sliding Distance	d	$\pm 7 = 14$	[μm]
Fretting cycles		$1.9 \cdot 10^6$	
Running time		5.3	[h]
Total Energy Dissipated	E_d	2800	[J]
Total Wear Volume	V_w	4.6	[μm mm^2]

TABLE V.1: Test 1: summary of experimental fretting wear results.

5.1.3 Friction coefficient updating

The friction coefficient has been introduced in section I.1.2. This parameter is obtained experimentally. Several recent studies [18, 84, 175] have focused on the friction coefficient evolution with fretting wear. Most of these researches have confirmed that the friction coefficient increases quickly during the first hundred fretting cycles (the running-in period) before reaching a steady state value. It was observed experimentally [61, 176] that during the first hundred fretting cycles, a specific transformed structure, called Tribologically Transformed Surface (TTS), from which debris is made, forms. It is due to the plastic deformation of the metals in contact. Then, there is a quick increase of the friction coefficient due to the removal of these layers (of different nature, such as oxide layers, adsorbed gas layers, nature pollution films, etc.), which increases the metal-to-metal adhesion between the contacting surfaces [84, 177, 178].

In the case of the fretting tests used as a reference, the friction coefficient increases rapidly at the beginning of each test until reaching a convergence towards a stable value

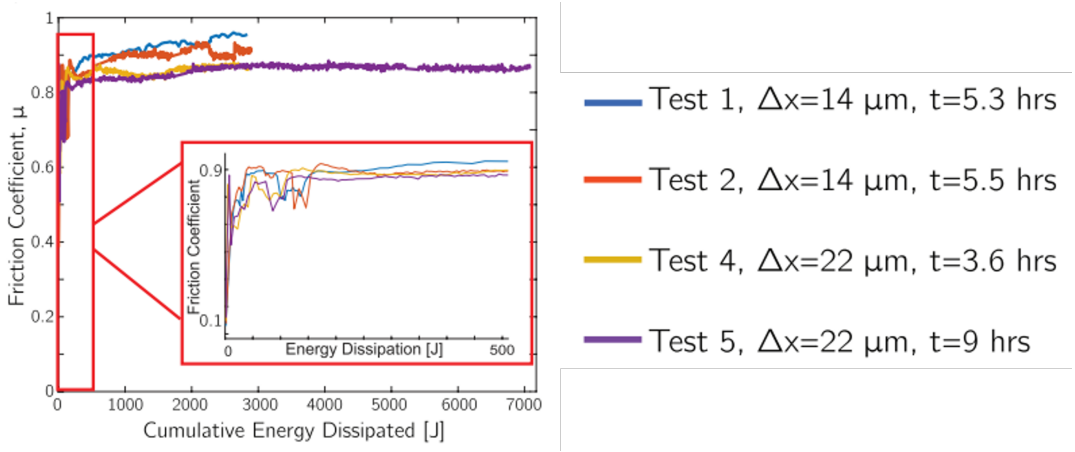

FIGURE V.1: Test 1: Identification of the friction coefficient (from [19]). The steady-state value reached after about 40000 fretting cycle corresponding to a cumulative dissipated energy of 50 J.

after about 40000 fretting cycles, following the previously observed fretting trends. The friction coefficient used here to perform the numerical investigation is the steady value reached, $\mu = 0.88$. In the following, for the numerical simulations, this value will be considered constant, assuming that it is unaffected by the wear evolution. It should be noted that in numerical simulations, the friction law focuses on a local friction coefficient, whereas a full-scale laboratory system refers to the macro scale, as macroscopic geometries and resulting total forces are considered.

5.1.4 Identification of the wear coefficient

The wear coefficient denoted as K_w has been introduced in section I.1.4.1. This parameter is evaluated experimentally. Commonly, one of the most used methods for determining the value of K_w is to press a stationary pin on the surface of a rotating disc, using a normal load P [179]. Given the normal preload P, the total sliding distance L can be calculated from the rotational speed and the disc's rotation time. Despite its limitations, the values of wear coefficients determined by the pin-on-disk method are accurate enough to be used in engineering analysis. Quantification of the wear coefficient K_w is conventionally performed by evaluating the change in mass (weight) and the worn volume V_w.

In the reference paper [19], Fantetti et al. represent the evolution of the wear volume as a function of the dissipated energy at the contact, as defined by Fouvry's studies in [61]. These results are shown in FIGURE V.2 and summarized in TABLE V.2. An almost linear relationship can be defined for the tests 3-4-5 conducted at 22 μm of sliding distance, indicating that the total wear volume is proportional to the cumulative energy dissipated. The slope of the best-fit line represents a wear energy coefficient α, as defined in [61]. Results of tests 1 and 2, conducted at 14 μm of sliding distance, show an almost similar wear volume of 4.6 μm mm^2 and 5.2 μm mm^2 respectively, since they dissipated almost the same amount of energy. The variability is less than 20% and this fairly small difference gives an idea of the variability of measurements. It could be caused by the difficulty in measuring the wear volume accurately due to such small quantities and irregularly worn area distributions.

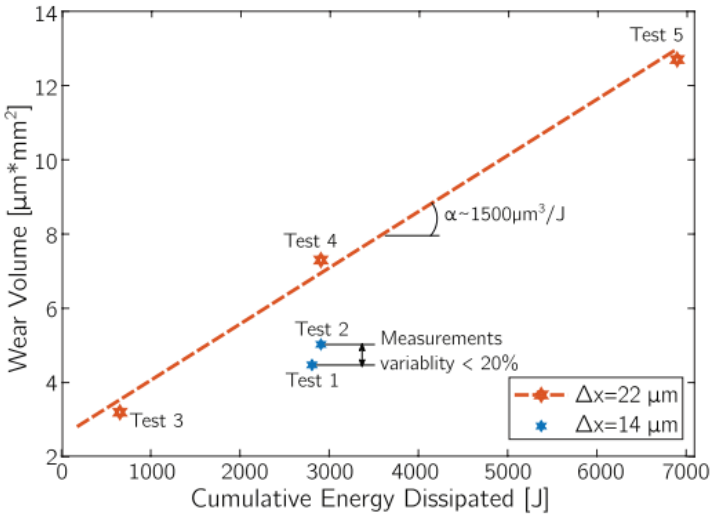

FIGURE V.2: Wear volume as a function of energy dissipated at the contact. Test conditions: excitation frequency $f = 100$ Hz, normal load $f_N = 60$ N (from [19]).

Test	Running time [h]	V_w [μm mm^2]	E_d [J]
1	5.3	4.6	2800
2	5.5	5.2	2900
3	0.6	3.2	500
4	3.6	7.3	2900
5	9	12.7	7000

TABLE V.2: Wear volume and energy dissipated for all the tests (from [19]).

Several numerical studies in the literature use the wear energy approach [61, 63]. In this work, the Archard model [56] is applied to quantify wear. In this formulation, the specific wear rate K_w is calculated as a ratio of wear volume to sliding distance multiplied by the applied load.

$$K_w = \frac{\text{Wear volume}}{\text{Normal load} \cdot \text{Total sliding distance}}.$$

As a reminder, the expression of Archard's law defined by Eq. (I.13) is given by:

$$K_w = \frac{V_w}{PL}.$$

K_w is the dimensional wear coefficient in [m^{3}m^{-1}N^{-1}] or the specific wear rate (the wear per unit load per unit sliding distance). In this regard, the added value for this numerical analysis is the possibility of having experimental data available. For test 1, data are listed in TABLE V.1, in particular:

- L represents the total sliding distance covered during the whole duration of the test corresponding to 5.3 hours;

- P is the normal load equal to 60 N;
- V_w is the total wear volume equal to 4.6 μm mm^2.

K_w is found equal to $5.76 \cdot 10^{-15}$ m^{3}m^{-1}N^{-1} and it is supposed not to evolve as wear increases. This coefficient represents a global parameter referred to the entire test 1.

This order of magnitude is comparable with that found experimentally for the same category of materials in recent works [180]. In the next section, the value of K_w obtained for test 1 will be used to evaluate the wear rate over one fretting cycle. In this regard, it should be noted that a local formulation of the Archard wear equation will be applied later. For this reason, it will be necessary to scale the quantities to the local contact area.

A limitation of this approach is that it does not consider microscopic effects such as asperity deformations and material tearing. The effects of temperature are neglected as well as plastic deformations and the influence of friction on the contact pressure distribution. However, some reasons for preferring this formulation in this work are outlined as follows. First, the Archard wear formulation includes all surface conditions in only one parameter. Also, it ignores surface details (for example, asperities), assuming that the entire surfaces are in contact, which is similar to the common assumption for contact in finite element modelling, where the surfaces are supposed to be smooth. Moreover, this formulation assumes that the direction of the load is constant and the load is unchanging, which may be the case with the experimental conditions under analysis. On the other hand, the presence and the effect of a third body layer, composed of particles or wear debris, are not taken into account within this approach. Hence, numerical investigations will be based on the assumption that the worn material is ejected out of the contact zone during the fretting wear tests.

Using the same procedure as for reference test 1, the values of the wear constants are derived for all 5 tests. They are listed in TABLE V.3. From an analysis of the values of K_w obtained for all tests, it can be noticed that the value of K_w changes according to the test considered. In accordance with what is shown in FIGURE V.2, the wear rates K_w for tests 1 and 2 are comparable. These two tests are conducted at the same sliding distance (14 μm) and have approximately the same duration. Also, test 4 has a similar wear rate but it is conducted at a highly sliding distance (22 μm), so a higher wear volume value is expected, according to Archard's law.

It is interesting to observe that the energy wear approach is equivalent to Archard's wear approach for a constant coefficient of friction μ which is the case assumed, as anticipated in section I.1.4.1. Both formulations do not explicitly consider the debris layer entrapped in the interface.

In the following numerical simulations, the wear volume will be evaluated during the whole duration of the test.

5.2 Numerical investigations strategy

Recently, various numerical investigations referring to these fretting wear tests have been performed [19, 181]. In [19], in addition to the experimental setup and the surface characterization of the samples, a numerical validation was proposed using a constitutive numerical modified Bouc-Wen model. This model allows the incorporation of the contact parameters extracted from experiments, in order to replicate the evolution of hysteresis

Test	K_w
1	$5.76 \cdot 10^{-15}$
2	$5.63 \cdot 10^{-15}$
3	$1.94 \cdot 10^{-14}$
4	$5.53 \cdot 10^{-15}$
5	$9.22 \cdot 10^{-15}$

TABLE V.3: Identification of the wear coefficients K_w expressed in $[\mathrm{m}^3\mathrm{m}^{-1}\mathrm{N}^{-1}]$ for all the tests.

loops. Further numerical analysis was performed introducing three different constitutive friction models modelled using the elastoplastic friction framework in [181].

In this work, the HBM coupled with the Dynamics Lagrangian Frequency-Time scheme (DLFT) with wear, described in chapter III, is used to perform the numerical simulations and coupling fretting wear and dynamics. As a reminder, a node-to-node contact element defines the contact zone. For each contact element, this method directly considers the Coulomb friction's law and the non-interpenetration condition to compute the contact forces in the time domain, without considering the tangential contact stiffness, extracted from test as used in [19]. The contacting surface is assumed to be perfectly flat and smooth. The initial contact state is supposed to be adherent.

Numerical simulations are carried out starting from a condition without wear so that the starting gap in the normal direction is

$$\mathbf{G} = 0.$$

The added value compared to previous numerical works using this strategy is the possibility of having experimental data available. The aim is mainly the experimental validation of the results obtained numerically. Indeed, in case of a lack of experimental evidence, the use of numerical calculations gives the possibility to go further and propose more plausible scenarios, assessing cases not foreseen by the tests.

5.2.1 Wear depth calculation for one fretting cycle

The strategy consists of incrementing the wear depth instead of time and involves the following steps. The first step consists in determining the nodal wear depth after a single fretting cycle, denoted as $\delta W^m_{(1)}$. This is obtained by wear integration over a period T_{ex}. Eq. III.15 is used and written for one cycle as follows:

$$\delta W^m_{(1)}(\eta) = \int_{\eta}^{\eta+T_{ex}} K_w |P^m_N(\tau,\eta)| \, \|\dot{\mathbf{u}}^m_{\mathbf{rT}}(\tau,\eta)\| \, \mathrm{d}\tau, \tag{V.1}$$

where P^m_N is the local contact pressure at node m and $\dot{\mathbf{u}}^m_{\mathbf{rT}}$ is the relative tangential velocity at node m, both obtained by the frequency resolution of the dynamic problem. T_{ex} is the period of the harmonic excitation. Eq. V.1 is a local formulation of the Archard

law and more specifically:

$$\frac{\text{Wear volume}}{\text{Contact area}} = K_w \frac{\text{Local normal load}}{\text{Elementary contact area}} \cdot \text{Local velocity} \cdot \text{Time increment}.$$

The order of magnitude of the wear depth after a single vibration cycle results: $\delta W_1^m = 10^{-7}$ μm. The wear depth map for the first fretting cycle is illustrated in FIGURE V.3. This order of value is so small that it would not result in any appreciable change in

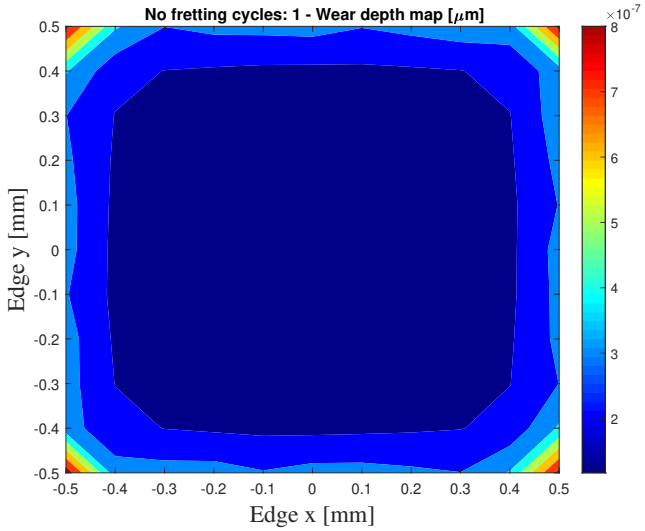

FIGURE V.3: Test 1: wear depth in μm over the interface, calculated after 1 vibration cycle.

the contact conditions and would have no significant impact on the nonlinear dynamic response if an iteration of wear was performed at each vibration cycle. This justifies the use of a jumped cycles strategy.

First, a wear acceleration factor is used, multiplying the wear depth calculated for one cycle by a given number of cycles ΔN_a. The use of this factor implies that wear has no significant impact on the contact behaviour before the ΔN_a cycles are considered. For this analysis, an acceleration factor equal to $\Delta N_a = 6 \cdot 10^4$ is chosen to begin the evaluation beyond the run-in period corresponding to the steady-state reached after about 50 J of cumulative energy dissipated for every test (see FIGURE V.1). Therefore, this acceleration factor will only be kept for the first wear depth update. For the rest of the calculations, the acceleration factor will be chosen according to a limited wear depth ΔW^* to be reached, as explained in the following.

5.2.2 Wear depth implementation by wear increment

The value of δW_1^m for one fretting cycle, calculated using Eq. V.1, is used to set heuristically the maximum allowable wear depth increment ΔW^* during a wear iteration k. The maximum allowable wear depth is limited to $\Delta W^* = 5 \cdot 10^{-2}$ μm. This fixed

value makes it possible to fix the number of cycles ΔN_c to be skipped through Eq. III.16:

$$\Delta N_c(\eta) = \frac{\Delta W^*}{\underset{m}{max}(\delta W^m(\eta))}.$$

The maximum wear depth after one cycle was found within the corners, with a value of $\delta W^m_{1(max)} = 8.7 \cdot 10^{-7}$ μm (see FIGURE V.3) and the maximum total number of fretting cycles, corresponding to the total test running time of 5.3 hours, is $N_{c_{tot}} = 1.9 \cdot 10^6$. These values allow a maximum indicative cumulative wear depth of 1.7 μm.

All nodal wear depths W^m are updated after ΔN_c cycles, defined so that the maximum wear increment is ΔW^* compared to the previous cycle. The updating is computed through the explicit scheme shown in FIGURE III.2 and given by Eq. III.17:

$$W^m(N_c + \Delta N_c) = W^m(N_c) + \Delta N_c \delta W^m(\eta).$$

As demonstrated in [161], the explicit scheme has the advantage of not changing the number of equations and not requiring a Jacobian computation of the wear law. Consequently, the contact conditions are modified, due to the implementation of the nodal wear depths in the normal direction as defined by Eq. (III.13), and a return to the beginning of the prediction/correction process is required to re-balance them (see FIGURE III.3).

Generally, once a suitable number of N_c has been calculated the analysis stops. In this case, the procedure is repeated until the maximum total number of fretting cycles $N_{c_{tot}} = 1.9 \cdot 10^6$, corresponding to the total test running time of 5.3 hours, is reached (see TABLE V.1), given the duration of a vibratory period at the considered frequency of 100 Hz. For this analysis, the number of wear increments necessary to reach the number of total fretting cycles is $c = 58$.

It is important to note that according to this jumping cycle strategy, each wear increment k corresponds to a different number of fretting cycles ΔN_c. The factor ΔN_c is a critical parameter for the analysis because it determines the contact analysis computational cost and the stability of the explicit scheme. A high value of the factor ΔN_c can reduce the calculation time but may lead to a reduction in the accuracy of the results. The number of allowable wear steps k, i.e. the steps in which an appropriately chosen limit wear depth ΔW^* is fixed, is the second critical parameter of the analysis, as it also determines the computational cost of the system. It results in very challenging finding *a priori* the appropriate value for these parameters, mainly because they can change over time, depending on wear dynamics.

5.3 Local contact evolution analysis

As previously described, the amount of wear that occurs is very small during only one vibration cycle and a certain running-in period is required to observe a loss of material at the contact and visualize the effect of wear on the system's dynamic response. This section refers to a local description of the wear evolution at the contact interface.

5.3.1 Wear profile over the contacting interface

In experimental investigations, an optical interferometer was used to characterise worn surfaces before and after testing. Results in FIGURE V.4 shows an apparent material transference between the top and bottom surfaces. This trend was present in all tests [19]. First, it is important to note that, at resonance, the vibration amplitude reaches

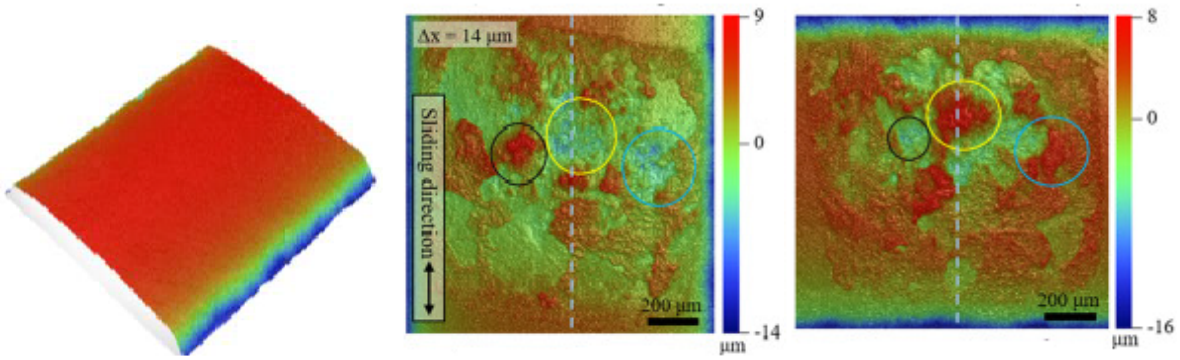

(a) (b) (c)

FIGURE V.4: Worn surface images highlighting the material transfer between the top and bottom specimens for test 1 after 5.3 hours of wear (from [19]): (a) Before wear; (b) Top specimen (moving); (c) bottom specimen (stationary).

the maximum and consequently, the maximum frictional dissipated energy would be observed. However, operating conditions will not always be excited at resonance. Thus, computing wear at resonance frequency would not be representative of the conditions experienced by the system. In this work, wear depths can be computed at each frequency. More specifically, being not conservative to use the resonance as a loading case, wear depths are computed at the excitation frequency 100 Hz, which represents the operating frequency of the test rig. Also, according to the test protocol detailed in [19], the contacts are never opened during the experiments. This prevents the possibility of obtaining an intermediate wear depth profilometry in the course of tests.

Numerically, the wear depth is identified as a variable w increasing the initial gap $\mathbf{G}$ between the contacting surfaces, so the wear profile, in terms of wear depth over the interface, and its evolution during the test, can be found. A limitation of this numerical strategy is that the presence of particles or wear debris is not considered, with the assumption that the worn material is ejected out of the contact zone. Thus, it gives us no information on how the debris was formed or removed. For these reasons, the calculations performed should be compared with precautions to the results provided by experiments.

FIGURE V.5 shows the wear depths over the contact interface observed after (a) $4.2 \cdot 10^5$, (b) $8.2 \cdot 10^5$ fretting cycles, (c) $1.2 \cdot 10^6$ fretting cycles and (d) $1.9 \cdot 10^6$ fretting cycles, at the end of the calculation.

From an analysis of the results, one can note that only after $4.2 \cdot 10^5$ fretting cycles, wear starts to be mainly localised within the corners of the contact interface, as shown in FIGURE V.5a. Then, intermediate results where this behaviour is more evident are displayed in FIGURE V.5b and FIGURE V.5c, after $8.2 \cdot 10^5$ fretting cycles and $1.2 \cdot 10^6$ fretting cycles respectively. Wear increases along the edges, continuing to be more

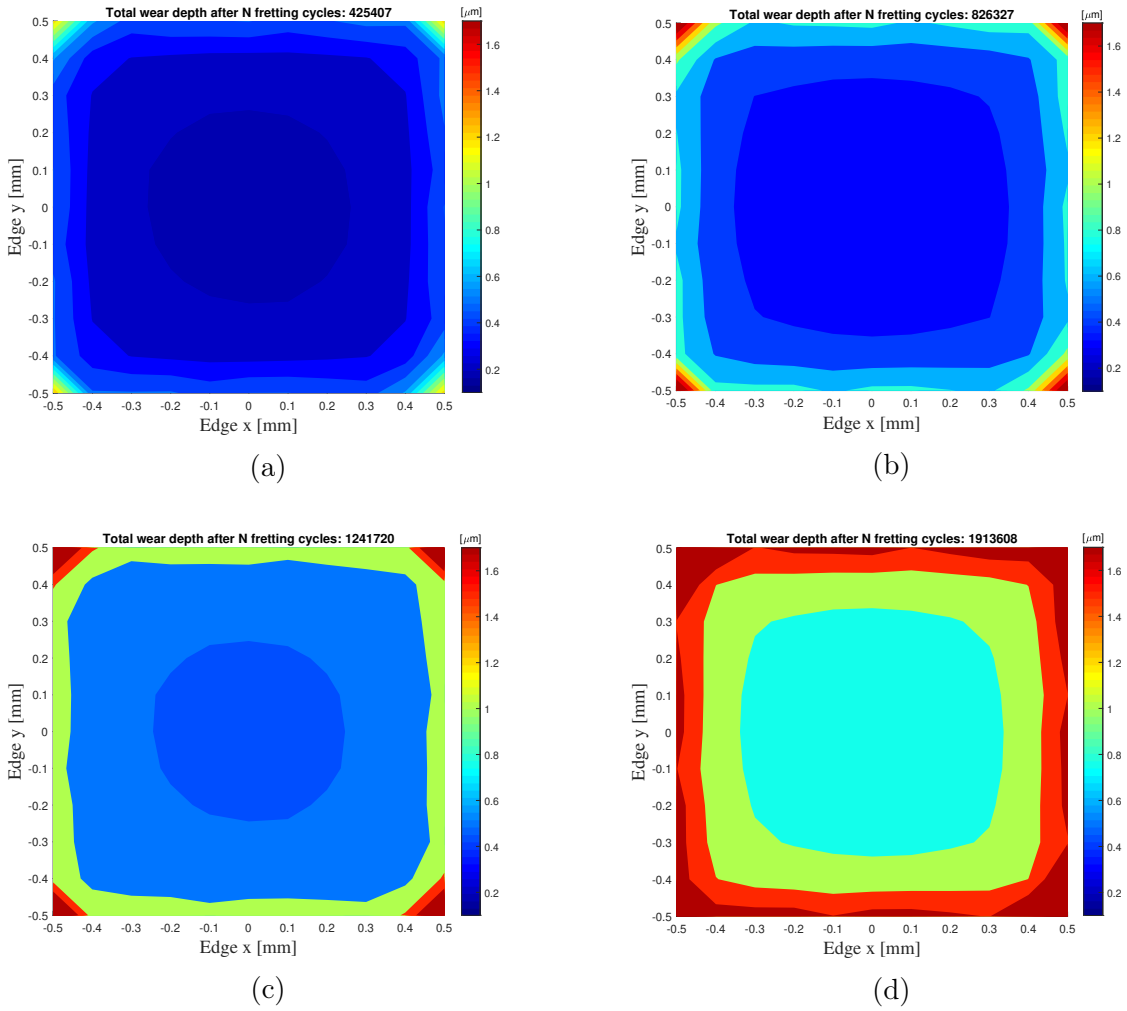

FIGURE V.5: Test 1. Wear depth over the contact interface in μm after various updated cycles: (a) after $4.2 \cdot 10^5$ fretting cycles, (b) after $8.2 \cdot 10^5$ fretting cycles, (c) after $1.2 \cdot 10^6$ fretting cycles, (d) after $1.9 \cdot 10^6$ fretting cycles, corresponding to the end of the test.

localized within the corners of the contact interface and tending to be more distributed over the whole contact area. Finally, at the end of the test, after $1.9 \cdot 10^6$ fretting cycles, wear results more uniformly distributed over the whole contact interface and wear in the corners seems not to increase more, see FIGURE V.5d. However, it can be seen that the worn numerical profiles are qualitatively similar to the experimental ones, with wear localised along the edges and mainly in the corners.

5.3.2 Local normal pressure

The pressure applied is constant during the whole test and equal to 60 Nmm^{-2}. The local distribution of the normal load at the interface continuously changes due to wear. As observed in the previous, results show wear concentrated along the four edges of the contacting area, mainly on the corners. The wear depth evolution over the interface contributes to changing the normal contact conditions at each updated wear depth, creating a new local normal load distribution for the next calculation.

FIGURE V.6a displays the evolution of the contact load pressure at the fretting cycles $4.2 \cdot 10^5$ and FIGURE V.6b at the final fretting cycles $1.9 \cdot 10^6$. Initially, the local normal force distribution is that expected for a flat-on-flat contact, as calculated in the previous chapter and illustrated in FIGURE IV.11b. Then, increasing the number of fretting cycles, the local normal force distribution leads to a slight increase at the centre of the contact interface, tending towards a more uniform forces distribution (see FIGURE V.6). However, the global behaviour remains consistent with the previous calculations, due to the more global distribution of forces over the contact area. Once the edges of the contact area are worn out, the normal load distribution tends to be no longer singular at these locations. This means that wear is rounding the edges, simultaneously decreasing the load's localisation.

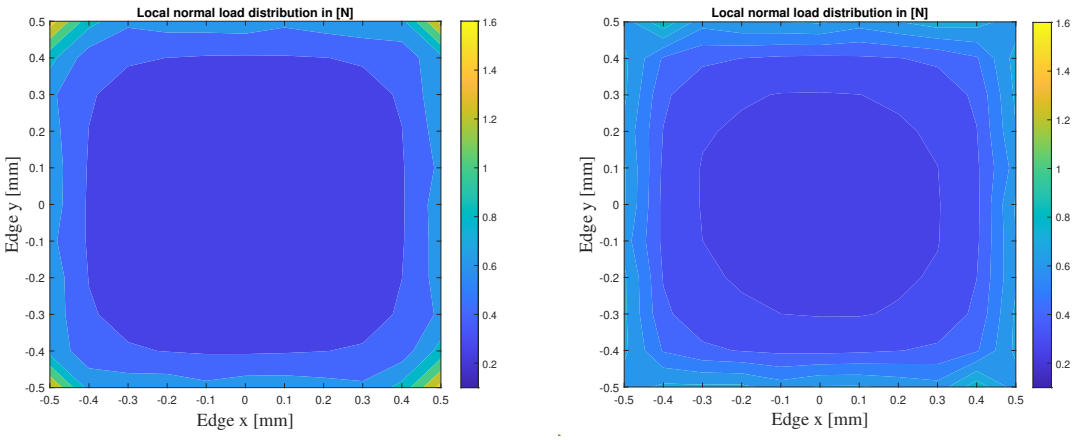

(a) (b)

FIGURE V.6: Normal load distribution over the interface at (a) $4.2 \cdot 10^5$ fretting cycles and at (b) $1.9 \cdot 10^6$ fretting cycles.

5.3.3 Evolution of the wear volume

Wear kinetics as a function of the number of cycles is numerically evaluated for studying the evolution of the wear volume during the whole test duration. The wear volume evolution is illustrated in FIGURE V.7. Numerical results show a continuously worn volume increment, with a wear rate quick enough from $0.1 \cdot 10^5$ fretting cycles, due to the first jumped cycles imposed, corresponding to the running-in phase. The total wear volume numerically obtained at the end of the test after $N_c = 1.9 \cdot 10^6$ fretting cycles (5.3 hours of duration), is $V_w = 3.8$ μm mm^2. It is notable that this value results lower than the experimental one $V_w = 4.6$ μm mm^2. This result remains within the range of experimental uncertainty. However, as mentioned in the previous section the assumption for numerical investigations is that the worn material, composed of particles and debris, is considered ejected out of the contact zone during the fretting wear tests. Thus, this underestimation could be explained as the presence of wear debris was not taken into account, as well as the plasticity of the material.

Also, this is probably because the wear is very localised and calculated on each node, and the maximum wear rate is not always found on the same node. FIGURE V.9

illustrates the evolution of the wear rate per cycle for some nodes of the contact interface. Some critical nodes over the interface and marked in FIGURE V.8 are considered. In fact, from the first fretting cycles, the node on the corner wears more than the other ones.

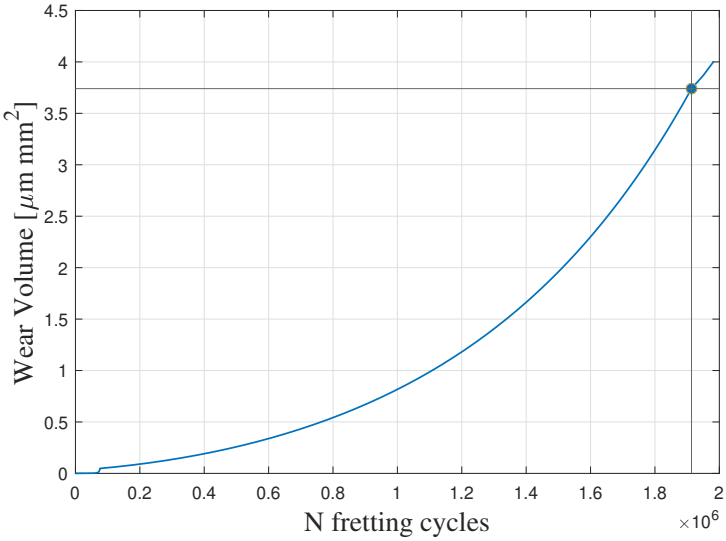

FIGURE V.7: Test 1. Evolution of the wear volume at 100 Hz.

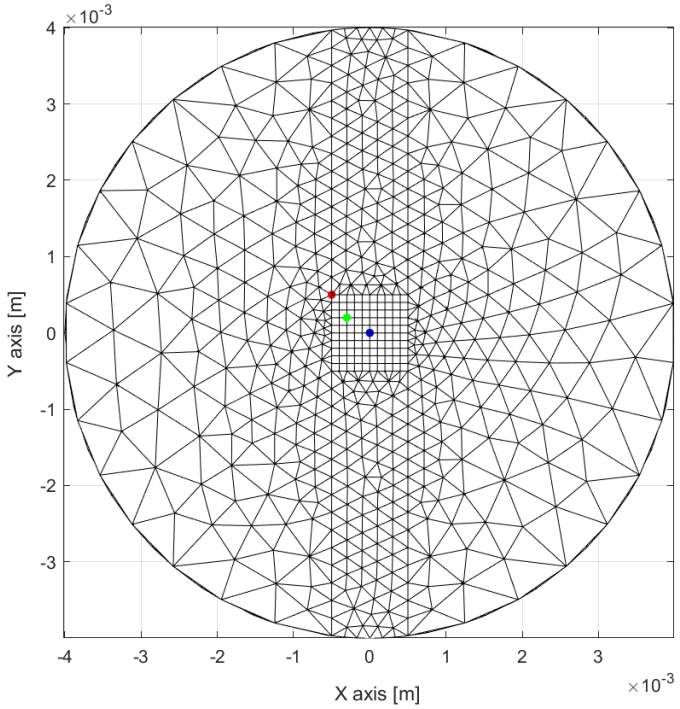

FIGURE V.8: Test 1. Some nodes at the interface.

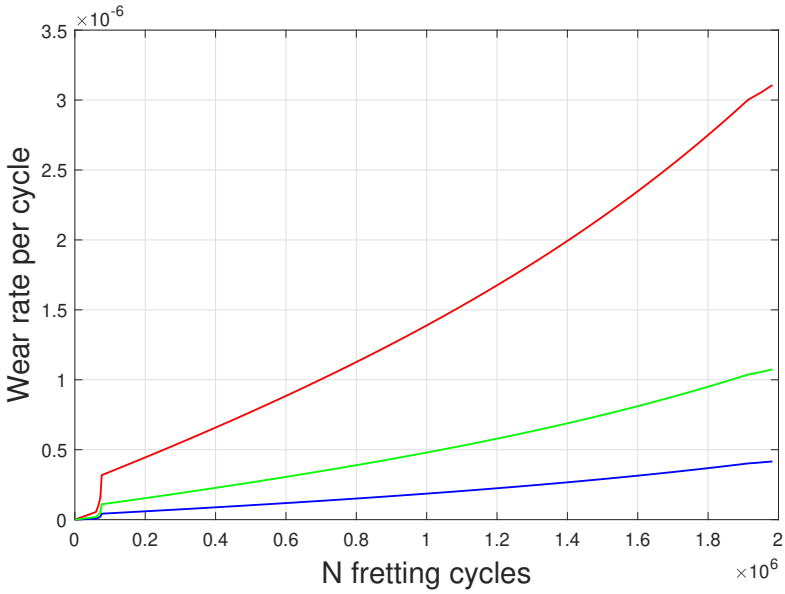

FIGURE V.9: Test 1. Evolution of the wear rate per cycle for some worn nodes.

5.4 Friction rig dynamics with wear

After having analysed the evolution of wear at the local contact interface, this section proposes to study the impact of wear on the structure's vibratory behaviour, evaluating the coupling between fretting wear and dynamics. The numerical update of the wear depth in the normal contact law used by the DLFT has been explained above in section V.5.2. From a purely numerical standpoint, $N_h = 3$ harmonics have been retained, with 128 time-step in the DFT procedures, as evaluated in the previous chapter, in section IV.4.3.1

5.4.1 Impact of wear on the dynamic response

Experimental FRFs before and after wear test 1 are illustrated in FIGURE V.10. The normal load for wear test 1 is $N = 60$ N. Results confirm that the modes of interest are the longitudinal ones, which are those influenced by the wear evolution at the specimens' contact interface. More specifically, of the two longitudinal modes, the first one is of most interest because it is the tangential mode in the same direction as the excitation input. The second mode does not exhibit notable variation due to wear. Numerical FRFs before and after wear test 1 are shown in FIGURE V.11. Numerical results are displayed in terms of accelerance (units of acceleration over external force) to be coherent with the experimental ones. Only the frequency range related to the first longitudinal mode, which is of most interest, is considered. The numerical prediction indicates a trend similar to the experimental results. As it can be observed, the wear produces a shift of the first mode (the in-phase mode) with an increase of its first natural frequency from 175 Hz to 205 Hz. This behaviour suggests an increase in the rigidity of the system with wear. This may be caused by an increased sticking of the contacting surfaces due to the presence of wear debris and/or surface damage. This represents a good result, considering the assumptions made for the friction coefficient and the identification of the

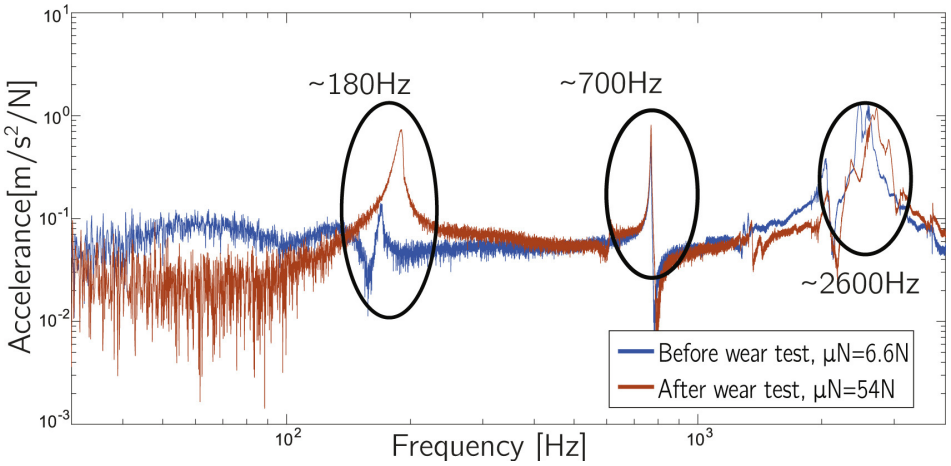

FIGURE V.10: Experimental FRFs for test 1: Normal load = 60 N (from [19]).

wear constant.

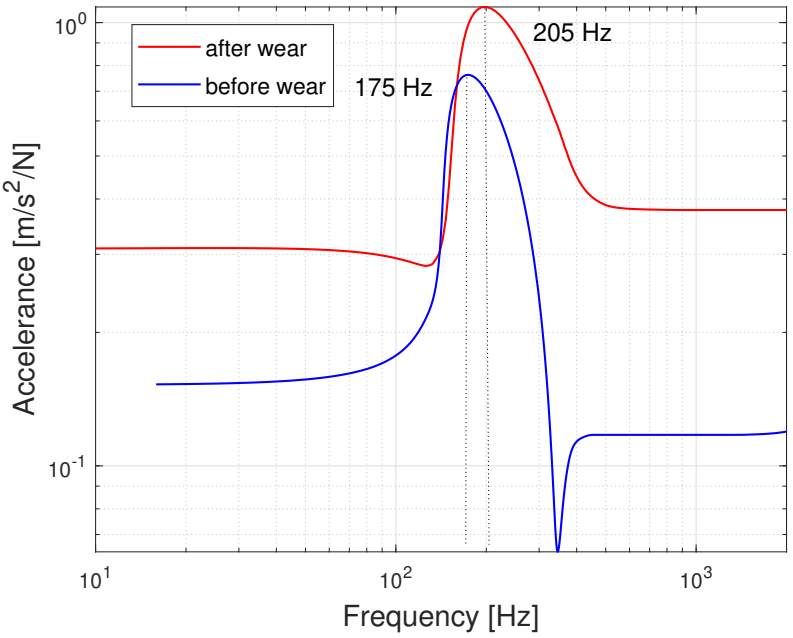

FIGURE V.11: Numerical FRFs for test 1: Normal load = 60 N.

5.4.2 Hysteresis loops

A hysteresis or fretting loop describes the force-displacement curve resulting from the vibratory movement of two contacting surfaces (see section I.1.3.1).

Observing the dynamic response before and after wear in FIGURE V.11, the system before wear is close to a stick regime, occurring during the early phase of the relative motion. This phase is characterised by a situation where the contact surfaces are still stuck. The contact undergoes stick and full slip each cycle according to the loading conditions. As the load increases, some asperities remain adhered to, while others start

to slip relatively, leading to the micro-slip regime. According to Coulomb's law, the entire interface results in a gross slip regime when the force reaches the friction limit. FIGURE V.12 shows the evolution of the numerical hysteresis loops with the progressing wear up to $1.9 \cdot 10^6$ cycles. The numerical hysteresis loops obtained during the first phases

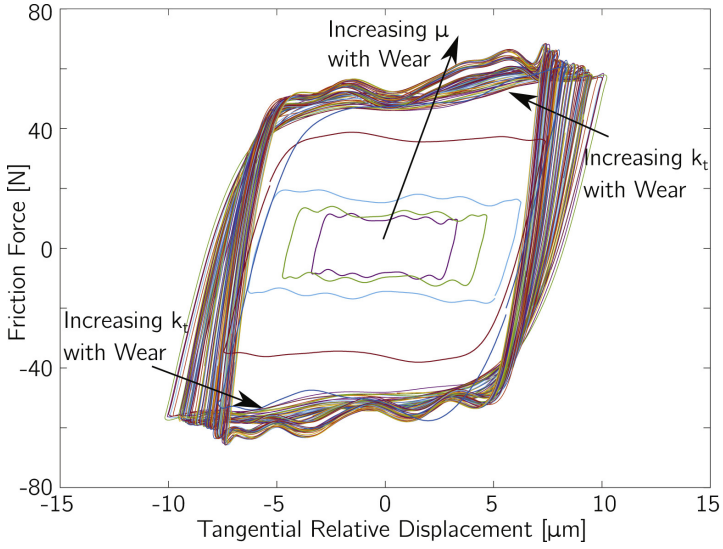

(a)

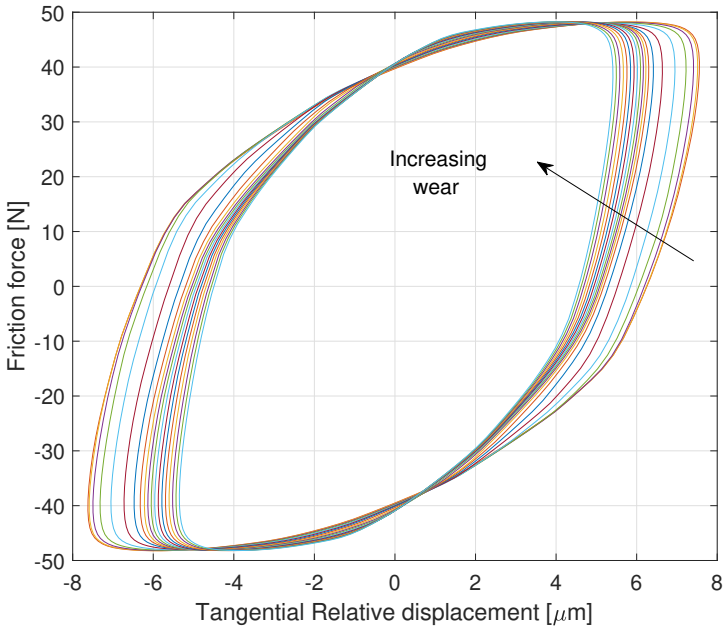

(b)

FIGURE V.12: Test 1. Excitation frequency = 100 Hz, normal load = 60 N, average sliding distance $s = \pm 7$ μm, total fretting cycles = $1.9 \cdot 10^6$. (a) Experimental hysteresis loops (from [19]). (b) Numerical hysteresis loops.

of running-in are ignored as the main interest is in the quasi-steady-state behaviour achieved in the first few hundred cycles of the start of the fretting wear test. As the number of cycles increases, the relative displacement is continuously decreasing and the

upper and lower friction limits ($\pm\mu N$) decrease. As this study assumes, when the friction coefficient is constant, the only other variable is the normal load. The results obtained are consistent with those given from experiments making it possible to demonstrate the method's applicability and evaluate the dynamic/wear coupling, with some limitations related to the assumptions used for calculating the wear updating.

5.5 Concluding remarks

After a description of the Imperial College test rig tests performed to experimentally study the effect of fretting wear on the forced response dynamics, this chapter provided a numerical prediction of the equivalent experimental results for validation. The experimental test rig made it possible to demonstrate the method's applicability and to evaluate the dynamic/wear coupling. Experimental results are given regarding hysteresis loops, the evolution of frequency response and wear volume at various wear conditions. The confocal images of the sample's surface are also provided and allow for qualitative scan tracking of the real worn area and its evolution. Concerning the numerical results, the phenomenology is quite well respected in terms of dynamics response before and after wear: with the resonance frequencies slightly increasing with wear; in terms of wear distribution over the interface, with the maximum amplitude in the corners as well as the order of magnitude of the wear depth are quite well replicate. Also, the final value of the total worn volume is in agreement with experiments, with the possibility to evaluate its evolution during the test. Moreover, the numerical results presented also include the evolution of the wear depth over the interface, the variation of the local normal load and the evolution of wear volume.

In addition, numerical simulations can provide guidance for new tests. For example, using different sample and contact area geometries, conducting parametric material studies of the contact samples, performing close-to-resonance tests, opening the contacts to evacuate the debris, and foreseeing infrared cameras. New experimental results can be used to update numerical models. The continuous iteration between experimental tests and numerical validation has the positive effect of developing the robustness of prediction tools.

The design of experimental test rigs is suitable for running several experimental campaigns and building a database of test results for the future exploitation and validation of currently existing numerical solvers studying the nonlinear forced response with friction contacts in the presence of fretting wear.

Conclusion and prospects

Brief overview of the present work

The main objective in the framework of the Work Package within the EXPERTISE project was to model interfaces under complex dynamic loading to integrate different physical phenomena like friction and wear occurring at the contact interfaces and implement them in numerical solvers. In fact, in the design of industrial assembled components, these phenomena play a relevant role in contact interfaces. Thus, it is crucial to correctly predict the nonlinear dynamic behaviour in the first phase of the design process to prevent damage and implement maintenance.

The current work aimed to study the effect of fretting wear on the dynamics of structures with friction contacts. Research has recently highlighted the need for predictive wear models and their shortcomings. Fretting wear occurs at the micro level but can have a significant impact on the response at the global system level. For this purpose, a numerical prediction tool coupling dynamics and wear phenomenon is used to validate the series of fretting tests performed with the experimental friction rig developed at the Imperial College London. Supported by experimental results, the numerical strategy is validated.

The numerical study of the dynamic behaviour was performed using a frequency method, the harmonic balancing method (HBM), allowing the direct analysis of the periodic regime without the need for transient calculations. The system's size was reduced by a substructuring method, the Craig-Bampton method with fixed interfaces, to avoid high computational costs generated by a nonlinear resolution. Since the frictional contact problems are nonlinear and have no expression in the frequency domain, a time-domain estimation procedure of the contact forces has been applied using Fourier transforms, allowing the passage between time and frequency domains. The Lagrangians Frequency-Time method is based on dynamic Lagrangians [123] and is coupled with the harmonic balance method, making it possible to study the forced response.

The multi-scale approach coupling fretting wear and dynamics, developed by Salles [161], is applied to evaluate the influence of the fretting wear on the dynamic response. This method simultaneously calculates the system's vibrations and the wear's evolution in fretting-wear situations by considering these two phenomena into two-time scales: a fast scale for the dynamics and a slow scale for tribological phenomena. The vibrations are analyzed in the frequency domain by using the harmonic balance method and AFT procedures. The evolution of the wear is integrated into the DLFT method on a slow time scale through an explicit scheme. A jump cycles strategy is implemented for updating wear, allowing a significant reduction of the computational time.

The numerical investigations are validated with the experimental results of the test

rig, demonstrating confidence in the method, whose implementation and computational benefits have already been demonstrated [13, 17, 124].

Concluding remarks and perspectives

This work contributes to the ongoing research in predicting the dynamic response of structures with friction contact nonlinearities in the presence of fretting wear. The test rig dynamic is a relevant industrial test since it is representative of the behaviour of friction dampers, which are known to wear significantly during their operational life. The influence of the wear phenomenon on the dynamics is investigated numerically, referring to a series of experimental data.

The numerical results highlight the sensitivity of the nonlinear dynamic response to changes at the contact interface. The wear contributes to a redistribution of the normal contact pressure, which changes the underlying nonlinear mechanisms at the interface from sliding localised at the edges to sliding over a more significant part of the contact area. Moreover, numerical investigations confirm that wear can affect the system's dynamic behaviour, leading to shifts in natural frequencies. In particular, wear mainly influences the sliding modes (i.e. the modes in the same direction of the fretting excitation), which activate the contact mechanisms. Consequently, wear must be included in the numerical analysis to accurately predict an assembled structure's nonlinear dynamic response during its operational life.

Concerning the numerical method, the DLFT procedure, coupled with a multi-scale approach in time to include wear, has shown its effectiveness and precision for the study of the dynamic behaviour of the system. In particular:

- the method allows the calculation of forced responses as functions of the wear depth. Numerical results appear in good agreement with the experimental ones, demonstrating the adequacy of the method used for coupling nonlinear dynamics and wear phenomena, which are computed simultaneously;
- the method can predict the evolution of wear depth and worn volume during the whole test duration.

The added value is the dialogue between experiments and updated simulations. This aspect enables verification for data comparable to measurements and the possibility of performing tests of the model fidelity. The possibility of referring to an experimental test has several advantages:

- having calibration tests enables the prediction of the dynamic behaviour to guarantee that the life expectancy calculations are faithful to reality. The model is calibrated by iteratively changing input values until the simulated output values match the observed data selecting parameters to optimise. In this case, a sensitivity analysis of a certain number of harmonics and time samples (a compromise between time calculation accuracy) and an evaluation of the reduction parameters keep the dynamic behaviour of the model. In model calibration (in terms of calculation parameters such as the number of harmonics or the mesh refining), the validation of the optimal number of elements is required to reach the targeted level of fidelity in predictions at reasonable costs.
- improving the understanding of these phenomena at work, reproducing the physics of the problem numerically. The choice to access elements of scenarios under the

scope of experiments because intrusive sensors prevent very local measurements; at the same time, calculations propose more detailed information at this level. In this case, the possibility to perform local analysis at the interface, studying the evolution during the local wear depth time to predict the worn geometry and estimate the wear volume.

Finally, the work presented in this thesis opens the way to several perspectives presented in the following and organised in three parts: the possible improvements that can be obtained regarding computational methods and costs, the refinement related to the experiments to improve the possible industrial fields of application, and some possible recommendations for further research, to better understand the coupling between dynamics and tribology.

- For the dynamic resolution of the contact via DLFT, some different simplifications have been introduced to facilitate the numerical simulations. The friction coefficient has been considered constant, but it is theoretically a function of loading, sliding speeds, temperature and other parameters. It could be interesting to consider a variable friction coefficient to better represent the real behaviour at the interface and offer, especially in the presence of experimental data, a better correlation with tests. Also, assuming the plasticity in the contact zone would enable a better prediction of contact pressures at the interfaces, considering that slip and wear levels in the contact zones depend on a good assessment of the local contact pressures. The accuracy of results is conditioned by the number of contact elements retained. Due to geometrical complexity, structural components and assembly models require a finer three-dimensional discretization of the contact zone and, therefore, a larger number of degrees of freedom. The order of the model becomes so large that the frequency response assumes a very high computational cost. The dynamic response is generally desired at more than one frequency, adding different folds to the computational effort. Additional efforts will be needed to speed up HBM solvers to reduce the computation time by implementing numerical techniques such as Finite Element Tearing and Interconnect (FETI) [182, 183], Domain Decomposition Methods (DDM), Substructuring [8], to reduce the problem into smaller parts and distribute it over more calculation nodes.

- The experiments considered in this manuscript for the numerical simulations have been performed for specimens with a flat-to-flat contact area. It may be helpful to consider different geometries, for instance, curved samples, and potentially perform test campaigns on more realistic geometries very close to industrial cases. The predictive tools validated for coupling dynamics and wear could then be applied to many other industrial cases, allowing the possibility to predict the dynamics behaviour and obtain a detailed evaluation of the interface. Given the lack of experimental tests rig studying the influence of wear on dynamics, it would be advisable to create numerical simulation models, which update and change as their physical counterparts change with variable parameters providing a basis for several configurations for the experimental tests. A numerical model can provide a valuable tool for performing sensitivity analyses and exploring design solutions, referring to data not experimentally tested. A numerical model makes it possible to evaluate the influence of several parameters to provide a basis for different test configurations to readjust the model about the experimental results and obtain a numerical-test

correlation. It can be beneficial and can be a guide to the optimisation process.

- The evolution of wear here evaluated numerically allows validating an experimental test. Still, it does not consider that fretting wear generates an intermediate heterogeneous layer composed of wear debris or particles (the so-called third body) at the interface. If expectancy calculations are faithful to reality, it would also be helpful to refer to an asymptotic approach to evaluate the asymptotic behaviour of this layer (and consequently of the worn geometry) directly, without time instants integration. In future works, it could be interesting to include explicit modelling of debris and implement the mass transfer [184] in dynamic simulations to develop an optimisation process aimed at rapidly detecting asymptotic worn geometry, if it exists.

List of Figures

List of Tables

Bibliography

[1] Srinivasan A.V. "Flutter and resonant vibration characteristics of engine blades" (1997). doi: 10.1115/1.2817053 (cit. on p. 1).

[2] Griffin J.H. "A review of friction damping of turbine blade vibration". *International Journal of Turbo and Jet Engines* 7.3-4 (1990), pp. 297–308. doi: 10.1515/TJJ.1990.7.3-4.297 (cit. on p. 1).

[3] Szwedowicz J. *Bladed disks: non linear dynamics*. 2008 (cit. on p. 1).

[4] Brake M.R.W. *The mechanics of jointed structures: recent research and open challenges for developing predictive models for structural dynamics*. 2017. url: http://link.springer.com/10.1007/978-3-319-56818-8. (cit. on p. 1).

[5] Salles L., Blanc L., Thouverez F., Gouskov A.M. and Jean P. "Dual time stepping algorithms with the high order harmonic balance method for contact interfaces with fretting-wear". *Journal of engineering for gas turbines and power* 134.3 (2012). doi: 10.1115/1.4004236 (cit. on pp. 2, 42).

[6] Firrone C.M., Zucca S. and Gola M. "Effect of static/dynamic coupling on the forced response of turbine bladed disks with under-platform dampers". *Turbo Expo: Power for Land, Sea, and Air*. Vol. 48876. 2009, pp. 429–440. doi: 10.1115/GT2009-59905 (cit. on p. 2).

[7] Zucca S., Firrone C.M. and Gola M. "Modeling under-platform dampers for turbine blades: a refined approach in the frequency domain". *Journal of Vibration and Control* 19.7 (2013), pp. 1087–1102. doi: 10.1177/107754631244080 (cit. on p. 2).

[8] Krack M., Salles L. and Thouverez F. "Vibration prediction of bladed disks coupled by friction joints". *Archives of Computational Methods in Engineering* 24.3 (2017), pp. 589–636. doi: 10.1007/s11831-016-9183-2 (cit. on pp. 2, 117).

[9] Williams J. *Engineering tribology*. 2005 (cit. on p. 2).

[10] Meng H.C. and Ludema K.C. "Wear models and predictive equations: their form and content". *Wear* 181 (1995), pp. 443–457. doi: 10.1016/0043-1648(95)90158-2 (cit. on pp. 2, 18, 25).

[11] Jareland M.H. and Csaba G. "Friction damper mistuning of a bladed disk and optimization with respect to wear". *Turbo Expo: Power for Land, Sea, and Air*. Vol. 78576. American Society of Mechanical Engineers. 2000, V004T03A009. doi: doi.org/10.1115/2000-GT-0363 (cit. on pp. 2, 26).

[12] Gallégo L., Nelias D. and Jacq C. "A comprehensive method to predict wear and to define the optimum geometry of fretting surfaces" (2006). DOI: 10.1115/1.2194917 (cit. on pp. 2, 25).

[13] Salles L., Blanc L., Thouverez F., Gouskov A.M. and Pierrick J. "Dynamic analysis of a bladed disk with friction and fretting-wear in blade attachments". *Turbo Expo: Power for Land, Sea, and Air*. Vol. 48876. 2009, pp. 465–476. DOI: 10.1115/GT2009-60151 (cit. on pp. 2, 26, 59 sq., 65, 67, 72, 75, 116).

[14] Salles L., Blanc L., Thouverez F. and Gouskov A.M. "Dynamic analysis of fretting-wear in friction contact interfaces". *International Journal of Solids and Structures* 48.10 (2011), pp. 1513–1524. DOI: 10.1016/j.ijsolstr.2011.01.035 (cit. on pp. 2, 26).

[15] Petrov E.P. "Analysis of nonlinear vibrations upon wear-induced loss of friction dampers in tuned and mistuned bladed discs". *Turbo Expo: Power for Land, Sea, and Air*. Vol. 55263. American Society of Mechanical Engineers. 2013, V07AT32A005. DOI: 10.1115/GT2013-95566 (cit. on pp. 2, 26).

[16] Armand J. "Nonlinear dynamics of jointed structures: a multiscale approach to predict fretting wear and its effects on the dynamic response". PhD thesis. Imperial College London, 2017. DOI: 10.25560/59072 (cit. on pp. 2, 26).

[17] Lemoine E., Nélias D., Thouverez F. and Vincent C. "Influence of fretting wear on bladed disks dynamic analysis". *Tribology International* 145 (2020), p. 106148. DOI: 10.1016/j.triboint.2019.106148 (cit. on pp. 2, 26, 65, 116).

[18] Schwingshackl C.W., Petrov E.P. and Ewins D.J. "Measured and estimated friction interface parameters in a nonlinear dynamic analysis". *Mechanical Systems and Signal Processing* 28 (2012), pp. 574–584 (cit. on pp. 3, 75, 78, 80, 99).

[19] Fantetti A., Tamatam L.R., Volvert M., Lawal I., Liu L., Salles L., Brake M.R.W., Schwingshackl C.W. and Nowell D. "The impact of fretting wear on structural dynamics: Experiment and Simulation". *Tribology International* 138 (2019), pp. 111–124. DOI: 10.1016/j.triboint.2019.05.023 (cit. on pp. 3, 8, 26 sqq., 77 sqq., 87, 89, 98 sqq., 106, 111 sq.).

[20] http://www.msca-expertise.eu/ (cit. on p. 4).

[21] Vakis A.I., Yastrebov V.A., Scheibert J., Nicola L., Dini D., Mynfray C., Almqvist A., Paggi M., Lee S., Limbert G. and al. "Modeling and simulation in tribology across scales: An overview". *Tribology International* 125 (2018), pp. 169–199. DOI: 10.1016/j.triboint.2018.02.005 (cit. on p. 8).

[22] Ko P.L. "Metallic wear—a review with special references to vibration-induced wear in power plant components". *Tribology International* 20.2 (1987), pp. 66–78. DOI: 10.1016/0301-679X(87)90092-2 (cit. on p. 8).

[23] Jean M. "The non-smooth contact dynamics method". *Computer methods in applied mechanics and engineering* 177.3-4 (1999), pp. 235–257. DOI: 10.1016/S0045-7825(98)00383-1 (cit. on p. 9).

[24] Petrov E.P. and Ewins D.J. "Analytical formulation of friction interface elements for the analysis of nonlinear multi-harmonic vibrations of bladed disks". *J. Turbomach.* 125.2 (2003), pp. 364–371. DOI: 10.1115/1.1539868 (cit. on pp. 10, 40).

[25] Laxalde D. "Étude d'amortisseurs non-linéaires appliqués aux roues aubagées et aux systèmes multi-étages". PhD thesis. École Centrale de Lyon, 2007 (cit. on pp. 10 sq., 49).

[26] Moreau J.J. "Sur les lois de frottement, de plasticité et de viscosité". *Comptes rendus hebdomadaires des séances de l'Académie des sciences* 271 (1970), pp. 608–611 (cit. on pp. 10, 60).

[27] Strömberg N., Johansson L. and Klarbring A. "Derivation and analysis of a generalized standard model for contact, friction and wear". *International Journal of Solids and Structures* 33.13 (1996), pp. 1817–1836. DOI: 10.1016/0020-7683(95)00140-9 (cit. on pp. 10 sq., 60).

[28] Strömberg N. "An augmented Lagrangian method for fretting problems". *European Journal of Mechanics, A/Solids* 16.4 (1997), pp. 573–593 (cit. on pp. 10 sq., 60, 71).

[29] Amontons G. "De la resistance causée dans les machines (About resistance and force in machines)". *Mémories de l'Académic Royale A* (1699), pp. 206–227 (cit. on p. 11).

[30] Coulomb C.A. "Theorie des machines simple (Theory of simple machines)". *Bachelier, Paris* (1821), p. 19 (cit. on p. 11).

[31] Morin A.J. "New friction experiments carried out at Metz in 1831–1833". *Proceedings of the French Royal Academy of Sciences* 4.1 (1833), p. 128 (cit. on p. 11).

[32] Joannin C. "Réduction de modèle par sous-structuration et modes non-linéaires-Application à la dynamique des roues aubagées". PhD thesis. École Centrale de Lyon, 2017 (cit. on p. 11).

[33] Reynolds O. "IV. On the theory of lubrication and its application to Mr. Beauchamp tower's experiments, including an experimental determination of the viscosity of olive oil". *Philosophical transactions of the Royal Society of London* 177 (1886), pp. 157–234 (cit. on p. 12).

[34] Richard Stribeck. "Die wesentlichen eigenschaften der gleit-und rollenlager". *Zeitschrift des Vereines Deutscher Ingenieure* 46 (1902), pp. 1341–1348 (cit. on p. 12).

[35] Brake M.R.W. "An overview of constitutive models". *The mechanics of jointed structures* (2018), pp. 207–221. DOI: 10.1007/978-3-319-56818-8_14 (cit. on p. 12).

[36] Bouc R. "A mathematical model for hysteresis". *Acta Acustica united with Acustica* 24.1 (1971), pp. 16–25 (cit. on p. 12).

[37] Wen Y-K. "Method for random vibration of hysteretic systems". *Journal of the engineering mechanics division* 102.2 (1976), pp. 249–263. DOI: https://doi.org/10.1002/mop (cit. on p. 12).

[38] Dahl P.R. "Solid friction damping of mechanical vibrations". *AIAA journal* 14.12 (1976), pp. 1675–1682. doi: https://arc.aiaa.org/doi/abs/10.2514/3.61511. (cit. on p. 13).

[39] de Wit C.C.,Olsson H., Astrom K.J. and Lischinsky P. "A new model for control of systems with friction". *IEEE Transactions on automatic control* 40.3 (1995), pp. 419–425. doi: 10.1109/9.376053 (cit. on p. 13).

[40] Hertz H. "On the contact of elastic solids". *Z. Reine Angew. Mathematik* 92 (1881), pp. 156–171 (cit. on pp. 13, 24).

[41] Hamilton G.M. and Goodman L.E. "The stress field created by a circular sliding contact" (1966). doi: 10.1115/1.3625051 (cit. on pp. 13, 24).

[42] Hamilton G.M. "Explicit equations for the stresses beneath a sliding spherical contact". *Proceedings of the Institution of Mechanical Engineers, Part C: Journal of Mechanical Engineering Science* 197.1 (1983), pp. 53–59. doi: 10.1243/PIME_PROC_1983_197_076_02 (cit. on p. 13).

[43] Hills D.A. "Mechanics of fretting fatigue". *Wear* 175.1-2 (1994), pp. 107–113. doi: 10.1016/0043-1648(94)90173-2 (cit. on p. 13).

[44] Cattaneo C. "Sul contatto de due corpi elastici: Distribuzione locale degli sforzi". *Rendiconti dell'Accademia nazionale dei Lincei* 6 (1996), pp. 342–349 (cit. on pp. 14, 24).

[45] Mindlin R.D. and Deresiewicz H. "Elastic spheres in contact under varying oblique forces" (1953). doi: 10.1115/1.4010702 (cit. on pp. 14, 24).

[46] McEwen E. "XLI. Stresses in elastic cylinders in contact along a generatrix (including the effect of tangential friction)". *The London, Edinburgh, and Dublin Philosophical Magazine and Journal of Science* 40.303 (1949), pp. 454–459. doi: 10.1080/14786444908521733 (cit. on pp. 14, 24).

[47] Lamacq V., Dubourg M-C. and Vincent L. "Crack path prediction under fretting fatigue — a theoretical and experimental approach" (1996). doi: 10.1115/1.2831599 (cit. on p. 14).

[48] Acary V. and Brogliato B. *Numerical methods for nonsmooth dynamical systems: applications in mechanics and electronics*. 2008 (cit. on pp. 14, 34).

[49] Produdhon H., Fouvry S. and Buffière J-Y. "A fretting crack initiation prediction taking into account the surface roughness and the crack nucleation process volume". *International Journal of fatigue* 27.5 (2005), pp. 569–579. doi: 10.1016/j.ijfatigue.2004.09.001 (cit. on p. 14).

[50] Ciavarella M., Hills D.A. and Monno G. "The influence of rounded edges on indentation by a flat punch". *Proceedings of the Institution of Mechanical Engineers, Part C: Journal of Mechanical Engineering Science* 212.4 (1998), pp. 319–327. doi: 10.1243/0954406981521259 (cit. on pp. 14, 24, 88).

[51] Mohrbacher H., Blanpain B., Celis J.P., Roos J-P., Stals L. and Van Stappen M. "Oxidational wear of TiN coatings on tool steel and nitrided tool steel in unlubricated fretting". *Wear* 188.1-2 (1995), pp. 130–137. doi: 10.1016/0043-1648(95)06637-3 (cit. on pp. 14, 20).

[52] Blanpain B., Mohrbacher H., Liu E., Celis J.P. and Roos J-P. "Hard coatings under vibrational contact conditions". *Surface and Coatings Technology* 74 (1995), pp. 953–958. DOI: 10.1016/0257-8972(95)08219-0 (cit. on pp. 14 sq.).

[53] Vincent L., Berthier Y., Dubourg M-C. and Godet M. "Mechanics and materials in fretting". *Wear* 153.1 (1992), pp. 135–148. DOI: 10.1016/0043-1648(92)90266-B (cit. on pp. 16, 18 sq.).

[54] Fouvry S., Kapsa P. and Vincent L. "Quantification of fretting damage". *Wear* 200.1-2 (1996), pp. 186–205. DOI: 10.1016/S0043-1648(96)07306-1 (cit. on pp. 16, 20).

[55] Vingsbo O. and Söderberg S. "On fretting maps". *Wear* 126.2 (1988), pp. 131–147. DOI: 10.1016/0043-1648(88)90134-2 (cit. on pp. 18 sq.).

[56] Archard J.F. "Contact and rubbing of flat surfaces". *Journal of applied physics* 24.8 (1953), pp. 981–988. DOI: 10.1063/1.1721448 (cit. on pp. 18, 20, 28, 101).

[57] Williams J.A. "Wear modelling: analytical, computational and mapping: a continuum mechanics approach". *Wear* 225 (1999), pp. 1–17. DOI: 10.1016/S0043-1648(99)00060-5 (cit. on p. 20).

[58] Lancaster J.K. "Wear mechanisms of metals and polymers". *Transactions of the IMF* 56.1 (1978), pp. 145–153. DOI: 10.1080/00202967.1978.11870471 (cit. on p. 20).

[59] Bhansali K.J. "Adhesive wear of nickel-and cobalt-base alloys". *Wear* 60.1 (1980), pp. 95–110. DOI: 10.1016/0043-1648(80)90251-3 (cit. on p. 20).

[60] Rabinowicz E. "An adhesive wear model based on variations in strength values". *Wear* 63.1 (1980), pp. 175–181. DOI: 10.1016/0043-1648(80)90085-X (cit. on p. 20).

[61] Fouvry S., Liskiewicz T., Kapsa P., Hannel S. and Sauger E. "An energy description of wear mechanisms and its applications to oscillating sliding contacts". *Wear* 255.1-6 (2003), pp. 287–298. DOI: 10.1016/S0043-1648(03)00117-0 (cit. on pp. 20 sq., 99 sqq.).

[62] Fouvry S., Kapsa P., Zahouani H. and Vincent L. "Wear analysis in fretting of hard coatings through a dissipated energy concept". *Wear* 203 (1997), pp. 393–403. DOI: 10.1016/S0043-1648(96)07436-4 (cit. on p. 21).

[63] Fouvry S., Duo P. and Perruchaut Ph. "A quantitative approach of Ti–6Al–4V fretting damage: friction, wear and crack nucleation". *Wear* 257.9-10 (2004), pp. 916–929. DOI: 10.1016/j.wear.2004.05.011 (cit. on pp. 21, 101).

[64] Dragon-Louiset M. "On a predictive macroscopic contact-sliding wear model based on micromechanical considerations". *International journal of solids and structures* 38.9 (2001), pp. 1625–1639. DOI: 10.1016/S0020-7683(00)00065-2 (cit. on p. 21).

[65] Godet M. "The third-body approach: a mechanical view of wear". *Wear* 100.1-3 (1984), pp. 437–452. DOI: 10.1016/0043-1648(84)90025-5 (cit. on p. 21).

[66] Godet M. "Third-bodies in tribology". *Wear* 136.1 (1990), pp. 29–45. DOI: 10.1016/0043-1648(90)90070-Q (cit. on p. 22).

[67] Berthier Y. "Maurice Godet's third body". *Tribology series*. Vol. 31. 1996, pp. 21–30. DOI: 10.1016/S0167-8922(08)70766-1 (cit. on p. 22).

[68] Denape J. "Third body concept and wear particle behavior in dry friction sliding conditions". *Key Engineering Materials*. Vol. 640. Trans Tech Publ. 2015, pp. 1–12. DOI: 10.4028/www.scientific.net/KEM.640.1 (cit. on p. 23).

[69] Iordanoff I., Berthier Y., Descartes S. and Hesmat H. "A review of recent approaches for modeling solid third bodies". *J. Trib.* 124.4 (2002), pp. 725–735. DOI: 10.1115/1.1467632 (cit. on pp. 23, 25).

[70] Temizer I. and Wriggers P. "A multiscale contact homogenization technique for the modeling of third bodies in the contact interface". *Computer Methods in Applied Mechanics and Engineering* 198.3-4 (2008), pp. 377–396. DOI: 10.1016/j.cma.2008.08.008 (cit. on p. 23).

[71] Bayada G., Chambat M., Lhalouani K. and Licht C. "Third Body Theoretical and Numerical Behaviour by Asymptotic Method". *Tribology Series* 27 (1994), pp. 415–415. DOI: 10.1016/S0167-8922(08)70327-4 (cit. on p. 23).

[72] Linck V., Bayada G., Baillet L., Sassi T. and Sabil J. "Finite element analysis of a contact with friction between an elastic body and a thin soft layer". *J. Trib.* 127.3 (2005), pp. 461–468. DOI: 10.1115/1.1866170 (cit. on p. 23).

[73] Johnson K.L. *Contact Mechanics*. 1987. ISBN: 9780521347969 (cit. on p. 24).

[74] Sackfield A. and Hills D.A. "Some useful results in the classical Hertz contact problem". *The Journal of Strain Analysis for Engineering Design* 18.2 (1983), pp. 101–105. DOI: 10.1243/03093247V182101 (cit. on p. 24).

[75] Nowell D.D. and Hills D.D. "Mechanics of fretting fatigue tests". *International Journal of Mechanical Sciences* 29.5 (1987), pp. 355–365 (cit. on p. 24).

[76] Goryacheva I.G., Rajeev P.T., and Farris T.N. "Wear in partial slip contact". *J. Trib.* 123.4 (2001), pp. 848–856. DOI: 10.1115/1.1338476 (cit. on p. 24).

[77] Andresen H., Hills D.A. and Vázquez J. "Closed-form solutions for tilted three-part piecewise-quadratic half-plane contacts". *International Journal of Mechanical Sciences* 150 (2019), pp. 127–134. DOI: 10.1016/j.ijmecsci.2018.09.024 (cit. on p. 25).

[78] Andresen H., Hills D.A., Barber J.R. and Vázquez J. "Frictional half-plane contact problems subject to alternating normal and shear loads and tension in the steady state". *International Journal of Solids and Structures* 168 (2019), pp. 166–171. DOI: 10.1016/j.ijsolstr.2019.03.025 (cit. on p. 25).

[79] Andresen H., Hills D.A., Barber J.R. and Vázquez J. "Steady state cyclic behaviour of a half-plane contact in partial slip subject to varying normal load, moment, shear load, and moderate differential bulk tension". *International Journal of Solids and Structures* 182 (2020), pp. 156–161. DOI: 10.1016/j.ijsolstr.2019.07.027 (cit. on p. 25).

[80] Chauda G. and Segalman D.J. "Two-Dimensional Contact Analysis Using Trigonometric Polynomials: Some Early Verification Problems". *International Design Engineering Technical Conferences and Computers and Information in Engineering Conference*. Vol. 51852. American Society of Mechanical Engineers. 2018, V008T10A015. doi: 10.1115/DETC2018-86099 (cit. on p. 25).

[81] Zienkiewicz O.C. and Taylor R.L. *The finite element method: solid mechanics*. Vol. 2. 2000 (cit. on p. 25).

[82] Wriggers P. and Laursen T.A. *Computational contact mechanics*. Vol. 2. 2006 (cit. on p. 25).

[83] Johansson L. "Numerical simulation of contact pressure evolution in fretting" (1994). doi: 10.1115/1.2927205 (cit. on p. 25).

[84] McColl I.R., Ding J. and Leen S.B. "Finite element simulation and experimental validation of fretting wear". *Wear* 256.11-12 (2004), pp. 1114–1127. doi: 10.1016/j.wear.2003.07.001 (cit. on pp. 25, 99).

[85] Paulin C., Fouvry S. and Meunier C. "Finite element modelling of fretting wear surface evolution: Application to a Ti–6A1–4V contact". *Wear* 264.1-2 (2008), pp. 26–36. doi: /10.1016/j.wear.2007.01.037 (cit. on p. 25).

[86] Banerjee P.K.,Banerjee P.K. and Butterfield R. *Boundary element methods in engineering science*. 1981 (cit. on p. 25).

[87] Man K.W. *Contact mechanics using boundary elements*. 1994 (cit. on p. 25).

[88] Sfantos G.K. and Aliabadi M.H. "Wear simulation using an incremental sliding boundary element method". *Wear* 260.9-10 (2006), pp. 1119–1128. doi: 10.1016/j.wear.2005.07.020 (cit. on p. 25).

[89] Sfantos G.K. and Aliabadi M.H. "Application of BEM and optimization technique to wear problems". *International journal of solids and structures* 43.11-12 (2006), pp. 3626–3642. doi: 10.1016/j.ijsolstr.2005.09.004 (cit. on p. 25).

[90] Kim T.W., Moon S.M. and Cho Y.J. "Prediction of fretting wear using boundary element method". *Tribology international* 44.11 (2011), pp. 1571–1576. doi: 10.1016/j.triboint.2010.10.009 (cit. on p. 25).

[91] Rodríguez-Tembleque L., Abascal R. and Aliabadi M.H. "Anisotropic fretting wear simulation using the boundary element method". *Computer Modeling in Engineering & Sciences(CMES)* 87.2 (2012), pp. 127–156 (cit. on p. 25).

[92] Aliabadi M.H. *The boundary element method, volume 2: applications in solids and structures*. Vol. 2. 2002 (cit. on p. 25).

[93] Fillot N., Iordanoff I. and Berthier Y. "Modelling third body flows with a discrete element method—a tool for understanding wear with adhesive particles". *Tribology International* 40.6 (2007), pp. 973–981. doi: 10.1016/j.triboint.2006.02.056 (cit. on p. 25).

[94] Leonard B.D. "An experimental and numerical investigation of the effect of coatings and the third body on fretting wear". PhD thesis. Purdue University, 2012 (cit. on p. 25).

[95] Leonard B.D., Patil P., Slack T.S., Sadeghi F., Shinde S. and Mittelbach M. "Fretting wear modeling of coated and uncoated surfaces using the combined finite-discrete element method". *Journal of tribology* 133.2 (2011). doi: 10.1115/1.4003482 (cit. on pp. 25, 27).

[96] Podra P. and Andersson S. "Simulating sliding wear with finite element method". *Tribology international* 32.2 (1999), pp. 71–81. doi: doi.org/10.1016/S0301-679X(99)00012-2 (cit. on p. 25).

[97] Varenberg M.,Halperin, G. and Etsion I. "Different aspects of the role of wear debris in fretting wear". *Wear* 252.11-12 (2002), pp. 902–910. doi: 10.1016/S0043-1648(02)00044-3 (cit. on p. 25).

[98] Paulin C., Fouvry S. and Deyber S. "Wear kinetics of Ti–6Al–4V under constant and variable fretting sliding conditions". *Wear* 259.1-6 (2005), pp. 292–299. doi: 10.1016/j.wear.2005.01.034 (cit. on pp. 25, 98).

[99] Knudsen J. "Vibro-impact dynamics of fretting wear". PhD thesis. Luleå tekniska universitet, 2001 (cit. on p. 26).

[100] Knudsen J. and Massih A.R. "Impact oscillations and wear of loosely supported rod subject to harmonic load". *Journal of sound and vibration* 278.4-5 (2004), pp. 1025–1050. doi: 10.1016/j.jsv.2003.10.060 (cit. on p. 26).

[101] Salles L., Gouskov A.M., Blanc L., Thouverez F. and Pierrick J. "Dynamic analysis of fretting-wear in joint interface by a multiscale harmonic balance method coupled with explicit or implicit integration schemes". *Turbo Expo: Power for Land, Sea, and Air*. Vol. 44014. 2010, pp. 1003–1013. doi: 10.1115/GT2010-23264 (cit. on pp. 26, 28, 67, 71).

[102] Krack M. and Gross J. *Harmonic balance for nonlinear vibration problems*. Vol. 1. 2019 (cit. on pp. 26, 28, 38, 47).

[103] Nacivet S., Pierre C., Thouverez F. and Jezequel L. "A dynamic Lagrangian frequency–time method for the vibration of dry-friction-damped systems". *Journal of Sound and Vibration* 265.1 (2003), pp. 201–219. issn: 0022-460X. doi: 10.1016/S0022-460X(02)01447-5 (cit. on pp. 26, 50, 54).

[104] Gallégo L. "Fretting et usure des contacts mécaniques: modélisation numérique". PhD thesis. Lyon, INSA, 2007 (cit. on p. 26).

[105] Armand J., Pesaresi L., Salles L. and Schwingshackl C.W. "A multiscale approach for nonlinear dynamic response predictions with fretting wear". *Turbo Expo: Power for Land, Sea, and Air*. Vol. 49835. American Society of Mechanical Engineers. 2016, V07AT32A003. doi: 10.1115/GT2016-56201 (cit. on p. 26).

[106] Armand J., Salles L., Schwingshackl C.W., Süss D. and Willner K. "On the effects of roughness on the nonlinear dynamics of a bolted joint: A multiscale analysis". *European Journal of Mechanics-A/Solids* 70 (2018), pp. 44–57. doi: j.euromechsol.2018.01.005 (cit. on p. 26).

[107] Earles S.W.E. and Williams E.J. "A linearized analysis for frictionally damped systems". *Journal of Sound and Vibration* 24.4 (1972), pp. 445–458. doi: 10.1016/0022-460X(72)90716-X (cit. on p. 27).

[108] Williams E.J. and Earles S.W.E. "Optimization of the response of frictionally damped beam type structures with reference to gas turbine compressor blading" (1974). doi: doi.org/10.1115/1.3438353 (cit. on p. 27).

[109] Rimkunas D.A. and Frye H.M. *Investigation of Fan Blade Shroud Mechanical Damping*. Tech. rep. PRATT and WHITNEY AIRCRAFT GROUP WEST PALM BEACH FL GOVERNMENT PRODUCTS DIV, 1979 (cit. on p. 27).

[110] Charleux D., Gibert C., Thouverez F. and Dupeux J. "Numerical and experimental study of friction damping blade attachments of rotating bladed disks". *International Journal of Rotating Machinery* 2006 (2006). doi: 10.1155/IJRM/2006/71302 (cit. on pp. 27, 55).

[111] Pierrick J., Gibert C., Dupont C. and Lombard J-P. "Test-model correlation of dry-friction damping phenomena in aero-engines". *Turbo Expo: Power for Land, Sea, and Air*. Vol. 43154. 2008, pp. 481–491. doi: 10.1115/GT2008-50891 (cit. on p. 27).

[112] Sever I. A., Petrov E. P. and Ewins D.J. "Experimental and numerical investigation of rotating bladed disk forced response using underplatform friction dampers". *Journal of engineering for gas turbines and power* 130.4 (2008). doi: 10.1115/1.2903845 (cit. on p. 27).

[113] Sextro W. "The calculation of the forced response of shrouded blades with friction contacts and its experimental verification". *Turbo Expo: Power for Land, Sea, and Air*. Vol. 78576. American Society of Mechanical Engineers. 2000, V004T03A067. doi: 10.1115/2000-GT-0540 (cit. on p. 27).

[114] Arnaud P., Fouvry S. and Garcin S. "A numerical simulation of fretting wear profile taking account of the evolution of third body layer". *Wear* 376 (2017), pp. 1475–1488. doi: 10.1016/j.wear.2017.01.063 (cit. on p. 27).

[115] Li D., Botto D., Xu C. and Gola M. "Fretting wear of bolted joint interfaces". *Wear* 458 (2020), p. 203411. doi: 10.1016/j.wear.2020.203411 (cit. on p. 27).

[116] Li D., Xu C., Li R. and Zhang W. "Contact parameters evolution of bolted joint interface under transversal random vibrations". *Wear* 500 (2022), p. 204351. doi: 10.1016/j.wear.2022.204351 (cit. on p. 27).

[117] Levy G. "Modelling of Coulomb damping and wear of vibrating systems". *Wear* 64.1 (1980), pp. 57–82. doi: 10.1016/0043-1648(80)90094-0 (cit. on p. 27).

[118] Pettigrew M.J. and Taylor C.E. "Vibration analysis of shell-and-tube heat exchangers: an overview—Part 2: vibration response, fretting-wear, guidelines". *Journal of Fluids and Structures* 18.5 (2003), pp. 485–500. doi: 10.1016/j.jfluidstructs.2003.08.008 (cit. on p. 27).

[119] Sextro W. and Poli C. "Dynamical Contact Problems with Friction: Models, Methods, Experiments and Applications. Lecture Notes in Applied Mechanics, Vol 3". *Appl. Mech. Rev.* 56.1 (2003), B2–B3. doi: 10.1115/1.1523352 (cit. on p. 27).

[120] Berthier Y., Colombié C., Vincent L. and Godet M. "Fretting wear mechanisms and their effects on fretting fatigue" (1988). doi: doi.org/10.1115/1.3261663 (cit. on p. 27).

[121] Söderberg S., Bryggman U. and McCullough T. "Frequency effects in fretting wear". *Wear* 110.1 (1986), pp. 19–34. DOI: 10.1016/0043-1648(86)90149-3 (cit. on p. 27).

[122] Fantetti A. and Schwingshackl C.W. "Effect of friction on the structural dynamics of built-up structures: an experimental study". *Turbo Expo: Power for Land, Sea, and Air*. Vol. 84232. American Society of Mechanical Engineers. 2020, V011T30A021. DOI: 10.1115/GT2020-14945 (cit. on pp. 28, 80, 88, 99).

[123] Nacivet S. "Modélisation du frottement en pied d'aube par une approche fréquentielle". PhD thesis. École Centrale de Lyon, 2002 (cit. on pp. 28, 50, 52, 54, 59, 115).

[124] Salles L., Blanc L., Thouverez F., Gouskov A.M. "Dynamic analysis of fretting-wear in friction contact interfaces". *Turbo Expo: Power for Land, Sea, and Air*. Vol. 43154. 2008, pp. 543–554. DOI: doi.org/10.1115/GT2008-51112 (cit. on pp. 28, 59, 65, 116).

[125] Meirovitch L. *Fundamentals of vibrations*. 2010 (cit. on pp. 32, 63).

[126] Liu M. and Gorman D.G. "Formulation of Rayleigh damping and its extensions". *Computers & structures* 57.2 (1995), pp. 277–285. DOI: 10.1016/0045-7949(94)00611-6 (cit. on p. 33).

[127] Rafiee M., Nitzsche F. and Labrosse M. "Dynamics, vibration and control of rotating composite beams and blades: A critical review". *Thin-Walled Structures* 119 (2017), pp. 795–819. DOI: 10.1016/j.tws.2017.06.018 (cit. on p. 34).

[128] Martin A. *Réduction en dynamique non-linéaire géométrique: Application au cas des structures à symétrie cyclique*. 2019. URL: https://hal.archives-ouvertes.fr/tel-02476146 (cit. on pp. 34, 46).

[129] Gérardin M. and Rixen D. *Théorie des vibrations : application à la dynamique des structures*. fre. Collection Physique fondamentale et appliquée. Paris [etc, 1993. ISBN: 2-225-83952-2 (cit. on pp. 35, 49).

[130] Dormand J. R. and Prince P.J. "A family of embedded Runge-Kutta formulae". *Journal of computational and applied mathematics* 6.1 (1980), pp. 19–26. DOI: 10.1016/0771-050X(80)90013-3 (cit. on p. 36).

[131] Newmark N.M. "A method of computation for structural dynamics". *Journal of the engineering mechanics division* 85.3 (1959), pp. 67–94. DOI: 10.1061/JMCEA3.0000098 (cit. on p. 36).

[132] Sundararajan P. and Noah S.T. "Dynamics of forced nonlinear systems using shooting/arc-length continuation method—application to rotor systems" (1997) (cit. on p. 37).

[133] Jones S. and Legrand M. "Vibrations of mechanical systems undergoing regularized unilateral contact conditions through the wavelet balance method" (2013) (cit. on p. 37).

[134] Urabe M. *Galerkin's procedure for nonlinear periodic systems*. Tech. rep. Wisconsin Univ Madison Mathematics Research Center, 1964. DOI: 10.1007/BF00284614 (cit. on p. 38).

[135] Lau S.L. and Zhang W-S. "Nonlinear vibrations of piecewise-linear systems by incremental harmonic balance method" (1992). DOI: 10.1115/1.2899421 (cit. on p. 38).

[136] Guskov M. *Dynamique non-linéaire des systèmes multirotors. Etudes numérique et expérimentale*. 2007. URL: https://tel.archives-ouvertes.fr/tel-00438353 (cit. on p. 38).

[137] Grolet A. and Thouverez F. "On a new harmonic selection technique for harmonic balance method". *Mechanical Systems and Signal Processing* 30 (2012), pp. 43–60. DOI: 10.1016/j.ymssp.2012.01.024 (cit. on p. 38).

[138] Petrov E.P. and Ewins D.J. "Models of friction damping with variable normal load for time-domain analysis of vibrations". *Proceedings of ISMA*. Vol. 1. 2002 (cit. on p. 40).

[139] Ciğeroğlu E. and Özgüven H.N. "Nonlinear vibration analysis of bladed disks with dry friction dampers". *Journal of Sound and Vibration* 295.3-5 (2006), pp. 1028–1043. DOI: 10.1016/j.jsv.2006.02.009 (cit. on p. 40).

[140] Cameron T.M. and Griffin J.H. "An alternating frequency/time domain method for calculating the steady-state response of nonlinear dynamic systems" (1989). DOI: 10.1115/1.3176036 (cit. on p. 40).

[141] Gruin M. "Dynamique non-linéaire d'une roue de turbine Basse Pression soumise à des excitations structurales d'un turboréacteur". PhD thesis. École Centrale de Lyon, 2012 (cit. on p. 40).

[142] Shannon C.E. "Communication in the presence of noise". *Proceedings of the IRE* 37.1 (1949), pp. 10–21. DOI: 10.1109/JRPROC.1949.232969 (cit. on p. 41).

[143] Fletcher R. *Practical methods of optimization*. 2013 (cit. on p. 42).

[144] Knoll D.A. and Keyes D.E. "Jacobian-free Newton–Krylov methods: a survey of approaches and applications". *Journal of Computational Physics* 193.2 (2004), pp. 357–397. DOI: 10.1016/j.jcp.2003.08.010 (cit. on p. 42).

[145] Conn A.R., Gould N.I. and Toint P.L. *Trust region methods. MPS-SIAM Series on Optimization, SIAM*. DOI: 10.1137/1.9780898719857 (cit. on p. 42).

[146] Lau S.L., Cheung Y.K. and Wu S-Y. "Incremental harmonic balance method with multiple time scales for aperiodic vibration of nonlinear systems" (1983). DOI: 10.1115/1.3167160 (cit. on p. 42).

[147] Keller, H.B. "Lectures on numerical methods in bifurcation problems". *Applied Mathematics* 217 (1987), p. 50 (cit. on p. 46).

[148] Cochelin B. and Vergez C. "A high order purely frequency-based harmonic balance formulation for continuation of periodic solutions". *Journal of sound and vibration* 324.1-2 (2009), pp. 243–262. DOI: 10.1016/j.jsv.2009.01.054 (cit. on p. 46).

[149] Karkar S., Cochelin B. and Vergez C. "A high-order, purely frequency based harmonic balance formulation for continuation of periodic solutions: The case of non-polynomial nonlinearities". *Journal of Sound and Vibration* 332.4 (2013), pp. 968–977. DOI: 10.1016/j.jsv.2012.09.033 (cit. on p. 46).

[150] Woiwode L., Balaji N.N., Kappauf J., Tubita F., Guillot L., Vergez C., Cochelin B., Grolet A. and Krack M. "Comparison of two algorithms for Harmonic Balance and path continuation". *Mechanical Systems and Signal Processing* 136 (2020), p. 106503. ISSN: 0888-3270. DOI: 10.1016/j.ymssp.2019.106503 (cit. on p. 47).

[151] Krack M. and Gross J. *Nlvib – a Matlab tool for nonlinear vibration problems*. URL: https://www.ila.uni-stuttgart.de/nlvib (cit. on p. 47).

[152] Karkar S., Vergez C., Thomas O. and Lazarus A. *Manlab user guide*. 2012. URL: http://manlab.lma.cnrs-mrs.fr/spip/ (cit. on p. 47).

[153] Petrov E.P. "A high-accuracy model reduction for analysis of nonlinear vibrations in structures with contact interfaces". *Journal of Engineering for Gas Turbines and Power* 133.10 (2011). DOI: 10.1115/1.4002810 (cit. on p. 48).

[154] Hurty W.C. "Dynamic analysis of structural systems using component modes". *AIAA journal* 3.4 (1965), pp. 678–685. DOI: 10.2514/3.2947 (cit. on p. 48).

[155] Craig Jr R.R. and Bampton M.C.C. "Coupling of substructures for dynamic analyses." *AIAA journal* 6.7 (1968), pp. 1313–1319. DOI: 10.2514/3.4741 (cit. on pp. 48, 84).

[156] Hou S.N. *Review of modal synthesis techniques and a new approach*. Tech. rep. 1969 (cit. on p. 48).

[157] McNeal R.H. "A hybrid method of component mode synthesis". *Computers & Structures* 1.4 (1971), pp. 581–601. DOI: 10.1016/0045-7949(71)90031-9 (cit. on p. 48).

[158] Allemang R.J. "A correlation coefficient for modal vector analysis". *Proc. 1st Int. Modal Analysis Conference*. 1982, pp. 110–116 (cit. on p. 50).

[159] Charleux D. "Etude des effets de la friction en pied d'aube sur la dynamique des roues aubagées". PhD thesis. Ecole Centrale de Lyon, 2006 (cit. on pp. 50, 55).

[160] Laxalde D., Thouverez F., Sinou J.J. and Lombard J.P. "Qualitative analysis of forced response of blisks with friction ring dampers". *European Journal of Mechanics-A/Solids* 26.4 (2007), pp. 676–687. DOI: 10.1016/j.euromechsol.2006.10.002 (cit. on p. 50).

[161] Salles L. "Etude de l'usure par fretting sous chargements dynamiques dans les interfaces frottantes: Application aux pieds d'aubes de turbomachines". PhD thesis. Ecully, Ecole centrale de Lyon, 2010 (cit. on pp. 50, 60, 62, 105, 115).

[162] Moreau J.J. "New variational techniques in mathematical physics". *CISM Course. Springer Berlin* 52 (1974), p. 53 (cit. on p. 60).

[163] Klarbring A. "Derivation and analysis of rate boundary-value problems of frictional contact". *European journal of mechanics. A. Solids* 9.1 (1990), pp. 53–85 (cit. on p. 60).

[164] Lemaitre J. and Chaboche J-L. *Mechanics of solid materials*. 1994 (cit. on p. 60).

[165] Oskay C. and Fish J. "Fatigue life prediction using 2-scale temporal asymptotic homogenization". *International Journal for Numerical Methods in Engineering* 61.3 (2004), pp. 329–359. DOI: 10.1080/15376490500259319 (cit. on p. 62).

[166] Gallego L., Fulleringer B., Deyber S. and Nélias D. "Multiscale computation of fretting wear at the blade/disk interface". *Tribology International* 43.4 (2010), pp. 708–718. ISSN: 0301-679X. DOI: 10.1016/j.triboint.2009.10.011 (cit. on p. 65).

[167] Schwingshackl C.W. "Measurement of friction contact parameters for nonlinear dynamic analysis". *Topics in Modal Analysis I, Volume 5*. 2012, pp. 167–177. DOI: 10.1007/978-1-4614-2425-3_16 (cit. on p. 77).

[168] Filippi S., Akay A. and Gola M.M. "Measurement of tangential contact hysteresis during microslip". *J. Trib.* 126.3 (2004), pp. 482–489. DOI: 10.1115/1.1692030 (cit. on p. 98).

[169] Schwingshackl CW, Petrov E.P. and Ewins D.J. "Validation of test rig measurements and prediction tools for friction interface modelling". *Turbo Expo: Power for Land, Sea, and Air*. Vol. 44014. 2010, pp. 1015–1024. DOI: 10.1115/GT2010-23274 (cit. on p. 98).

[170] Lavella M., Botto D. and Gola M.M. "Test rig for wear and contact parameters extraction for flat-on-flat contact surfaces". *International Joint Tribology Conference*. Vol. 54747. 2011, pp. 307–309. DOI: 10.1115/IJTC2011-61234 (cit. on p. 98).

[171] Botto D. and Umer M. "A novel test rig to investigate under-platform damper dynamics". *Mechanical Systems and Signal Processing* 100 (2018), pp. 344–359. DOI: 10.1016/j.ymssp.2017.07.046 (cit. on p. 98).

[172] Ferhatoglu E., Gastaldi C., Botto D. and Zucca S. "An experimental and computational comparison of the dynamic response variability in a turbine blade with under-platform dampers". *Mechanical Systems and Signal Processing* 172 (2022), p. 108987. DOI: 10.1016/j.ymssp.2022.108987 (cit. on p. 98).

[173] Tamatam L.R., Botto D. and Zucca S. "A novel test rig to study the effect of fretting wear on the forced response dynamics with a friction contact". *Nonlinear Dynamics* 105.2 (2021), pp. 1405–1426. DOI: 10.1007/s11071-021-06658-y (cit. on p. 98).

[174] Mary C. and Fouvry S. "Numerical prediction of fretting contact durability using energy wear approach: Optimisation of finite-element model". *Wear* 263.1-6 (2007), pp. 444–450. DOI: 10.1016/j.wear.2007.01.116 (cit. on p. 98).

[175] Berthier Y.,Godet M. and Brendle M. "Velocity accommodation in friction". *Tribology Transactions* 32.4 (1989), pp. 490–496. DOI: 10.1080/10402008908981917 (cit. on p. 99).

[176] Sauger E., Fouvry S., Ponsonnet L., Kapsa P., Martin J.M. and Vincent .L. "Tribologically transformed structure in fretting". *Wear* 245.1-2 (2000), pp. 39–52. DOI: 10.1016/S0043-1648(00)00464-6 (cit. on p. 99).

[177] Tongyan Y. and Wahab M.A. "Finite element analysis of fretting wear under variable coefficient of friction and different contact regimes". *Tribology International* 107 (2017), pp. 274–282. DOI: 10.1016/j.triboint.2016.11.044 (cit. on p. 99).

[178] Milestone W.D. and Janeczko J.T. "Friction between steel surfaces during fretting". *Wear* 18.1 (1971), pp. 29–40. DOI: 10.1016/j.triboint.2016.11.044 (cit. on p. 99).

[179] Vijay R., Kumar V.N. Aju, Sadiq A. and Pillai R. Rakesh. "Numerical analysis of wear characteristics of zirconia coated aluminum 6061 alloy". *IOP Conference Series: Materials Science and Engineering*. Vol. 1059. 1. IOP Publishing. 2021, p. 012020. DOI: 10.1088/1757-899X/1059/1/012020 (cit. on p. 100).

[180] Alvi S., Saeidi K. and Akhtar F. "High-temperature tribology and wear of selective laser melted (SLM) 316L stainless steel". *Wear* 448 (2020), pp. 203–228. DOI: 10.1016/j.wear.2020.203228 (cit. on p. 102).

[181] Lawal Y.G. "A computational mechanics framework for modeling tribology experiments with friction and wear". PhD thesis. Rice University, 2021 (cit. on pp. 102 sq.).

[182] Farhat C. and Roux F-X. "A method of finite element tearing and interconnecting and its parallel solution algorithm". *International journal for numerical methods in engineering* 32.6 (1991), pp. 1205–1227. DOI: 10.1002/nme.1620320604 (cit. on p. 117).

[183] Jenovencio G., Sivasankar A., Saeed Z. and Rixen D. "A Delayed frequency preconditioner approach for speeding-up frequency response computation of structural components". *XI International Conference on Structural Dynamics*. 2020. DOI: 10.47964/1120.9005.19155 (cit. on p. 117).

[184] Basseville S., Proudhon H., Héripré E. and Cailletaud G. "Étude numérique des paramètres affectant les profils d'usure en fretting". *Matériaux & Techniques* 101.2 (2013), p. 207. DOI: 10.1051/mattech/2013069 (cit. on p. 118).

Appendix A

Evaluation of the analytical Jacobian matrix

1 Analytical Jacobian matrix of a nonlinear problem

The evaluation of the Jacobian matrix can be done numerically by finite differences. However, this strategy is computationally expensive because it needs to be repeated at each iteration of the resolution algorithm. The compact form in the frequency domain of the nonlinear dynamic system to solve is:

$$\mathbf{r}(\tilde{\mathbf{u}}, \omega) = \mathbf{Z}(\omega)\tilde{\mathbf{u}} + \tilde{\mathbf{f}}_{\mathbf{nl}}(\tilde{\mathbf{u}}, \omega) - \tilde{\mathbf{f}}_{\mathbf{ex}}. \tag{A.1}$$

The analytic Jacobian matrix $\mathbf{J}$ is calculated from the partial derivatives of the system (A.1), with respect to the variables $\mathbf{u}$ and ω and is given by:

$$\mathbf{J}(\tilde{\mathbf{u}}, \omega) = \left(\frac{\partial \mathbf{r}(\tilde{\mathbf{u}}, \omega)}{\partial \tilde{\mathbf{u}}} \quad \frac{\partial \mathbf{r}(\tilde{\mathbf{u}}, \omega)}{\partial \omega} \right) \tag{A.2}$$

. The partial derivatives of the residual function $\mathbf{r}(\tilde{\mathbf{u}}, \omega)$ are then expressed as:

$$\frac{\partial \mathbf{r}(\tilde{\mathbf{u}}, \omega)}{\partial \tilde{\mathbf{u}}} = \mathbf{Z}(\omega) + \frac{\partial \tilde{\mathbf{f}}_{\mathbf{nl}}(\tilde{\mathbf{u}}, \omega)}{\partial \tilde{\mathbf{u}}}, \tag{A.3}$$

$$\frac{\partial \mathbf{r}(\tilde{\mathbf{u}}, \omega)}{\partial \omega} = \frac{\partial \mathbf{Z}(\omega)}{\partial \omega}\tilde{\mathbf{u}} + \frac{\partial \tilde{\mathbf{f}}_{\mathbf{nl}}(\tilde{\mathbf{u}}, \omega)}{\partial \omega}, \tag{A.4}$$

in which the partial derivatives of the vector $\tilde{\mathbf{f}}_{\mathbf{ex}}$ do not appear in Eqs. (A.3) and (A.4), since the excitation force depends neither on $\tilde{\mathbf{u}}$ neither on ω in the frequency domain.

Dynamic stiffness matrix. The partial derivative of the dynamic stiffness matrix with respect to ω keeps the block-diagonal form of the dynamic stiffness matrix $\mathbf{Z}$. Its expression is:

$$\frac{\partial \mathbf{Z}(\omega)}{\partial \omega} = \begin{bmatrix} 0 & & & & & \\ & \frac{\partial \mathbf{Z}_1(\omega)}{\partial \omega} & & & & \\ & & \ddots & & & \\ & & & \frac{\partial \mathbf{Z}_k(\omega)}{\partial \omega} & & \\ & & & & \ddots & \\ & & & & & \frac{\partial \mathbf{Z}_{N_h}(\omega)}{\partial \omega} \end{bmatrix}, \tag{A.5}$$

whose each k_{th} block defines the derivative of the dynamic stiffness matrix for the k_{th} harmonic:

$$\frac{\partial \mathbf{Z}_k(\omega)}{\partial \omega} = \begin{bmatrix} -2k^2\omega\mathbf{M} & k\mathbf{C} \\ -k\mathbf{C} & -2k^2\omega\mathbf{M} \end{bmatrix} \quad k = 1, \dots, N_h. \tag{A.6}$$

Nonlinear terms. The terms of the Jacobian matrix relating to the derivation of the nonlinear forces $\tilde{\mathbf{f}}_{\mathbf{nl}}$ are evaluated by derivating directly its temporal analytical expression $\mathbf{f}_{\mathbf{nl}}(\mathbf{u}(t), \dot{\mathbf{u}}(t))$, with respect to the variables $\mathbf{u}$ and $\dot{\mathbf{u}}$.

$$\frac{\partial \tilde{\mathbf{f}}_{\mathbf{nl}}(\tilde{\mathbf{u}}, \omega)}{\partial \tilde{\mathbf{u}}} = \mathcal{F}\frac{\partial \mathbf{f}_{\mathbf{nl}}}{\partial \mathbf{u}}\bar{\mathcal{F}} + \mathcal{F}\frac{\partial \mathbf{f}_{\mathbf{nl}}}{\partial \dot{\mathbf{u}}}\bar{\mathcal{F}}\nabla(\omega), \tag{A.7}$$

$$\frac{\partial \tilde{\mathbf{f}}_{\mathbf{nl}}(\tilde{\mathbf{u}}, \omega)}{\partial \omega} = \mathcal{F}\frac{\partial \mathbf{f}_{\mathbf{nl}}}{\partial \dot{\mathbf{u}}}\bar{\mathcal{F}}\frac{\partial \nabla(\omega)}{\partial \omega}\tilde{\mathbf{u}}. \tag{A.8}$$

The Direct $\mathcal{F}$ and Inverse $\bar{\mathcal{F}}$ Discrete Fourier Transforms, defined by Eqs. (II.38) and (II.44) respectively, can be taken out of the partial derivatives, since not dependant on ω, as already mentioned in section II.2.2.2. The partial derivative of the differential operator ∇ with respect to ω presents also a block-diagonal form whose each k_{th} block, defined for each k_{th} harmonic, is written as:

$$\frac{\partial \nabla_k(\omega)}{\partial \omega} = \begin{bmatrix} 0 & k \\ -k & 0 \end{bmatrix} \otimes \mathbf{I}_{\mathrm{n_{dofs}}}, \quad \forall k \in [1, N_h]. \tag{A.9}$$

Solution continuation. The solution's continuation techniques have been defined in section II.2.3.1. The use of a sequential continuation expressed by the system (II.57) to follow the evolution of the control parameter ω does not require the evaluation of the partial derivatives of the residual $\mathbf{r}$ for ω since it is fixed at each iteration. On the contrary, an arc-length continuation defined by the system (II.58), in addition to requiring the evaluation of the partial derivatives of $\mathbf{r}$ for ω, needs the partial derivatives of the closure equation $\mathbf{p}$, here recalled:

$$\mathbf{p}(\tilde{\mathbf{u}}, \omega) = \|\tilde{\mathbf{u}}_{i+1} - \tilde{\mathbf{u}}_i\|^2 + (\omega_{i+1} - \omega_i)^2 - \mathrm{d}s^2 = 0, \tag{A.10}$$

$$\frac{\partial \mathbf{p}(\tilde{\mathbf{u}}, \omega)}{\partial \tilde{\mathbf{u}}} = 2\tilde{\mathbf{u}}, \tag{A.11}$$

$$\frac{\partial \mathbf{p}(\tilde{\mathbf{u}}, \omega)}{\partial \omega} = 2\omega. \tag{A.12}$$

2 Analytical Jacobian matrix in DLFT formulation

The analytical Jacobian matrix in DLFT is necessary to reduce the computational time of a Newton-Raphson-type resolution algorithm. Remembering the residual function expressed in the section II.2.5.3 by Eq. (II.84):

$$\mathbf{r}(\tilde{\mathbf{u}}_\mathbf{r}) = \mathbf{Z}_\mathbf{r}\tilde{\mathbf{u}}_\mathbf{r} + \tilde{\boldsymbol{\lambda}} - \tilde{\mathbf{f}}_\mathbf{r} \tag{A.13}$$

and the splitting of the contact forces into two terms of prediction $\tilde{\boldsymbol{\lambda}}_\mathbf{u}$ and correction $\tilde{\boldsymbol{\lambda}}_\mathbf{x}$, as defined by Eq. (II.92):

$$\tilde{\boldsymbol{\lambda}} = \tilde{\boldsymbol{\lambda}}_\mathbf{u} - \tilde{\boldsymbol{\lambda}}_\mathbf{x}, \tag{A.14}$$

the Jacobian matrix with respect to the relative displacement $\tilde{\mathbf{u}}_\mathbf{r}$ of the residual function (A.13) is defined as follows:

$$\mathbf{J} = \frac{\mathrm{d}\mathbf{r}(\tilde{\mathbf{u}}_\mathbf{r})}{\mathrm{d}\tilde{\mathbf{u}}_\mathbf{r}}, \tag{A.15}$$

from which, considering the Eq. A.14:

$$\mathbf{J} = \mathbf{Z}_\mathbf{r} + \frac{\mathrm{d}\tilde{\boldsymbol{\lambda}}}{\mathrm{d}\tilde{\mathbf{u}}_\mathbf{r}} = \mathbf{Z}_\mathbf{r} + \left(\frac{\mathrm{d}\tilde{\boldsymbol{\lambda}}_\mathbf{u}}{\mathrm{d}\tilde{\mathbf{u}}_\mathbf{r}} - \frac{\mathrm{d}\tilde{\boldsymbol{\lambda}}_\mathbf{x}}{\mathrm{d}\tilde{\mathbf{u}}_\mathbf{r}}\right). \tag{A.16}$$

The correction term $\tilde{\boldsymbol{\lambda}}_\mathbf{x}$ is determined in the time domain as a function of the predicted contact state: separation, stick or slip as defined in section II.2.5.4 by Eqs. (II.93),(II.94) and (II.95), respectively. For each time instant, the three components of the vector $\boldsymbol{\lambda}_\mathrm{x}^k$ are $\boldsymbol{\lambda}_\mathbf{x}^{k,\mathrm{N}}$ in the normal direction, $\boldsymbol{\lambda}_\mathbf{x}^{k,\mathrm{T1}}$ and $\boldsymbol{\lambda}_\mathbf{x}^{k,\mathrm{T2}}$ in the tangential directions (in an orthonormal basis of the tangential contact plane, perpendicular to the normal $\mathbf{n_c}$, defined in section II.2.1.1).

Following the same scheme introduced in the section II.2.5.4 for each contact condition:

- **Separation:** $\lambda_\mathrm{pre}^{k,\mathrm{N}} \geq \mathrm{N}_{0\mathrm{t}}$, where $\mathrm{N}_{0\mathrm{t}}$ is the static pre-load.

$$\begin{cases} \dfrac{\mathrm{d}\boldsymbol{\lambda}_\mathbf{x}^{k,\mathrm{N}}}{\mathrm{d}\tilde{\mathbf{u}}_\mathbf{r}} = \dfrac{\mathrm{d}\boldsymbol{\lambda}_\mathbf{u}^{k,\mathrm{N}}}{\mathrm{d}\tilde{\mathbf{u}}_\mathbf{r}} \\ \dfrac{\mathrm{d}\boldsymbol{\lambda}_\mathbf{x}^{k,\mathrm{T1}}}{\mathrm{d}\tilde{\mathbf{u}}_\mathbf{r}} = \dfrac{\mathrm{d}\boldsymbol{\lambda}_\mathbf{u}^{k,\mathrm{T1}}}{\mathrm{d}\tilde{\mathbf{u}}_\mathbf{r}} \\ \dfrac{\mathrm{d}\boldsymbol{\lambda}_\mathbf{x}^{k,\mathrm{T2}}}{\mathrm{d}\tilde{\mathbf{u}}_\mathbf{r}} = \dfrac{\mathrm{d}\boldsymbol{\lambda}_\mathbf{u}^{k,\mathrm{T2}}}{\mathrm{d}\tilde{\mathbf{u}}_\mathbf{r}} \end{cases} \tag{A.17}$$

- **Stick:** $\lambda_\mathrm{pre}^{k,\mathrm{N}} < \mathrm{N}_{0\mathrm{t}}$ and $||\boldsymbol{\lambda}_\mathrm{pre}^{k,\mathrm{T}}|| < \mu \left|\lambda_\mathrm{pre}^{k,\mathrm{N}} - N_{0t}\right|$.

$$\begin{cases} \dfrac{\mathrm{d}\boldsymbol{\lambda}_\mathbf{x}^{k,\mathrm{N}}}{\mathrm{d}\tilde{\mathbf{u}}_\mathbf{r}} = 0 \\ \dfrac{\mathrm{d}\boldsymbol{\lambda}_\mathbf{x}^{k,\mathrm{T1}}}{\mathrm{d}\tilde{\mathbf{u}}_\mathbf{r}} = \dfrac{\mathrm{d}\boldsymbol{\lambda}_\mathbf{u}^{k-1,\mathrm{T1}}}{\mathrm{d}\tilde{\mathbf{u}}_\mathbf{r}} \\ \dfrac{\mathrm{d}\boldsymbol{\lambda}_\mathbf{x}^{k,\mathrm{T2}}}{\mathrm{d}\tilde{\mathbf{u}}_\mathbf{r}} = \dfrac{\mathrm{d}\boldsymbol{\lambda}_\mathbf{u}^{k-1,\mathrm{T2}}}{\mathrm{d}\tilde{\mathbf{u}}_\mathbf{r}} \end{cases} \tag{A.18}$$

- **Slip:** $\lambda_{\text{pre}}^{k,\text{N}} < \text{N}_{0\text{t}}$ and $||\boldsymbol{\lambda}_{\text{pre}}^{k,\text{T}}|| \geq \mu \left|\lambda_{\text{pre}}^{k,\text{N}} - N_{0t}\right|$.

$$
\begin{cases}
\dfrac{\text{d}\boldsymbol{\lambda}_{\mathbf{x}}^{k,\text{N}}}{\text{d}\tilde{\mathbf{u}}_{\mathbf{r}}} = 0 \\
\dfrac{\text{d}\boldsymbol{\lambda}_{\mathbf{x}}^{k,\text{T1}}}{\text{d}\tilde{\mathbf{u}}_{\mathbf{r}}} = \dfrac{\text{d}\boldsymbol{\lambda}_{\mathbf{u}}^{k-1,\text{T1}}}{\text{d}\tilde{\mathbf{u}}_{\mathbf{r}}} + \dfrac{\text{d}\boldsymbol{\lambda}_{\text{pre}}^{k,\text{T1}}}{\text{d}\tilde{\mathbf{u}}_{\mathbf{r}}} \left(1 - \mu \dfrac{\left|\lambda_{\text{pre}}^{k,\text{N}} - N_{0t}\right|}{||\boldsymbol{\lambda}_{\text{pre}}^{k,\text{T}}||}\right) + \mu \dfrac{\text{d}\lambda_{\text{pre}}^{k,\text{N}}}{\text{d}\mathbf{u}_{\mathbf{r}}} \dfrac{\boldsymbol{\lambda}_{\text{pre}}^{k,\text{T1}}}{||\boldsymbol{\lambda}_{\text{pre}}^{k,\text{T}}||} \\
\qquad\qquad + \mu \left|\lambda_{\text{pre}}^{k,\text{N}} - N_{0t}\right| \boldsymbol{\lambda}_{\text{pre}}^{k,\text{T1}} \dfrac{\boldsymbol{\lambda}_{\text{pre}}^{k,\text{T1}} \dfrac{\text{d}\boldsymbol{\lambda}_{\text{pre}}^{k,\text{T1}}}{\text{d}\tilde{\mathbf{u}}_{\mathbf{r}}} + \boldsymbol{\lambda}_{\text{pre}}^{k,\text{T2}} \dfrac{\text{d}\boldsymbol{\lambda}_{\text{pre}}^{k,\text{T2}}}{\text{d}\tilde{\mathbf{u}}_{\mathbf{r}}}}{||\boldsymbol{\lambda}_{\text{pre}}^{k,\text{T}}||^3} \\
\dfrac{\text{d}\boldsymbol{\lambda}_{\mathbf{x}}^{k,\text{T2}}}{\text{d}\tilde{\mathbf{u}}_{\mathbf{r}}} = \dfrac{\text{d}\boldsymbol{\lambda}_{\mathbf{u}}^{k-1,\text{T2}}}{\text{d}\tilde{\mathbf{u}}_{\mathbf{r}}} + \dfrac{\text{d}\boldsymbol{\lambda}_{\text{pre}}^{k,\text{T2}}}{\text{d}\tilde{\mathbf{u}}_{\mathbf{r}}} \left(1 - \mu \dfrac{\left|\lambda_{\text{pre}}^{k,\text{N}} - N_{0t}\right|}{||\boldsymbol{\lambda}_{\text{pre}}^{k,\text{T}}||}\right) + \mu \dfrac{\text{d}\lambda_{\text{pre}}^{k,\text{N}}}{\text{d}\mathbf{u}_{\mathbf{r}}} \dfrac{\boldsymbol{\lambda}_{\text{pre}}^{k,\text{T2}}}{||\boldsymbol{\lambda}_{\text{pre}}^{k,\text{T}}||} \\
\qquad\qquad + \mu \left|\lambda_{\text{pre}}^{k,\text{N}} - N_{0t}\right| \boldsymbol{\lambda}_{\text{pre}}^{k,\text{T2}} \dfrac{\boldsymbol{\lambda}_{\text{pre}}^{k,\text{T1}} \dfrac{\text{d}\boldsymbol{\lambda}_{\text{pre}}^{k,\text{T1}}}{\text{d}\tilde{\mathbf{u}}_{\mathbf{r}}} + \boldsymbol{\lambda}_{\text{pre}}^{k,\text{T2}} \dfrac{\text{d}\boldsymbol{\lambda}_{\text{pre}}^{k,\text{T2}}}{\text{d}\tilde{\mathbf{u}}_{\mathbf{r}}}}{||\boldsymbol{\lambda}_{\text{pre}}^{k,\text{T}}||^3}
\end{cases}
\tag{A.19}
$$

Having calculated $\dfrac{\text{d}\boldsymbol{\lambda}_{\mathbf{u}}^{k,\text{T}}}{\text{d}\tilde{\mathbf{u}}_{\mathbf{r}}}$ and $\dfrac{\text{d}\boldsymbol{\lambda}_{\mathbf{x}}^{k,\text{T}}}{\text{d}\tilde{\mathbf{u}}_{\mathbf{r}}}$, it is possible to evaluate:

$$
\frac{\text{d}\boldsymbol{\lambda}_{\mathbf{pre}}^{k,\text{T}}}{\text{d}\tilde{\mathbf{u}}_{\mathbf{r}}} = \frac{\text{d}\boldsymbol{\lambda}_{\mathbf{u}}^{k,\text{T}}}{\text{d}\tilde{\mathbf{u}}_{\mathbf{r}}} - \frac{\text{d}\boldsymbol{\lambda}_{\mathbf{x}}^{k,\text{T}}}{\text{d}\tilde{\mathbf{u}}_{\mathbf{r}}}. \tag{A.20}
$$

In the frequency domain:

- $\dfrac{\text{d}\tilde{\boldsymbol{\lambda}}_{\mathbf{x}}^{\text{T}}}{\text{d}\tilde{\mathbf{u}}_{\mathbf{r}}}$ is calculated through the Discrete Fourier Transform (DFT) of $\left.\dfrac{\text{d}\boldsymbol{\lambda}_{\mathbf{x}}^{k,\text{T}}}{\text{d}\tilde{\mathbf{u}}_{\mathbf{r}}}\right|_{k=1\cdots n_t}$,
- $\dfrac{\text{d}\tilde{\boldsymbol{\lambda}}_{\mathbf{u}}^{\text{T}}}{\text{d}\tilde{\mathbf{u}}_{\mathbf{r}}}$ is calculated by:

$$
\frac{\text{d}\tilde{\boldsymbol{\lambda}}_{\mathbf{u}}^{\text{T}}}{\text{d}\tilde{\mathbf{u}}_{\mathbf{r}}} = \text{IDFT}(-\mathbf{Z}_{\mathbf{r}} + \varepsilon\mathbf{I}), \tag{A.21}
$$

  where $\mathbf{I}$ is the identity matrix (of the same size as $\mathbf{Z}_{\mathbf{r}}$).

dernière page de la thèse

AUTORISATION DE SOUTENANCE

Vu les dispositions de l'arrêté du 25 mai 2016 modifié par l'arrêté du 26 août 2022,

Vu la demande du directeur de thèse

Monsieur F. THOUVEREZ

et les rapports de

Mme E. SADOULET-REBOUL
Maître de Conférences HDR- ENSMM, Département Mécanique Appliquée, équipes V3MQI, D-SMART, UFC - UFR ST, 15B avenue des Montboucons, 25030 Besançon cedex

et de

M. S. ZUCCA
Professeur - Politecnico di Torino, DIMEAS, Corso Duca degli Abruzzi, 24 | 10129 Torino, ITALY

Madame TUBITA Fabia

est autorisée à soutenir une thèse pour l'obtention du grade de **DOCTEUR**

Ecole doctorale Mécanique, Energétique, Génie Civil, Acoustique

Fait à Ecully, le 31 mai 2023

Pour le directeur de l'Ecole centrale de Lyon
Le directeur de la Recherche

Christophe CORRE